Cross-Section Measurement of Single-Top *t*-Channel Production at ATLAS

D I S S E R T A T I O N

zur Erlangung des akademischen Grades

d o c t o r r e r u m n a t u r a l i u m
(Dr. rer. nat.)

im Fach Physik

eingereicht an der
Mathematisch-Naturwissenschaftlichen Fakultät
der Humboldt-Universität zu Berlin

von

Dipl.-Phys. Ruth Hedwig Margarete Herrberg-Schubert

Präsident der Humboldt-Universität zu Berlin:
Prof. Dr. Jan-Hendrik Olbertz

Dekan der Mathematisch-Naturwissenschaftlichen Fakultät:
Prof. Dr. Elmar Kulke

Gutachter:
1. Prof. Dr. Thomas Lohse
2. Prof. Dr. Heiko Lacker
3. PD Dr. Klaus Mönig

Tag der mündlichen Prüfung: 28.04.2014

Für Hedwig, Heinz und Margarete, für Barbara und Rainer
und für den Bären und das Symbiöntchen.

Abstract

This study presents the cross-section measurement of electroweak single-top quark production in the t-channel with a semi-leptonically decaying top quark. The study is based on $4.7\,\mathrm{fb}^{-1}$ of proton-proton collision data recorded with the ATLAS detector at the Large Hadron Collider in the year 2011. Selected events contain two highly energetic jets, one of which is identified as originating from a beauty quark, as well as a highly energetic electron or muon and transverse missing energy. The case of three and four jets is also considered but eventually discarded since their inclusion degrades the precision of the result. The event reconstruction is done with a chi-square-based kinematic fit using W boson and top quark mass constraints. The chi-square value in each event serves to classify the event as a signal-like or background-like process. The cross-section is extracted by performing a template-based maximum likelihood fit to the distribution that displays the best discriminatory power: This distribution is chosen such that the shape differences between signal and background with respect to the typical forward light jet kinematics of the t-channel are exploited. An observation of the single-top t-channel process with a significance of 5.7σ is obtained, and the cross-section is measured to be $111^{+29}_{-28}\,\mathrm{pb}$. Assuming $|V_{\mathrm{tb}}|^2 \gg |V_{\mathrm{td}}|^2 + |V_{\mathrm{ts}}|^2$ as well as a $(\mathrm{V}-\mathrm{A})$, CP-conserving interaction, and allowing for the presence of anomalous couplings at the W-t-b vertex, the associated value of the CKM matrix element times an anomalous form factor is determined as $|V_{\mathrm{tb}} f_1^{\mathrm{L}}| = 1.30^{+0.13}_{-0.16}$. The corresponding lower limit in the standard model scenario $0 \leq |V_{\mathrm{tb}}| \leq 1$ amounts to $0.77 < |V_{\mathrm{tb}}|$ at 95 % confidence level.

Zusammenfassung

Diese Studie stellt die Messung des Wirkungsquerschnitts der elektroschwachen Einzel-Top-Quark-Produktion im t-Kanal vor, bei der das Top-Quark semileptonisch zerfällt. Die Studie basiert auf $4.7\,\mathrm{fb}^{-1}$ an Daten aus Proton-Proton-Kollisionen, die vom ATLAS-Detektor am Large Hadron Collider im Jahr 2011 aufgezeichnet wurden. Die ausgewählten Ereignisse beinhalten zwei hochenergetische Jets, von denen einer als von einem b-Quark stammend identifiziert wurde, sowie ein hochenergetisches Elektron oder Myon und fehlende Transversalenergie. Der Fall von drei und vier Jets wird ebenfalls betrachtet, aber schließlich verworfen, da ihre Miteinbeziehung die Präzision des Ergebnisses herabsetzt. Die Ereignisrekonstruktion erfolgt durch einen Chi-Quadrat-basierten kinematischen Fit mit W-Boson- und Top-Quark-Massenzwangsbedingungen. Der Wert des Chi-Quadrat in jedem Ereignis dient dazu, das Ereignis als signal- oder untergrundähnlich zu klassifizieren. Der Wirkungsquerschnitt wird mittels eines template-basierten Maximum-Likelihood-Fits an die Verteilung, die die beste Trennschärfe besitzt, extrahiert: Die Verteilung is derart gewählt, dass die Formunterschiede zwischen Signal und Untergrund bezüglich der Kinematik des typischen leichten Vorwärtsjets des t-Kanals ausgenutzt werden. Eine Beobachtung des Single-Top-t-Kanal-Prozesses mit einer Signifikanz von 5.7σ wird erreicht, und der Wirkungsquerschnitt wird zu $111^{+29}_{-28}\,\mathrm{pb}$ gemessen. Unter der Annahme $|V_{\mathrm{tb}}|^2 \gg |V_{\mathrm{td}}|^2 + |V_{\mathrm{ts}}|^2$ sowie einer $(\mathrm{V}-\mathrm{A})$-, CP-erhaltenden Wechselwirkung, und unter Berücksichtigung von möglichen anomalen Kopplungen am W-t-b-Vertex, wird der Wert des entsprechenden CKM-Matrixelements mal einem anomalen Formfaktor zu $|V_{\mathrm{tb}} f_1^{\mathrm{L}}| = 1.30^{+0.13}_{-0.16}$ bestimmt. Dies führt zu einer unteren Grenze im Standardmodell-Szenario $0 \leq |V_{\mathrm{tb}}| \leq 1$ von $0.77 < |V_{\mathrm{tb}}|$ bei einem 95 % Konfidenzintervall.

Contents

The Great Architect of the universe built it of good stuff.
Jules Verne, Journey to the Centre of the Earth

1. Introduction

The "Large Hadron Collider" (LHC) was built to improve and broaden our understanding of nature at its most fundamental level. It was designed to allow the best possible insight into the most basic processes of our universe that manifest themselves in its matter content of elementary particles and the spectrum of their interactions.

The underlying theoretical framework of this endeavour which, at the same time, is put to the acid test by it, is the well-accepted "Standard Model of Particle Physics". Despite the standard model's predictive power and notable achievements in categorizing the particles and forces known today, it remains incomplete and unsatisfactory in many aspects. The most obvious shortcoming being its inability to accommodate gravity to the three other fundamental forces, it does also not provide an explanation for the different coupling strengths of these three forces or for the hierarchical mass spectra of particles observed in experiments. From the viewpoint of cosmology, it is incapable of accounting for the detected amount of dark matter and dark energy and does not offer a conclusive mechanism of baryogenesis. Apart from displaying these conceptual inadequacies, the standard model also requires about two dozen (seemingly) unrelated numerical constants as input parameters, a highly undesirable feature for such a fundamental scheme.

In order now to probe the standard model and shed light on these open questions, there are two possible approaches for the experimenter: Firstly, seeking to measure the *known* particle properties and couplings contained in the model to the utmost precision achievable as to ensure that no inconsistencies are found already at the outset. Secondly, striving to discover *new* particles that exceed the model's current framework, belonging to one of the many extensions that have been proposed by theorists. The first ansatz amounts to an *indirect* detection of new physics, the second one to a *direct* detection, and both methods also allow for the setting of limits. The work at hand is pursuing the former approach and provides the measurement of the electroweak coupling between the two quarks of the third fermion generation: the top quark and the beauty quark. This is achieved by extracting the cross-section of the electroweak production of single top quarks in the t-channel, one of the three sub-channels contributing to this process. The analysis is performed on data from proton-proton collisions delivered by the LHC at a centre-of-mass energy of 7 TeV which were recorded by the ATLAS detector in the year 2011.

This thesis is organized as follows: In Chap. 2, a brief overview of the known properties of the top quark is given and its production and decay mechanisms are discussed. Chapter 3 describes the experiment at which the measurement is performed: the ATLAS detector at the LHC. The samples modelling the signal and

background processes as well as the data sample that these are compared to in the analysis are outlined in Chap. 4. In this chapter, also the object definitions and the event preselection that is performed are given. The analysis method of the kinematic fit is depicted in Chap. 5 and the application to the single-top t-channel is explained. The final results of the analysis are presented in Chap. 6 where also the sources of systematic uncertainties are discussed; in addition, a comparison to other studies is drawn. Eventually, Chap. 7 summarizes this study and concludes with an outlook.

So lasst uns jetzt mit Fleiß betrachten,
was durch die schwache Kraft entspringt.
Friedrich Schiller, Die Glocke

2. The Top Quark

The standard model is formulated as a relativistic quantum field theory, and its particles correspond to excitations of its fundamental fields.

The *field formulation* is crucial since it allows for the description of multi-particle phenomena such as the appearance of virtual particles (e.g. vacuum fluctuations or higher order terms in perturbation theory) in accordance with the uncertainty principle. The field character of the theory also gives rise to the notion of antiparticles that in turn ensure the preservation of causality within this framework. Furthermore, it enables transitions between states of different particle number, thus providing a tool to compute scattering amplitudes and cross-sections. However, yet another feature is needed in order for this ansatz to yield predictions of observable quantities: The standard model is a perturbatively renormalizable theory in that the divergences associated with perturbative energy shifts can be reabsorbed into the fundamental constants of the Lagrangian by procedures known as mass and charge renormalization.

Another important property of the standard model is its set of *symmetries*: Its fermionic matter fields display invariance when exposed to local phase transformations, so-called gauge transformations, requiring the introduction of additional gauge fields to obtain invariant derivatives of the Dirac fields. These gauge fields are of bosonic nature and correspond to the force carriers of the respective interactions:

The *strong interaction* part of the theory is called quantum chromodynamics (QCD). It is based upon the gauge group $\mathrm{SU}(3)_\mathrm{C}$, an exact symmetry, and describes the action of the colour force in form of eight massless gauge bosons, the gluons, on all fundamental fermions carrying colour charge "red", "blue" or "green" (i.e. the quarks). The gluons themselves also carry colour charge (a colour and an anti-colour) which gives rise to self-interactions. Stable objects are obtained as colour-singlet bound states of either two quarks, a quark and an antiquark (mesons), or three quarks/antiquarks (baryons). This phenomenon known as "quark confinement" is due to the fact that the coupling strength of the strong force increases with increasing distance scales ("running coupling").

The *electroweak sector* unifies the electromagnetic and weak forces and is realized as the $\mathrm{SU}(2)_\mathrm{L} \times \mathrm{U}(1)_Y$ gauge group with the associated couplings of weak left-handed isospin T and weak hypercharge Y. Since the weak interaction solely couples to left-handed fermions, the Dirac fields Ψ are split up into left-handed and right-handed components

$$\Psi_{\mathrm{L/R}} = \frac{1}{2}(1 \mp \gamma_5)\Psi \tag{2.1}$$

rendering the standard model a chiral gauge theory. The quarks and leptons are

thus arranged in left-handed weak isospin $T = \frac{1}{2}$ *doublets* where the up-type and down-type quarks carry the third component of weak isospin $T_3 = +\frac{1}{2}$ and $T_3 = -\frac{1}{2}$, respectively, as well as right-handed $T = 0$ *singlets*:

$$\begin{pmatrix} u \\ d \end{pmatrix}_{\mathrm{L}} \quad \begin{pmatrix} c \\ s \end{pmatrix}_{\mathrm{L}} \quad \begin{pmatrix} t \\ b \end{pmatrix}_{\mathrm{L}} \qquad \begin{matrix} u_{\mathrm{R}} & c_{\mathrm{R}} & t_{\mathrm{R}} \\ d_{\mathrm{R}} & s_{\mathrm{R}} & b_{\mathrm{R}} \end{matrix}$$

$$\begin{pmatrix} \nu_e \\ e \end{pmatrix}_{\mathrm{L}} \quad \begin{pmatrix} \nu_\mu \\ \mu \end{pmatrix}_{\mathrm{L}} \quad \begin{pmatrix} \nu_\tau \\ \tau \end{pmatrix}_{\mathrm{L}} \qquad \begin{matrix} \nu_{e\mathrm{R}} & \nu_{\mu\mathrm{R}} & \nu_{\tau\mathrm{R}} \\ e_{\mathrm{R}} & \mu_{\mathrm{R}} & \tau_{\mathrm{R}} \end{matrix}$$

The relation between T_3 and the electromagnetic charge Q defines the weak hypercharge Y via

$$Q = T_3 + \frac{Y}{2}\,. \tag{2.2}$$

T_3 as well as Y (like Q) are conserved quantum numbers in general.

It is an important feature of the electroweak theory depicted that adding mass terms to the Lagrangian violates the $\mathrm{SU}(2)_{\mathrm{L}} \times \mathrm{U}(1)_Y$ gauge invariance. The favoured proposed mechanism to account for the observed masses of the fermions and the carriers of the weak interaction is the introduction of an additional scalar field, the so-called "Higgs field". This is thought to bring about electroweak symmetry breaking (EWSB) by reducing the $\mathrm{SU}(2)_{\mathrm{L}} \times \mathrm{U}(1)_Y$ gauge group to $\mathrm{U}(1)_{\mathrm{QED}}$. By EWSB, the three gauge bosons of the electroweak sector, the neutral Z_0 boson and the charged $\mathrm{W}^+, \mathrm{W}^-$ bosons acquire mass whereas the photon of quantum electrodynamics (QED) remains massless [Gol61; GSW62].

Recently, ATLAS [ATL12o] and CMS [CMS12b] have observed a new bosonic particle at a mass of about 126 GeV consistent with the excitation of this field, known as the "Higgs particle". This mass indeed corresponds to the most probable region of the Higgs mass, predicted by electroweak precision fits of the standard model [Fla+09]. The properties of this Higgs-like boson probed so far, i.e. its coupling strength to W and Z bosons [ATL13a] as well as its zero spin [ATL13b], agree with the standard model expectation.

By virtue of the Higgs field, the fermions of the theory can also obtain mass terms via Yukawa couplings, and flavour symmetry breaking (FSB) can be accomplished, though not explained. The action of the charged current part of the electroweak force on the fermions in this framework is now

$$\mathcal{L}_{\mathrm{CC}} = -\frac{g}{\sqrt{2}} \left[\bar{u}_i \gamma^\mu \frac{1-\gamma^5}{2} V_{ij}^{\mathrm{CKM}} d_j + \bar{\nu}_i \gamma^\mu \frac{1-\gamma^5}{2} e_i \right] W_\mu^+ + \mathrm{h.c.} \tag{2.3}$$

where all fermions are left-handed, g is the $\mathrm{SU}(2)_{\mathrm{L}}$ coupling and the γs are the Dirac matrices representing the underlying Clifford algebra. The shorthand "h.c." denotes the respective Hermitian conjugate terms. V_{ij}^{CKM} is the Cabibbo-Kobayashi-Maskawa matrix [KM73] mixing the mass eigenstates of the quarks into the weak charged current eigenstates, denoted by dashed symbols (by convention, the mixing of mass

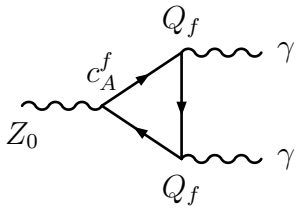

Figure 2.1. Fermion triangle diagram in higher order of perturbation theory capable of introducing an anomaly into the standard model.

and weak eigenstates is ascribed to the down-type quarks):

$$\begin{pmatrix} d' \\ s' \\ b' \end{pmatrix}_{\mathrm{L}} = V^{\mathrm{CKM}} \begin{pmatrix} d \\ s \\ b \end{pmatrix}_{\mathrm{L}} \equiv \begin{pmatrix} V_{ud} & V_{us} & V_{ub} \\ V_{cd} & V_{cs} & V_{cb} \\ V_{td} & V_{ts} & V_{tb} \end{pmatrix} \begin{pmatrix} d \\ s \\ b \end{pmatrix}_{\mathrm{L}} . \tag{2.4}$$

As can be seen in (2.3), the weak charged current interaction possesses a "vector minus axial vector" structure (called (V − A) in the following).

As mentioned in the beginning of this chapter, renormalizability is the basic prerequisite for the consistency of the standard model framework. In fact, this requirement was one reason to postulate the existence of the top quark well prior to its discovery. When considering contributions to scattering amplitudes arising from higher order corrections in perturbation theory like the diagram shown in Fig. 2.1, a divergence originating from the integration over the unconstrained fermion loop momentum is found. The amplitude of this diagram is proportional to $c_A^f Q_f^2$, the product of the weak neutral current axial coupling $c_A^f = T_3$ and the square of the electromagnetic fermion charge Q_f^2. In order for this anomaly to cancel completely, the sum of $T_3 Q_f^2$ over all fermion generations N_{gen} must vanish; the contributions of the charged leptons and the quarks of all colours N_{C} reads

$$\sum_{i=1}^{N_{\mathrm{gen}}} \left(-\frac{1}{2}(-1)^2 + \frac{1}{2} N_{\mathrm{C}} \left(+\frac{2}{3} \right)^2 - \frac{1}{2} N_{\mathrm{C}} \left(-\frac{1}{3} \right)^2 \right) \stackrel{!}{=} 0 . \tag{2.5}$$

Thus, the number of lepton and quark doublets needs to be the same and with the discovery of the tau lepton in 1975 [Per+75], the existence of a third generation of quarks was required.

What is now the motivation for studying the up-type quark of this third generation of fermions? The top quark is by far the heaviest fermion of the standard model. This property has two important consequences: One is that of all the standard model particles it has the largest coupling to the Higgs sector and is supposed to play a crucial role in the mass generation process. The other one is that it is the only quark that decays before it can hadronize.

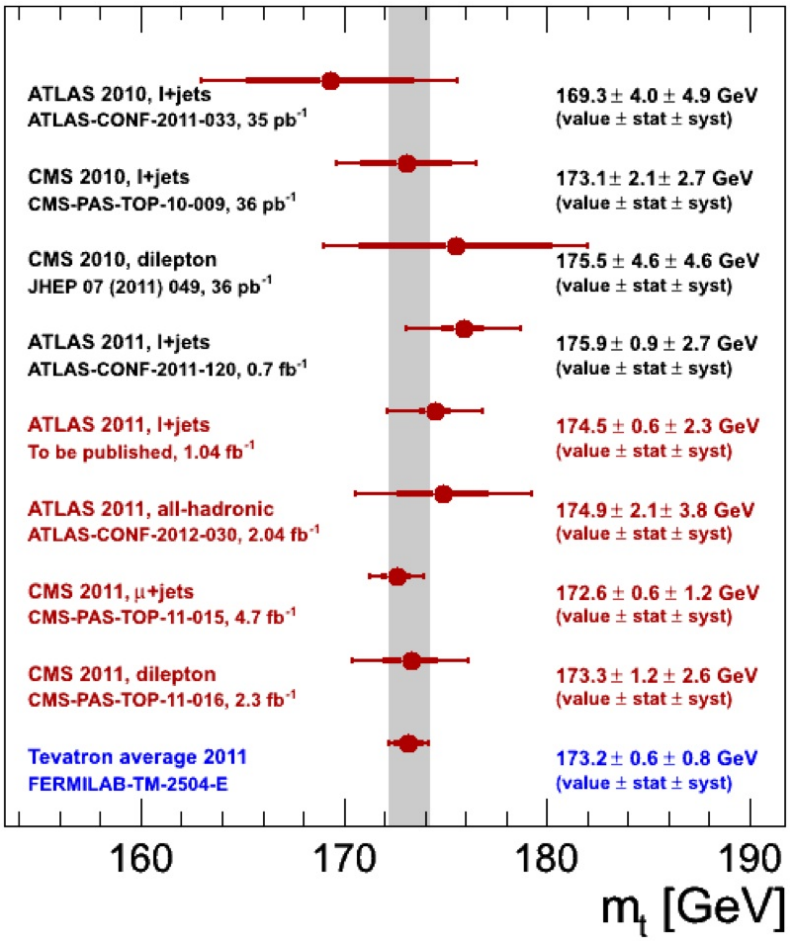

Figure 2.2. Top mass measurements of the LHC and Tevatron experiments [Bly12].

2.1. Top Quark Mass

The top quark was discovered at Fermilab's Tevatron $p\bar{p}$ collider in the year 1995 by the experiments CDF [CDF95] and D0 [D0 95]. Its mass was determined in a combined result by CDF and D0 in Run I with a dataset of $109\,\mathrm{pb}^{-1}$ at a centre-of-mass energy of $\sqrt{s} = 1.8\,\mathrm{TeV}$ to be $m_\mathrm{t} = (178.0 \pm 4.3)\,\mathrm{GeV}$ [CDF04] and refined to $m_\mathrm{t} = (173.2 \pm 0.9)\,\mathrm{GeV}$ in Run II using up to $5.8\,\mathrm{fb}^{-1}$ of data at $\sqrt{s} = 1.96\,\mathrm{TeV}$ [Tev11]. At the LHC experiments recording pp collisions at $\sqrt{s} = 7\,\mathrm{TeV}$, the top quark mass was also measured by ATLAS on a data set of $1.04\,\mathrm{fb}^{-1}$ as $m_\mathrm{t} = (174.5 \pm 2.4)\,\mathrm{GeV}$ [ATL12k] and by the CMS collaboration on $36\,\mathrm{pb}^{-1}$ as $m_\mathrm{t} = (175.5 \pm 6.5)\,\mathrm{GeV}$ [CMS11b]. An overview of the Tevatron and LHC results in the lepton plus jets, dilepton and all-hadronic channels of top pair production (cp. Sec. 2.3.2) is shown in Fig. 2.2. Because of this high mass of the top quark that is of the same order as the scale of EWSB, i.e. the vacuum expectation value of the Higgs field $v \approx 246\,\mathrm{GeV}$ [Ber+12], it is assumed to play a crucial role in the EWSB mechanism.

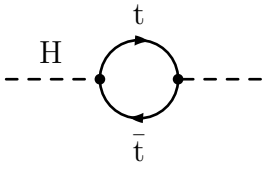

Figure 2.3. Radiative correction of the Higgs boson propagator by a top quark loop.

The low relative uncertainty of the Tevatron result (0.5 %) makes the top quark mass the most precisely known quark mass to date. The exact determination of the top quark mass is crucial because it enters as an important parameter in electroweak precision fits aiming at testing the consistency of the standard model and constraining standard model parameters like the mass of the Higgs boson [Fla+09]. For instance, there is a correction of the Higgs propagator by a top quark loop as illustrated in Fig. 2.3. By now, the top quark mass is measured to such an accuracy that the ambiguity arising from computing the top quark mass in different renormalization schemes becomes important. Two *perturbative* approaches are commonly used: the pole-mass scheme and the $\overline{\text{MS}}$ (minimal subtraction) scheme (or a variant of it). The problem of relating the theoretically defined top quark mass as a parameter of the standard model Lagrangian to the experimentally measured value is twofold:

- Traditionally, the kinematically reconstructed top quark mass is interpreted as the pole-mass, i.e. the mass appearing in the top quark propagator. However, this interpretation is not thorough: although the top quark decays before hadronizing, its decay products are subject to the *non-perturbative* hadronization process (see Sec. 2.2 on top quark decay). Thus, the kinematical reconstruction of the hadron jets (cp. Chap. 3) introduces an uncertainty due to colour reconnections (cp. Sec. 4.2.1) that is expected to be of the order of Λ_{QCD} [SW07]. Furthermore, the intrinsic uncertainty of the pole-mass scheme is also of the order of Λ_{QCD} [BB94]. Therefore, a high-level precision in the pole-mass approach is not achievable.

- The top quark mass measurements by kinematic fitting do not utilize a NLO prediction of the observable. Since a specific renormalization scheme is to be fixed only beyond Born-level, there is no uniquely defined renormalization scheme underlying these kinds of measurements.

Consequently, the cleanest approach is to compute the top quark mass via the measurement of a quantity with well-defined renormalization scheme dependence within the $\overline{\text{MS}}$ framework. The observable of choice is the total hadronic cross-section of $\text{t}\bar{\text{t}}$ production [LMU10] (cp. Sec. 2.3.1 and 2.3.2 and Fig. 2.8). The relation of the "running mass" of the $\overline{\text{MS}}$ scheme $\overline{m}(\mu_{\text{r}})$ and the pole-mass m_{t} is given by

$$m_{\text{t}} = \overline{m}(\mu_{\text{r}}) \left(1 + \frac{\alpha_s(\mu_{\text{r}})}{\pi} c_1 + \left(\frac{\alpha_s(\mu_{\text{r}})}{\pi}\right)^2 c_2 + \cdots\right) \tag{2.6}$$

with the constants c_1, c_2 and the strong coupling α_s that also depends on the renormalization scale μ_r.

The theoretical top quark mass resonance derived from the top quark propagator follows a relativistic Breit-Wigner distribution for the probability density function

$$f_\mathrm{BW}(E) = \frac{k}{(E^2 - M^2)^2 + M^2\Gamma^2} \tag{2.7a}$$

with the constant of probability

$$k = \frac{2\sqrt{2}M\Gamma\gamma}{\pi\sqrt{M^2 + \gamma}} \tag{2.7b}$$

where

$$\gamma = \sqrt{M^2(M^2 + \Gamma^2)}\,. \tag{2.7c}$$

Here, $E = \sqrt{s}$ denotes the centre-of-mass energy of the production process, $M = m_\mathrm{t}$ is the top quark pole mass and $\Gamma = \Gamma_\mathrm{t}$ is the top decay width that will be the topic of the next section.

2.2. Top Quark Decay

The top quark total decay width defined as the parameter Γ in Eq. (2.7a) was computed including first order QCD corrections and assuming $|V_\mathrm{tb}| = 1$ and $|V_\mathrm{td}| = |V_\mathrm{ts}| = 0$ to be [Kuh96; JK89]

$$\Gamma_\mathrm{t} = |V_\mathrm{tb}|^2 \frac{G_\mathrm{F}\, m_\mathrm{t}^3}{8\pi\sqrt{2}} \left(1 - \frac{m_\mathrm{W}^2}{m_\mathrm{t}^2}\right)^2 \left(1 + 2\frac{m_\mathrm{W}^2}{m_\mathrm{t}^2}\right) \left[1 - \frac{2\alpha_\mathrm{s}}{3\pi}\left(\frac{2\pi^2}{3} - \frac{5}{2}\right)\right]. \tag{2.8}$$

α_s is the strong coupling constant and G_F denotes the Fermi constant. The value of Γ_t depends on the top quark mass and for $m_\mathrm{t} = 172.5$ GeV, the theoretical prediction amounts to 1.33 GeV. In tension with this, Γ_t was so far only measured by the D0 experiment as $\Gamma_\mathrm{t} = 2.00^{+0.47}_{-0.43}$ GeV [D0 12a] which directly translates to the mean life time of the top quark:

$$\tau_\mathrm{t} = 3.29^{+0.90}_{-0.63} \cdot 10^{-25}\,\mathrm{s}\,. \tag{2.9}$$

It is because of its large mass that the available phase space for the decay of the top quark is large, resulting in this extremely short lifetime which is an order of magnitude smaller than the characteristic hadronization time $\tau_\mathrm{had} = 28 \cdot 10^{-25}\,\mathrm{s}$ of QCD. Consequently, the top quark is the only quark whose decay permits to study the properties of a single quark free from confinement effects. Above all, the top quark's spin information is retained in its decay products.

In the standard model, the top quark's Yukawa coupling to the beauty quark, V_tb, is experimentally found to be close to unity assuming three quark generations as well as unitarity of the CKM matrix [Eid+04]; the *indirectly* constrained values at

90 % confidence level (C.L.) read

$$|V_{\mathrm{td}}| = 0.0048 \quad - \quad 0.014\,, \tag{2.10a}$$
$$|V_{\mathrm{ts}}| = 0.037 \quad - \quad 0.043\,, \tag{2.10b}$$
$$|V_{\mathrm{tb}}| = 0.9990 \quad - \quad 0.9992\,. \tag{2.10c}$$

Thus, the electroweak production and decay of the top quark proceeds almost exclusively via the term of the Lagrangian representing the W-t-b vertex,

$$\mathcal{L}_{\mathrm{Wtb}} = -\frac{g}{\sqrt{2}}\,\bar{b}\,W_{\mu}^{-}\,\gamma^{\mu}\,V_{\mathrm{tb}}\,f_1^{\mathrm{L}}\,P_{\mathrm{L}}\,t + \mathrm{h.c.}\,, \tag{2.11}$$

where f_1^{L} is the weak charged current left-handed vector coupling taken to be 1 within the standard model, as mentioned in the introduction of this section. P_{L} denotes the left-handed chirality projector (cp. Eq. (2.1)):

$$P_{\mathrm{L}} = \frac{1-\gamma_5}{2}\,. \tag{2.12}$$

If, however, new physical effects come into play, they could well surface in modified weak top quark couplings. It is noteworthy, that if the assumption of three quark generations is dropped whilst retaining unitarity of an expanded CKM matrix, the constraints of Eq. (2.10) are relaxed to [Eid+04]

$$|V_{\mathrm{td}}| = 0 \quad - \quad 0.08\,, \tag{2.13a}$$
$$|V_{\mathrm{ts}}| = 0 \quad - \quad 0.11\,, \tag{2.13b}$$
$$|V_{\mathrm{tb}}| = 0.07 \quad - \quad 0.9993\,. \tag{2.13c}$$

Since the ranges of Eq. (2.10) are inferred from B-meson mixing, this measurement technique only gives access to the ratios of V_{td}, V_{ts} and V_{tb}. Only via the electroweak single-top quark production process, a *direct* determination of these three quantities is possible [JS92]: As can be seen in Fig. 2.11 of Sec. 2.3.3, the single-top production rate in each subchannel is directly proportional to the squared norm of the involved CKM matrix element. Thus, only a measurement of the single-top production cross-section allows a model-independent determination crucial for uncovering effects of new physics in the top quark sector.

The first value of $|V_{\mathrm{tb}}|$ determined directly was derived from a measurement of the single-top production cross-section at the CDF experiment [CDF10] via

$$|V_{\mathrm{tb}}|^2 = |V_{\mathrm{tb}}^{\mathrm{SM}}|^2\,\frac{\sigma_{\text{single-top}}}{\sigma_{\text{single-top}}^{\mathrm{SM}}}\,, \tag{2.14}$$

where the variables indexed with "SM" represent the theoretically expected standard model values and the variables without indices denote the experimentally measured values. Measurements by D0 [D0 11], CMS [CMS12a] and ATLAS [ATL12j] followed,

Experiment	$\lvert V_{\mathrm{tb}}\rvert$	Uncertainty	Limit at 95 % C.L.
CDF	0.91	$\pm 0.11\,(\mathrm{exp.}) \pm 0.07\,(\mathrm{theor.})$	> 0.71
D0	1.02	$+0.10/-0.11$	> 0.79
CDF & D0	0.88	± 0.07	> 0.77
CMS	1.02	$\pm 0.05\,(\mathrm{exp.}) \pm 0.02\,(\mathrm{theor.})$	> 0.92
ATLAS	1.13	$+0.14/-0.13$	> 0.75
CDF	0.96	$\pm 0.09\,(\mathrm{exp.}) \pm 0.05\,(\mathrm{theor.})$	> 0.78
D0	1.12	$+0.09/-0.08$	> 0.92

Table 2.1. Measured values and lower limits of the CKM matrix element $|V_{\mathrm{tb}}|$, derived from the cross-section of single-top production [CDF10; D0 11; CDF09; CMS12a; ATL12j; CDF13; D0 13].

and there was also a combined result of the Tevatron experiments [CDF09]. Recently, there have also been updates of the CDF [CDF13] and D0 [D0 13] values. The values obtained and the corresponding lower limits at a 95 % C.L. are collected in Tab. 2.1. Here, all measurements assume $0 \leq |V_{\mathrm{tb}}| \leq 1$, $f_1^{\mathrm{L}} = 1$ and negligible contributions of $|V_{\mathrm{td}}|$ and $|V_{\mathrm{ts}}|$:

$$|V_{\mathrm{tb}}|^2 \gg |V_{\mathrm{td}}|^2 + |V_{\mathrm{ts}}|^2 \,. \tag{2.15}$$

In experiments, the top quark covers on average a distance of $\mathcal{O}(10^{-16}\,\mathrm{m})$ before it decays, a value well beyond the spatial resolution of current particle detectors. Therefore, it cannot be identified directly but must be reconstructed by its daughter particles, the W boson and the beauty quark, of which the W boson has a lifetime of about $\tau_{\mathrm{W}} = 3 \cdot 10^{-25}\,\mathrm{s}$ [Bol11]. While the b-quark hadronizes, the W boson can decay either hadronically into two mostly light quarks or leptonically into a charged lepton and its neutrino. Although the neutrino escapes undetected from the experimental apparatus, the leptonic decay mode is usually chosen for reconstruction since the signature of a charged high-energetic lepton is much cleaner in the detector than that of two light quark jets, and thus it stands out from the overwhelming background of QCD multi-jet production (cp. Sec. 4.3.1). The leptonic W boson decay proceeds with equal probabilities ("branching fractions" BF) of the different lepton flavours:

$$BF(\mathrm{W} \to \ell\nu_\ell) = \frac{1}{9} \,, \quad \ell \in \{e, \mu, \tau\} \,. \tag{2.16}$$

Unlike in weak decays induced by the lighter quarks, the W boson from the top decay is on-shell and not virtual. This results in different W helicity fractions: In the top quark case, the longitudinal polarization is enhanced. In Fig. 2.4, the top quark decays associated with the three possible W boson polarizations are pictured. Since the beauty quark mass is much smaller than the W boson and top quark mass, it carries a large momentum in the decay process and is thus left-handedly polarized. If the top quark is also left-handed, the W boson must carry a longitudinal polarization due to spin conservation. However, if the top quark is right-handed, the

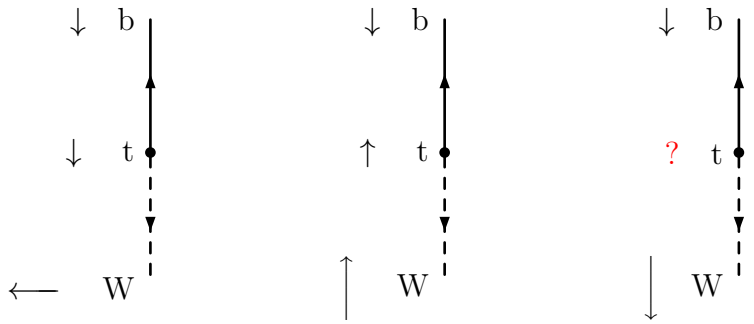

Figure 2.4. The three different W helicities from top quark decays: longitudinal, left-handed and right-handed polarizations.

	f_L	f_-	f_+
Theory prediction	0.70	0.30	$3.6 \cdot 10^{-4}$
Tevatron (CDF & D0 comb.)	0.722 ± 0.081	—	-0.033 ± 0.046
LHC (ATLAS)	0.67 ± 0.07	0.32 ± 0.04	0.01 ± 0.05

Table 2.2. Predicted and measured helicity fractions of the W boson from the top decay [Fis+01; CDF12; ATL12l]. f_L, f_- and f_+ denote the longitudinal, left-handed and right-handed fractions, respectively.

W boson must be left-handedly polarized. The third case of a right-handed W boson is forbidden by angular momentum conservation.

The helicity fractions are defined as the normalized partial decay widths of the W boson,

$$f_\mathrm{L} = \frac{\Gamma_\mathrm{L}}{\Gamma_0}\,, \quad f_- = \frac{\Gamma_-}{\Gamma_0}\,, \quad f_+ = \frac{\Gamma_+}{\Gamma_0}\,, \qquad f_\mathrm{L} + f_- + f_+ = 1\,, \tag{2.17}$$

where f_L, f_- and f_+ and Γ_L, Γ_- and Γ_+ are the longitudinal, left-handed and right-handed polarization fractions and partial decay widths, respectively, and Γ_0 is the total decay width. The W polarization fractions from the top decay are computed on Born level to be (assuming $m_\mathrm{b} \neq 0$)

$$f_\mathrm{L} = \frac{1}{1+2x^2}\,, \qquad f_- = \frac{2x^2}{1+2x^2}\,, \qquad f_+ = y^2\frac{2x^2}{(1-x^2)^2\,(1+2x^2)} \tag{2.18}$$

for small y, where $x = \frac{m_\mathrm{W}}{m_\mathrm{t}}$ and $y = \frac{m_\mathrm{b}}{m_\mathrm{t}}$ [Fis+01].

The measurements of the helicity fractions of the W boson from the top quark decay have been performed in $\mathrm{t\bar{t}}$ events at the Tevatron [CDF12] and at the LHC [ATL12l]. Their results are given in Tab. 2.2 where also the predictions are listed. Up until now, all findings are in agreement with the standard model.

The enhancement of the longitudinal component can be understood by comparing

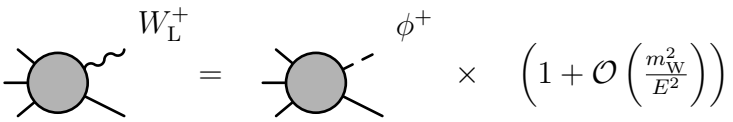

Figure 2.5. Visualization of the Goldstone boson equivalence theorem. W_{L}^{+} denotes the longitudinally polarized W boson and ϕ^{+} the corresponding Goldstone boson.

the total decay rate Γ_0 of the top quark via a W boson, given by [PS95]

$$\Gamma_0 = \frac{g^2}{64\pi}\frac{m_{\mathrm{t}}^3}{m_{\mathrm{W}}^2}\left(1-\frac{m_{\mathrm{W}}^2}{m_{\mathrm{t}}^2}\right)^2\left(1+2\frac{m_{\mathrm{W}}^2}{m_{\mathrm{t}}^2}\right), \tag{2.19}$$

with the expression resulting from a computation of the longitudinal partial decay width of the W via the Goldstone boson equivalence theorem (GBET). Choosing the so-called R_ξ gauge in which the Goldstone bosons are not yet eliminated from the theory, the GBET holds which states that on tree-level and in the high-energy limit ($E \geq m_{\mathrm{t}}$ and for $m_{\mathrm{t}} \gg m_{\mathrm{W}}$), the couplings of longitudinal gauge bosons become those of their associated Goldstone bosons. Thus, the W boson's longitudinal partial decay width is given by the decay rate of the top quark via the Goldstone boson to an accuracy of $\mathcal{O}(\frac{m_{\mathrm{W}}^2}{m_{\mathrm{t}}^2})$. The GBET is illustrated in Fig. 2.5. The decay rate of the top quark via the Goldstone boson Γ_{GB} turns out to be

$$\Gamma_{\mathrm{GB}} = \frac{g^2}{64\pi}\frac{m_{\mathrm{t}}^3}{m_{\mathrm{W}}^2} \overset{\mathrm{GBET}}{=} \Gamma_{\mathrm{L}} \tag{2.20}$$

which in the given limit is indeed the dominant contribution to Γ_0.

So far, only the top quark decay according to Eq. (2.11) was considered. However, one can write down a much more general Lagrangian term for the W-t-b vertex [CLY05], namely

$$\begin{aligned}\mathcal{L}_{\mathrm{Wtb}}^{\mathrm{eff}} = &-\frac{g}{\sqrt{2}}\,\bar{b}\,W_\mu^-\,\gamma^\mu\,V_{\mathrm{tb}}\left(f_1^{\mathrm{L}}\,P_{\mathrm{L}}+f_1^{\mathrm{R}}\,P_{\mathrm{R}}\right)t \\ &-\frac{g}{\sqrt{2}}\,\bar{b}\,W_\mu^-\,\frac{i\sigma^{\mu\nu}q_\nu}{m_{\mathrm{W}}}V_{\mathrm{tb}}\left(f_2^{\mathrm{L}}\,P_{\mathrm{L}}+f_2^{\mathrm{R}}\,P_{\mathrm{R}}\right)t \quad + \quad \text{h.c.}\end{aligned} \tag{2.21}$$

where the additional terms originate from *anomalous* couplings: Whilst f_1^{L} is the standard model's left-handed vector coupling, f_1^{R}, f_2^{L} and f_2^{R} denote a right-handed vector coupling as well as left- and right-handed tensor couplings. Here, the 4-momentum of the W boson

$$q_\nu = (p_{\mathrm{t}} - p_{\mathrm{b}})_\nu \tag{2.22}$$

and the commutator of γ matrices

$$\sigma^{\mu\nu} = \frac{i}{2}[\gamma^\mu, \gamma^\nu] \tag{2.23}$$

enter. The anomalous couplings express the possibility that also the right-handed

quarks couple weakly, and whereas the vector couplings describe chirality preserving processes, the tensor couplings implement flips of chirality. The generic analogue of Eq. (2.18) becomes then

$$f_{\mathrm{L}} = \frac{1}{A}\left(\frac{m_{\mathrm{t}}^2}{m_{\mathrm{W}}^2}\left(\left(f_1^{\mathrm{L}} + f_2^{\mathrm{R}}\frac{m_{\mathrm{W}}}{m_{\mathrm{t}}}\right)^2 + \left(f_1^{\mathrm{R}} + f_2^{\mathrm{L}}\frac{m_{\mathrm{W}}}{m_{\mathrm{t}}}\right)^2\right)\right), \tag{2.24a}$$

$$f_{-} = \frac{1}{A}\,2\left(f_1^{\mathrm{L}} + f_2^{\mathrm{R}}\frac{m_{\mathrm{t}}}{m_{\mathrm{W}}}\right)^2, \tag{2.24b}$$

$$f_{+} = \frac{1}{A}\,2\left(f_1^{\mathrm{R}} + f_2^{\mathrm{L}}\frac{m_{\mathrm{t}}}{m_{\mathrm{W}}}\right)^2, \tag{2.24c}$$

where $A = A\left(f_1^{\mathrm{L}}, f_1^{\mathrm{R}}, f_2^{\mathrm{L}}, f_2^{\mathrm{R}}, \frac{m_{\mathrm{t}}}{m_{\mathrm{W}}}\right)$. By performing a precision measurement of the W helicity fractions from the top decay, one can therefore conclude whether new physics processes contribute. Candidates are e.g. the Minimal Supersymmetric Standard Model (MSSM) [Cao+03] or the Topcolour-Assisted Technicolour Model (TC2) [WZQ05] in which the fractions deviate from the standard model at the percent level. However, this approach can only determine ratios of the couplings since four unknowns $f_1^{\mathrm{L}}, f_1^{\mathrm{R}}, f_2^{\mathrm{L}}$ and f_2^{R} need to be computed from the three Equations (2.24). Complementing the measurements of the W polarizations, single-top production in the t-channel and s-channel modes provides additional information; their dependence on the anomalous couplings are quoted as deviations from the standard model expectations:

$$\begin{aligned}
\Delta\sigma_{t\text{-chan}} = {} & a_0\left(\left(f_1^{\mathrm{L}} + f_2^{\mathrm{R}}\frac{m_{\mathrm{W}}}{m_{\mathrm{t}}}\right)^2 + \left(f_1^{\mathrm{R}} + f_2^{\mathrm{L}}\frac{m_{\mathrm{W}}}{m_{\mathrm{t}}}\right)^2 - 1\right) \\
& + a_m\left(\left(f_1^{\mathrm{L}} + f_2^{\mathrm{R}}\frac{m_{\mathrm{t}}}{m_{\mathrm{W}}}\right)^2 - 1\right) \\
& + a_p\left(f_1^{\mathrm{R}} + f_2^{\mathrm{L}}\frac{m_{\mathrm{t}}}{m_{\mathrm{W}}}\right)^2 \\
& + a_5\left(\frac{m_{\mathrm{t}}}{m_{\mathrm{W}}}\right)^2\left((f_2^{\mathrm{L}})^2 + (f_2^{\mathrm{R}})^2\right),
\end{aligned} \tag{2.25}$$

$$\begin{aligned}
\Delta\sigma_{s\text{-chan}} = {} & b_0\left(\left(f_1^{\mathrm{L}} + f_2^{\mathrm{R}}\frac{m_{\mathrm{W}}}{m_{\mathrm{t}}}\right)^2 + \left(f_1^{\mathrm{R}} + f_2^{\mathrm{L}}\frac{m_{\mathrm{W}}}{m_{\mathrm{t}}}\right)^2 - 1\right) \\
& + b_m\left(\left(f_1^{\mathrm{L}} + f_2^{\mathrm{R}}\frac{m_{\mathrm{t}}}{m_{\mathrm{W}}}\right)^2 - 1\right) \\
& + b_p\left(f_1^{\mathrm{R}} + f_2^{\mathrm{L}}\frac{m_{\mathrm{t}}}{m_{\mathrm{W}}}\right)^2 \\
& + b_5\left(\frac{m_{\mathrm{t}}}{m_{\mathrm{W}}}\right)^2\left((f_2^{\mathrm{L}})^2 + (f_2^{\mathrm{R}})^2\right),
\end{aligned} \tag{2.26}$$

where the values of the fit parameters a_i, b_i are listed in the reference paper [CLY05]. It should be noted, however, that if only W helicity fractions and single-top pro-

duction cross-sections are utilized to set limits on anomalous couplings at the W-t-b vertex, the effect of possible cancellations among the contributions of different anomalous couplings is disregarded [AB10]. This can be cured by including top polarization-related observables to define a completely model-independent approach. The variable of choice for partially polarized top quark decays is the angular distribution of a decay product X ($X = \ell, \nu, \mathrm{b}, \ldots$, the so-called "spin analysers") in the top quark rest frame,

$$\frac{1}{\Gamma}\frac{d\Gamma}{d\cos\theta_X} = \frac{1}{2}(1 + P\alpha_X \cos\theta_X)\,, \tag{2.27}$$

where θ_X is the angle between the three-momentum of X in the top rest frame and the top spin direction. The constants α_X denote the "spin analysing power" of X with $\alpha_X \in [-1, 1]$ and P is the degree of polarization,

$$P = \frac{N_+ - N_-}{N_+ + N_-}\,, \tag{2.28}$$

with N_+/N_- the number of top quarks polarized along/against the chosen spin axis. From the angular distributions, forward-backward asymmetries can then be computed as

$$A_{X,\mathrm{FB}} = \frac{N(\cos\theta_X > 0) - N(\cos\theta_X < 0)}{N(\cos\theta_X > 0) + N(\cos\theta_X < 0)} \tag{2.29}$$

which eventually allow to determine the products $P\alpha_X$:

$$A_{X,\mathrm{FB}} = \frac{1}{2}P\alpha_X\,. \tag{2.30}$$

The spin analysing power constants depending on the values of the anomalous couplings are also given in the reference paper mentioned [AB10].

The first measurement of the top quark's polarization from Equations (2.29) and (2.30) for the case of $X = \ell$ in the t-channel of single-top quark production[1] has only recently been realized by the CMS collaboration [CMS13b]: Based on $20\,\mathrm{fb}^{-1}$ of proton-proton collision data at $\sqrt{s} = 8\,\mathrm{TeV}$, the value $P = 0.82 \pm 0.34$ was found, compatible with the SM. There are also some analyses currently measuring angular distributions of this kind in the single-top t-channel at ATLAS [LS12; Bou+10]. Regarding the asymmetry of Eq. (2.29) for $X = \ell$ along another spin direction[2], taken together with the prediction of the top's polarization in the t-channel, gives access to the imaginary part of f_2^{R} [AB10]; this has been exploited in a study on the $\sqrt{s} = 7\,\mathrm{TeV}$ $4.7\,\mathrm{fb}^{-1}$ data set that determined values of $A_{\ell,\mathrm{FB}}$ and f_2^{R} consistent

[1] In this analysis, the spin axis was chosen as the direction of the top polarization in the so-called "helicity basis"; for details, see e.g. [TY00].

[2] Here, the direction normal to the plane of the top polarization and the W boson momentum in the helicity basis was employed.

Scenario	W helicity	Single-Top	Combination
$\lvert f_1^{\mathrm{R}}\rvert^2$	0.62	0.89	0.30
$\lvert f_2^{\mathrm{L}}\rvert^2$	0.14	0.07	0.05
$\lvert f_2^{\mathrm{R}}\rvert^2$	0.18	0.18	0.12

Table 2.3. Upper limits at 95 % C.L. on anomalous couplings at the W-t-b vertex, derived from W helicity and single-top cross section measurements separately ($f_1^{\mathrm{L}} = 1$) and in combination (f_1^{L} free) at D0 [D0 12b].

with the SM expectation of zero [ATL13e].[3] Previously, in an analysis by D0, the information obtained with $5.4\,\mathrm{fb}^{-1}$ of data from measuring the W helicities on a $\mathrm{t\bar{t}}$ sample was combined with the results from single-top t- and s-channel cross-section determinations where an orthogonality of the samples used for the two approaches was ensured [D0 12b]. By fixing two of the three anomalous couplings to be zero and setting the standard model coupling to $f_1^{\mathrm{L}} = 1$ for the separate approaches and letting it vary for the combination, the constraints recorded in Tab. 2.3 were obtained. As becomes apparent from the above, to conclude on the magnitude of any anomalous couplings at the W-t-b vertex and in order to judge the validity of different models of EWSB, the single-top cross-sections need to be measured with high-level precision.

2.3. Top Quark Production

In the standard model, there are two main production modes of top quarks in hadron collisions: top quark pair production via the strong interaction and single-top quark production via the weak interaction. Top quark pair production can also proceed via a weak process where quarks annihilate to form a Z boson or a photon, but the corresponding cross-sections are negligible compared to the strong production modes discussed here.

2.3.1. Hadronic Cross-Section

In order to measure the production cross-section of a specific final state at a hadron collider like the LHC, the notion of a hadronic cross-section needs to be defined. Since the colliding protons are composite objects made up of valence quarks, gluons and sea quarks there are several possible production channels for any particular final state. To start with, the so-called factorization scale μ_{F} of the interaction is introduced, that allows to distinguish the hard scattering from softer subprocesses in the collision. Similarly, since quarks and gluons in the final state hadronize to form colour-neutral hadrons, another scale, the renormalization scale μ_{R}, is defined, to set

[3] This analysis provided the first experimental limit on the imaginary part of f_2^{R}.

the hard scattering apart from these lowly energetic QCD processes. Then, in order to describe the matrix element of the hard scattering, the momenta of the incoming partons have to be provided. The probability densities of the longitudinal parton momenta inside a proton (parton distribution functions or PDFs) are parametrized by the parton type and the negative four-momentum transfer $Q^2 = -q^2$ of the hard scattering,

$$f_i(x, Q^2)\,, \tag{2.31}$$

where x is the fraction of the proton momentum carried by the parton i. By virtue of the factorization theorem [CSS86] a cross-section for the scattering of parton i from the first proton and parton j from the second proton, resulting in the final state X, can be defined as

$$\sigma_{ij}(ij \to X) = \int_0^1 \mathrm{d}x_1 \mathrm{d}x_2\, f_i(x_1, Q^2) f_j(x_2, Q^2) \hat{\sigma}_{ij}(ij \to X; \hat{s}, Q^2)\,. \tag{2.32}$$

The quantity $\hat{\sigma}_{ij}$ is the partonic cross-section depending on the centre-of-mass energy of the hard partonic process, which, for the LHC as a symmetric collider, is given by

$$\sqrt{\hat{s}} = \sqrt{x_i x_j s}\,. \tag{2.33}$$

Here, $\sqrt{s}$ denotes the centre-of-mass energy of the pp collision. The partonic cross-section depends furthermore on the scale Q^2 of the interaction, where a commonly used unified notation is adopted for the factorization and renormalization scales ($\mu_\mathrm{F} = \mu_\mathrm{R} = Q^2$). $\hat{\sigma}_{ij}$ includes averaging over colours and spins in the initial state and summing over colours and spins in the final state. For instance, the explicit expression for the leading order partonic cross-section of single-top production in the t-channel involving an up quark in the initial state (ub $\to$ dt) reads [Kid06]

$$\hat{\sigma}_\mathrm{ub} = \frac{\pi\alpha^2 |V_\mathrm{tb}|^2 |V_\mathrm{ud}|^2}{4\sin^4\theta_\mathrm{w}} \frac{(\hat{s} - m_\mathrm{t}^2)^2}{m_\mathrm{W}^2 \hat{s}(\hat{s} - m_\mathrm{t}^2 + m_\mathrm{W}^2)} \tag{2.34}$$

with the centre-of-mass energy $\sqrt{\hat{s}} > m_\mathrm{t}$, the fine-structure constant $\alpha = \frac{e^2}{4\pi}$ and the weak mixing angle θ_w where $\cos\theta_\mathrm{w} = m_\mathrm{W}/m_\mathrm{Z}$.

On hadron level, the total cross-section is then obtained from (2.32) by summing over all possible parton configurations in the initial state:

$$\sigma_\mathrm{had}(\mathrm{pp} \to X) = \sum_{i,j} \sigma_{ij}(ij \to X) \tag{2.35}$$

Since the partons inside the proton are subject to the strong force on very small distance scales, the parton distribution functions (2.31) cannot be computed perturbatively from first principles but need to be extracted by fits to experimentally measured data. This was accomplished by experiments probing deep inelastic scattering of leptons by protons, e.g. by the experiments ZEUS [ZEU92] and H1 [H1 97] at HERA. The PDFs can be extracted in several different ways, and there is a

multitude of PDF sets on the market like the CTEQ 6.6 set [Nad+08] or the MSTW 2008 set [Wat12]. For illustration, Fig. 2.6 shows the MSTW 2008 PDFs of the gluon, the up quark, the down quark and the sea-quarks. Analyses using simulations based on these PDF sets are therefore dependent on the parametrizations of the respective fits and this brings about a PDF-related systematic of the analysis (cp. Sec. 6.1).

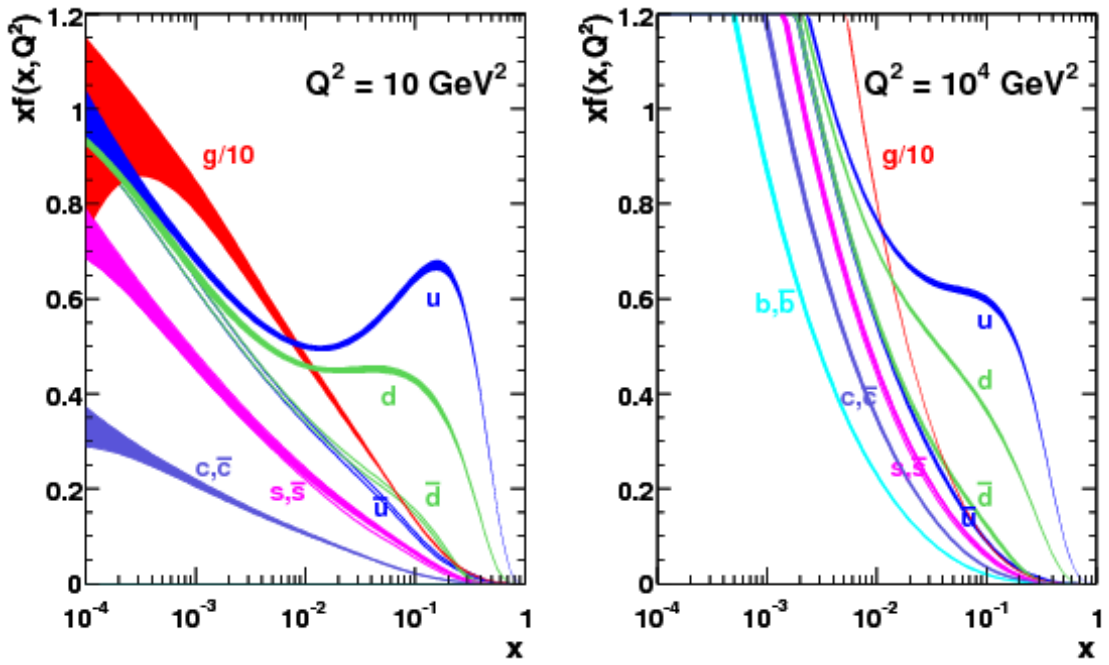

Figure 2.6. MSTW 2008 NNLO parton distribution functions at 68 % C.L. of the gluon, the up quark, the down quark and the sea-quarks for low and high values of Q^2, i.e. the momentum transfer.[4]

2.3.2. Top Quark Pair Production

The Feynman graphs of the possible processes for top-pair production via the strong interaction in leading order (LO) are shown in Fig. 2.7. There is either a quark-antiquark pair or a pair of gluons in the initial state. The gluon fusion modes can be divided into s-channel, t-channel and u-channel contributions. Top pair production possesses a larger cross-section than the single-top process and thus is already accessible on datasets with smaller integrated luminosity: It was the discovery channel of the top quark at the Tevatron [CDF95; D0 95] where semi-leptonic and dileptonic decay modes of the W boson from the two top decays were considered (see Sec. 2.2 for details on top quark decay modes). In the Tevatron's proton-antiproton collisions, top quark pairs were predominantly produced in the quark annihilation

[4] G. Watt. *MSTW PDFs: Key Plots*. Nov. 2013. URL: `http://mstwpdf.hepforge.org/plots/plots.html`

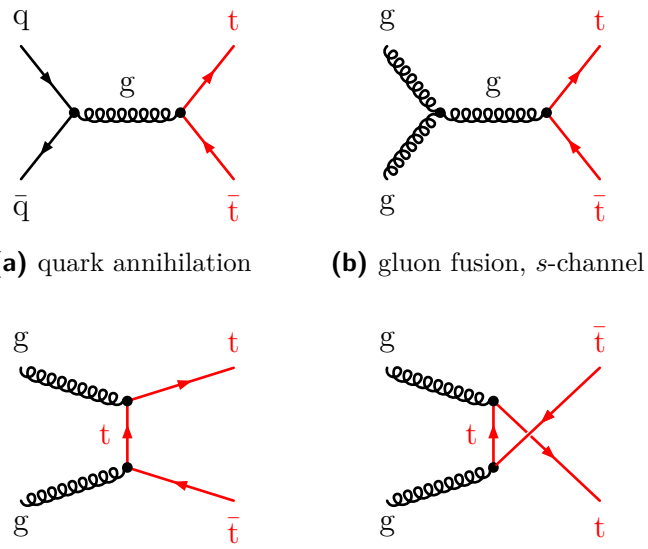

(a) quark annihilation **(b)** gluon fusion, s-channel

(c) gluon fusion, t-channel **(d)** gluon fusion, u-channel

Figure 2.7. The two modes of strong $t\bar{t}$ production: Quark annihilation (a) and gluon fusion processes (b), (c) and (d) in the initial state yield a top quark pair.

mode from a highly energetic valence quark of one proton and a respective valence anti-quark from the anti-proton. Since its centre-of-mass energy was relatively low compared to the top quark mass, the gluon fusion mode at low momentum fractions x was PDF-suppressed at the Tevatron (cp. Fig. 2.6) and only accounted for about 10 % to 20 % of the $t\bar{t}$ processes [Cac+04]. In the more energetic proton-proton collisions at the LHC, in contrast, the gluon-fusion modes of $t\bar{t}$ dominate, also because here, antiquarks are solely accessible from sea-quark PDFs situated at low x.

The predicted total hadronic cross-section of top-pair production is strongly dependent on the top quark mass. In Fig. 2.8, the dependence is shown for $\sqrt{s} = 14\,\text{TeV}$ at the LHC including NLO and approximate NNLO α_s predictions [LMU09] and using the aforementioned MSTW 2008 PDF set [Wat12]. The coloured bands show the uncertainties associated with the PDFs and with the simultaneous variations of the renormalization and factorization scales $\mu_R = \mu_F = \mu$ within $[m_t/2, 2m_t]$.

The values for the top pair production cross-section measured by the CDF and D0 experiments at the Tevatron as well as early measurements performed by the LHC experiments ATLAS and CMS are collected in Fig. 2.9 as a function of the centre-of-mass energy $\sqrt{s}$ of the colliding hadrons [ATL11e]. In this figure, the predictions for proton-proton and proton-antiproton collisions obtained using the HATHOR tool [Ali+11] include the scale and PDF uncertainties with the CTEQ6.6 PDFs [Nad+08] and assume a top quark mass of 172.5 GeV. The latest results for the $t\bar{t}$ production rate in the single-lepton, dilepton and all-hadronic channels, measured at $\sqrt{s} = 7$ TeV by ATLAS are displayed in Fig. 2.10. The currently best value of the combination of all measurements is $\sigma_{t\bar{t}}^{\text{exp}} = 177^{+11}_{-10}\,\text{pb}$ [ATL12r] which amounts

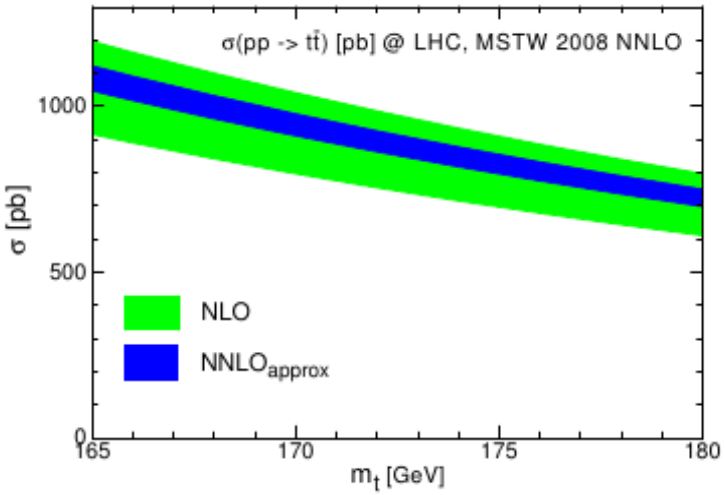

Figure 2.8. Predicted total hadronic cross-section of top-pair production at the LHC for $\sqrt{s} = 14\,\text{TeV}$ depending on the top quark mass. The NLO and approximate NNLO predictions are displayed. The bands represent the uncertainties from scale variations and PDFs [LMU09].

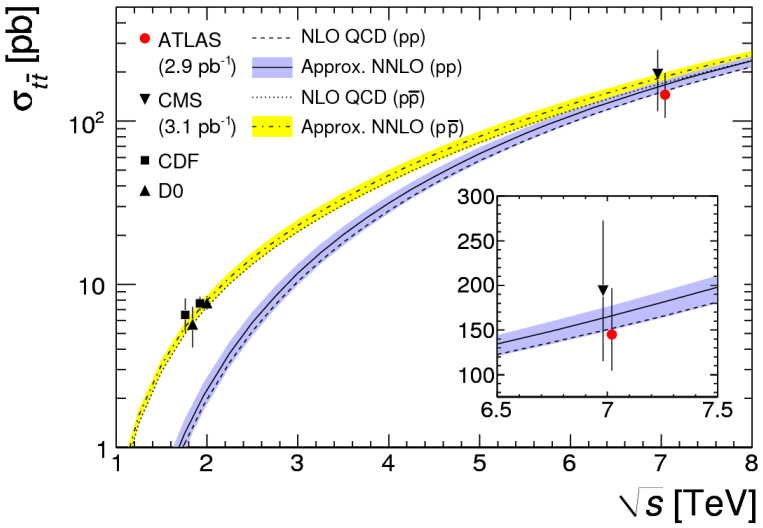

Figure 2.9. Top quark pair-production cross-section at hadron colliders as a function of the centre-of-mass energy $\sqrt{s}$. The predictions as well as the measurements by CDF and D0 at the Tevatron and by CMS and ATLAS at the LHC are shown. The predictions for proton-proton and proton-antiproton collisions include the scale and PDF uncertainties [ATL11e].

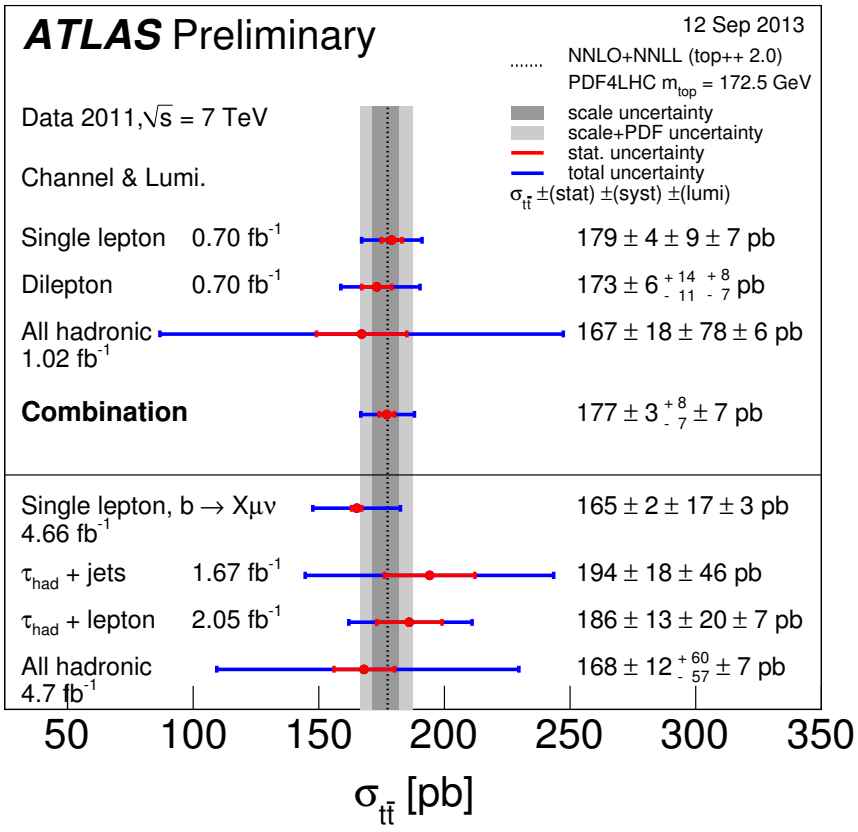

Figure 2.10. Latest results for the $t\bar{t}$ production cross-section in the single-lepton, dilepton and all-hadronic channels at $\sqrt{s} = 7\,\text{TeV}$ as measured by the ATLAS experiment.[5] The dashed line with the grey band denotes the approximate NNLO prediction and its uncertainty.

to a precision of 6 %. It has already the same precision as the theory value and is in agreement with the approximate NNLO prediction quoted as $\sigma_{t\bar{t}}^{\text{theo}} = 165^{+11}_{-16}\,\text{pb}$ for a top mass of 172.5 GeV [Ali+11].

The measurement of top quark production via the strong force, however, does not provide enough information about the top quark's weak couplings. The two top quarks decay weakly in the final state, but a decay is relatively insensitive to the magnitude of the coupling involved. Furthermore, any new physics characterized by some higher energy scale Λ may become the more apparent the closer the energy of the reaction approaches Λ: Whereas top decay processes would scale with $(m_t/\Lambda)^n$, new contributions to single-top production would scale with $(\sqrt{s}/\Lambda)^n$, where $n \in \mathbb{N}_0$ [TY00]. Thus, the desired information can only be obtained from studying the electroweak production of single top quarks at high $\sqrt{s}$ at a hadron collider.

[5] ATLAS Collaboration. *ATLAS Physics Summary Plots*. Sept. 2013. URL: `https://twiki.cern.ch/twiki/bin/view/AtlasPublic/CombinedSummaryPlots`

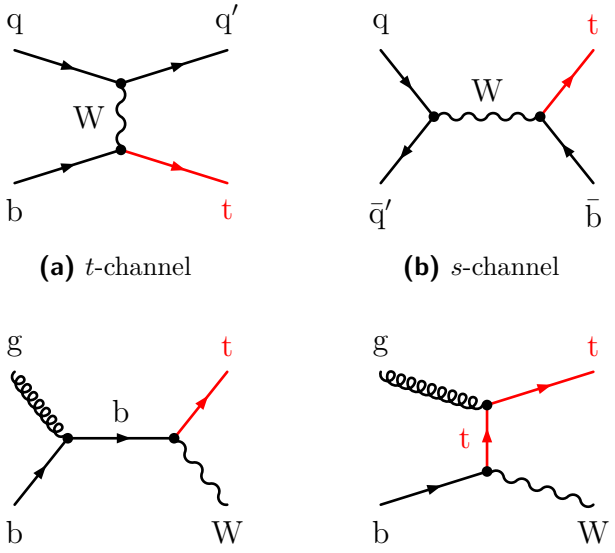

(a) t-channel **(b)** s-channel

(c) Wt-channel (fusion) **(d)** Wt-channel (scattering)

Figure 2.11. The three modes of electroweak single-top production: the t-channel (a), the s-channel (b) and the two variants of the Wt-channel (c) and (d).

2.3.3. Single-Top Quark Production

Turning now to the electroweak production of single top quarks, the contributing Feynman diagrams in LO are shown in Fig. 2.11. There is a t-channel, an s-channel and a Wt-channel of single-top production that differ in the virtuality Q^2 of the involved W boson ($Q^2 = -q^2$, with the four-momentum q^2 of the W): In the t-channel, a space-like W is exchanged ($q^2 < 0$) whilst the s-channel proceeds via a time-like W ($q^2 \geq (m_\mathrm{t} + m_\mathrm{b})^2$). The Wt-channel, finally, displays an on-shell or close to real W boson ($q^2 = m_\mathrm{W}^2$). In Fig. 2.12, some NLO contributions to the t-channel process are shown: Whereas the graphs in Fig. 2.11a, 2.12c and 2.12d assume a b-quark PDF, the graphs in Fig. 2.12a, 2.12b make use of the gluon PDF and depict a b-quark pair and a top quark pair emerging from a gluon splitting in one proton. Further examples of Feynman graphs contributing at NLO are a correction to the b-quark vertex in Fig. 2.12c and a correction to the light quark vertex in Fig. 2.12d. As is visible in the Feynman graphs, the processes include the W-t-b vertex in the scattering and thus, their production rates are directly proportional to $|V_\mathrm{tb}|^2$ which makes single-top quark production an ideal testing ground of the electroweak sector of the standard model (cp. also Sec. 2.2). The t-channel is particularly sensitive to flavour changing neutral currents (FCNCs) [TY00]: The virtual W boson, for example, can be replaced by a Z boson within a model allowing for FCNCs. This FCNC mode would even be enhanced relative to the SM mode due to the higher proton's parton density of the u or c quark replacing the b quark in the initial state; this applies independently of a presumably small coupling at the Z–t–u,c vertex itself.

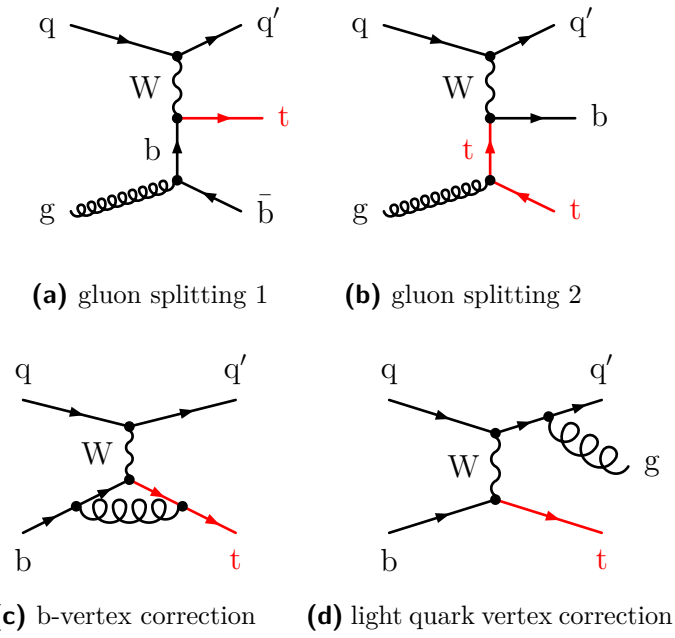

(a) gluon splitting 1 **(b)** gluon splitting 2

(c) b-vertex correction **(d)** light quark vertex correction

Figure 2.12. Contributions to the NLO of single-top t-channel production: gluon splittings in the initial state (a) and (b) as well as corrections to the b-vertex (c) and to the light quark vertex (d).

In contrast, the t-channel is rather insensitive to any new heavy particle replacing the space-like W boson (like a W′) since these contributions get suppressed according to the square of that particle's mass in the propagator [TY00].

Since the initial state of the s-channel contribution consists of a quark and an antiquark, this channel is PDF-suppressed in pp collisions whereas it was produced more abundantly at the Tevatron (cp. quark-annihilation mode of $\mathrm{t\bar{t}}$ production in Sec. 2.3.2). The t- and Wt-channels that have gluons in the initial state appear more frequently at the LHC where, like at the Tevatron, the t-channel contribution is still the dominant one. The predicted cross-sections at approximate NNLO for the three modes are listed in Tab. 2.4 along with the scale and PDF uncertainties: The t-channel values for the Tevatron ($\sqrt{s} = 1.96\,\mathrm{TeV}$) and the LHC ($\sqrt{s} = 7\,\mathrm{TeV}$) are quoted in [Kid11] and utilize the MSTW 2008 NNLO PDF set [Mar+09a]; the LHC t-channel cross-section has been computed in the year 2011 and is used in the simulation samples of the signal employed here (cp. Chap. 4). The most recent t-channel value computed in 2012 for $m_\mathrm{t} = 173\,\mathrm{GeV}$ [Kid12] is also quoted as well as an NLO value [Kan+13] calculated with HATHOR [Ali+11] and the CT10NNLO PDF set [Gao+13]. The s-channel cross-sections for both colliders are taken from [Kid10a]. The Wt-channel production rate at the LHC is given in [Kid10b] whereas the mode is negligible at the Tevatron. The Tevatron values are taken at $m_\mathrm{t} = 173\,\mathrm{GeV}$, the

$\sqrt{s}$ (TeV)	Process	σ_{sgtop} (pb)	Scale Unc. (pb)	PDF Unc. (pb)
1.96	t-channel	2.08	+0.00 /-0.04	±0.12
1.96	s-channel	0.523	+0.001/-0.005	+0.030/-0.028
1.96	Wt-channel	—	—	—
7	t-channel (2011)	64.57	+2.63/-1.74	
7	t-channel (2012)	65.9	+2.1 /-0.7	+1.5 /-1.7
7	t-channel (NLO)	65.39	+1.79 /-1.10	+0.92 /-0.85
7	s-channel	4.63	+0.20/-0.18	
7	Wt-channel	15.74	+1.17/-1.21	

Table 2.4. Predicted cross-sections at approximate NNLO of the single-top production processes for the Tevatron experiments ($\sqrt{s} = 1.96\,\text{TeV}$, at $m_\text{t} = 173\,\text{GeV}$) and the LHC experiments ($\sqrt{s} = 7\,\text{TeV}$, at $m_\text{t} = 172.5\,\text{GeV}$ except for the t-channel from 2012, computed at $m_\text{t} = 173\,\text{GeV}$) [Kid11; Kid12; Kan+13; Kid10a; Kid10b].[6] The PDF error of the NLO value also includes an α_S uncertainty. The Wt-channel contribution at the Tevatron is negligible.

Experiment	Luminosity	Process	σ_{sgtop} (pb)	Uncertainty (pb)
CDF	$2.2\,\text{fb}^{-1}$	t-ch. & s-ch.	2.2	+0.7/-0.6
D0	$2.3\,\text{fb}^{-1}$	t-ch. & s-ch.	3.94	±0.88
CDF & D0	$3.2\,\text{fb}^{-1}/2.3\,\text{fb}^{-1}$	t-ch. & s-ch.	2.76	+0.58/-0.47
CMS	$36\,\text{pb}^{-1}$	t-ch.	83.6	±30
ATLAS	$35\,\text{pb}^{-1}$	t-ch.	53	+46/-36
ATLAS	$156\,\text{pb}^{-1}$	t-ch.	76	+41/-21
ATLAS	$0.7\,\text{fb}^{-1}$	t-ch.	90	+32/-22
CMS	$1.17\,\text{fb}^{-1}/1.56\,\text{fb}^{-1}$	t-ch.	67.2	±6.1

Table 2.5. Single-top production cross-sections as measured by the Tevatron and LHC experiments [CDF08; D0 09; CDF09; CMS11a; ATL11h; ATL11g; ATL11d; CMS12a].

LHC values are extrapolated for $m_\text{t} = 172.5\,\text{GeV}$.[6] Like for $\text{t}\bar{\text{t}}$ production, the exact cross-section values depend on the top mass entering the computation, the PDF set used and the $\mu_\text{R}/\mu_\text{F}$ scales chosen; the corresponding excursions for a variation of m_t by a few GeV, for the (intra-)PDF error[7] at 90 % C.L. and for a halving/doubling of the scales $\mu_\text{R} = \mu_\text{F} = m_\text{t}$ are typically at the level of a few percent for the NLO t-channel calculation. Through the PDFs, there is also an α_S dependence of a few percent included in the PDF error of the HATHOR value.

[6] L. Mijovic. *ATLAS TWiki: Top group's MC11(a,b,c) Samples For 2011 Data Analyses*. Dec. 2012. URL: `https://twiki.cern.ch/twiki/bin/viewauth/AtlasProtected/TopMC11`.

[7] For details on the uncertainties associated with PDF sets, refer to Sec. 6.1.1.

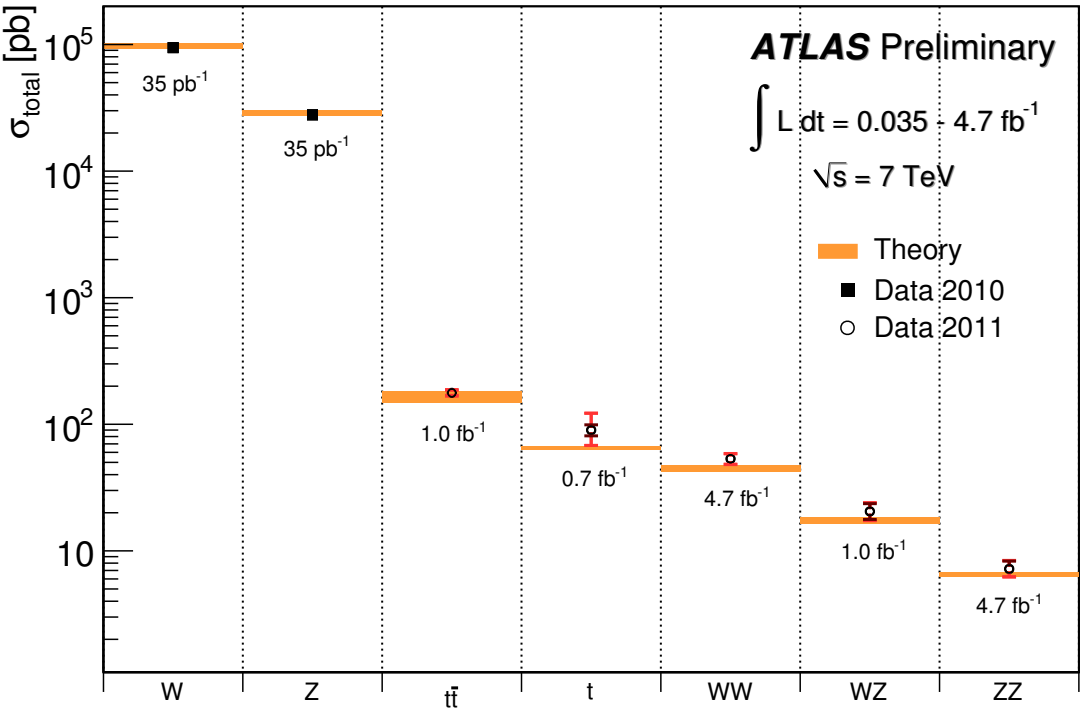

Figure 2.13. Cross-sections of standard model processes measured up to spring 2012 by ATLAS.[8] The black error intervals denote the statistical uncertainty, the red error intervals represent the systematic errors.

The single-top process was discovered at the Tevatron in the year 2008 by CDF [CDF08] in a combined measurement of the t-channel and s-channel modes. In 2009, a measurement by D0 followed [D0 09] and a combination of results was also published in 2009 [CDF09]. The single-top t-channel process was then measured again by the LHC experiments: ATLAS [ATL11h] and CMS [CMS11a] reported their findings on the data of the first year of LHC's running. The result by ATLAS was updated twice in this early period [ATL11g; ATL11d], and there is also a current value from CMS [CMS12a]. Table 2.5 collects the Tevatron measurements as well as early LHC results and the most recent CMS value for the t-channel (cp. predictions in Tab. 2.4).

Concentrating on the ATLAS experiment, Fig. 2.13 gives an overview of the standard model cross-sections measured until spring 2012: The single-top cross-section refers to the t-channel mode and displays the biggest systematic uncertainty. The corresponding measurement was a combination of results of a neural network (NN) approach and a cut-based scheme which was updated on a larger dataset with a total integrated luminosity of $1.04\,\mathrm{fb}^{-1}$ [ATL12j] to yield the result shown at the top of Fig. 2.14; the most recent result on $4.7\,\mathrm{fb}^{-1}$ of data was a NN measurement of

[8] ATLAS Collaboration. *ATLAS Physics Summary Plots*. Mar. 2012. URL: `https://twiki.cern.ch/twiki/bin/view/AtlasPublic/CombinedSummaryPlots`

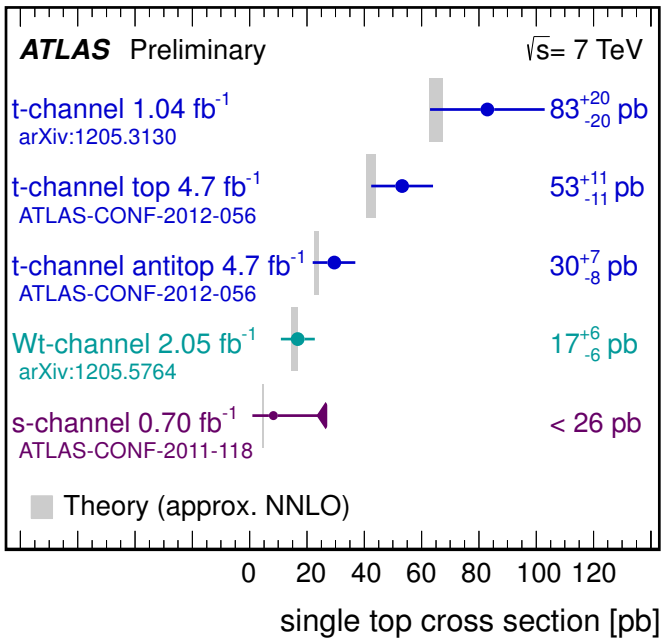

Figure 2.14. Single-top cross-section measurements published until summer 2012 by ATLAS.[9] The respective theoretical predictions at approximate NNLO including uncertainties are shown as grey bands.

the ratio of top and anti-top quark production [ATL12i], which is also shown in the figure. The latter two as well as the current CMS result will be compared in detail to the outcome of this work in Sec. 6.3 of Chap. 6. Also the Wt-channel mode has been measured with good precision although the production rate is lower; this is due to the fact that the shown measurement refers to a clean dileptonic signature. For the s-channel, only limits have been derived so far by ATLAS. Fig. 2.15 displays the ATLAS results again in the context of the standard model predictions as a function of the centre-of-mass energy.

Meanwhile, however, a 3.7σ evidence of this process has been observed at D0 [D0 13] on a dataset of $9.7\,\mathrm{fb}^{-1}$, as depicted in Fig. 2.16: The 2D observed posterior probability density distributions of the cross-sections of the t-channel (denoted by "tqb") and s-channel (denoted by "tb") modes are shown in the form of their one (green), two (yellow) and three (blue) standard deviation (SD) contours. The black dot marks the central value of this measurement, whereas the standard model expectation [Kid06] is shown as a solid red box. The plot also includes the predictions of some theories beyond the standard model, i.e. the case of four quark generations with $|V_{\mathrm{ts}}| = 0.2$ [Alw+07] as a hollow diamond, a top-flavour model with new heavy bosons of mass $m_x = 1\,\mathrm{TeV}$ [TY00] as a hollow circle, an approach postulating charged top-pions of mass $m_{\pi^\pm} = 250\,\mathrm{GeV}$ [TY00] as a hollow triangle

[9] ATLAS Collaboration. *ATLAS Physics Summary Plots*. July 2012. URL: `https://twiki.cern.ch/twiki/bin/view/AtlasPublic/CombinedSummaryPlots`

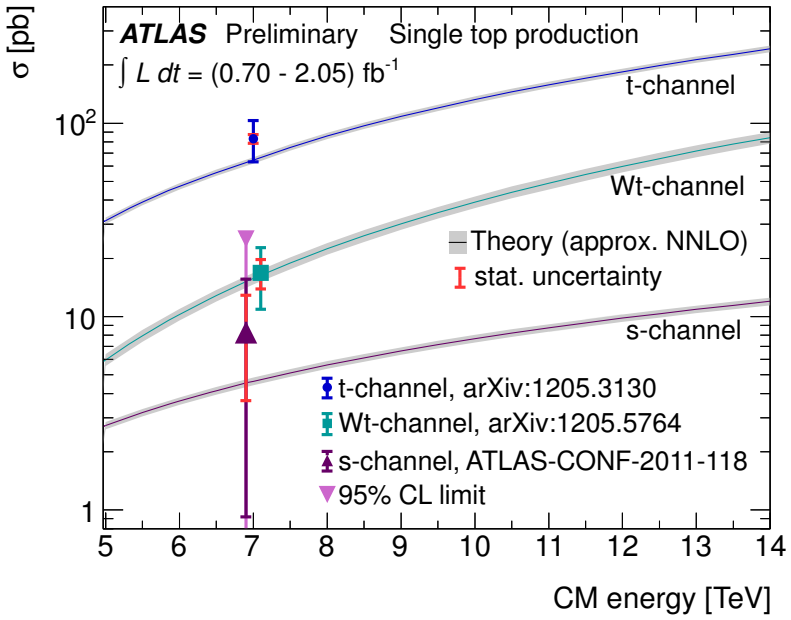

Figure 2.15. Single-top cross-section measurements published by ATLAS and approximate NNLO prediction as a function of the centre-of-mass energy.[10] The black error intervals denote the statistical uncertainty, the red error intervals represent the systematic errors. The standard model prediction includes the theoretical uncertainties as shaded bands.

as well as a scheme allowing for FCNCs with an up quark/top quark/gluon coupling of $\kappa_u/\Lambda = 0.036$ [TY00; D0 07] as a hollow box. As can be seen, these exotic models are by no means excluded according to the current level of knowledge.

In order now to arrive at more precise results it is instructive to study alternative methods of extracting the single-top cross-sections from data as to ensure a thorough understanding of these production modes and a further suppression of systematic effects. To provide an increased level of precision for the t-channel cross-section measurement is the aim of this study. Before the analysis method applied here is described in detail in Chap. 5, the LHC machine and the ATLAS detector, which delivered the data for the cross-section analysis, will be described in the next chapter.

[10] ATLAS Collaboration. *ATLAS Physics Summary Plots*. July 2012. URL: `https://twiki.cern.ch/twiki/bin/view/AtlasPublic/CombinedSummaryPlots`

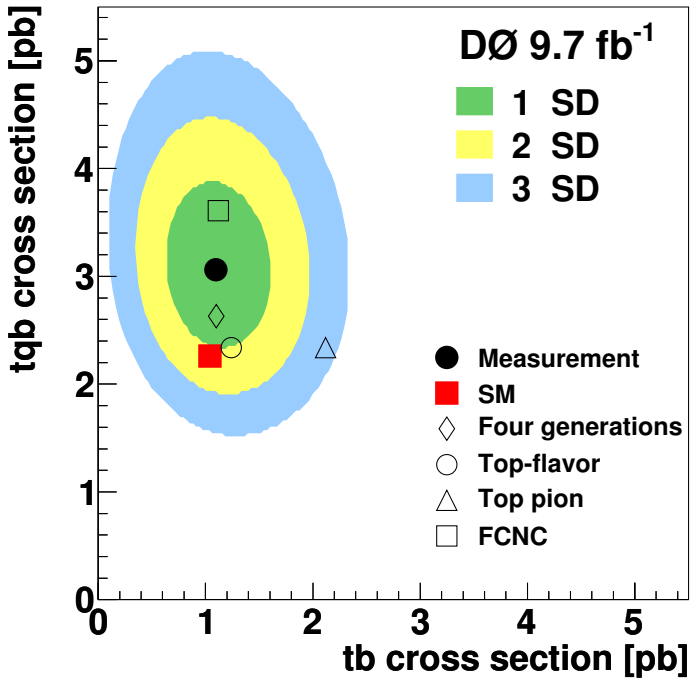

Figure 2.16. Single-top t-channel vs. s-channel cross-section measurements by D0; the plot is taken from [D0 13]. The standard model expectation is shown as well as predictions of models including a fourth quark generation, top-flavour with new heavy bosons, top pions and flavour changing neutral currents.

That great giant, Atlas, whose
shoulders bear the circling sky.
Ovid, Metamorphoses

3. The ATLAS Detector at the LHC

The ATLAS detector is one of the major experiments at the Large Hadron Collider (LHC) [Bru+04] of the European Centre of Nuclear Research (CERN) near Geneva, Switzerland. In its proton-proton collision mode, the LHC delivers collision events at a nominal rate of 40 MHz to its four major experiments along the collider ring: ATLAS [ATL08] and CMS [CMS08] are both multi-purpose detectors, equipped to detect a wide range of known and hypothesized standard model and beyond standard model particles resulting from the collisions. The LHCb detector [LHC08] specializes in rare B-meson decays and aims at precision measurements in flavour physics. To this end, unlike ATLAS and CMS, it is constructed asymmetrically in the forward and backward region. The fourth big experiment is the ALICE detector [Lou96] suited to record collisions of lead ions that are also delivered by the LHC in its alternative run mode. The aim of the ALICE collaboration are investigations of a very hot and dense state of matter, the quark-gluon plasma.

3.1. The LHC Machine

After fourteen years of planning and building, this impressive machine took up operation on the 10th of September 2008 when the first proton beams circulated through the LHC. Following some initial technical difficulties, the first proton-proton collisions were finally recorded on the 23rd of November 2009, and on the 30th of March 2010, the data-taking of proton-proton collisions at a centre-of-mass energy of $\sqrt{s} = 7\,\text{TeV}$ (3.5 TeV per beam) commenced. However, since the LHC beam specifications apart from $\sqrt{s}$ still changed when data-taking was taken up again in 2011, the 2010 part of the dataset is discarded for analyses, also because it corresponds to a very small amount of the total data collected: The total integrated luminosity (see Sec. 3.2.1) obtained in 2010 is only $45\,\text{pb}^{-1}$ as compared to $5.25\,\text{fb}^{-1}$ from 2011, $4.7\,\text{fb}^{-1}$ of which are used in this study.[1]

In Fig. 3.1, the LHC accelerator complex is shown and the locations of the four major experiments are marked with yellow dots. The protons are produced by ionizing hydrogen and are then fed into a linear accelerator, the LINAC 2, which brings them up to an energy of 50 MeV. The protons then pass to a first circular pre-accelerator, the PS BOOSTER, where the incident beam is split and distributed to four stacked rings, accelerating the protons to 1.4 GeV. The protons from the four rings are then recombined and transferred to the PS (proton synchrotron), another circular

[1] ATLAS Collaboration. *Luminosity Public Results*. Nov. 2013. URL: `https://twiki.cern.ch/twiki/bin/view/AtlasPublic/LuminosityPublicResults`.

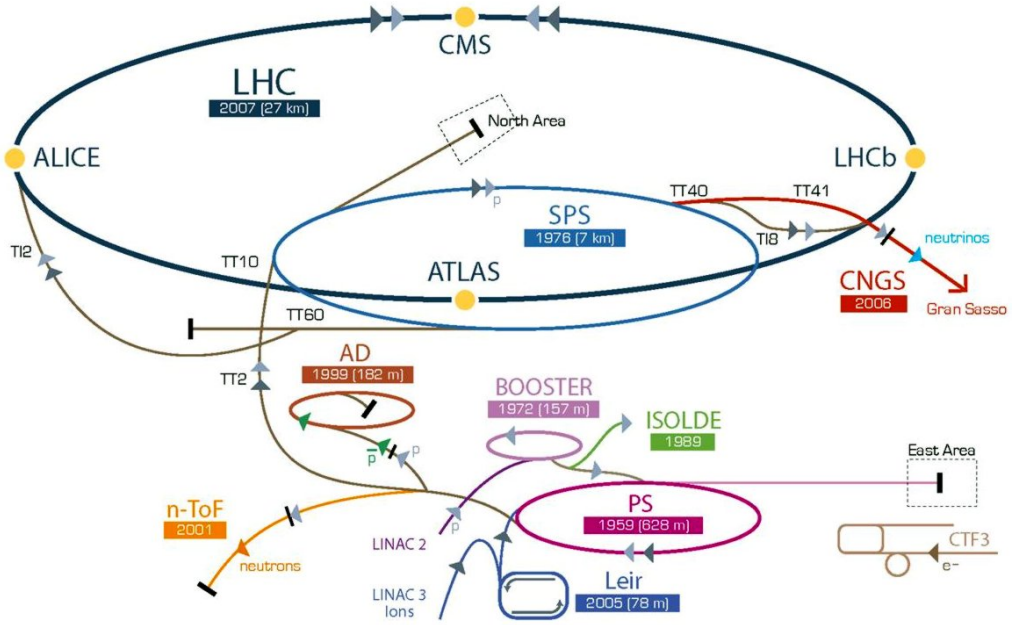

Figure 3.1. The CERN accelerator complex with the LHC, its pre-accelerators and its major experiments, marked as yellow dots: ATLAS, CMS, LHCb and ALICE.[2] The way of the protons from the LINAC 2 to the BOOSTER, the PS and the SPS into the LHC is shown. Some other CERN experiments are also displayed (e.g. the neutrinos sent to the Gran Sasso laboratory).

pre-accelerator, where a proton energy of about 30 GeV is obtained. The final pre-acceleration step takes place in the SPS (super proton synchrotron) ring which delivers protons of an energy of 450 GeV to the main LHC accelerator tunnel, in which a proton energy of 3.5 TeV is achieved.

The LHC tunnel has a circumference of 27 km and stretches beneath Swiss and French territory. It is situated at a depth of around 100 m and consists of eight straight sections as well as eight connecting arcs. In the straight sections, the protons are accelerated in superconducting radio-frequency (RF) cavities operating at 400 MHz. The arc sections serve to bend the path of the protons and are equipped with superconducting dipole magnets, quadrupole magnets and multipole corrector magnets that are operated at a temperature of 1.9 K. The dipole magnets evoke a magnetic field of up to 8.6 T. As the protons are accelerated, the magnetic field strength and the frequency of the RF cavities rise to adapt. The two-in-one magnet design allows for two beams circulating in opposite directions in separate beam pipes. The beams cross in four points along the ring at the locations of the detectors. At the LHC, there is also an extensive machine protection system in place including beam-monitoring diagnostics, and it possesses facilities for beam-cleaning. The LHC beam specifications for the 2011 data taking period are collected in Tab. 3.1. The

[2]CERN. *Exhibition BIG SCIENCE – The LHC in pictures*. July 2012. URL: `http://bigscience.web.cern.ch/bigscience/en/lhc/lhc2.html`

Beam Characteristics	2011	Nominal
Number of Protons per Bunch	$15 \cdot 10^{10}$	$11.5 \cdot 10^{10}$
Number of Proton Bunches	200 – 1380	2808
Bunch Spacing	50 ns	25 ns
Peak Instantaneous Luminosity	$3.65 \cdot 10^{33}\,\mathrm{cm^{-2}s^{-1}}$	$1.0 \cdot 10^{34}\,\mathrm{cm^{-2}s^{-1}}$
Mean Number of Pile-Up Interactions	9	19
β^*	1.5 m	0.55 m

Table 3.1. Beam characteristics of the LHC during most of the running period of the year 2011 as well as the corresponding design parameters (nominal) [Bru+04; Ber+12].[3]

instantaneous luminosity will be the topic of Sec. 3.2.1 and is defined there along with the mean number of pile-up interactions per bunch-crossing. The length β^* denotes the amplitude function of the beam at the interaction point and is thus a parameter describing the degree of collimation of the colliding beams: It is a measure of the distance from the interaction point at which the beam is twice the size of that at the interaction point.

3.2. The ATLAS Detector

The ATLAS detector (A Toroidal LHC ApparatuS) [ATL08; ATL99] is a large instrument measuring 44 m along the beampipe and 25 m across from it. It is designed to detect all known particles of the standard model either directly (if they are stable) or indirectly via their decay products. To this end, the detector is shaped like an onion with multiple layers of different components, arranged concentrically around the interaction point in the centre, see Fig. 3.2. Each of the detector components is suited to detect a particular type of particle and serves to measure specific kinematic properties. The single detector components are described in detail in Sections 3.2.3, 3.2.4, 3.2.5 and 3.2.6, whereas the respective methods of particle identification are depicted in the third major part of this chapter, namely Sec. 3.3. The first part of this section, Sec. 3.2.1, however, is dedicated to the yet more basic task of determining the instantaneous luminosity entering the detector, i.e. the reference rate of inelastic interactions taking place. The section succeeding the outline of the detector components, Sec. 3.2.7, finally, concludes this second section by presenting the trigger system employed to filter out the interesting part of the data to be used for analyses; some technical details of the electronic data acquisition system are also mentioned.

At this point, some nomenclature must be introduced:

[3] Mike Lamont. *LHC Commissioning With Beam*. Nov. 2013. URL: `http://lhc-commissioning.web.cern.ch/lhc-commissioning/progress2011.htm`; ATLAS Collaboration. *Luminosity Public Results*. Nov. 2013. URL: `https://twiki.cern.ch/twiki/bin/view/AtlasPublic/LuminosityPublicResults`

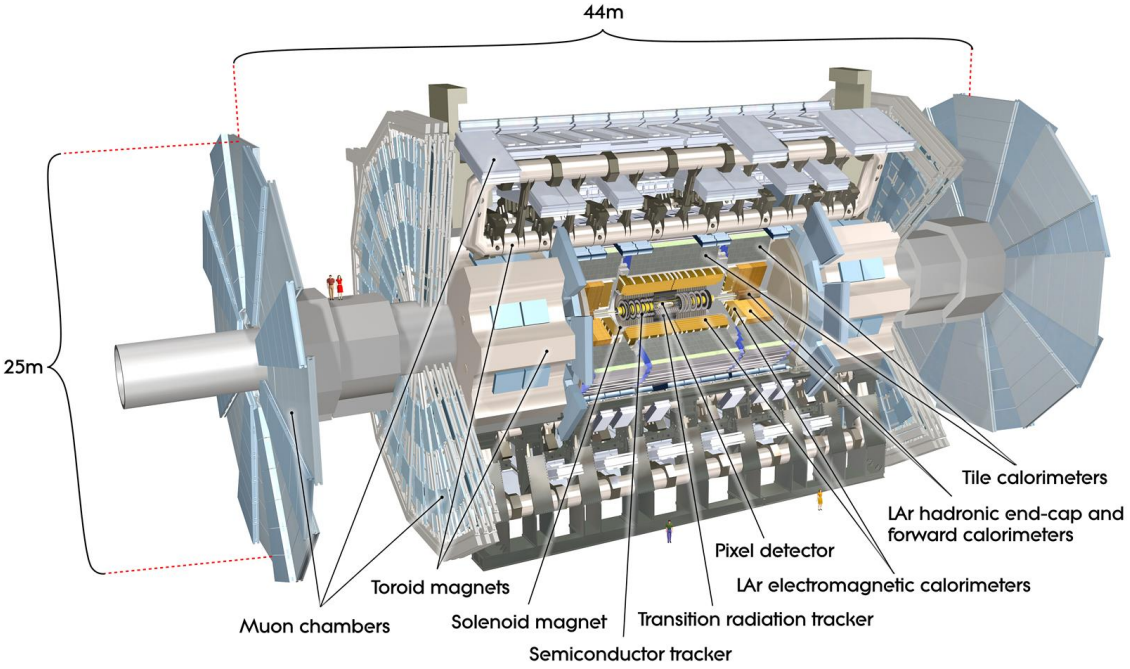

Figure 3.2. The ATLAS detector with its different layers of components: the tracking chambers in the innermost layers, surrounded by the central solenoid magnet, the electromagnetic calorimetry and the hadronic calorimetry. The outermost detector parts are the extensive muon chambers, submerged in the magnetic field of the large air-core toroid magnets. Picture taken from [ATL08].

- The ATLAS coordinate system is a right-handed system with the x-axis pointing to the centre of the LHC ring, the y-axis pointing upwards and the z-axis aligned with the beam-direction.

- The azimuthal angle ϕ is measured clock-wise from the positive x-axis looking into the positive z-direction and spans the range $[-\pi, \pi]$.

- The polar angle θ is measured from the positive z-axis.

- The rapidity y and the pseudorapidity η are defined as[4]

$$y = \frac{1}{2} \ln \left(\frac{E + p_z}{E - p_z} \right) , \tag{3.1a}$$

$$\eta = -\ln \left(\tan \frac{\theta}{2} \right) , \tag{3.1b}$$

[4]Massless particles are described by y, massive ones by η.

where E is the particle's energy and p_z is its momentum component in z-direction.

- The distance ΔR in the space of the pseudorapidity and the azimuthal angle is given by
$$\Delta R = \sqrt{(\Delta\eta)^2 + (\Delta\phi)^2}\,. \tag{3.2}$$
- The transverse momentum p_{T} is defined as the momentum component perpendicular to the beampipe of the LHC.

3.2.1. Luminosity Measurement

A precise determination of the absolute rate of inelastic interactions taking place in the collision of the proton bunches in ATLAS is a crucial prerequisite for any subsequent data analysis. At the LHC, multiple inelastic collisions are taking place in each bunch-crossing, an effect called in-time pile-up.[5] For a certain sample of bunch-crossings, the number of these pile-up interactions is Poisson distributed with some mean μ (cp. Tab. 3.1). A particular luminosity detector then measures a visible number of interactions
$$\mu^{\mathrm{vis}} = \epsilon\mu \tag{3.3}$$
depending on the method's efficiency and acceptance, expressed as the factor ϵ. The so-called instantaneous luminosity of the interactions within one luminosity block (LB)[6] is then defined as [Hed11]
$$\mathscr{L}_{\mathrm{LB}} = \frac{f_{\mathrm{LHC}}}{\sigma_{\mathrm{inel}}} \sum_{j=1}^{n_{\mathrm{b}}} \mu_j = \frac{f_{\mathrm{LHC}}}{\sigma^{\mathrm{vis}}} \sum_{j=1}^{n_{\mathrm{b}}} \mu_j^{\mathrm{vis}} \tag{3.4}$$
where f_{LHC} is the LHC revolution frequency and n_{b} is the number of bunches in that LB. The total inelastic cross-section σ_{inel} is connected to the visible cross-section σ^{vis} in an analogous manner to Eq. (3.3) by
$$\sigma^{\mathrm{vis}} = \epsilon\sigma_{\mathrm{inel}}\,. \tag{3.5}$$
In ATLAS, there are two detectors capable of measuring μ^{vis} for individual bunch-crossings: LUCID (LUminosity measurement using Cerenkov Integrating Detector) [Gro10] and the BCM (Beam Conditions Monitor) [Dol09]. LUCID consists of two gas Cerenkov detectors surrounding the beampipe on both sides of the interaction point in the pseudorapidity region $5.6 < |\eta| < 6$. The BCM has four diamond detectors (2 horizontal, 2 vertical ones) on each side of the interaction point at $|\eta| \sim 4$. By measuring the fraction of bunch-crossings in a LB triggering a signal

[5] There is also the notion of out-of-time pile-up, referring to the effects of preceding and subsequent bunch-crossings.

[6] Time span of typically a few minutes in a run during which the instantaneous luminosity is assumed to be constant.

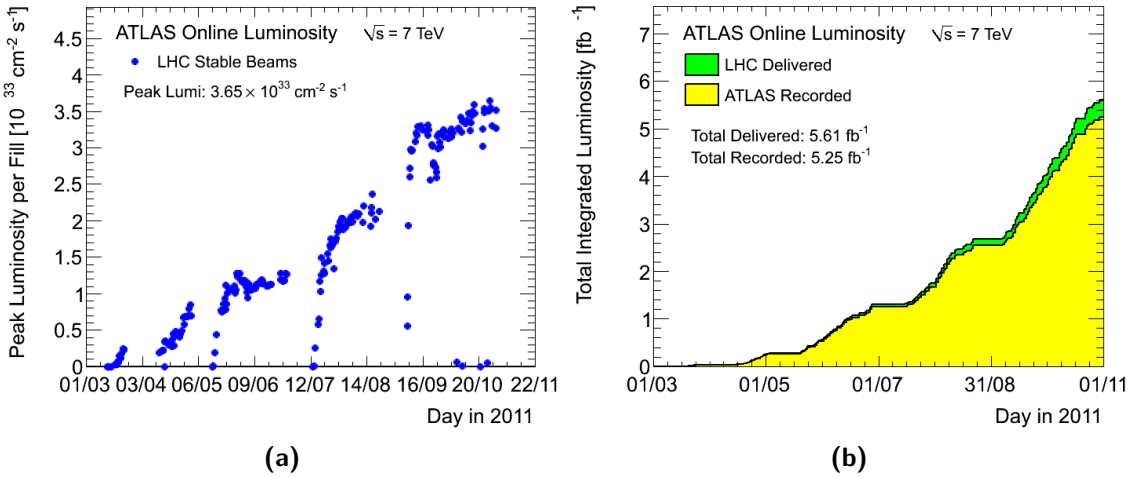

Figure 3.3. Peak instantaneous luminosity of ATLAS by LHC fill (a) and chronology of the integrated luminosity accumulated by ATLAS (b) in the year 2011.[7]

in a detector component on one side of the interaction point ("Event OR") or on both sides ("Event AND"), μ^{vis} can be determined [ATL11c]. The instantaneous luminosity is also measured by calorimeter components: The Forward Calorimeter (FCal) and the Hadronic Tile Calorimeter (Tile) monitor the currents due to inelastic collisions that are proportional to the luminosity. They are not able to measure the luminosity per bunch-crossing, though.

The calibration constant σ^{vis} in Eq. (3.4) must also be derived from measurements. It is obtained from a procedure called "van der Meer scan" that consists of measuring the evolution of the interaction rate in a beam separation scan. The scan is done separately in the horizontal (x) and vertical (y) direction, yielding two bell-shaped curves per colliding bunch pair, from which the scan widths Σ_x and Σ_y can be read off. The maximum luminosity of a colliding bunch pair $\mathscr{L}^{\text{peak}}$ can be gained from the overlap integral of the transverse proton density functions $\rho_1(x, y)$ and $\rho_2(x, y)$ of the two beams that are related to the scan widths by

$$\mathscr{L}^{\text{peak}} = f_{\text{LHC}} n_{\text{p1}} n_{\text{p2}} \int \rho_1(x, y)\rho_2(x, y)\,\mathrm{d}x\mathrm{d}y = f_{\text{LHC}} n_{\text{p1}} n_{\text{p2}} \frac{1}{2\pi\Sigma_x\Sigma_y}\,. \tag{3.6}$$

Here, $n_{\text{p1(2)}}$ are the number of protons in the respective bunch that are determined by DC current transformers measuring the total LHC current and fast beam current transformers assigning a fraction of the total current to each bunch. Combining

[7] ATLAS Collaboration. *ATLAS Data Summary – Luminosity in 2011*. Aug. 2012. URL: `https://atlasop.cern.ch/operRef.php?subs=http://atlas.web.cern.ch/Atlas/GROUPS/DATAPREPARATION/DataSummary/`

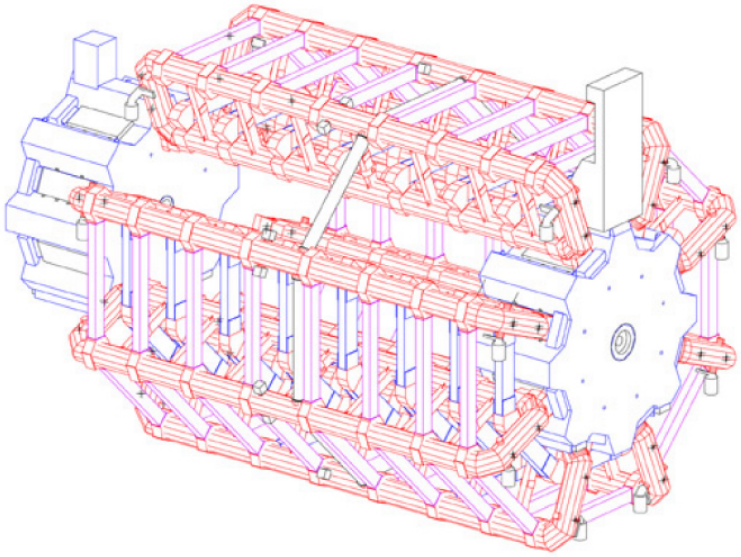

Figure 3.4. System of toroid magnets of ATLAS in the barrel and end-cap regions.[8]

Eq. (3.4) with Eq. (3.6), the visible cross-section is found to be

$$\sigma^{\text{vis}} = 2\pi \frac{\mu^{\text{vis}}_{\text{peak}} \Sigma_x \Sigma_y}{n_{\text{p1}} n_{\text{p2}}} \,. \tag{3.7}$$

According to Eq. (3.4), the instantaneous luminosity is then computed, and its time-integral, the so-called "integrated luminosity", i.e. the size of the accumulated data sample for analysis, can be determined. The evolution of both quantities for the ATLAS detector in the year 2011 is shown in Fig. 3.3.

3.2.2. Magnet System

The ATLAS detector is equipped with a sophisticated system of superconducting magnets for the bending of charged particles. The magnet system consists of two major components: the Central Solenoid (CS) [ATL97f] surrounding the inner tracking detectors and the toroid magnets in the outermost layers, supplying the magnetic field for the muon chambers. There is a central toroidal structure, the Barrel Toroid (BT) [ATL97d], and a corresponding part in the forward region of the detector, the End-Cap Toroids (ECT) [ATL97e], see Fig. 3.4. Since all magnets are operated at a temperature of 4.5 K, extensive cooling structures are assembled as well. The common superconductor material used is a NbTi/Cu/Al composite in form of a flat cable embedded in an aluminium stabilizer with rectangular cross-section. There is also an adequate quench protection system in place [ATL97c], ensuring a controlled

[8] ATLAS Collaboration. *ATLAS Magnet System – Illustrations*. Sept. 2012. URL: `http://atlas-bt.web.cern.ch/atlas-bt/gallery/images/`

dissipation of the stored energy in case of sudden energy dumps.

The CS is a single-layer coil measuring 5.3 m in length with a diameter of 2.4 m, situated between the TRT (see Sec. 3.2.3) and the Liquid Argon Calorimeter (see Sec. 3.2.4). Bearing a current of 7.6 kA, it provides a 2 T strong magnetic field in the central tracking volume and is constructed with a minimum thickness to decrease particle scattering effects. In order to reduce material build-up and enhance particle transparency, the CS shares its cryostat with the Liquid Argon Calorimeter.

The BT consists of eight 25 m long toroidal coils symmetrically arranged around the beam axis that generate the magnetic field for the central region of the muon detector. It is operated at a current of 20.5 kA and reaches a peak magnetic field of 3.9 T. The assembly weighs 830 t and is maintained by 16 supporting rings. One cryogenic ring connects the eight coils that are mounted in individual cryostats and indirectly cooled by liquid helium flowing in tubes attached to the coil casing.

The ECT is positioned inside the BT, consisting of two symmetrical parts at each end of the CS. It provides the magnetic field in the forward direction for radii between 1.7 m and 5 m. One end-cap has a diameter of 11 m and a width of 5 m and contains eight coils assembled in a common cryostat which can be retracted in order to access the central detector components. The coils of the ECT are rotated by 22.5° with respect to the BT coils allowing a radial overlap and thus an optimization of the magnetic bending power in the interface region of the toroids. The ECT is connected in series with the BT, also operating at a current of 20.5 kA evoking a peak magnetic field of 3.9 T.

3.2.3. Inner Detector

The inner part of the ATLAS detector [ATL99; ATL97a; ATL97b; Lac12] is dedicated to detecting tracks of charged particles and determining their vertices. It consists of three components (see Fig. 3.5): The innermost is the Pixel Detector (Pixel) which is embedded in the next layer, the Semi-Conductor Tracker (SCT) which again is surrounded by the Transition Radiation Tracker (TRT). The Pixel and the SCT are high-resolution semiconductor tracking devices complemented by the TRT, a straw tube detector, permitting tracking over a longer range using higher hit multiplicities. All three inner detector components consist of barrel and end-cap parts and are submerged in the magnetic field of the CS (see Sec. 3.2.2). The radii of the different inner detector components with respect to the beampipe are shown in Fig. 3.6. Their acceptance range is limited to $|\eta| \leq 2.5$.

Pixel Detector

The Pixel Detector is a silicon semiconductor tracking device arranged in three concentrical layers around the beampipe in its barrel part. In the forward region, it consists of five end-cap disks on either side that are oriented perpendicular to the beam axis. The pixel layers are segmented in $R\phi$ and z and provide typically measurement resolutions of $\sigma_{R\phi} = 10\,\mu\text{m}$ and $\sigma_z = 115\,\mu\text{m}$. There are about 140

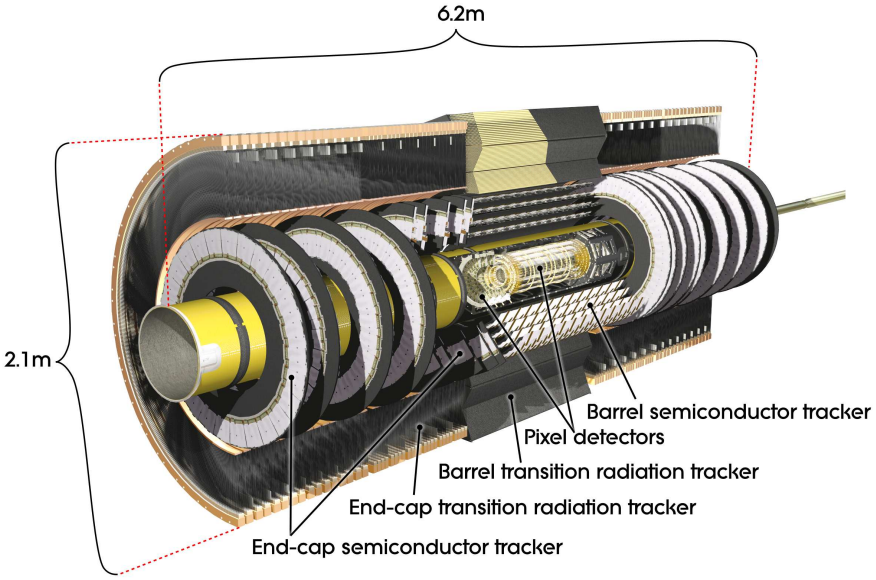

Figure 3.5. Inner detector components of ATLAS in the barrel and forward regions [ATL08].

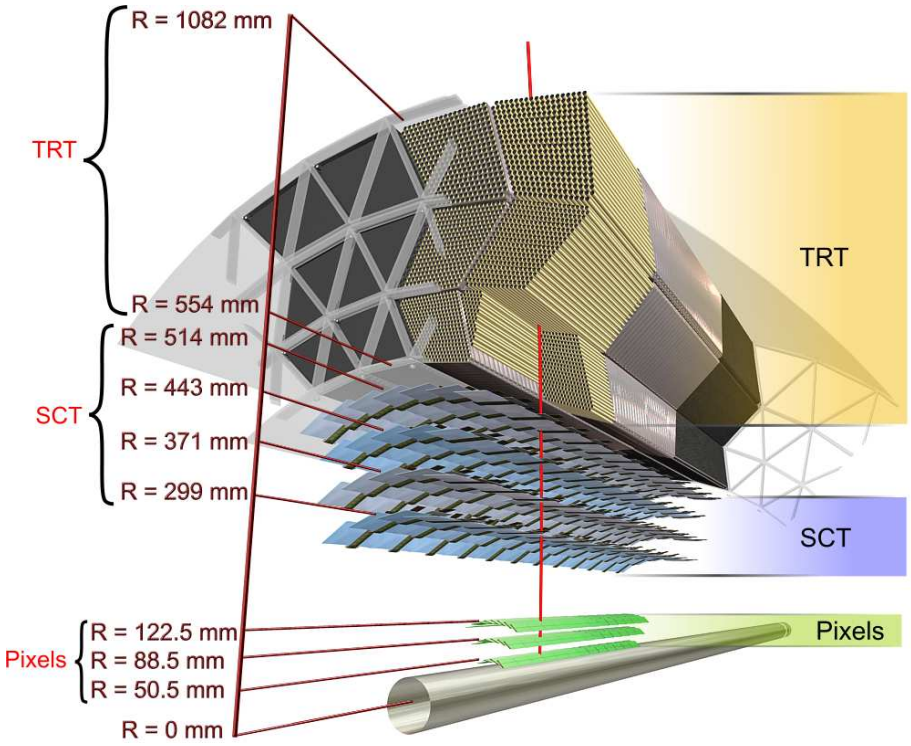

Figure 3.6. Distance of the inner detector layers of ATLAS to the beampipe [ATL08].

million pixel elements in total with a width of 50 µm in $R\phi$ direction and a length of 300 µm in z direction. The pixels are situated on 1,500 barrel and 700 disk modules of a size of 62.4 mm by 21.4 mm each. The modules are overlapping to provide hermetic geometrical coverage for the high track density environment of the LHC and supply at least 3 precision hits per track.

The pixel technology offers high-precision and high-granularity measurements and is employed as close to the interaction point as possible. Hence, the single components are required to be radiation-hardened and have only a life-time of a few years. For this reason, the innermost pixel layer, the B-layer, is mounted in a way that it can be replaced. Its reliable performance is vital since it allows for the detection of impact parameters and secondary vertices of heavy particle decays. In the context of this study, its capability to resolve the decay lengths of B-mesons (which are of the order of millimetres) is of particular importance, since this kind of secondary vertex recognition ("b-tagging", cp. Sec. 3.3.2) is used in the event preselection of the analysis in Sec. 4.4.

SCT

The SCT is a silicon microstrip detector, providing hits on eight barrel strip layers (corresponding to four space-points) for each track in the intermediate radial range from the beam axis. In the forward region, it is equipped with nine end-cap layers on either side. The SCT modules consist of four single-sided p-on-n silicon sensors of which two are daisy-chained together, respectively. The two sensor pairs are glued back-to-back. In the barrel part, the strips on one side of the module are aligned parallel to the beam axis and thus measure R and ϕ. In order to also allow for a measurement of the z coordinate, the strips on the other side of the module are rotated by a 40 mrad angle with respect to the strips on the other side. In the end-caps, the strips are running radially, again with the second layer rotated by 40 mrad. One sensor measures $6.36\,\mathrm{cm}^2 \times 6.40\,\mathrm{cm}^2$ and contains 768 readout strips at a pitch of 80 µm. There are in total 6.2 million readout channels distributed across an unprecedented active detector area of $61\,\mathrm{m}^2$ of silicon. A spatial resolution of 17 µm in $R\phi$ and 580 µm in z is achieved, and tracks of a separation exceeding 200 µm can be distinguished.

TRT

The TRT is a straw tube detector with straws aligned with the beam axis in the barrel part. The end-caps consist of radial straws arranged into 18 wheels. The outermost wheels in z extend further towards the beampipe in order to guarantee full η-coverage. The TRT typically provides 36 space points per track, thus majorly contributing to the momentum measurement. Although the precision of the individually measured coordinates is much lower than that of the semiconductor tracking devices, 130 µm per straw, the high number of hits up to large radii still allow for an excellent pattern recognition and a combined measurement accuracy of 50 µm on average. Furthermore,

the TRT possesses electron identification capabilities: Between the straws, radiator material is inserted that prompts electrons to emit transition radiation photons that can be detected in the gas of the tubes. To this end, the gas mixture is chosen to be made up of 70 % Xe, 20 % CO_2 and 10 % CF_4. The straws have a diameter of 4 mm and contain a 30 µm thick gold-plated W-Re wire that supports a maximum straw length of 144 cm in the barrel part. The 50,000 barrel straws are split in the middle to allow for read out at both ends, providing a measurement of the z-coordinate. The 320,000 end-cap straws are read out at the far ends. Each of the 420,000 electronic channels yields drift-time information as well as two threshold decisions for tracking hits (lower threshold) and transition radiation hits (higher threshold).

3.2.4. Electromagnetic Calorimetry

The Electromagnetic Calorimeter (EMCAL) [ATL99; ATL96a; ATL96c; Sol12] consists of a barrel and two end-cap (EMEC) parts (light brown segments in Fig. 3.7). The 6.8 m long barrel part is divided in the middle by a gap of 6 mm for cabling and services and covers the range of $|\eta| < 1.475$. The end-caps are composed of two coaxial wheels: an inner one covering the region $2.5 < |\eta| < 3.2$ and an outer one, extending between $1.375 < |\eta| < 2.5$. The EMCAL is a sampling calorimeter employing lead as the shower material and liquid Argon (LAr) as the signal medium. An accordion-shaped geometry of lead absorber plates and electrodes ensures that no particles are lost in the gaps between the plates, cp. Fig. 3.8. In the barrel, the thickness of the lead absorbers is optimized as a function of η whilst retaining a constant width of the LAr gap of 2.1 mm. In the end-caps, the amplitude of the accordion structures increases with increasing radius, keeping a constant absorber thickness and thus varying the LAr gap width. In terms of radiation lengths X_0, the thickness of the EMCAL corresponds to $> 24\,X_0$ in the barrel and $> 26\,X_0$ in the end-caps. In the range $|\eta| < 2.5$ relevant for precision measurements, the EMCAL is segmented into three concentrical layers whose specifications are depicted in Fig. 3.8: a strip layer in the first sampling, a layer of square towers in $\Delta\eta \times \Delta\phi$ in the second sampling and an even coarser segmentation in the third sampling. The compartment of the first sampling serves as a 'preshower' detector for improved particle identification (e.g. γ/π_0 and e/π separation) and η position measurement. An additional presampler layer in front of the first EMCAL sampling is employed to correct for energy losses of particles in preceding material layers throughout the range $|\eta| < 1.8$. The region $1.37 < |\eta| < 1.52$, called "crack region" in the following, features a large amount of material in front of the EMCAL and is not used for physics measurements. In total, the EMCAL is read out via 190,000 channels and its energy resolution amounts to

$$\frac{\sigma_E}{E} \approx \frac{10\,\%}{\sqrt{E/\mathrm{GeV}}} + 0.7\,\% \tag{3.8}$$

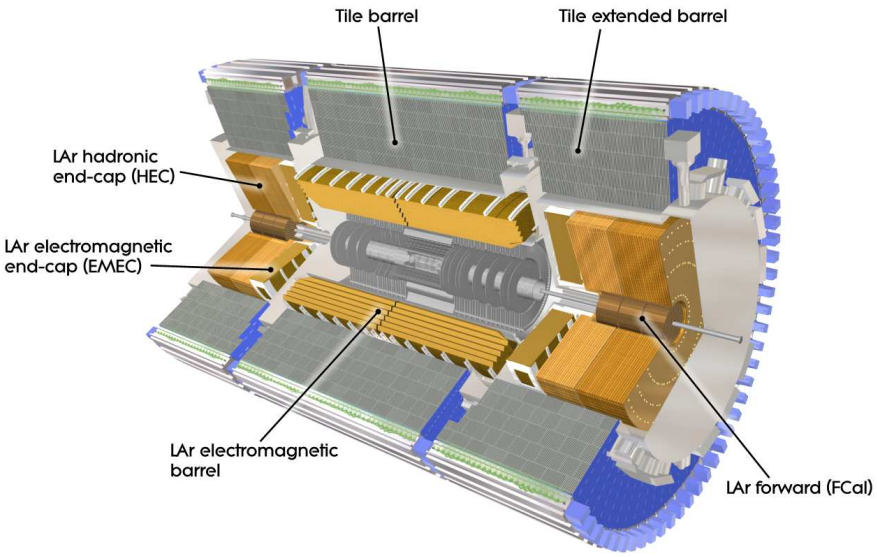

Figure 3.7. Electromagnetic and hadronic calorimetry of the ATLAS detector [ATL08].

where the first term originates from sampling fluctuations ("sampling term") and the second one describes imperfections in correcting for energy losses due to lateral or longitudinal leakage or inhomogeneities in ϕ ("local constant term").

3.2.5. Hadronic Calorimetry

The Hadronic Calorimeter (HCAL) [ATL99; ATL96c; ATL96b; ATL96a; Sol12] consists of a barrel part, an extended barrel part and an end-cap part (HEC) (grey and brown sections in Fig. 3.7). Directly surrounding the beampipe within the HEC, there is still another calorimeter dedicated to the detection of very forward objects, the Forward Calorimeter (FCAL) (dark brown parts in Fig. 3.7).

The barrel and extended barrel compartments of the HCAL extend over radii from 2.28 m to 4.25 m and cover the range $|\eta| < 1.8$. They are sampling calorimeters employing iron as absorber material and scintillating plastic tiles as active medium. Hadronic particles evoke showers in the iron layers that cause the scintillating sections to emit light collected by wavelength shifting fibres that are read out by two photomultipliers per tile. There are three samplings composed of 3 mm thick tiles and iron plates of 14 mm thickness. Azimuthally, the wedge-shaped tiles are arranged in 64 modules. The resulting granularity is $\Delta\eta \times \Delta\phi = 0.1 \times 0.1$ for the two inner samplings and $\Delta\eta \times \Delta\phi = 0.2 \times 0.1$ for the outer sampling, amounting to a total of 10,000 read-out channels. The 68 cm wide gap between the barrel and extended barrel sections of the HCAL houses services and electronics as well as a supplementary calorimeter part, the intermediate tile calorimeter (ITC), which is of like design as the barrel calorimeter and improves the thickness of the HCAL in this sector.

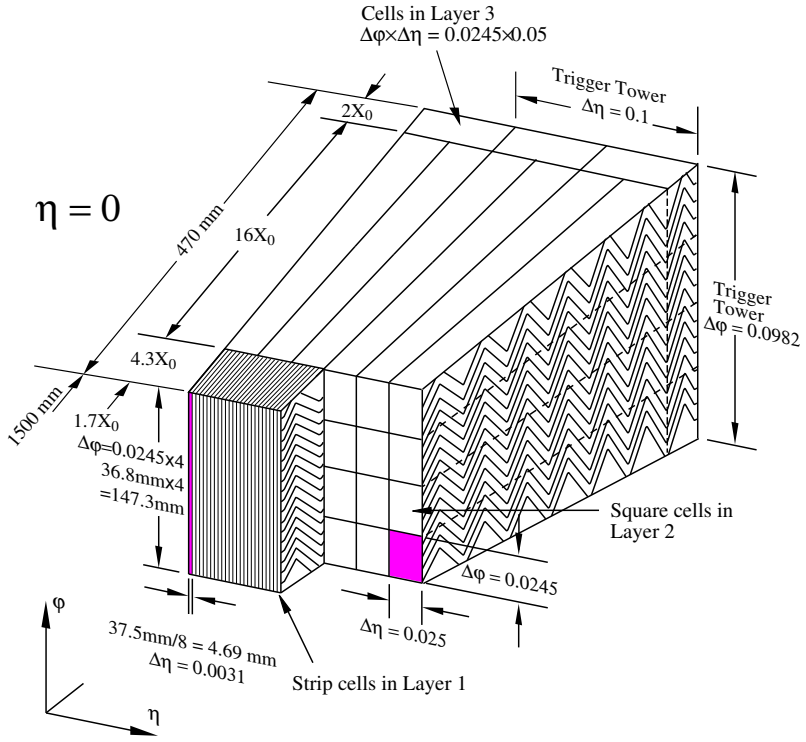

Figure 3.8. Segmentation in the η - ϕ plane of the electromagnetic LAr calorimeter of the ATLAS detector [ATL96a]: The accordion-shaped geometry is segmented into strip cells in the innermost layer and square towers of increasing coarseness in the second and third layers. Several segments are summed up into trigger towers as shown (cp. Sec. 3.2.7).

The total thickness of the tile calorimeter corresponds to 11 nuclear interaction lengths (λ) at $\eta = 0$, ensuring good containment of hadronic showers and minimizing punch-through into the muon system. Also, this thickness allows for a good energy resolution of highly energetic jets and, in combination with the hermetic η-coverage, for a sufficiently accurate measurement of the missing transverse energy ($E_{\mathrm{T}}^{\mathrm{miss}}$, see Sec. 3.3.6) in the event. The energy resolution (cp. Eq. (3.8)) amounts to

$$\frac{\sigma_E}{E} \approx \frac{50\,\%}{\sqrt{E/\mathrm{GeV}}} + 3\,\%\,. \tag{3.9}$$

Each HEC consists of two independent wheels that cover the region $1.5 < |\eta| < 3.2$. For the four samplings, respectively, LAr technology is chosen for improved radiation-hardness. Each wheel has an outer radius of 2.03 m and contains parallel plates of 25 mm (upstream) and 50 mm (downstream) thick copper as radiators. With a segmentation into 32 modules per wheel, a granularity of $\Delta\eta \times \Delta\phi = 0.1 \times 0.1$ in $1.5 < |\eta| < 2.5$ and of $\Delta\eta \times \Delta\phi = 0.2 \times 0.2$ in $2.5 < |\eta| < 3.2$ is achieved. The resolution is again given by Eq. (3.9).

The FCAL covers the range $3.1 < |\eta| < 4.9$ at a separation of 4.7 m from the interaction point. It also utilizes LAr technology and is built of high-density material in order to withstand a high dose of radiation and ensuring a thickness of $9.5\,\lambda$. Its three samplings consist of rod- and tube-shaped electrodes in a copper (first sampling, used as electromagnetic calorimetry) or tungsten matrix (outer samplings, used as hadronic calorimetry). In total, the FCAL provides a granularity of $\Delta\eta \times \Delta\phi \approx 0.2 \times 0.2$ and 3,584 read-out channels. Its energy resolution is parametrized as

$$\frac{\sigma_E}{E} \approx \frac{100\,\%}{\sqrt{E/\mathrm{GeV}}} + 10\,\%\,. \tag{3.10}$$

3.2.6. Muon System

The Muon Spectrometer (MS) [ATL99; ATL08; ATL97g; CS12; Mik12; Bin11] is the largest detector component of ATLAS, covering an area of 12 100 m^2 in total. The layout of the muon chambers is pictured in Fig. 3.9: Its barrel part consists of three concentrical layers of chambers, at radii of 5 m, 7.5 m and 10 m, that cover the range $|\eta| < 1$. The end-caps are composed of four vertical disks around the beampipe at distances of 7 m, 10 m, 14 m and 21 m to 23 m from the interaction point and extend over the region $1 < |\eta| < 2.7$. The barrel and end-cap chambers are arranged in a 16-fold segmentation in the azimuthal direction, mirroring the eightfold symmetry of the toroidal magnet system. The MS measures the deflection of muon tracks in the magnetic field of the large air-core toroid magnets: Within $|\eta| \leq 1$, the field is provided by the BT whereas in the region $1.4 \leq |\eta| \leq 2.7$, the ECT supplies the field. In the transition region $1.0 \leq |\eta| \leq 1.4$, the combined field of BT and ECT bends the tracks. The design ensures that each track traverses three stations in the MS. The z-coordinate is measured by the barrel components, the radial coordinate is determined in the transition and end-cap regions. For a detector part of the dimension of the MS, it is impossible to provide a sufficiently precise and lasting alignment of 30 µm by mechanical means. The strategy in ATLAS is thus to constantly monitor the positions of the single components with respect to one another. The barrel chambers are arranged into projective towers that are optically connected by alignment rays monitoring the relative chamber positions. In contrast, the alignment in the end-caps is ensured by monitoring complete chamber planes.

Of the four different chamber technologies employed in the MS, two are designed to provide high-precision tracking whereas the other two serve as triggering chambers: The Monitored Drift Tubes (MDTs) and the Cathode Strip Chambers (CSCs) are used as tracking chambers, the Resistive Plate Chambers (RPCs) and the Thin Gap Chambers (TGCs) are the faster triggering chambers. Here, the chambers providing trigger signals up to $|\eta| < 2.4$ serve three purposes:

- bunch crossing identification, requiring an excellent time resolution falling below the 25 ns bunch spacing;
- well-defined p_T cut-offs for the trigger, requiring a granularity of about 1 cm;

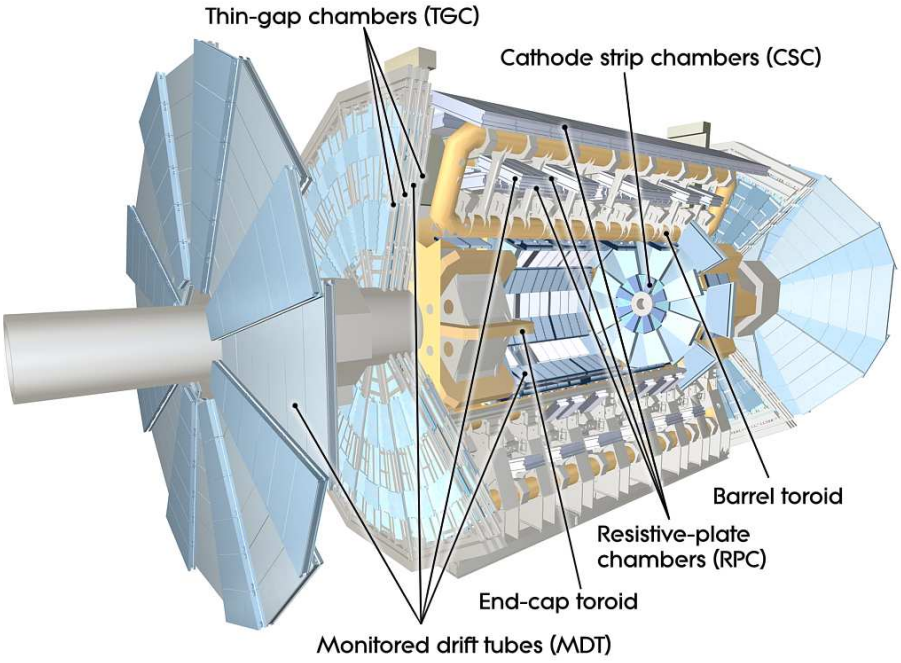

Figure 3.9. Layout of the instrumentation of the muon system of the ATLAS detector, equipped with four different chamber technologies [ATL08].

- complementing the position measurement of the precision chambers in the orthogonal direction, requiring a spatial resolution of 5–10 mm.

The MDTs are the main chamber type covering $|\eta| < 2.7$, installed in three stations in the barrel part and also in three layers in the end-caps. They consist of aluminium drift tubes with a diameter of 30 mm and a central W-Re wire. The tubes are oriented parallel to the beam axis and feature lengths between 0.7 m and 6 m. The gas mixture employed as detecting medium in the tubes is composed of 93 % Ar and 7 % CO_2. The maximum drift time is about 700 ns and the single-wire resolution amounts to 80 µm. A spatial resolution of 40 µm can be gained from a combined measurement of several stations.

The CSCs are positioned at large pseudorapidities, $2 < |\eta| < 2.7$, and close to the interaction point since they allow for a higher granularity and are more radiation resistant. This chamber type is a multi-wire proportional chamber with cathode strip readout. The gas employed is a mixture of 30 % Ar, 50 % CO_2 and 20 % CF_4. Electron drift times of 30 ns, a time resolution of 7 ns and a spatial resolution of 60 µm are achieved.

The RPC units cover the range $|\eta| < 1.05$ and consist of two parallel resistive Bakelite plates, separated by insulating spacers. The gap in between is filled with a gas mixture based upon $C_2H_2F_4$ with a small SF_6 component. By applying an electric field of 4.5 kV/mm, primary ionization electrons are amplified to avalanche signals, read out via capacitive coupling by metal strips on the sides of the module.

The realized space-time resolution amounts to 1 cm×4 ns, and about 99 % of bunch-crossings are assigned correctly.

The TGCs, situated between $1.05 < |\eta| < 2.7$ are designed like multi-wire proportional chambers with 50 µm thick anode wires parallel to the MDTs. The readout strips are arranged orthogonal to the wires, allowing for the measurement of the second coordinate. The gas filling is a mixture of 55 % CO_2 and 45 % n-C_5H_{12}. The TGCs operate at an efficiency that correspond to 99 % correct assignments of bunch-crossings and achieve a space-time resolution similar to the RPCs.

3.2.7. Trigger and Data Acquisition System

In order to filter out the interesting events of the multitude of collision data arriving at a rate of 40 MHz of bunch-crossings from the LHC, the ATLAS detector possesses an elaborate system for fast pattern recognition: It consists of the three trigger levels called LVL1 (level one), LVL2 (level two) and EF (event filter), cp. Fig. 3.10, that provide an increasingly refined filtering. These three trigger levels successively select or reject the event information online, thus reducing the rate of events by a factor of 10^7 to the maximum output rate of about 200 Hz to 500 Hz that can be permanently stored offline. Additionally, there is a procedure of vetoing a fraction of certain types of events by applying so-called "prescale factors", meaning that only a corresponding fraction of those events passing the LVL1, LVL2 or EF is accepted (in the extreme case, no events are accepted). The prescale factors can be changed run-wise to largely reduce the data amount and thus accommodate disk space limitations.

The LVL1 trigger [ATL99; ATL98] is a fast hardware trigger whose decision is based upon reduced-granularity information from the calorimeters (EMCAL, HCAL, HEC, FCAL) and the muon system (RPCs in the barrel, TGCs in the end-caps). A coarser division is achieved by combining several components of the respective sub-detector into trigger towers (cp. Fig. 3.8). The trigger objects are high-p_T muons for the muon system and for the calorimeters high-p_T electrons, photons, τ-leptons (for which isolation requirements can be applied) and jets. There are also triggers for energy sums in the event like the scalar sum of jet transverse energies, the total scalar transverse energy or the missing transverse energy (cp. Sec. 3.3.6), computed as a sum over trigger towers. Per trigger object type, typically 6–8 different p_T or energy thresholds exist. The LVL1 decision itself is then a requirement for a certain combination of trigger objects to fulfil a coincidence or a veto. Due to the processing capabilities of the ATLAS front-end systems, the accept rate of the LVL1 trigger is limited to 75 kHz. The LVL1 trigger also serves to identify the bunch-crossing of interest.

To keep the LVL1 latency as short as possible (2 µs), the detector information is conserved in pipeline memories. For accepted events, this data is then read out into readout drivers (RODs) and transferred to readout buffers (ROBs) that await the LVL2 decision. If the LVL2 accepts the event, the information from the different ROBs is bundled event-wise in the process of event building and passed on to the EF processors. If the LVL2 declines the event, the information is discarded.

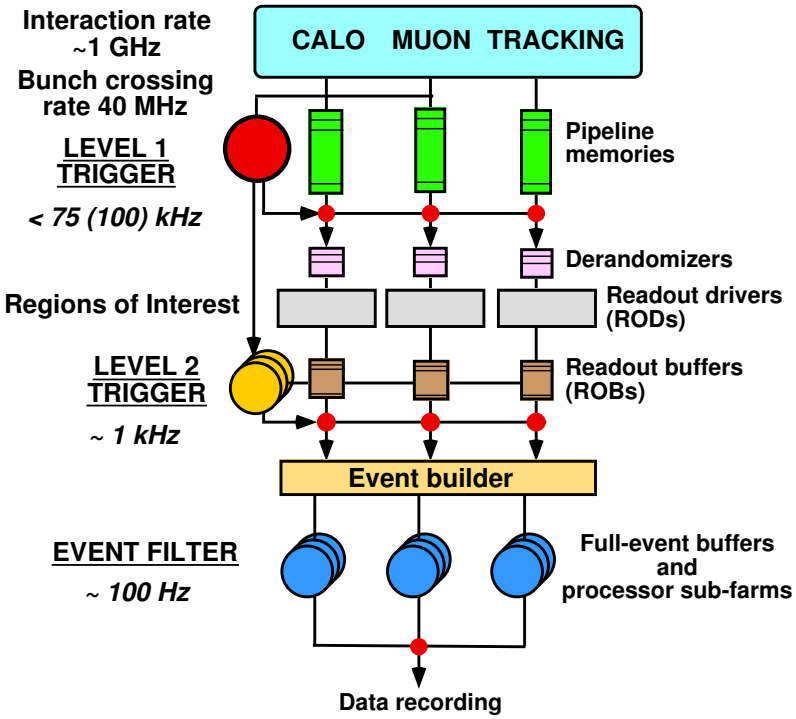

Figure 3.10. The three trigger levels employed in the data-taking at ATLAS [ATL98]: level 1 trigger, level 2 trigger and event filter. The total event rate is reduced by about seven orders of magnitude by employing an increasingly refined filtering.

The LVL2 trigger [ATL99; ATL03] is a software trigger making use of the information provided by the LVL1 on the so-called "regions of interest" (RoIs): These are limited detector regions centred around the LVL1 trigger objects.[9] By only accessing the small fraction of the event data contained in the RoIs (η - ϕ position and p_{T} of the candidate objects, energy sums), in which the LVL2 can query the full detector granularity, a latency of 1 ms to 10 ms is achieved. The number of events is reduced further with respect to the LVL1 rate by applying more precise p_{T} and isolation requirements by virtue of the increased granularity and the possibility to combine with information from the ID (matching of tracks in the MS or clusters in the calorimeters to ID tracks). The output rate of the LVL2 step amounts to about 1 kHz.

The last trigger step, the EF [ATL99; ATL03], is also a software based trigger that finally employs refined offline reconstruction algorithms, calibration and alignment information and the magnetic field map. The selected events are sorted into trigger-streams, depending on which objects were reconstructed (for details on the object reconstruction, see Sec. 3.3); the available streams are *Egamma*, *Muons*, *BPhysics*,

[9] There are primary and secondary RoIs: Primary RoIs originate from objects contributing to the selection of the event, secondary RoIs from objects that did not (mostly low-p_{T} objects).

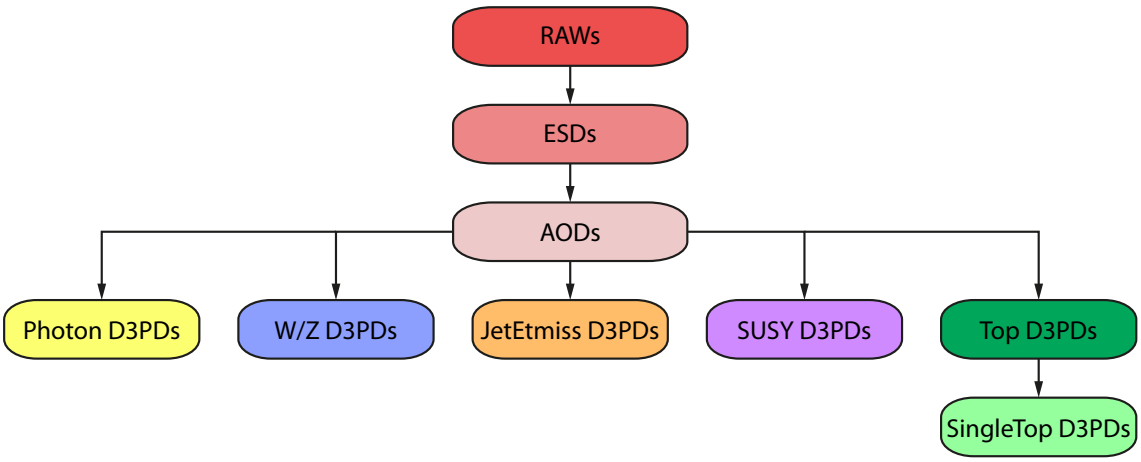

Figure 3.11. Refined data formats of ATLAS, derived from the raw detector information: The RAW data is formatted according to its physical content to form ESDs (event summary data) and AODs (analysis object data) to meet analyzer's needs. To further refine and filter for purposes of specific types of analyses, D3PD (dedicated physics data) formats are created from AODs. For analyses involving top quark signatures, the Top D3PDs are made. The SingleTop D3PDs are a derived format, including already tightened event selection cuts (cp. Sec. 4.4).

MinBias and *JetTauEtmiss*. In this study, only the *Egamma* and *Muons* streams are used for data analysis. Events containing an electron object are saved to the *Egamma* stream, events containing a reconstructed muon enter the *Muons* stream. If an electron as well as a muon are found, the event enters both streams, i.e. the streams are not mutually exclusive. The data then is sent to mass storage at a rate of about 100 Hz and serve as input for physics analyses.

In order to be suited for offline physics analyses the raw digitized information from the ATLAS data-taking is refined in several steps, schematically shown in Fig. 3.11. Each step implies a reduction of the event size and a more specific selection of physics objects. The samples used in this analysis are the SingleTop D3PDs, a data format derived from the general format produced for top quark physics analyses (Top D3PDs). Details on the samples can be found in [Sta13b]. The huge amount of data is distributed to analysers via a dedicated worldwide LHC Computing Grid [Bir+05].

3.3. Object Reconstruction

Whereas the ATLAS detector hardware recording the information from pp collision events has been depicted in detail in the last section, this section is describing the reconstruction of physics objects, achieved by custom-made software. The algorithms utilizing information from the ID that allow for high-precision tracking and vertexing are the topic of Sec. 3.3.1, whilst the derived elaborate methods of identifying B-

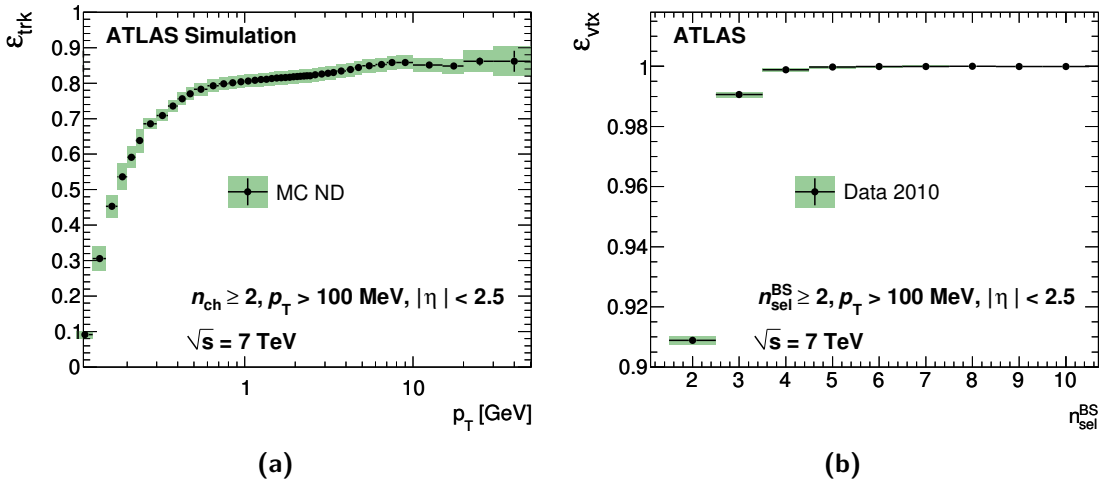

Figure 3.12. The inner detector tracking efficiency (a) as a function of p_T of the particle and vertexing efficiency (b) depending on the number of reconstructed tracks [ATL11a].

meson decays are discussed in Sec. 3.3.2. In Sec. 3.3.3, the criteria for the formulation of an electron hypothesis are given, in Sec. 3.3.4 the jet-finding algorithms are outlined and Sec. 3.3.5 is devoted to the muon reconstruction. In Sec. 3.3.6, the notion of the transverse missing energy is defined.

3.3.1. Tracking and Vertexing

The ID components are employed to provide a track and vertex reconstruction [Hir10; Was12] for charged particles.

The track reconstruction proceeds in the following manner: In a first step, neighbouring silicon hits are clustered to form space-point measurements. A minimum of three space-points in the silicon tracking detectors (Pixel, SCT) then form a seed for the track reconstruction algorithm that determines a preliminary track direction. The track candidate is extrapolated successively to the outer layers and finally to the TRT, refitting the trajectory with a Kalman filter algorithm along the way. Ambiguities between track candidates are resolved by applying a pattern recognition algorithm that assigns scores according to the fit quality of the hits. For instance, tracks that carry a very low transverse momentum ($p_T < 400\,\text{MeV}$) are rejected in this procedure. In Fig. 3.12a, the tracking efficiency of the ID as a function of the p_T of the charged particle is shown.

Once tracks are established, a vertex reconstruction sets in which serves to identify the interaction point (IP) as well as secondary decay vertices of particles. The IP, also called Primary Vertex, is defined as the vertex with the highest sum of track transverse momenta ($\sum_{\text{tracks}} p_T^2$). To find the primary vertex, vertex seeds are formed from tracks compatible with originating from the interaction region (beam spot

constraint). An adaptive vertex fit then uses these seeds to conclude on the vertex position and its error matrix. The fit is χ^2-based and down-weights contributions of outliers. Tracks that are found to be incompatible with the primary vertex hypothesis enter a new vertex fitting iteration; thus, secondary vertices are built. The efficiency of the vertex reconstruction as a function of the number of reconstructed tracks is displayed in Fig. 3.12b.

3.3.2. B-Tagging

A method used to identify tracks originating from b-hadron decays is termed b-tagging. There is a multitude of different b-tagging algorithms used at ATLAS [ATL11b; Alv+10] exploiting the large flight path length resulting from the long b-hadron lifetime. This section will be restricted to presenting the method employed in this study, the *MV1* tagger [Bou+12; Ach+12]. This tagger is realized as a neural network-based algorithm utilizing the output weights of three other taggers as its input: It combines information of the *IP3D*, the *SV1* and the *JetFitterCombNN* tagging algorithms that are explained below. Additionally, the p_{T} and η values of the jet are used.

Since b-tagging operates on ID tracks, several quality criteria must be met and each track must be associated with a jet. In the context of b-tagging, a track feature called impact parameter is of importance which measures the distance of the point of closest approach of the track to the IP. There are transverse and longitudinal impact parameters denoted by d_0 and $|z_0| \sin\theta$ (where z_0 is a helix parameter of the track) that refer to the projection onto the $R\phi$ plane and to the z coordinate of the 3D impact parameter distance, respectively. The impact parameter is a signed quantity, bearing positive sign if the track extrapolation crosses the jet direction in front of the primary vertex and negative if it crosses it behind the IP. For B-meson and other heavy particle decays in-flight, positive impact parameters are expected. Furthermore, to give more weight to precisely measured tracks, the signed impact parameter significances d_0/σ_{d_0} and z_0/σ_{z_0} are defined. Now, in order not to select fake tracks or tracks originating from long-lived particles or material interactions, the following track quality requirements must be fulfilled:

- At least seven precision hits in the Pixel and SCT,
- Amongst these, at least two hits in the Pixel, one of which must be a b-layer hit,
- $p_{\mathrm{T}} > 1\,\mathrm{GeV}$,
- $|d_0| < 1\,\mathrm{mm}$,
- $|z_0| \sin\theta < 1.5\,\mathrm{mm}$.

Additionally, only tracks matched with a jet within $\Delta R(p_{\mathrm{T}}^{\mathrm{jet}})$ are considered; the values range from $\Delta R = 0.45$ for $p_{\mathrm{T}} = 20\,\mathrm{GeV}$ to $\Delta R = 0.25$ for $p_{\mathrm{T}} = 150\,\mathrm{GeV}$.

Whilst usually several tracks are associated with the same jet, the assignment of a track to a jet must be unique. The invariant masses of track pairs from vertices are used to reject tracks from K_S decays, photon conversions and the like, and a comparison of the radius of the vertex with a material map of the Pixel further reduces tracks from secondary interactions. For all taggers, the distribution of a measured discriminating variable S_i of the particular jet is compared to reference distributions $b(S_i)$ of b-jets and $u(S_i)$ light jets, extracted from MC. The resulting discriminant is called b-tag weight of the jet and is defined as

$$\ln\left(\sum_{\text{tracks}} \frac{b(S_i)}{u(S_i)}\right) . \tag{3.11}$$

The *IP3D* ("impact parameter 3D") tagging algorithm employs a ratio likelihood technique for comparing smoothed, normalized template distributions from MC to the corresponding input distributions: Two-dimensional histograms of d_0/σ_{d_0} versus z_0/σ_{z_0} of all tracks in a jet are probed for both, the b-jet and the light-jet hypothesis. Thus, the correlations between the two significances are exploited.

The *SV1* ("secondary vertex 1") tagger builds an inclusive vertex from all two-track vertices that cannot be assigned to long-lived particle decays or material interactions. This inclusive vertex is formed in an iterative procedure, removing the worst track until a good χ^2 of the fit is achieved. To enable the method to identify long-lived particle decays and material interactions, the efficiency of the track selection is enhanced by partially loosening the track quality cuts mentioned above: $p_T > 400\,\text{MeV}$, $|d_0| < 3.5\,\text{mm}$, only one Pixel hit (regardless of whether it is found in the b-layer), no more than one shared hit and the z_0 requirement is dropped altogether. Subsequently, three variables of the purified vertex are combined in a likelihood ratio technique: the invariant mass of all tracks assigned to the vertex, the ratio of the sum of track energies at the vertex to the energy sum of all tracks in the jet and the number of two-track vertices. The first two variables enter via a 2D, the third via a 1D distribution. The ΔR between the jet axis and the line connecting the primary and the secondary vertex is also utilized.

The *JetFitterCombNN* tagger, finally, is itself a combination of the *IP3D* and the *JetFitter* tagging weights. The *JetFitter* part attempts to find a common line along which the IP, the b-hadron vertex and the subsequent c-hadron vertex lie and their approximate positions on this line. This is accomplished by employing a neural network-based Kalman filter. The advantage of this approach is the disentanglement of the b- and c-vertices even if they only possess one track each. The method's ability to distinguish light jets, b-jets and c-jets is drawn from forming a likelihood of distributions of masses, momenta, flight-length significances and track multiplicities of the reconstructed vertices.

3.3.3. Electron Reconstruction

The electron reconstruction [KI12; ATL12f; Lam+08] has to be designed such as to separate isolated electrons from

- Genuine hadrons,
- Background conversion-electrons,
- Non-isolated electrons originating from the decays of heavy flavour particles.

To this end, a procedure is employed for central electrons ($|\eta| < 2.47$) where clusters in the EMCAL serve as seeds for the reconstruction and are associated with tracks in the ID. These seed clusters are built in the following way: The EMCAL is divided into a grid in the η-ϕ plane with cell units of $\Delta\eta \times \Delta\phi = 0.025 \times 0.025$. Each cell consists of a longitudinal tower throughout all layers of the EMCAL; the E_{T} of the tower amounts to the sum of the transverse energies of all tower cells. Now, the seed clusters are built by a "sliding-window algorithm": A window of fixed size 3×5 cell units in η - ϕ space is slided to each node of the tower grid, searching for local E_{T} maxima. Here, the E_{T} of the window is the sum of transverse energies of the towers it contains. If the window's E_{T} exceeds 2.5 GeV, a seed cluster is formed. A window with smaller size then serves to compute the cluster position. If overlapping clusters are found, the one with larger E_{T} is kept and the duplicate discarded. The seed cluster positions allow for the filling of the final cluster which consists of all cells inside a rectangle around the seed position. This cluster is then matched to an ID track by extrapolating the track from its last measurement point in the ID to the middle layer of the EMCAL. For a successful match, a distance $\Delta\eta < 0.05$ is required between the track impact point in the calorimeter and the cluster position. To correct for bremsstrahlung losses, an asymmetric $\Delta\phi$ condition is applied (0.1 on the side that the track is bent to by the solenoid, 0.05 on the other). If at least one track is matched to the seed cluster, an electron has been reconstructed. If several tracks point to the cluster, a track with silicon hits is preferred and the one with the closest match in ΔR to the cluster is selected. Then, the cluster is rebuilt using 3×7 (5×5) longitudinal towers of cells in the barrel (endcap) region. The cluster energy is computed by summing up the following contributions:

- Estimated energy deposition in upstream material from the EMCAL,
- Measured cluster energy,
- Estimated lateral leakage outside the cluster (within the EMCAL),
- Estimated longitudinal leakage into downstream material (mainly HCAL).

The electron four-momentum is determined from the final cluster information and the best track matched to the original seed cluster. The electron energy is taken to be the cluster energy whereas the η and ϕ coordinates are set to the ID track parameters.

In the forward region ($2.5 < |\eta| < 4.9$), electrons can also be reconstructed although there is no tracking available: Here, the algorithms completely rely on calorimeter information. Since only central electrons are used in the analysis at hand, these methods will not be discussed here.

Once an electron candidate is found by the reconstruction, additional refined identification criteria are applied. There are three sets of cuts corresponding to an increased background rejection power: *loose*, *medium* and *tight*. Whereas the *loose* criterion is based upon shower shape variables in the EMCAL middle layers and variables associated with leakage into the HCAL, the *medium* selection applies additional requirements on the track quality, on the track-cluster matching and on variables involving the EMCAL strip layer. The *tight* selection finally refines this further by adding cuts on E/p, on the particle identification provided by the TRT, on b-layer hits in order to discriminate against conversion photons and even on variables carrying information on reconstructed conversion vertices. The exact definitions of cut variables, optimized in 10 bins of cluster η and 11 bins of cluster E_{T}, are listed in [ATL12f]. In the context of this study, the signal electron is always required to satisfy the *tight* criterion (cp. Sec. 4.4).

3.3.4. Jet Finding and Calibration

A multitude of methods for jet-finding are available to ATLAS analyses. Here, only the algorithm used to build the jets selected in this study will be outlined, the anti-k_{t} jet clustering algorithm [CSS08]. The calibration of the jet energy by Monte Carlo (MC) simulations [Ado+12] is also depicted.

Generally, jet clustering algorithms define distances between different entities i and j (associated with energy depositions in the calorimeters in case of collision data and with generated particles in case of MC simulations) and between an entity i and the beam B: d_{ij} and $d_{i\mathrm{B}}$. Clustering proceeds by determining the smallest of the two distances: If it is d_{ij}, then the entities i and j are combined. However, if $d_{i\mathrm{B}}$ is the smallest, the entity i is regarded as a jet and removed from the list of entities. The distances are recalculated and thus an iterative procedure is executed until no entities are left. In the case of the anti-k_{t} algorithm, jet clusters are formed according to the distance measures

$$d_{ij} = \min\left(k_{\mathrm{t}i}^{-2}, k_{\mathrm{t}j}^{-2}\right) \frac{\Delta_{ij}^2}{R^2}\,, \tag{3.12a}$$

$$d_{i\mathrm{B}} = k_{\mathrm{t}i}^{-2}\,, \tag{3.12b}$$

where $\Delta_{ij}^2 = (y_i - y_j)^2 + (\phi_i - \phi_j)^2$ corresponds to an angular (geometrical) distance and $k_{\mathrm{t}i}$, y_i and ϕ_i denote the transverse momentum, the rapidity and the azimuthal angle of the particle i, respectively. R is the geometrical reference radius used, selected to be 0.4 in this study. From (3.12a), it is obvious that in case a soft entity i is compared to a hard entity j, d_{ij} is completely determined by the hard entity's momentum. If, in contrast, the encounter of two soft objects i and j with the same

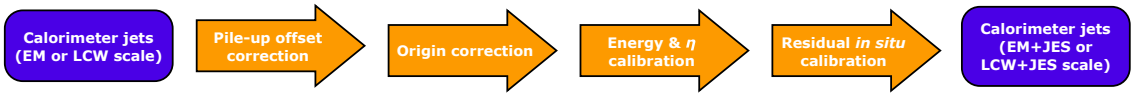

Figure 3.13. Jet calibration scheme encompassing energy scale as well as directional corrections [Ado+12].

geometrical distance Δ_{ij}^2 as in the previous case is considered, a much larger d_{ij} value results. Therefore, soft particles tend to cluster around hard ones before clustering among themselves. This feature of the anti-k_t scheme produces a jet boundary that is resilient with respect to soft radiation but flexible with respect to hard radiation, making it quite stable against underlying event fluctuations.

The subsequent jet calibration in ATLAS consists of several steps, as pictured in Fig. 3.13. Directly after the jet finding, the jet four momentum is taken to be the four momentum sum of the jet constituents. The jet energy is the cluster energy measured at the electromagnetic (EM) energy scale.[10] This cluster energy is then in turn corrected for several effects: firstly, for the expected energy offset due to pile-up interactions. This calibration is derived from MC simulations and depends on μ (cp. Sec. 3.2.1) and the number of primary vertices N_{PV} in the event. Secondly, an origin correction is applied to ensure that the calorimeter jet points to the reconstructed primary vertex instead of the centre of the ATLAS detector. This is a purely geometrical correction and does not affect the jet energy. Thirdly, the jet energy and its η are calibrated to the particle jet scale, relating the reconstructed quantities to the true kinematics of the jet formed from stable particles entering the detector. The latter is the actual jet energy scale (JES) correction and is also derived from MC. Jets thus calibrated are referred to as jets at EM+JES energy scale. An additional calibration step applied exclusively to data consists of a residual *in situ* correction derived from data and MC by techniques exploiting the transverse momentum balance between a jet and a reference object (for details, see [Ado+12]).

3.3.5. Muon Reconstruction

The muon reconstruction in ATLAS [Van+07] [11] is done making use of four different strategies: Depending on what kind of information of certain sub-detectors is utilized, a muon candidate can be identified by

- Tracing back MS tracks to the interaction point (*standalone* algorithms),
- Combining ID tracks with full tracks in the MS (*combined* algorithms),

[10] The "local cluster weighting" calibration scheme (LCW) can then be employed, but it is not used for the jets in this analysis and will therefore not be described here.

[11] E. Moyse. *ATLAS TWiki: Muon Performance*. Sept. 2012. URL: `https://twiki.cern.ch/twiki/bin/viewauth/AtlasProtected/MuonPerformance`; E. Etzion. *ATLAS TWiki: Muon Reco Pedia*. Feb. 2010. URL: `https://twiki.cern.ch/twiki/bin/viewauth/AtlasProtected/MuonRecoPedia`; J. Snuverink. *ATLAS TWiki: Moore / Muid General Description*. May 2009. URL: `https://twiki.cern.ch/twiki/bin/viewauth/Atlas/MooreMuidInfo`.

- Combining ID tracks with track segments from the MS stations (*segment tagging* algorithms),

- Extrapolating ID tracks to the calorimeters and combining with energy depositions (*calorimeter tagging* algorithms).

Every algorithm class is realized in several alternative approaches. In the following, the discussion will be restricted to the implementation chosen in this study: the MuIDCombined method of the *combined* algorithm class.

Before a combined reconstruction of muons can be done, a standalone MS track must be built that can then be matched to an ID track. This standalone MS reconstruction proceeds in two steps: pattern recognition and track-fitting. These steps are implemented as the MOORE algorithm that identifies active MS regions along linear paths in the R-ϕ and R-z planes with the use of trigger chamber hits. In these regions, MDT segments are formed locally by precision MDT hits that are then converted into drift circles. For every pair of drift circles, the four possible tangent lines connecting the two circles are used as linear seeds to which more hits are added. The combination of hits that result in the lowest residuals are saved as track segments. The track segments of the outer and middle MS stations are traced back into the inner layers and finally, a global MS track fit is performed on the collection of hits. The MOORE procedure is then complemented by the MuIDStandalone algorithm that provides back-propagation of the MOORE track through all of the detector material up to the interaction point. This gives the five vertex parameters of the MOORE/MuIDCombined track: radial impact parameter, impact parameter along z, ϕ, $\cot\theta$ and signed $1/p$.

Now, the combination with the ID track can be done: The MuIDCombined algorithm first attempts a track-matching of the ID and MS tracks by means of a χ^2 minimization with five degrees of freedom according to

$$\chi^2_{\text{match}} = (P - P_{\text{ID}})^{\text{T}} \times C_{\text{ID}}^{-1} \times (P - P_{\text{ID}}) + (P - P_{\text{MS}})^{\text{T}} \times C_{\text{MS}}^{-1} \times (P - P_{\text{MS}}) \quad (3.13)$$

where $P_{\text{ID}}, P_{\text{MS}}$ are the vectors containing the five track parameters of the ID track and the MS track, and $C_{\text{ID}}, C_{\text{MS}}$ are their corresponding covariances from the original ID and MS fits. P is the vector of parameters of the sought matched track. For all matches yielding a chi-square probability $\mathcal{P}(\chi^2_{\text{match}}) > 0.001$, a combined fit is executed: This combined fit amounts to a global refit of all hits associated with the ID and MS tracks, including all measurements and scattered hits from the ID, the calorimeters and the MS. Here, the material density profile of the calorimeter is taken into account by approximating it with two scattering planes. If the combined fit satisfies a certain quality threshold[12], the reconstructed object is identified as a combined muon of tight quality. The latter are used exclusively in this analysis.

[12]The combined fit is compatible in position and direction if the energy/momentum balances $(E_{\text{ID}} - E_{\text{Calo+MS}}) < 6\,\sigma_{E_{\text{Calo}}}$ and $(p_{\text{T,combined}} - p_{\text{T,ID}}) < 6\,\sigma_{p_{\text{T,ID}}}$ are met.

3.3.6. Missing Transverse Energy

In a proton-proton collision event with zero initial momentum in the plane transverse to the beam, an imbalance of the p_{T} sum of all detected final state particles and calorimeter entries signals the presence of non-interacting particles. In the context of this analysis, the undetectable objects are interpreted as neutrinos, according to the particle content of the standard model framework.

The transverse vectorial momentum imbalance is termed "missing transverse energy" and is defined as [ATL12p; ATL12q]

$$E_{\mathrm{T}}^{\mathrm{miss}} = \sqrt{(E_x^{\mathrm{miss}})^2 + (E_y^{\mathrm{miss}})^2}\,, \tag{3.14}$$

with its azimuthal coordinate given by

$$\phi^{\mathrm{miss}} = \arctan(E_y^{\mathrm{miss}}/E_x^{\mathrm{miss}})\,. \tag{3.15}$$

In this study, the x and y components amount to

$$\begin{aligned} E_{x,y}^{\mathrm{miss}} = {} & E_{x,y}^{\mathrm{miss,\ Elec}} + E_{x,y}^{\mathrm{miss,\ Jet}} + E_{x,y}^{\mathrm{miss,\ SoftJet}} \\ & + E_{x,y}^{\mathrm{miss,\ Muon}} + (E_{x,y}^{\mathrm{miss,\ CaloMuon}}) + E_{x,y}^{\mathrm{miss,\ CellOut}}\,. \end{aligned} \tag{3.16}$$

The different terms denote the contributions of electrons, high-p_{T} jets, soft jets, muons and cells in the calorimeters that are not associated with any physics object in the event. Generally, contributions from the calorimeters on one hand (Elec, Jet, SoftJet, CaloMuon, CellOut) and from the muon system on the other hand (Muon) are treated separately. The CaloMuon term, though, is written in brackets since it is not added for all muons (see below).

The calorimeter cells are assigned to reconstructed and identified particles in the fixed order electrons, photons, hadronically decaying τ-leptons, jets and muons, and then calibrated accordingly, as described in the previous sections. Energy depositions of photons and tauons, however, are neglected in this analysis. Cells not associated with any of these particle types enter the $E_{\mathrm{T}}^{\mathrm{miss}}$ computation as the CellOut term. Thus, the x and y components of each calorimeter term are calculated from the single cells as the negative sum of calibrated cell energies E_i inside each object,

$$E_x^{\mathrm{miss,\ term}} = -\sum_{i=1}^{N_{\mathrm{cells}}^{\mathrm{term}}} E_i \sin\theta_i \cos\phi_i\,, \tag{3.17a}$$

$$E_y^{\mathrm{miss,\ term}} = -\sum_{i=1}^{N_{\mathrm{cells}}^{\mathrm{term}}} E_i \sin\theta_i \sin\phi_i\,, \tag{3.17b}$$

where the summation includes all cells assigned to objects up to $|\eta| < 4.5$. In order to suppress noise, the cells used have to belong to topological calorimeter clusters that are seeded by cells exhibiting a strong signal of $|E_i| > 4\sigma_{\mathrm{noise}}$; here, σ_{noise} denotes the Gaussian width of the cell energy distribution measured in randomly

triggered events far from collision bunches. The electron term is composed of all *tight* electrons with $p_{\mathrm{T}} > 10\,\mathrm{GeV}$. The high-$p_{\mathrm{T}}$ jet term refers to jets with EM+JES calibrated $p_{\mathrm{T}} > 20\,\mathrm{GeV}$ whereas the soft jet term sums up all cell contributions from jets calibrated at the EM scale with $7\,\mathrm{GeV} < p_{\mathrm{T}} < 20\,\mathrm{GeV}$. The CaloMuon term denotes the contribution of the energy loss of muons in the calorimeters. The CellOut term, finally, is determined using only the p_{T} of tracks found by a track-cluster matching to cells not associated with physics objects, thus exploiting the better p_{T} resolution of low energetic tracks as opposed to the calorimeter cell resolution. If several topoclusters are matched to a track, the track is assigned to the one with the highest energy. Even tracks of objects not reaching the calorimeter or not seeding a topocluster are considered and their track p_{T} added. Topoclusters not matching any track contribute as well according to their cluster energy. The tracks used for the matching need to satisfy $p_{\mathrm{T}} > 400\,\mathrm{MeV}$ and some basic track quality criteria.

The muon term is computed as the p_{T} sum of all muon tracks up to $|\eta| < 2.7$:

$$E_{x,y}^{\text{miss, Muon}} = -\sum_{\text{muons}} p_{x,y}^{\mu}\,. \tag{3.18}$$

In this study, the muons are required to be reconstructed by the MuID algorithm. In the range $|\eta| < 2.5$, only MuIDCombined muons are taken into account to reduce the number of fake muons due to calorimeter punch-through. Furthermore, isolated and non-isolated muons are treated differently: Non-isolated muons are defined as being within $\Delta R < 0.3$ of a reconstructed jet and thus, their energy depositions in the calorimeter are already partially included in the jet terms. Therefore, the CaloMuon term is added for non-isolated muons whereas the Muon term itself is computed in an MS *standalone* way to only retrieve the muon momentum after energy loss in the calorimeter. In contrast, the p_{T} of the isolated muons is computed from the combined ID and MS information and accounts for the energy loss in the calorimeters. In order not to double count these energy depositions, the CaloMuon term is omitted in this case. Muons in the range $2.5 < |\eta| < 2.7$ do not carry tracking information and here, the MS p_{T} is employed for isolated as well as non-isolated muons. At $|\eta| \sim 1.2$, muons from *segment tagging* (cp. Sec. 3.3.5) are also considered.

Legion heiße ich;
denn wir sind viele.
Markus 5:9

4. Data and Simulation Samples

Now that the manner of data acquisition has been presented, the data and MC simulation samples entering the analysis will be depicted. The first section, Sec. 4.1, specifies the subset of the data accumulated by ATLAS in the year 2011 that is used in this study. The event generation procedure for MC simulation samples in general is the topic of Sec. 4.2; here, also the generators used are outlined. In the following, Sec. 4.3 is dedicated to the description of the different background processes of single-top production and lists the MC generators and cross-sections used for the modelling of all simulation samples that are then compared to the measured data. Finally, Sec. 4.4 collects all preselection cuts that are applied in order to roughly filter out the signature of the single-top t-channel process.

4.1. Data Samples

Not all data taken by ATLAS are suitable for the analysis of the single-top t-channel process. First of all, to ensure that all detector components needed were active and fully functional, so-called "data quality flags" were assigned to the data during recording; according to those flags, events are collected into "good run lists". Dedicated good run lists for top quark physics are employed to select the subset of events considered in this study. Furthermore, as already mentioned in Sec. 2.2, only those channels are considered for analysis where the W boson from the top quark decays leptonically, allowing to reject the vast majority of events originating from QCD multi-jet production that do not possess a true lepton. This is achieved by filtering the data for the signature of a high-p_{T} lepton making use of the *Egamma* and *Muons* trigger streams (cp. Sec. 3.2.7): An event is required to be selected by a high-p_{T} electron or muon EF trigger.[1] The involved exact p_{T}-threshold depends on the run-period since some trigger items are prescaled with increasing instantaneous luminosity (cp. Sec. 3.2.7). The trigger items used in this study for run periods of a given total integrated luminosity are listed in detail in Tab. 4.1 [Ach+12] [2]. The total integrated luminosity used for this analysis thus amounts to $(4.66 \pm 0.08)\,\mathrm{fb}^{-1}$.

[1] The decay of the W boson into a τ and a neutrino is not used since the τ decays mostly into hadrons producing jets – a signature that can hardly be isolated from QCD multi-jet production. The τ can also decay leptonically into an electron or a muon, in which case the charged lepton is accompanied by two neutrinos; thus, also the leptonic mode is challenging to extract since it bears a more complicated signature.

[2] A. Lister. *ATLAS TWiki: Top Good Run Lists*. Sept. 2012. URL: `https://twiki.cern.ch/twiki/bin/viewauth/AtlasProtected/TopGRLs`.

Run Period	Luminosity [pb^{-1}]	Electron Trigger	Muon Trigger
B–D	176.249	e_20_medium	mu_18
E–H	937.710	e_20_medium	mu_18
I	333.242	e_22_medium	mu_18
J	223.490	e_22_medium	mu_18_medium
K	583.266	e_22_medium	mu_18_medium
L–M	2401.770	e_22vh_medium1	mu_18_medium

Table 4.1. Run-period dependence of the trigger requirements. Here, e_XX_YY and mu_XX_YY denote electron and muon trigger items with thresholds for the transverse momentum of XX GeV and lepton identification quality YY [Ach+12]. [3]

4.2. Monte Carlo Simulation

The production of MC simulation samples [ATL05; Dob+04; Ber+12] proceeds in several steps: To begin with, the matrix elements of the respective hard scattering process are sampled at random; this is the first MC step done by the main matrix element generator and will be described in Sec. 4.2.1. Then, a MC parton shower simulation is executed on the initial and final state partons, often by another program, the parton shower generator, yielding initial and final state radiation (ISR/FSR). This MC generator is also used to account for the hadronization processes, for beam remnant interactions and the underlying event (UE) as well as for the decays of the particles. The tasks of the parton shower generator are also outlined in Sec. 4.2.1; a brief description of the MC generators chosen for the present study concludes this section. Eventually, the final state particles are subjected to a detector simulation and a digitization step in order to become comparable to the measured objects in ATLAS data; subsequently, also a trigger simulation is run. These three steps are the topic of Sec. 4.2.2.

4.2.1. Event Generation

For the computation of the final state particle momenta from the hard scattering, perturbation theory can be employed and the respective *Matrix Elements* calculated. The subsequent *Parton Shower* formation is also still treatable via perturbative methods. For the modelling of additional long-range radiative processes like hadronization and subsequent decays, the need for phenomenological methods arises, since perturbation theory breaks down at these large distances due to the increasing coupling strength of QCD. The phenomenological part is here collected under the designations *Hadronization and Decays* as well as *Underlying Event*. The *MC Generators* used in this study offer matrix element computation and parton shower simulation or only one of the two functionalities.

[3] A. Lister. *ATLAS TWiki: Top Good Run Lists*. Sept. 2012. URL: `https://twiki.cern.ch/twiki/bin/viewauth/AtlasProtected/TopGRLs`

Matrix Elements

To sample the matrix element of a particular hard scattering process, several options are at hand. First of all, one can choose a leading order (LO) or a next-to-leading order (NLO) accuracy of the simulation. Depending on the process to be simulated, the NLO option may not currently be available by any MC generator. Once the matrix element generator is selected, a corresponding PDF set (cp. Eq. (2.31)) must be used in the simulation procedure: For a LO matrix element, a LO PDF is required whereas a NLO matrix element needs to be complemented by a NLO PDF.[4] The PDF sets are employed multiple times in the event generation process: for sampling the initial state parton momenta and initial state radiations as well as for the parton shower development and multiple parton interactions (MPIs) in the final state. Therefore, in general, two different PDF sets can be utilized for the matrix element and the parton shower part.

The matrix element generators used in this study are AcerMC [KR04], MC@NLO [FW02], Alpgen [Man+03] and Herwig [Cor+01] (cp. Tab. 4.2). For a given hadronic collision process (here proton-proton collisions at $\sqrt{s} = 7\,\text{TeV}$) and a given final state (e.g. single-top t-channel), these generators sample the types of the initial state partons as well as their longitudinal momentum fractions x_1, x_2 inside the proton, see Eq. (2.31), according to parametrizations of the corresponding PDFs which need to be provided. With this sampled value of $\hat{s}$, see Eq. (2.33), the corresponding matrix element and thus the partonic cross-section, e.g. the one from Eq. (2.34), can be computed. In order now to conclude on the kinematics of the final state partons, the partonic cross-section $\hat{\sigma}_{ij}$ is taken in its differential form and normalized to unity, yielding a probability density function for the partonic cross-section as a function of the kinematic variables. This probability density function is then inverted, resulting in a probability density function for the kinematic variables in terms of the partonic cross-section. In this manner, the four-vectors of the final state partons are calculated from the partonic cross-section. Since this technically amounts to a phase space integration of the differential partonic cross-section using Monte Carlo sampling methods, the procedure is termed MC matrix element generation.

Parton Shower

The final state partons obtained from the hard matrix element generation are coloured objects and can radiate gluons which, in turn, can radiate again, an effect termed FSR. Thus, any fixed order QCD description is not sufficient to describe the complexity of jet formation. It is the task of the parton shower algorithm to simulate the effect of all higher orders as an evolution in momentum transfer down from the scale of the hard process to the scale Λ_{QCD} where hadronization sets in. This is accomplished as follows [Buc+11a]:

[4] Actually, this is not completely true since the PDFs have several applications in the event generation procedure and it turns out that the usage of LO PDFs for the ISR and UE part is recommended at any rate, see [Sjo12].

In general, the differential cross-section of a hard process accompanied by one parton emission displays universal divergences that are associated with a parton emission in the *collinear* and in the *soft* limit, meaning that contributions from those phase space regions are enhanced where either the opening angle between the radiating parton and the emitted parton approaches zero ($\theta \to 0$, $\theta \to \pi$) or the emitted parton's energy goes to zero ($E_{\text{parton}} \to 0$).

In the *collinear* limit, the additional emission part can be factorized from the cross-section of the hard process in a very convenient way: The cross-section with one emission amounts to the hard cross-section times the sum of all separate possible parton emissions. By realizing that the partons can be treated individually, an iterative MC procedure can be devised: A collinear splitting is added to the original hard process and then the resulting final state is taken as a new hard process for which successive collinear splittings can be generated in this manner. However, such a MC method relies on a well-defined probability distribution for sampling the first emission. Therefore, in order to deal with the collinear divergence, the notion of resolvable partons is defined such that their opening angle θ must exceed some cutoff θ_0. Only for these cases, the probability distribution will be considered, since completely collinear partons do not give a physical effect anyway. Furthermore, aiming at the distributions of exclusive multi-parton events instead of the inclusive distribution from the cross-section, the distributions of individual partons are separated by introducing an ordering variable for the shower evolution. The most convenient choice turns out to be θ^2, enabling also the modelling of the soft emissions described below. Now, the total probability of having no resolvable branchings from a particular parton, the Sudakov form factor, can be defined as well as the non-branching probability for a certain range of the evolution variable θ^2 and also the corresponding θ^2-dependent probability distribution of the first branching. This first emission probability is then sampled at random within the range $[0, 1]$, allowing to solve for the value of θ^2. If $\theta^2 \geq \theta_0^2$, a resolvable emission is added, otherwise the evolution is terminated. For a resolvable branching, the value of E_{parton} is drawn from a universal flavour-dependent splitting function $P_{ji}(E_{\text{parton}})$ of a parton j emitted by a parton i.

In the *soft* emission limit, in contrast to the collinear limit, the factorization of the hard process and the additional parton emission is only valid on amplitude level. Thus, when computing the cross-section by summing amplitudes and squaring, interference terms are encountered; this seemingly spoils an independent parton evolution as in the collinear case that enabled a MC treatment. However, it turns out that two cases can be distinguished:

- If the soft emission to be modelled takes place at a relatively wide angle, the contributions arising from several rather collinear hard partons emitting such a soft wide-angle parton can be described by a simplified configuration in which a single hard parton replaces the collinear pair, bearing the same total longitudinal momentum.

- If the soft emission takes place at an angle to one hard parton that is smaller than that between the hard partons it can be emitted from, then the cross-

section factorization as in the collinear case is valid again, since the contributions are of very different size.

Thus, also the soft limit can be modelled by the MC procedure employed for the collinear case, provided that the evolution variable is chosen to be the opening angle θ. This approach to MC parton shower simulations is known as "angular-ordered parton shower". The starting scale $\theta_{\max}$ of this angular evolution is derived from considerations of colour-coherence effects: The colour flow in an event can be traced to identify pairs of partons at the incoming and outgoing ends of each colour line; in order to capture all the event's kinematic properties, it has proven essential to start the shower from each parton with a maximum allowed opening angle given by the angle to its "colour partner".

An alternative ansatz to the angular-ordered parton shower evolution is the "p_{T}-ordered" parton showering, also called "dipole approach" [GP88]. This scheme formulates the shower in terms of emissions from sets of colour dipoles. The basic observation leading to this approach is that in the large-N_{c} limit (N_{c} is the number of colours involved), the colour flow of an arbitrarily complex system of partons can be represented by single colour lines which, in the large-N_{c} and soft-gluon limit, emit independently of each other. This implies a validity of the dipole ansatz only for gluon emissions that have small p_{T} w.r.t. the axis of the colour line as compared to the scale associated with the production of that colour line. Therefore, the p_{T} is the natural choice of the ordering variable in a dipole shower evolution. To begin with, a particular colour flow of an event is sampled according to its probability. Then, the highest-p_{T} emission of any colour line in the event is generated. Since a recoil of this first emission is expected to influence the parton ensemble as a whole via gluons carrying two colour lines, the p_{T} associated with this first emission acts as an upper limit on any subsequent emission in the ensemble. In this global evolution scheme, the respective recoil effects are also propagated properly. It was shown that collinear emissions can be incorporated as well in dipole showers.

The modelling of ISR, i.e. the showering of partons entering the hard scattering, is done for both approaches in a very similar manner as described above, but it must be ensured that shower partons not participating in the hard process are collapsed back into the proton remnant. This is achieved by a backward evolution: The incoming partons of the hard process are fixed and subsequently dressed with additional emissions in the initial state down to the infrared cutoff scale. This backward evolution is based upon the DGLAP equations [GL72; Dok77; AP77] of the PDFs.

Hadronization and Decays

After the parton shower evolution, the non-perturbative regime is entered at a scale Λ_{QCD} of the order of a few hundred MeV [CGM98]. For its description, one of two

alternative models is usually employed in MC generators: either the "Lund string model" or the "cluster hadronization model".

In the *Lund string model* [And+83; And97], the linear properties of colour confinement are emphasized. The final state quarks of an event are pictured as being connected by a colour field tube whose symmetry axis is formed by a colour string. The corresponding confinement potential rises linearly with the quark separation r and amounts to $V(r) = \kappa r$ with the string constant $\kappa \approx 0.2\,\mathrm{GeV}^2$. As the quarks move apart from each other, the string extends until its stored energy exceeds the production threshold of a $\mathrm{q\bar{q}}$ pair: Then, the string breaks and the resulting $\mathrm{q\bar{q}}$ pair is connected by a newly formed string that can fragment again. In terms of an iterative MC procedure, this is realized by a product of probabilities for $n-1$ string breakups in an event with n hadrons in the final state. Here, two adjacent string breaks may only take place if the created string piece is on the mass shell for the produced hadron w.r.t. the transverse mass $m_\mathrm{T}^2 = E^2 - p_z^2$. Therefore, the total probability of an event to be formed is given by the product of $n-1$ breakup vertex probabilities times n delta functions for the transverse hadron masses. The quarks inserted in the string breaks do not include heavy c- and b-quarks but only light quarks; heavy quarks can form the ends of the original string, though. An additional gluon is represented as an energy- and momentum-carrying kink on the colour string, being attached to two string pieces since it carries a colour and an anti-colour. Also closed-gluon strings can be described in events with only gluons in the final state. In three-jet events with a $\mathrm{q\bar{q}g}$ final state, a central prediction of the string model is the enhancement of particle production in the angular regions between the gluon and one of the quarks, respectively, and a depletion of activity in the $\mathrm{q\bar{q}}$ region due to an according boost of string fragments. One major virtue is the collinear and infrared safe nature of the string model: If an almost collinear or very soft gluon is emitted, the impact on the string is very small and the event can effectively be treated like one with an unperturbed colour string without any gluon kink. One disadvantage of the string model is that it does not provide a way to account for interactions of several overlapping initial strings as expected from MPI dynamics but instead always starts from one isolated single string.

The alternative approach, the *cluster hadronization model* [FW80; FW83], is based upon the notion of the so-called preconfinement property of parton showers [AV79]: Given a particular shower cutoff scale Q_0, the colour structure of the shower allows to form colour singlet combinations of partons, termed "clusters" in the following, displaying an invariant mass distribution that is universal w.r.t. the scale Q of the original hard process, meaning that it only depends on Q_0 and Λ_QCD; this statement holds asymptotically for $Q \gg Q_0$. Since these partons connected in colour are adjacent in the event, the clusters formed from them contain objects adjacent in phase space which leads to a suppression of large masses. Thus, typical clusters have an invariant mass of only about Q_0. The cluster hadronization procedure starts with enforcing non-perturbative gluon splittings into $\mathrm{q\bar{q}}$ pairs at the cutoff scale Q_0 and then collecting colour-connected pairs into clusters. For low enough cluster energies, the clusters can be treated like excited mesons that then undergo two-body decays

into less excited states. The two-body decay channels are sampled at random among those allowed by flavour and kinematics with probabilities weighted by their available phase spaces, respectively. For low-mass clusters, the formation of single hadrons is also allowed. High-mass clusters are handled differently, forcing the products of a sequential binary fragmentation of the cluster to travel along the axis of its original constituent partons until the single cluster energies fall below some threshold; below that, the standard phase space decay is resumed. Like the string model, the cluster model has the disadvantage of not considering interactions between clusters in busy event topologies.

Eventually, the unstable hadrons resulting from the hadronization step need to be *decayed* into stable particles that can interact with the detector material in the subsequent detector simulation. To this end, the types of hadrons included in the simulation must be specified as well as the decay modes considered and how they should be simulated. These choices depend on the generator at hand and also on the hadronization scheme employed. The procedure is much more complex than just choosing from a list of PDG values: Rather, one resorts to including matrix element computations and spin correlations. Often, additional packages for more sophisticated treatment of hadron decays, tauon decays and QED radiation of decay products are interfaced to the main generator.

Underlying Event

All soft QCD processes in an event that are not directly connected to the hard parton scattering are collected under the term "underlying event". Since bunches of protons collide in the LHC, the events are expected to be quite busy beyond the actual hard proton-proton interaction. However, the contributions arising from collisions of neighbouring protons, termed "pile-up", are not considered here (see Sec. 3.2.1 instead), but rather types of processes involving only the two protons of the hardest scattering.

In general, several different contributions to this kind of additional activity in the event can be distinguished: Elastic and inelastic soft collisions can take place, where elastic ones denote all reactions in which only momentum is exchanged in contrast to inelastic ones where quantum numbers and masses can change such that new particles occur. Furthermore, if non-elementary objects such as the protons themselves undergo inelastic collisions, the corresponding processes are divided into "diffractive" and "non-diffractive" (ND) topologies: An event is classified as "single-diffractive" (SD), "double-diffractive" (DD) or "centrally diffractive" (CD), respectively, if it involves the dissociation of one of the colliding particles by diffractive excitation with the other remaining intact, or if both suffer dissociation, or if both remain intact, leaving an excited system in the central region between them. Consequently, diffractive events display rather large rapidity gaps in the overall activity. All in all, the total inelastic collision cross-section can thus be written as the sum of diffractive and

non-diffractive cross-sections at a certain centre-of-mass energy $\sqrt{s}$:

$$\sigma_{\text{inel}}(s) = \sigma_{\text{SD}}(s) + \sigma_{\text{DD}}(s) + \sigma_{\text{CD}}(s) + \sigma_{\text{ND}}(s)\,. \tag{4.1}$$

Diffractive reactions are modelled by the exchange of so-called pomerons, colour-neutral and potentially composite objects. The exact definitions of diffractive and non-diffractive events are generator-specific, though.

From the point of view of the proton-proton collision resulting in the hard scattering process, multiple parton interactions (MPI) are possible. Partly, these are to be treated as perturbative processes resulting in additional observable jets, and they also require some showering mechanism. Mostly, however, the MPI interactions are rather soft, entailing contributions to the total amount of scattered energy and causing colour exchange between the beam remnants, increasing the overall particle multiplicities in the hadronization stage. Events with a small impact parameter of the colliding protons naturally produce the highest numbers of MPIs and thus bear an increased probability of displaying hard additional jets ("pedestal effect"). The specific dependencies of the MPI multiplicity on colour screening and saturation effects as well as on $\sqrt{s}$ are poorly understood. Along with ambiguities in colour correlations between different MPIs in the same event, an effect termed "colour reconnections", they represent the main tunable aspects of the underlying event modelling.

MC Generators

This section briefly presents the MC generators used in this analysis and the corresponding choices w.r.t. the several steps of event modelling discussed above.

The AcerMC generator [KR04] is a LO matrix-element-based generator designed to produce standard model background processes to new physics searches. Its LO matrix element code is derived from the MADGRAPH package [SL94] and it relies on a supervising universal generator, e.g. Pythia or Herwig, for the parton shower part. Since AcerMC is built to adapt the phase-space selection procedure to the dynamics of the process to be modelled, it provides a higher generation efficiency than can be achieved by a universal generator. It is used in version 3.8 for the t-channel signal sample in this study and interfaced to Pythia 6.425 [SMS06; Buc+11b] for the parton showering. The LO PDF set MRST LO** [ST08] and the ATLAS AUET2b tune [Buc+11b] are utilized.

MC@NLO [FW02] is a NLO matrix element generator providing a way of matching the exact matrix element of the hard scattering at fixed NLO to a parton shower. This is not a trivial task since tree-level matrix elements are *inclusive*, in that they refer to *at least* n partons in the final state, computed exactly to lowest order in α_{s}, whereas the corresponding parton shower handles *exclusive* states with *exactly* n partons calculated approximately to all orders in α_{s} [Buc+11a]. The NLO matching further ensures that in the process of combining the matrix element with the shower, no double countings or omissions of phase space regions occur, and it propagates

the NLO correctional effect to the total cross-section. It must be noted that in MC@NLO, about 15 % of the generated events carry negative weights (-1). Here, its version v4.01 is employed in combination with the PDF set CT10 [Lai+10] for modelling the background top quark processes $t\bar{t}$ and single-top Wt-channel and s-channel. The parton shower and hadronization is done by Herwig v6.520 and the underlying event is simulated by Jimmy 4.31 [BFS96] using the CT10 Herwig and Jimmy ATLAS AUET2 tune [ATL11f].

The Alpgen generator [Man+03] is again a LO matrix element generator, also relying on another generator for the parton shower part. It specializes in producing standard model processes with high jet multiplicities in the final state. Events are generated with a fixed number of hard partons in the final state, yielding exclusive samples of a certain number of jets matched to these partons. Only the highest multiplicity jet sample, e.g. Np5, is inclusive, containing at least five jets matched to hard partons and allowing for an arbitrary number of additional jets not matched to any parton that result from the showering step. In this analysis, Alpgen is chosen for all production processes of single vector bosons and interfaced with Herwig and Jimmy for parton showering and UE modelling, respectively. For the matrix element computation as well as the parton shower evolution, the CTEQ6.1 PDF is used, again with the Herwig and Jimmy ATLAS AUET2 tune.

Herwig [Cor+01] is a general-purpose MC event generator. It provides LO matrix element generation as well as matching of many hard processes at NLO with the POWHEG method [FNO07; Buc+11a]. Herwig is also capable of parton showering employing the scheme of an angular-ordered shower. For the hadronization part, the cluster hadronization model is utilized. A sophisticated hadronic particle decay scheme is applied for b-quarks and τ-leptons, and all decays are done including full spin correlations. Furthermore, the UE can be modelled by hard and soft MPIs. Here, the diboson production samples are simulated by Herwig in a standalone mode.

Pythia [SMS06] is, like Herwig, a universal MC generator, providing LO matrix element computation and a p_{T}-ordered parton showering approach. Hadronization is done according to the string model. Pythia is serving as the supervising parton shower generator for AcerMC which is used to simulate the single-top t-channel process in this study.

Jimmy [BFS96] is a tool providing an underlying event modelling. The simulation of MPIs proceeds by taking the coloured proton remnants of the hard parton scattering and labelling it as a new incoming "hadron" capable of further scattering; the gluons inside are then labelled as its valence partons. If the ISR-related backward evolution does not produce a gluon in the initial state, an additional emission is forced to produce one. The outgoing remnant of this second scattering is only distinguished from the remnant of the first scattering by a reduced momentum. This procedure can then be iterated in order to produce the required number of MPIs. The probability for m hard scatters is here computed respecting the constraint of the total energy available in the original hard scattering.

4.2.2. Detector Simulation and Digitization

After the event generation by MC methods, the outgoing physics objects have to be subjected to a detailed detector simulation modelling the material response to the traversing particles. To this end, the GEANT framework for detector simulation, briefly outlined in the next section, is employed. Subsequently, the information gained from the GEANT step is translated to electronic output signals as received from the real detector in the so-called *Digitization* step. Eventually, the trigger response is modelled in the last step of event generation, the *Trigger Simulation*.

GEANT Detector Simulation

The GEANT detector simulation framework [Ago+03; ATL99] provides a way of modelling the detector response to the passage of the final state particles of the MC event generation step. It allows to approximately describe the experimental setup by a structure of geometrical volumes filled with a designated medium, respectively. Particles are transported through the detector material taking into account volume boundaries, particle-type specific physical effects, the particles' interactions with the material and with the magnetic field; this involves the use of various parametrizations and approximations. The particles' trajectories are then recorded as well as the responses of the detector components sensitive to these particles. GEANT can also visualize the subdetectors and particle trajectories. The GEANT tool is designed to handle particle energies from 10 eV up to several TeV. The particle four-vectors are tracked through the entire detector volume and hits with corresponding measurement errors are recorded. The program must cope with a high degree of complexity in modelling the experimental conditions that involve effects like event pile-up, radiation background, detector occupancies and background noise. Complete bunch-crossings at a given instantaneous luminosity cannot be simulated at once due to the high mean number of pile-up interactions; instead, single events must be simulated and added up subsequently to properly reproduce the beam crossing. The background noise, which heavily depends on the instantaneous luminosity, must even be inserted after the GEANT simulation. For the samples used in this study, version 4 of the GEANT package [Cos+05] is applied.

Digitization

The second step in the detector simulation consists of translating the GEANT4 output hits into digital signals as received from the readout electronics in the actual experimental setup. Consequently, this procedure is termed "digitization" of the event information [ATL99]. It involves parametrizations of the response characteristics of each particular readout element and needs to be kept up-to-date to the current experimental status. The results of the digitization step are written out and can then be passed on to the offline reconstruction algorithms also used in the processing of genuine ATLAS data as described in detail in Sec. 3.3.

Trigger Simulation

As the last step in the event generation process, the simulation of the trigger response to the reconstructed objects is run: According to the probability of accepting the event at EF level with the current prescale settings (cp. Sec. 3.2.7), generated events are accepted or rejected.

4.3. Signal and Background Samples

The signal and background samples used to compare the model expectation to the data distributions and to obtain the acceptances of the analysis are listed in Tab. 4.2. The shorthand NpX ($X = 0, ..., 5$) denotes the number of additional partons generated on matrix element level in an event of the respective sample; here, the samples with the highest parton multiplicities are inclusive in the sense outlined in Sec. 4.2.1. QCD multi-jet production is not listed since it is not simulated by a MC generator but estimated with a data-driven technique. In the following, the different backgrounds to single-top t-channel production will be detailed and their modelling described.

The main background processes for the single-top t-channel are, in order of decreasing production rate: QCD multi-jet production, W+jets (light and heavy flavour jets), Z+jets, top-pair production and the two other single-top production channels, associated Wt production and s-channel production. A comparison of the absolute cross-sections of the main backgrounds (QCD multi-jets, W+jets, Z+jets, $t\bar{t}$) as a function of the centre-of-mass energy $\sqrt{s}$ is displayed in Fig. 4.1 [Ple09]. Whereas the QCD and the W+jets backgrounds are estimated by fully or partially data-driven methods, all other background processes as well as the t-channel signal process are taken from MC simulations. More details concerning the data-driven background estimates common to all analyses of the top quark working group of ATLAS are to be found in the top group reconstruction note [Ach+12].

4.3.1. QCD Multi-Jets

The production of jets by the strong interaction is termed QCD multi-jet production. Examples of Feynman graphs contributing to this process are shown in Fig. 4.2. Here, the quarks in the final state are assumed not to be top quarks. Thus, quarks and gluons are produced that either radiate more gluons or directly form hadrons: A multi-jet final state is observed. In an ideal experimental setup, this kind of final state could not be mistaken for a semi-leptonic single-top t-channel process, since there is no prompt high-p_{T} lepton present. In a real experiment, however, jets are sometimes misidentified as electrons, and signal muons can be faked by non-prompt muons originating from the decay of heavy hadrons. Despite a small probability of such object misidentifications, QCD multi-jet production constitutes a major background due to its huge overall production rate: QCD multi-jet processes

Process	σ (pb)	$\sigma \cdot k$ (pb)	k-Factor	MC Generator	N_{MC}
single-top t-channel $e\nu$	8.06	6.97	0.865	AcerMC+Pythia	999,295
single-top t-channel $\mu\nu$	8.06	6.97	0.865	AcerMC+Pythia	999,948
single-top t-channel $\tau\nu$	8.05	6.97	0.866	AcerMC+Pythia	998,995
single-top s-channel $e\nu$	0.47	0.500	1.064	MC@NLO+H/J	299,948
single-top s-channel $\mu\nu$	0.47	0.500	1.064	MC@NLO+H/J	299,998
single-top s-channel $\tau\nu$	0.47	0.500	1.064	MC@NLO+H/J	299,899
single-top Wt-channel (incl.)	14.59	15.74	1.079	MC@NLO+H/J	899,694
$t\bar{t}$ (incl. semi-/dileptonic)	79.01	90.5	1.146	MC@NLO+H/J	14,983,835
$W \to \ell\nu$ + Np0	6932	8283	1.195	Alpgen+H/J	17,333,409
$W \to \ell\nu$ + Np1	1305	1560	1.195	Alpgen+H/J	12,485,917
$W \to \ell\nu$ + Np2	378	452	1.195	Alpgen+H/J	11,288,355
$W \to \ell\nu$ + Np3	102	122	1.195	Alpgen+H/J	3,027,339
$W \to \ell\nu$ + Np4	26	31	1.195	Alpgen+H/J	754,948
$W \to \ell\nu$ + Np5	7.0	8.4	1.195	Alpgen+H/J	204,999
$W \to \ell + c$ + Np0	644.4	979	1.52	Alpgen+H/J	6,497,837
$W \to \ell + c$ + Np1	205.0	312	1.52	Alpgen+H/J	2,069,646
$W \to \ell + c$ + Np2	50.8	77.2	1.52	Alpgen+H/J	519,998
$W \to \ell + c$ + Np3	11.4	17.3	1.52	Alpgen+H/J	115,000
$W \to \ell + c$ + Np4	2.8	4.26	1.52	Alpgen+H/J	30,000
$W \to \ell + c\bar{c}$ + Np0	127.53	153	1.2	Alpgen+H/J	1,274,846
$W \to \ell + c\bar{c}$ + Np1	104.68	126	1.2	Alpgen+H/J	1,049,847
$W \to \ell + c\bar{c}$ + Np2	52.08	62.5	1.2	Alpgen+H/J	524,947
$W \to \ell + c\bar{c}$ + Np3	16.96	20.4	1.2	Alpgen+H/J	170,000
$W \to \ell + b\bar{b}$ + Np0	47.35	56.8	1.2	Alpgen+H/J	474,997
$W \to \ell + b\bar{b}$ + Np1	35.76	42.9	1.2	Alpgen+H/J	205,000
$W \to \ell + b\bar{b}$ + Np2	17.33	20.8	1.2	Alpgen+H/J	174,499
$W \to \ell + b\bar{b}$ + Np3	7.61	9.1	1.2	Alpgen+H/J	69,999
$Z \to \ell\ell$ + Np0	668	836	1.25	Alpgen+H/J	23,846,693
$Z \to \ell\ell$ + Np1	134	168	1.25	Alpgen+H/J	6,003,330
$Z \to \ell\ell$ + Np2	40.4	50.5	1.25	Alpgen+H/J	5,008,983
$Z \to \ell\ell$ + Np3	11.2	14.0	1.25	Alpgen+H/J	1,609,692
$Z \to \ell\ell$ + Np4	2.8	3.5	1.25	Alpgen+H/J	444,947
$Z \to \ell\ell$ + Np5	0.79	0.99	1.25	Alpgen+H/J	145,000
WW	11.50	17.02	1.48	Herwig	2,489,244
WZ	3.46	5.54	1.60	Herwig	999,896
ZZ	0.97	1.26	1.30	Herwig	249,999

Table 4.2. MC simulation samples used in the analysis. The cross-section σ is corrected to NLO by the k-factor quoted; in the column $\sigma \cdot k$, the cross-section already includes the k-factor. The cross-sections and k-factors of the single lepton channels ($e\nu$, $\mu\nu$, $\tau\nu$) for W+jets, accompanied by light flavour quarks, as well as for Z+jets are averaged values for display purposes; for these samples, the event numbers listed are the sums of all lepton channels. The shorthand "H/J" denotes the combined Herwig/Jimmy parton shower and UE modelling.

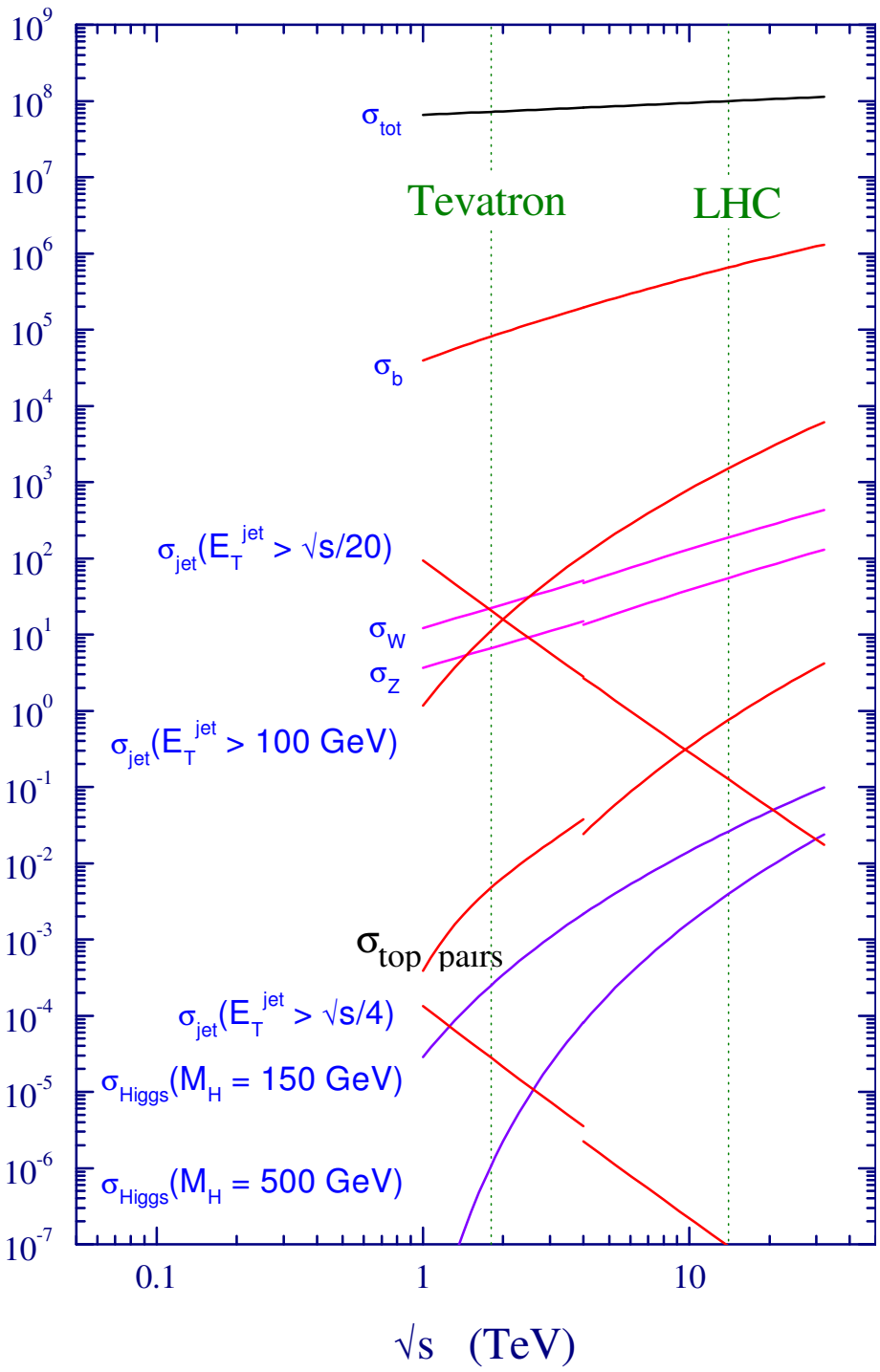

Figure 4.1. Comparison of the cross-sections of some standard model processes with high production rates as a function of $\sqrt{s}$ in pp and $p\bar{p}$ collisions. The nominal operating points of the Tevatron ($\sqrt{s} = 1.96\,\text{TeV}$) and the LHC ($\sqrt{s} = 14\,\text{TeV}$) are marked with dashed vertical lines. σ_{tot} denotes the total inelastic cross-section and $\sigma_{\text{jet}}, \sigma_{\text{b}}, \sigma_{\text{W}}, \sigma_{\text{Z}}, \sigma_{\text{top pairs}}$ and σ_{Higgs} refer to the cross-sections of QCD multi-jet, b-quark, W+jets, Z+jets, $t\bar{t}$ and Higgs production, respectively [Ple09].

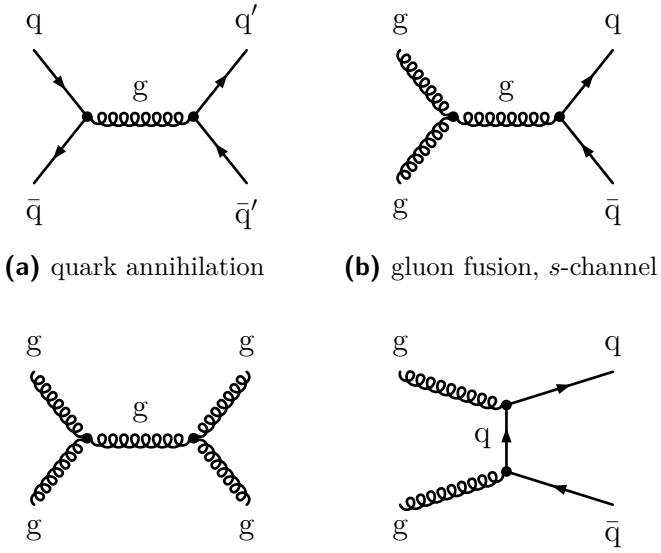

(a) quark annihilation **(b)** gluon fusion, s-channel

(c) gluon fusion, s-channel **(d)** gluon fusion, t-channel

Figure 4.2. Several modes of QCD multi-jet production: Quark annihilation (a) and gluon fusion processes (b), (c) and (d) in the initial state yield a final state with multiple jets.

appear more frequently than single-top production by many orders of magnitude, cp. Fig. 4.1.

In this study, the QCD multi-jets background is modelled jet bin-wise by a data-driven method, the so-called jet-electron model [Abi+10; Ach+12]. The jet-electron method derives a shape for the QCD-multi-jet background by selecting events that display similar kinematic features as the signal selection but with a jet replacing the signal electron. The jet-electron sample is selected with a jet trigger requiring a jet $E_{\mathrm{T}} > 20\,\mathrm{GeV}$. The jet resembling an electron in the event has to satisfy

- $E_{\mathrm{T}} > 25\,\mathrm{GeV}$,
- $|\eta| < 2.47$ excluding the crack region,
- An energy fraction deposited in the EMCAL of $0.8 < f_{\mathrm{EM}} < 0.95$,
- At least four tracks to reduce converted photons.

The QCD shape thus derived and all other MC samples containing real leptons are then combined, and the QCD shape is fitted to data utilizing a QCD enriched sideband in a discriminant distribution: The QCD normalization in the sideband, i.e. the fraction of fake leptons in data, is obtained by performing a binned likelihood fit to the $E_{\mathrm{T}}^{\mathrm{miss}}$ distribution after applying all selection cuts except the $E_{\mathrm{T}}^{\mathrm{miss}}$ cut. This sideband estimate is then extrapolated to the signal region $E_{\mathrm{T}}^{\mathrm{miss}} > 30\,\mathrm{GeV}$ (cp. Sec. 4.4). The concept of the extrapolation from a sideband in the jet-electron model is

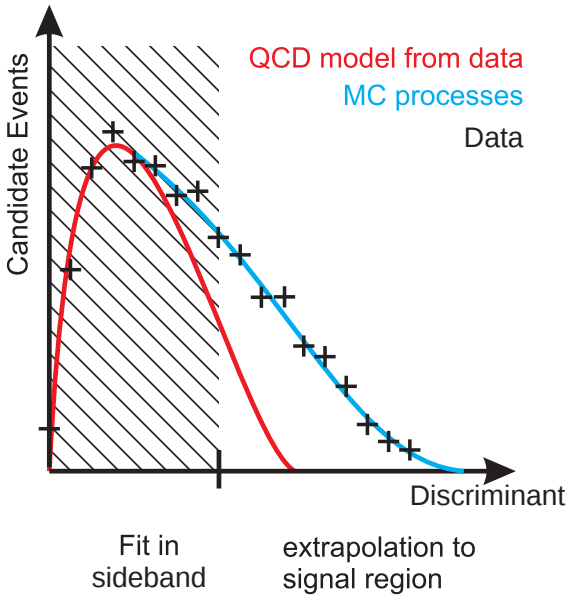

Figure 4.3. Concept of a sideband extrapolation in the jet-electron model [Ach+12].

Jet Bin	$f_{\mathrm{QCD}}^{e,\mathrm{central}}$ (%)	$f_{\mathrm{QCD}}^{e,\mathrm{forward}}$ (%)	f_{QCD}^{μ} (%)
2	6.36	15.40	6.79
3	5.34	8.93	3.51
4	0.23	2.32	1.26

Table 4.3. Expected fraction of QCD events in data in the *tag selection*, derived from the jet-electron model, dependent on the jet bin and signal lepton flavour.[5]

illustrated in Fig. 4.3. The uncertainty of the jet-electron QCD estimate is given by the error of the binned likelihood fit, and also systematic uncertainties originating from pile-up effects are considered; furthermore, a comparison with another data-driven technique is done, which also adds a contribution to the overall systematic error (cp. Sec. 6.1.1 for details).

Since this approach turned out to also yield good results when applied to the muon channel, it is here used for both lepton flavours. In order to ensure an optimal performance of the jet-electron model, the electron channel is split into events with the signal electron being central ($|\eta| < 1.5$) and forward ($|\eta| \geq 1.5$). The $E_{\mathrm{T}}^{\mathrm{miss}}$ control distribution resulting from the jet-electron fit in the 2-jet bin *tag selection* (see Sec. 4.4) in the central electron channel is shown in Fig. 4.4. The QCD fractions of the data derived by the jet-electron method are used to scale this QCD estimate to the data luminosity on the sample defined as *tag selection* and are listed in Tab. 4.3. The resulting QCD event yields in the *tag selection* are collected in Tab. 4.4.

[5] D. Hirschbühl. *ATLAS TWiki: The Jet-Electron QCD Model*. Oct. 2012. URL: `https://twiki.cern.ch/twiki/bin/viewauth/AtlasProtected/JetElectronQCDModel`

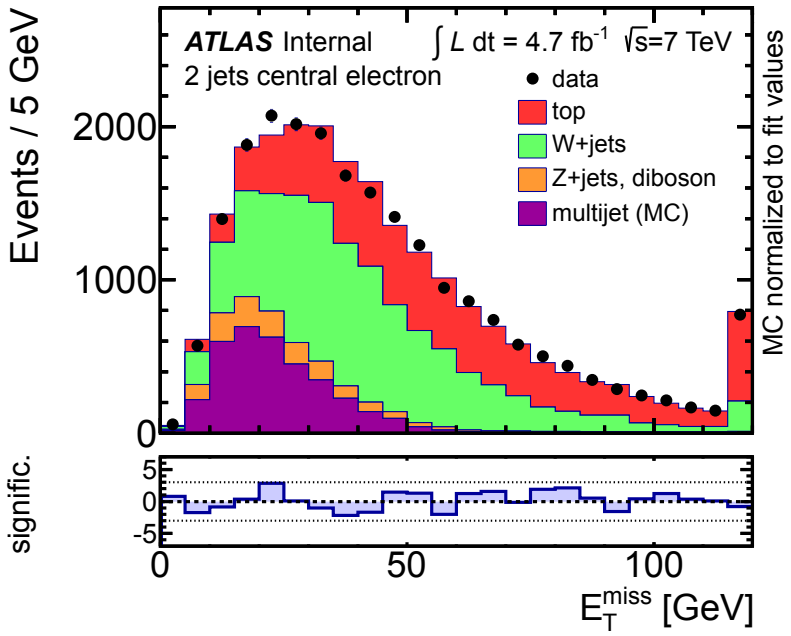

Figure 4.4. $E_{\mathrm{T}}^{\mathrm{miss}}$ distribution normalized to the jet-electron fit result in the 2 jet bin *tag selection* in the central electron channel.[6]

Jet Bin	$N_{\mathrm{QCD}}^{e,\mathrm{central}}$	$N_{\mathrm{QCD}}^{e,\mathrm{forward}}$	N_{QCD}^{e}	N_{QCD}^{μ}
2	772.9	609.5	1382.4	1292.9
3	451.9	203.2	655.1	438.5
4	11.4	26.2	37.6	87.9

Table 4.4. Number of expected QCD events from the jet-electron model in the *tag selection*, dependent on the jet bin and signal lepton flavour. For the electron channel, the central and forward contributions are quoted separately in the first two columns, whereas the total is listed in the third column.

4.3.2. W+Jets

The production of W bosons in association with jets is the second-largest background to the single-top t-channel, occurring at a rate that is some orders of magnitude higher. Two contributing Feynman diagrams are collected in Fig. 4.5. There can be any number of additional jets originating from gluon radiations of the initial or final state gluons or quarks. Since the W boson can decay leptonically, the semi-leptonic W+jets processes are a major background in this study. On top of this similar signature, even the W mass constraint of the kinematic fit reconstruction is fulfilled (cp. Sec. 5.2.1). If there is also a b-quark amongst the final state particles,

[6] D. Hirschbühl. *ATLAS TWiki: The Jet-Electron QCD Model*. Oct. 2012. URL: `https://twiki.cern.ch/twiki/bin/viewauth/AtlasProtected/JetElectronQCDModel`

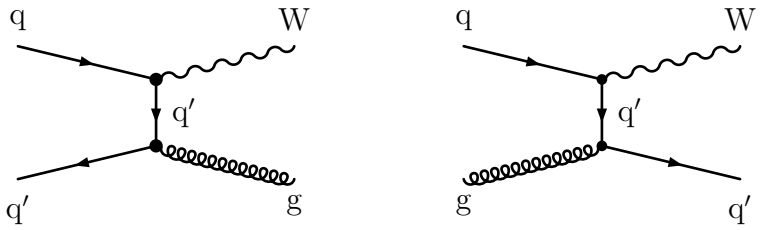

(a) quark annihilation, t-channel **(b)** quark-gluon scattering, t-channel

Figure 4.5. Two modes of W+jets production: Quark annihilation (a) and quark-gluon scattering processes (b) in the t-channel yield a final state with a W boson accompanied by jets.

the W+jets event can hardly be distinguished from a single-top t-channel event.

The overall rate of W+jets events in data as well as the relative rates of W-boson production in association with different combinations of heavy quarks are not accurately known in theory [Ach+12]. Therefore, like in the case of QCD multi-jet production, a data-driven approach is employed to aid in estimating the W+jets background contribution. However, here, the MC samples of W+jets, produced with the Alpgen generator and showered with Herwig/Jimmy (cp. Tab. 4.2), are used for analysis and reweighted subsequently according to the result of the data-driven method. The different samples model leptonically decaying W bosons produced in association with a certain number of jets originating from light or heavy flavour quarks. The heavy flavour final states considered are $\mathrm{W}+\mathrm{c}$, $\mathrm{W}+\mathrm{c\bar{c}}$ and $\mathrm{W}+\mathrm{b\bar{b}}$, and will be termed W+HF in the following as opposed to the light flavour final states, denoted by W+LF. The analysis is performed on the MC samples of W+jets and, subsequently, the contributions of the four different types (W+LF, $\mathrm{W}+\mathrm{c}$, $\mathrm{W}+\mathrm{c\bar{c}}$ and $\mathrm{W}+\mathrm{b\bar{b}}$) are reweighted with respect to each other according to scale factors derived from data. Additionally, the overall W+jets normalization is estimated from data. The extraction of the scale factors is accomplished by the charge-asymmetry method [Ach+12] which relies on the data yield as well as on the QCD yield and the MC yields of all non-W+jets background processes. This method makes use of the fact that W+jets is the only background process of the single-top t-channel (except for the rare single-top s-channel, WZ and WW processes) which displays a charge-asymmetrical production rate. Below, this partially data-driven scale factor estimation will be briefly outlined.

The W+jets scale factor estimation is done jet-bin wise and consists of three steps which are detailed further in the following:

1. Determining the W+jets overall normalization for the 2-jet bin as well as for the current i-jet bin in form of the total number of W+jets events in the *pretag* and *tag selections* (defined in Sec. 4.4.2), denoted by $N_2^{\mathrm{W,pretag}}$, $N_i^{\mathrm{W,pretag}}$, $N_2^{\mathrm{W,tag}}$ and $N_i^{\mathrm{W,tag}}$, respectively,

2. With the knowledge of the 2-jet bin *tag* and *pretag* yields, computing the four different W+jets flavour fractions for the *pretag* yields of the exclusive 2-jet bin, denoted here by $F_{\mathrm{LF},2}$, $F_{\mathrm{c},2}$, $F_{\mathrm{cc},2}$ and $F_{\mathrm{bb},2}$, and then recomputing the W+jets overall normalization in the 2-jet bin from those in an iterative analytical procedure,

3. Finally, concluding on the W+jets *pretag* flavour fractions in the i-jet bin, $F_{\mathrm{LF},i}$, $F_{\mathrm{c},i}$, $F_{\mathrm{cc},i}$ and $F_{\mathrm{bb},i}$, by extrapolating from the 2-jet bin.

Thus, the W+jets overall normalization and the W+jets flavour fractions are determined simultaneously with this method. The same procedure is applied for both lepton channels on the samples defined by the *pretag* and *tag selections*.

Step 1: Due to the proton valence quark content, W^+ bosons are more copiously produced than W^- bosons, leading to a charge asymmetry in the observable production of the respective decay leptons. All other background channels considered in this analysis are charge-symmetric except for the single-top s-channel. The ratio of the two W boson production cross-sections,

$$r \equiv \frac{\sigma(\mathrm{pp} \to \mathrm{W}^+)}{\sigma(\mathrm{pp} \to \mathrm{W}^-)}\,, \tag{4.2}$$

is a quantity known to higher precision than the overall rate of W+jets production. This theoretical knowledge can be exploited by extracting the number of W+jets *pretag* events in data for each jet bin from the formula

$$\begin{aligned} N^{\mathrm{W,pretag}} = N^{\mathrm{W}^+} + N^{\mathrm{W}^-} &= \frac{N^{\mathrm{W}^+}_{\mathrm{MC}} + N^{\mathrm{W}^-}_{\mathrm{MC}}}{N^{\mathrm{W}^+}_{\mathrm{MC}} - N^{\mathrm{W}^-}_{\mathrm{MC}}} (N^{+}_{\mathrm{data}} - N^{-}_{\mathrm{data}}) \\ &= \left(\frac{r_{\mathrm{MC}}+1}{r_{\mathrm{MC}}-1}\right)(N^{+}_{\mathrm{data}} - N^{-}_{\mathrm{data}})\,, \end{aligned} \tag{4.3}$$

where $N^{+/-}_{\mathrm{data}}$ are the total *pretag* yields in data[7] for the corresponding lepton charges. Though not explicitly denoted, all yields refer to the *pretag* selection. Furthermore, r_{MC} is the ratio of Eq. (4.2), evaluated from the MC simulation prediction, at first from the uncorrected one (when iterating the procedure, the information on the W+jets flavour fractions gained from step 2 corrects this prediction, entering into the ratio r_{MC}). Now, for each jet bin i, the total W+jets yield in the *tag* sample is given by

$$N_i^{\mathrm{W,tag}} = N_i^{\mathrm{W,pretag}} f_2^{\mathrm{tag}} f_{2\to i}^{\mathrm{tag}}\,, \tag{4.4}$$

where f_2^{tag} is the tagging fraction in the 2-jet bin, i.e. the ratio of the number of events with exactly one b-tag and the number of all *pretag* events; it is measured from data after subtracting all non-W contributions (i.e. the data-driven yield for

[7] In order for Eq. (4.3) to be valid, the charge-asymmetric single-top t- and s-channel contributions are already subtracted from the data yields according to the corresponding MC estimates such that $(N^{+}_{\mathrm{data}} - N^{-}_{\mathrm{data}}) \approx (N^{\mathrm{W}^+} - N^{\mathrm{W}^-})$.

QCD and the MC yields for all other channels) from the data yield.[8] Finally, $f_{2\to i}^{\text{tag}}$ is the ratio of the tagging fractions in the i-jet bin and the 2-jet bin, derived from the MC prediction. The overall normalization scale factor for the W+jets yield in each jet bin i is then defined as

$$W_{\text{norm},i}^{\text{pretag/tag}} = W_{\text{norm},i} = \frac{N_{\text{data},i}^{\text{W,tag}}}{N_{\text{MC},i}^{\text{W,tag}}}\,. \tag{4.5}$$

Step 2: The flavour composition part of the normalization is done by first determining the W+jets *pretag* flavour fractions in the 2-jet bin $F_{\text{LF},2}$, $F_{\text{c},2}$, $F_{\text{cc},2}$ and $F_{\text{bb},2}$, defined as

$$F_{xx,2} = \frac{N_{xx,2}^{\text{W,pretag}}}{N_2^{\text{W,pretag}}}, \quad xx \in \{\text{LF, c, cc, bb}\}\,. \tag{4.6}$$

This is accomplished by writing the total number of W+jets events in the *tag* sample in terms of the number of *pretag* events as

$$N_2^{\text{W,tag}} = N_2^{\text{W,pretag}}(F_{\text{LF},2}P_{\text{LF},2} + F_{\text{c},2}P_{\text{c},2} + F_{\text{cc},2}P_{\text{cc},2} + F_{\text{bb},2}P_{\text{bb},2}) \tag{4.7}$$

with the b-tagging probabilities $P_{xx,2}$ for the respective flavour-types in the 2-jet bin that are extracted from MC simulation. Also, the flavour fractions must add up to unity:

$$F_{\text{LF},2} + F_{\text{c},2} + F_{\text{cc},2} + F_{\text{bb},2} = 1\,. \tag{4.8}$$

Now, the sample is split into events with positive and negative leptons in order to gain another equation[9], and the ratio of the fractions of W+cc and W+bb events is fixed to its MC estimate $k_{\text{cc}\to\text{bb}}$, giving

$$N_2^{\text{W,tag}\pm} = N_2^{\text{W,pretag}\pm}(F_{\text{LF},2}P_{\text{LF},2} + F_{\text{c},2}P_{\text{c},2} + k_{\text{cc}\to\text{bb}}F_{\text{bb},2}P_{\text{cc},2} + F_{\text{bb},2}P_{\text{bb},2})\,. \tag{4.9}$$

Here, the *pretag* yields normalized to data for both charges are known from Eq. (4.3) of step 1, and the corresponding number of *tagged* MC events is also taken to be equal to the one in data, given by Eq. (4.4).[10] Thus, the three unknown flavour fractions $F_{\text{LF},2}$, $F_{\text{c},2}$ and $F_{\text{bb},2}$ can be calculated from the three Equations (4.8) and (4.9). As mentioned before, the resulting flavour fractions are then used to recompute the ratio r_{MC} and the W+jets overall normalization, starting an iterative procedure that terminates when the values stabilize.

Step 3: From the flavour fractions in the 2-jet bin, the flavour fractions for the i-jet bin can be derived in form of the flavour fraction scale factors K_{LF}, K_{c}, K_{cc}

[8] As a result of the iterative procedure described in step 2, the tagging fractions in data and MC are always identical resulting in the same W overall normalization scale factor (defined in Eq. (4.5)) in the *pretag* and *tag* samples.

[9] This operation implies that the $F_{\text{xx},2}$ are independent of the lepton charge in the event, an assumption that is valid to first order according to the author of the method [Vre13].

[10] For the 2-jet bin, the translation factor $f_{2\to i}^{\text{tag}}$ is not needed.

and K_{bb}, defined as

$$K_{xx,i} = \frac{F_{xx,i}^{\mathrm{data}}}{F_{xx,i}^{\mathrm{MC}}} \,. \tag{4.10}$$

Up until now, these are only known for the 2-jet bin. In order to conclude on the flavour fraction scale factors in the current i-jet bin, the 2-jet bin factors are applied to the MC flavour fractions in the i-jet bin[11],

$$K_{\mathrm{LF},2} F_{\mathrm{LF},i}^{MC} + K_{\mathrm{c},2} F_{\mathrm{c},i}^{MC} + K_{\mathrm{cc},2} F_{\mathrm{cc},i}^{MC} + K_{\mathrm{bb},2} F_{\mathrm{bb},i}^{MC} = C \,, \tag{4.11}$$

and, by renormalizing to unity,

$$\frac{1}{C} \left(K_{\mathrm{LF},2} F_{\mathrm{LF},i}^{MC} + K_{\mathrm{c},2} F_{\mathrm{c},i}^{MC} + K_{\mathrm{cc},2} F_{\mathrm{cc},i}^{MC} + K_{\mathrm{bb},2} F_{\mathrm{bb},i}^{MC} \right) = 1 \,, \tag{4.12}$$

the flavour fraction scale factors for the i-jet bin turn out to be

$$K_{xx,i} = \frac{K_{xx,2}}{C} \,. \tag{4.13}$$

There are many alternative ways of deriving the W overall normalization and flavour composition similar to the procedure presented above, but this one proved to yield the most stable results. However, here, the W+jets processes are treated as the only charge-asymmetric contributions to the data after the subtraction of the single-top t- and s-channels which are also charge-asymmetric. Since the signal channel of this analysis is the single-top t-channel, the *tag selection* is already enriched in t-channel events. Thus, in order to avoid a strong dependence of the W+jets scale factors on the signal yield, a W-enriched control region with very low signal contribution should be exploited, which is not done here. Ideally, such a region would be defined by some or all of the following "anti-t-channel" cuts:

- $|\eta^{\text{light jet}}| \leq 2.0$
- $m_{\mathrm{top}} \leq 150$ GeV or $m_{\mathrm{top}} \geq 190$ GeV
- $H_{\mathrm{T}} \leq 210$ GeV,
- $\Delta\eta\,(\text{b-jet,light jet}) \leq 1.0$ (only 2-jet bin)
- $m_{\text{all jets}} \leq 450$ GeV (only 3-jet bin)

where H_{T} is the scalar sum of the signal lepton p_{T}, the $E_{\mathrm{T}}^{\mathrm{miss}}$ and the p_{T} of all selected jet candidates,

$$H_{\mathrm{T}} = p_{\mathrm{T}}^{\mathrm{lepton}} + E_{\mathrm{T}}^{\mathrm{miss}} + \sum_{\text{all jets}} p_{\mathrm{T}}^{\mathrm{jet}} \,, \tag{4.14}$$

and the b-jet and the light jet are defined as

[11] This is done assuming that the $K_{xx,2}$ are actually applicable to all jet bins.

Electron-Channel					
Jet Bin	K_{LF}	K_{c}	K_{cc}	K_{bb}	W_{norm}
2	0.95	0.82	1.62	1.62	0.87
3	0.92	0.80	1.57	1.57	0.86
4	0.90	0.77	1.53	1.53	0.86
Muon-Channel					
Jet Bin	K_{LF}	K_{c}	K_{cc}	K_{bb}	W_{norm}
2	0.97	0.83	1.46	1.46	0.91
3	0.95	0.82	1.42	1.42	0.87
4	0.93	0.80	1.39	1.39	0.94

Table 4.5. Factors for heavy flavour fraction reweighting of W+LF (K_{LF}) and W+HF (K_{c}, K_{cc}, K_{bb}) MC events and overall W+jets normalization factors (W_{norm}) in the *tag selection* for jet bins 2, 3 and 4 in the electron and muon channel.

- The first and second leading jet in the *pretag selection* (cp. Sec. 4.4.2): The first is taken to be the b-jet, the second is assumed to be the light jet,
- The first b-jet and the leading non-b-jet in the *tag selection* (cp. Sec. 4.4.2).

The W+jets scale factors should then be computed from the data and MC yields in the *pretag selection* as well as on this W control region instead of the *tag selection*; this procedure has been attempted and proved to be stable w.r.t the (very small) remaining fraction of signal events in that region. However, due to a missing QCD background estimate for the W control region[12], the *tag selection* is used instead in this study. The resulting flavour fraction and overall normalization scale factors (cp. Equations (4.5) and (4.10)) in the *tag selection* that are used in this analysis are listed in Tab. 4.5 for the different jet bins and both lepton flavours.[13] The corresponding expected event yields in the *tag selection* of the W+LF and W+HF processes are listed in Tab. 4.6. The control plots of the transverse mass distribution of the W boson are shown in Sec. 4.4.4 in Fig. 4.8c for the *pretag* sample and in Fig. 4.13d for the *tag* sample for the electron channel in the 2-jet bin.

4.3.3. Z+Jets

Z bosons in association with jets can be produced according to the Feynman graphs of Fig. 4.6. The initial and final state gluons and quarks can radiate further gluons, giving a multi-jet final state. If the Z boson decays into charged leptons and one lepton is lost in the reconstruction or drops out of the detector acceptance region,

[12] No reliable QCD yield could be produced for this region since the jet-electron fit was reported to not converge.

[13] It is always $K_{\mathrm{cc}} = K_{\mathrm{bb}}$ by construction, since the ratio of the flavour fractions $F_{\mathrm{cc},2}$ and $F_{\mathrm{bb},2}$ in data was fixed to its MC estimate in step 2.

Electron-Channel				
Jet Bin	W+LF	$W + c$	$W + c\bar{c}$	$W + b\bar{b}$
2	833.9	3018.3	1849.3	2687.4
3	198.4	680.9	671.6	1143.0
4	55.2	139.6	225.5	374.7
Muon-Channel				
Jet Bin	W+LF	$W + c$	$W + c\bar{c}$	$W + b\bar{b}$
2	1210.3	3788.2	2117.3	3374.2
3	335.4	910.0	822.4	1314.2
4	76.2	178.5	269.6	479.3

Table 4.6. Expected event yields in the *tag selection* of W+LF and W+HF ($W + c$, $W + c\bar{c}$, $W + b\bar{b}$) processes using the factors recorded in Tab. 4.5 for jet bins 2, 3 and 4 in the electron and muon channel.

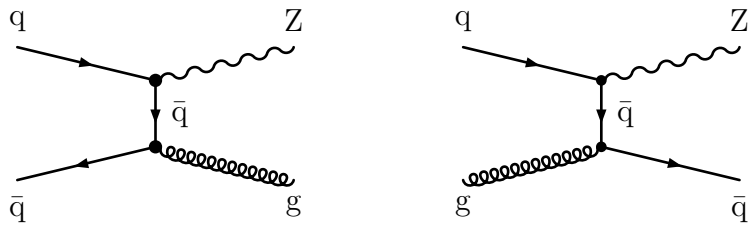

(a) quark annihilation, t-channel **(b)** quark-gluon scattering, t-channel

Figure 4.6. The two modes of Z+jets production: Quark annihilation (a) and quark-gluon scattering processes (b) in the t-channel yield a final state with a Z boson accompanied by jets.

this process contributes to the background of the single-top t-channel. It is found not to be a major background, though, also because its leptonic modes occur at a rate of only about 40 times that of the single-top t-channel. Like for W+jets, the Z+jets MC samples are generated by Alpgen using Herwig/Jimmy for the shower simulation. Only Z boson decays into charged leptons are considered.

4.3.4. Diboson Production

The simultaneous production of two vector bosons can proceed via the channels pictured in Fig. 4.7. In the MC samples considered here, at least one and up to four real leptons are present in the final state. Due to a second lepton veto applied in the preselection (cp. Sec 4.4), these processes are only selected if high-p_{T} leptons are lost in the reconstruction or drop out of the acceptance region. This is rarely the case, and since the production of two vector bosons requires a large energy of

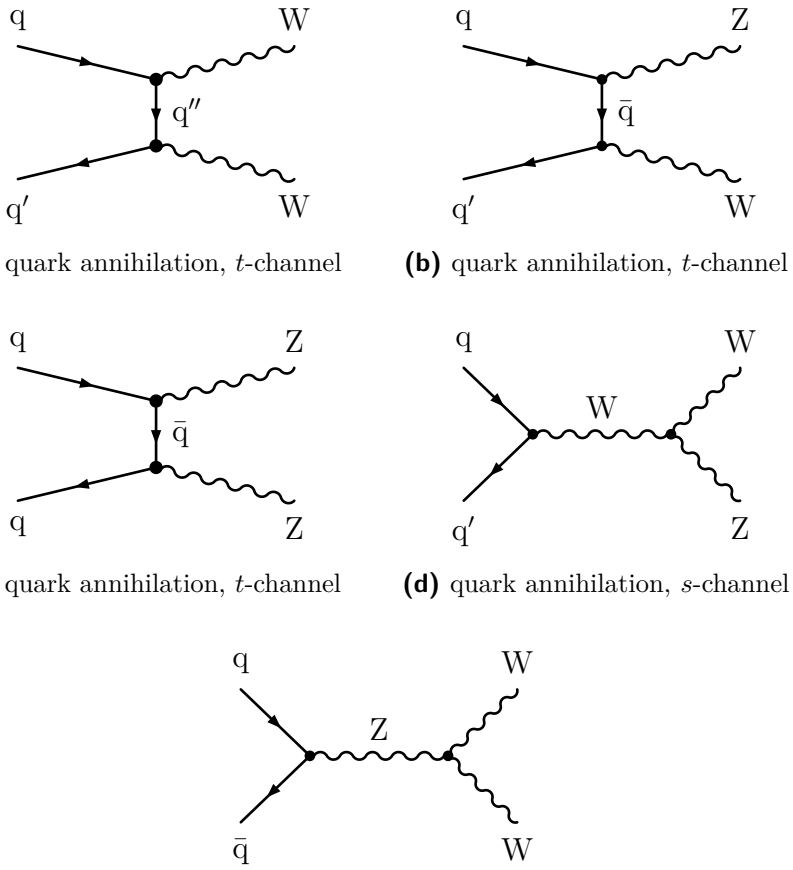

(a) quark annihilation, t-channel

(b) quark annihilation, t-channel

(c) quark annihilation, t-channel

(d) quark annihilation, s-channel

(e) quark annihilation, s-channel

Figure 4.7. Different modes of diboson production: Quark annihilation processes in the t-channel (a), (b), (c), and in the s-channel (d), (e) yield a final state with two W bosons, two Z bosons or a W and a Z boson.

the hard scattering, the diboson processes are also occurring at a low rate similar to that of single-top itself. However, the events surviving the preselection are hard to discern if at least one real W is present. Still, the diboson processes constitute a minor background of the single-top t-channel signal.

The MC samples modelling diboson processes were created by the Herwig generator in standalone mode. They are LO samples without additional partons in the final state and are filtered to contain at least one lepton with $p_{\mathrm{T}} > 10\,\mathrm{GeV}$.

4.3.5. $\mathrm{t\bar{t}}$ Production

The production of top quark pairs has already been discussed at length in Sec. 2.3.2. Since there are real top quarks present, an analysis method simply reconstructing top quarks will not only select single-top but also all $\mathrm{t\bar{t}}$ events. This makes $\mathrm{t\bar{t}}$ production a major background of single-top t-channel processes that can only be reduced by

placing a veto on a second reconstructed top quark or exploiting differences in the event kinematics (the analysis details will be the topic of Sections 4.4 and 5.2.3).

For the modelling of $\mathrm{t\bar{t}}$ processes, MC samples produced by the MC@NLO generator and showered by Herwig/Jimmy are used. The top quark mass is set to 172.5 GeV. Semi-leptonic as well as dileptonic final states are provided. All-hadronic final states are not included in the sample since they are not expected to pass the signal lepton requirement.

4.3.6. Single-Top Production

The single-top production processes were described in detail in Sec. 2.3.3. Since the t-channel is the dominant production mode, the Wt- and the s-channel are minor albeit almost irreducible backgrounds. In order to reject Wt-channel events, a veto on a second W boson can be devised (cp. Sec. 5.2.3).

The single-top MC samples were generated by different setups: The t-channel process is modelled by the AcerMC generator utilizing Pythia for the parton shower while the Wt- and s-channel are produced by the MC@NLO generator with Herwig/Jimmy showering. The top quark mass is again set to 172.5 GeV, and the electroweak couplings of the top quark are taken to be

$$|V_{\mathrm{td}}| = 0.00862\,, \tag{4.15a}$$
$$|V_{\mathrm{ts}}| = 0.0403\,, \tag{4.15b}$$
$$|V_{\mathrm{tb}}| = 0.99152\,. \tag{4.15c}$$

These values imply a branching ratio of the top quark decaying to a W boson and a b quark of nearly 100 % as well as a mode of production of the t-channel exclusively via a b quark from the proton sea. While the t- and s-channel samples are divided by lepton flavour, the Wt-channel sample is fully inclusive w.r.t. the W boson decays. The theoretical cross-sections used as input of the MC event generation are the ones listed in Tab. 2.4, and the value for the t-channel process is the first one quoted there (computed at $m_{\mathrm{t}} = 172.5\,\mathrm{GeV}$).

4.4. Event Preselection

The data as well as the MC samples described are subjected to an extensive filtering in order to increase the signal selection efficiency of the analysis procedure. Before the filtering is applied, the energy scales and resolutions of the different physics objects first need to be corrected according to calibrations derived from data. Then, many different kinds of requirements are applied to the reconstructed objects in the event, resulting in simple event veto cuts. Subsequently, additional scale factors are applied to reweight the MC events in a manner that renders them comparable to the data events. All of this is done in a preselection step before the method of the kinematic fit is invoked.

4.4.1. Energy Scale and Resolution Corrections

Before defining the final analysis physics objects and formulating requirements for a cut-based preselection step, it must be ensured that the same calibration corrections are used for simulated physics objects in MC events as to the ones in data events. To this end, the corresponding corrections to their energy scales and resolutions are applied before imposing any analysis-specific requirements on them.

Electrons

The electron cluster energy scale s_{cluster} is obtained from $\text{Z} \to e^+e^-$, $\text{W} \to e\nu$ and $\text{J}/\Psi \to e^+e^-$ samples as a function of η_{cluster}, ϕ_{cluster} and E_{T}; it depends on the detector material, the presampler energy scale, the event selection, the pile-up and the material modelling, and is applied to electrons in data events via[14]

$$E_{\text{cluster, corrected}} = \frac{E_{\text{cluster}}}{1 + s_{\text{cluster}}} \,. \tag{4.16}$$

Additionally, the electron E_{T} in MC is smeared to reflect the resolution in data. There is also a calibration correction for the extended crack region in the range $1.52 < |\eta_{\text{cluster}}| < 1.55$ which is applied to data as well as to MC electrons.

Muons

In contrast to the electron energy, the muon p_{T} receives a scale shift in MC to match the situation in data. In an analogous manner to the electron case, the muon p_{T} resolution in MC is smeared; however, here, the ID and MS extrapolated transverse momenta from MC are smeared separately and then, the average of the two smeared components is computed, weighted by their expected resolutions.[15] Only subsequently, this combined muon p_{T} scale is shifted.

Jets

The jet energy calibration proceeds for data and MC events according to the scheme already detailed in Sec. 3.3.4. It was found that no additional energy resolution smearing for jets is required since data and MC agree well in this respect [Ach+12].

Missing Transverse Energy

Since $E_{\text{T}}^{\text{miss}}$ is a quantity composed of several terms, each of which belongs to another kind of physics object in the event (cp. Sc. 3.3.6), all energy scale shifts and smeared resolutions of these objects, as described above, are propagated to the $E_{\text{T}}^{\text{miss}}$ in an

[14] F. Hubaut. *ATLAS TWiki: Energy Rescaler*. Jan. 2012. URL: `https://twiki.cern.ch/twiki/bin/viewauth/AtlasProtected/EnergyRescaler`.

[15] M. Owen. *ATLAS TWiki: Top Common Scales 2011*. July 2012. URL: `https://twiki.cern.ch/twiki/bin/viewauth/AtlasProtected/TopCommonScales2011`.

adequate way. In general, the resolution of $E_{\mathrm{T}}^{\mathrm{miss}}$ depends on that of the scalar energy sum of all calorimeter cells, $\sum E_{\mathrm{T}}$. In MC events where non-interacting particles are present, the true missing transverse energy is defined to originate from all non-interacting particles, and its components are denoted by $E_{x,y}^{\mathrm{NonInt}}$. The component resolutions $\sigma_{E_x^{\mathrm{miss}}}$ and $\sigma_{E_y^{\mathrm{miss}}}$ can then be estimated from a Gaussian fit to the residuals $(E_{x,y}^{\mathrm{miss}} - E_{x,y}^{\mathrm{NonInt}})$ in bins of $\sum E_{\mathrm{T}}$; the two are equivalent, and the overall resolution is gained from a Gaussian fit to the combined residual distribution.

4.4.2. Event Preselection Requirements

This section collects the candidate requirements of all physical objects involved as well as the preselection event level cuts applied in this study. The details of the reconstruction of physical objects in the event were already presented in Sec. 3.3, and further information can also be found in [Ach+12]. The physical objects' energy scales and resolutions are at this stage already modified as outlined in the last section.

Trigger Requirements

An event is required to be selected by a high-p_{T} electron or muon event filter (EF) trigger. The involved exact p_{T}-threshold depends on the run-period and was already listed in Tab. 4.1. To account for discrepancies of the trigger efficiencies in data and MC, scale factors are applied to MC events as outlined in Sec. 4.4.3.

Electrons

Electron candidates are required to be reconstructed by an algorithm combining the information of tracking and calorimeter components of the detector. They must be of "tight" identification quality and need to have a transverse momentum[16] $p_{\mathrm{T}} > 30\,\mathrm{GeV}$. The pseudorapidity of their electromagnetic calorimeter cluster must be $|\eta_{\mathrm{cluster}}| < 2.47$ excluding the crack region of the overlapping calorimeter components at $1.37 < |\eta_{\mathrm{cluster}}| < 1.52$. To avoid the selection of jets misreconstructed as electrons, the electron candidates have to fulfil an isolation criterion: The reconstructed absolute energy deposited in a cone of $\Delta R = 0.2$ around the electron and the absolute sum of track-p_{T} in a cone of $\Delta R = 0.3$ around the electron direction must be accepted by the isolation algorithms working at 90 % efficiency w.r.t. the "tight" definition[17], $E_{\mathrm{T}}^{\mathrm{cone20}}$@90% and $p_{\mathrm{T}}^{\mathrm{cone30}}$@90%. In order not to double-count electrons as jets, jets within $\Delta R = 0.2$ of the electron track direction are removed from the event; subsequently, the electron is discarded if another jet with $p_{\mathrm{T}} > 20\,\mathrm{GeV}$ is found within $\Delta R = 0.4$ of the electron.

The electromagnetic cluster energies used here have been rescaled in data, and a resolution smearing was done as well (see corresponding paragraphs in Sec. 4.4.1).

[16] Here, the transverse momentum is computed as $E_{\mathrm{cluster}}/\cosh(\eta_{\mathrm{track}})$.
[17] The working points of these algorithms are defined w.r.t. cuts in the $(\eta_{\mathrm{cluster}}, E_{\mathrm{T}})$-plane.

Furthermore, scale factors need to be applied for electron candidates in simulated events to correct for the mismodelling of the actual η and E_{T} dependent trigger, identification and reconstruction efficiencies compared to real data; also, the efficiency of the isolation cut must be accounted for (cp. Sec. 4.4.3).

Muons

Muon candidates are required to be reconstructed by an algorithm combining the information of the inner tracking devices and the outer muon spectrometer tracking chambers of the detector, namely the MuID algorithm. They must be of "tight" identification quality and need to have a transverse momentum $p_{\mathrm{T}} > 30\,\mathrm{GeV}$. Their pseudorapidity must lie within $|\eta| < 2.5$. In addition, the ID track of the muon has to satisfy the following quality criteria:[18]

- A pixel b-layer hit is required except for cases in which the extrapolated muon track passes an uninstrumented or dead area of the b-layer,
- The total number of pixel hits and of crossed dead pixel sensors should be at least two,
- The total number of SCT hits and of crossed dead SCT sensors should be at least six,
- The total number of crossed pixel holes[19] and SCT holes should be below three,
- A successful extension of the track into the TRT is required: Let $N_{\mathrm{TRT\ hits}}$ denote the number of TRT hits on the muon track, $N_{\mathrm{TRT\ outliers}}$ the number of TRT outliers[20] on the muon track, and $N \equiv N_{\mathrm{TRT\ hits}} + N_{\mathrm{TRT\ outliers}}$. Two cases are distinguished:
  - $|\eta| < 1.9$: Require $N > 5$ and $N_{\mathrm{TRT\ outliers}} < 0.9\,N$,
  - $|\eta| \geq 1.9$: If $N > 5$, then require $N_{\mathrm{TRT\ outliers}} < 0.9\,N$.

To avoid the selection of muons originating from heavy flavour meson decays inside jets, the muon candidates have to fulfil an isolation criterion: The absolute energy deposited in a cone of $\Delta R = 0.2$ around the muon must satisfy $E_{\mathrm{T}}^{\mathrm{cone20}} < 4\,\mathrm{GeV}$ and the absolute sum of track-p_{T} in a cone of $\Delta R = 0.3$ around the muon direction is restricted to $p_{\mathrm{T}}^{\mathrm{cone30}} < 2.5\,\mathrm{GeV}$. For the same reason, muons running within $\Delta R = 0.4$ of a jet with $p_{\mathrm{T}} > 25\,\mathrm{GeV}$ and a jet vertex fraction $|\mathrm{JVF}| > 0.75$ (as defined in the paragraph on jets below) are rejected.

Here, a muon energy scaling and smearing was already done on MC (cp. Sec. 4.4.1).

[18] A. Salvucci. *ATLAS TWiki: Muon Combined Performance Group Recommendations for Release 17 Analyses.* Aug. 2012. URL: `https://twiki.cern.ch/twiki/bin/viewauth/AtlasProtected/MCPAnalysisGuidelinesRel17MC11a`.

[19] A hole is a space-point on the track where a hit would have been expected but was not observed.

[20] An outlier is a hit relatively far from the main track, down-weighted in the refit of the track (cp. Sec. 3.3.1).

Furthermore, scale factors need to be applied for muon candidates in simulated events to correct for the mismodelling of the actual η and p_{T} dependent reconstruction, identification and trigger efficiencies as well as the isolation cut efficiency w.r.t. the data (see corresponding paragraphs in Sec. 4.4.3).

Jets

The jets used in the analysis are reconstructed with the anti-k_{t} topological clustering algorithm with a width parameter of 0.4 (cp. Sec. 3.3.4). In order to avoid counting electron candidates as jets, jet candidates that are within $\Delta R < 0.2$ of an electron candidate (as defined above) are removed. The remaining jets are required to have $E_{\mathrm{T}} \geq 0$ [21] and $p_{\mathrm{T}} > 30\,\mathrm{GeV}$, and must lie within $|\eta| < 4.5$. In order to reduce the effects of pile-up a cut on the jet vertex fraction $|\mathrm{JVF}| > 0.75$ is applied. The JVF is a jet property that allows for the identification and selection of jets originating from the hard scattering through the use of tracking and vertexing information.[22] By combining tracks and their primary vertices with calorimeter jets, a discriminant is defined, the JVF, which measures the probability that a jet originated from a particular vertex, e.g. the primary one: Here, the JVF is the fraction of tracks of the jet that can be associated with the primary vertex of the event. Jet selection based upon this discriminant is shown to be insensitive to the contributions from simultaneous uncorrelated soft collisions that occur during in-time pile-up interactions.

To correct the MC w.r.t. the data, scale factors for the efficiencies of the jet reconstruction and the JVF cut need to be applied (see corresponding paragraphs in Sec. 4.4.3).

Missing Transverse Energy

$E_{\mathrm{T}}^{\mathrm{miss}}$ is the amount of energy corresponding to the total energy missing in the transverse plane in an event and thus is a measure for the transverse component of the neutrino momentum. In order to reject QCD multi-jet events in which no high-p_{T} neutrinos occur, the $E_{\mathrm{T}}^{\mathrm{miss}}$ is required to exceed a certain minimal value (see list of event level cuts below).

B-Tagging of Jets

To identify jets originating from b-quarks, the MV1 algorithm is used. For resulting b-tag weights larger than 0.905363, the jet is accepted as a b-jet candidate. This

[21] As an artefact of the jet calibration, jets are sometimes assigned unphysical negative energy values. In these cases, the extrapolation of the calibration to the region of phase space concerned is not trustworthy, and therefore these objects are disregarded in analyses.

[22] G. Facini. *ATLAS TWiki: Jet Vertex Fraction: Selecting jets in pile-up events using jet-vertex association.* Apr. 2012. URL: `https://twiki.cern.ch/twiki/bin/view/Main/JetVertexFraction`.

working point corresponds to a b-tag efficiency of 59.6 % [ATL11b; Hei12] [23]. The b-tagging is based upon track and vertex reconstruction in the inner detector and thus is restricted to the acceptance region of the inner tracking devices, leading to b-jets in the range $|\eta| < 2.5$. In order to gain more statistics in QCD multi-jet events, a working point of 0.0714225 with an increased b-tagging efficiency of 84.7 % is chosen on the jet-electron sample and the template subsequently rescaled in order to reflect the QCD fractions given in Tab. 4.3.

Event Level Cuts

In this study, the analysis in the electron as well as the muon channel is restricted to exclusive jet bins with two, three and four jets, respectively. The following event selection cuts are applied in this order:

- Events with noise bursts and data integrity errors in the LAr calorimeter are vetoed.
- The run-dependent EF trigger item listed in Tab. 4.1 must have accepted the event.
- The number of tracks of the primary vertex in the event must be at least five. This cut is applied in order to reject non-collision background events.
- Exactly one signal lepton candidate (electron or muon) according to the above definition is required. No second lepton of signal quality must be present in the event; this event veto rejects dileptonic backgrounds like some modes of $\mathrm{t\bar{t}}$ and Wt-channel production as well as Z+jets and diboson events.
- The selected signal lepton must be matched to the above trigger object within $\Delta R < 0.15$.
- The event is rejected if a selected electron and a muon satisfying all the cuts except the jet-muon overlap removal at $\Delta R = 0.4$ share a track.
- Events containing a "bad jet"[24] with $E_{\mathrm{T}} > 20\,\mathrm{GeV}$ are rejected.
- A minimum missing transverse energy of $E_{\mathrm{T}}^{\mathrm{miss}} > 30\,\mathrm{GeV}$ is required to reduce QCD multi-jets and Z+jets background contributions.
- There must be at least two good jet candidates, as defined above. According to the jet bin in question, the number of jets is fixed to 2, 3 or 4 in this step.

[23] F. Filthaut. *ATLAS TWiki: B-Tagging Benchmarks*. Dec. 2012. URL: `https://twiki.cern.ch/twiki/bin/viewauth/AtlasProtected/BTaggingBenchmarks`.

[24] "Bad jets" are jets not associated with real energy depositions in the calorimeter; they arise from hardware deficiencies like noisy calorimeter cells or non-collision beam background as well as cosmic ray showers.

- The transverse mass of the W-boson can be reconstructed from the signal lepton and the missing transverse energy according to

$$\begin{aligned} m_{\mathrm{T}}^{\mathrm{W}} =& \sqrt{(E_{\mathrm{T}}^{\mathrm{W}})^2 - (\vec{p}_{\mathrm{T}}^{\,\mathrm{W}})^2} \\ =& \sqrt{(E_{\mathrm{T}}^{\mathrm{miss}} + E_{\mathrm{T}}^{\ell})^2 - (\vec{E}_{\mathrm{T}}^{\mathrm{miss}} + \vec{p}_{\mathrm{T}}^{\,\ell})^2} \\ \overset{m_\nu=0=m_\ell}{=}& \sqrt{2\, p_{\mathrm{T}}^{\ell} E_{\mathrm{T}}^{\mathrm{miss}} (1 - \cos(\phi^{\ell} - \phi^{E_{\mathrm{T}}^{\mathrm{miss}}}))}\,, \end{aligned} \tag{4.17}$$

  where m_ν denotes the mass of the neutrino associated with the $E_{\mathrm{T}}^{\mathrm{miss}}$ which can be set to zero when compared to m_{W}, just like the lepton mass m_ℓ. Now, the transverse mass of the W boson must satisfy $m_{\mathrm{T}}^{\mathrm{W}} > 30\,\mathrm{GeV}$. This cut mainly reduces the number of selected QCD multi-jets and Z+jets events.

- At least one of the selected jets must be b-tagged according to the definition of b-jet candidates given above. This requirement mainly rejects W in association with light flavour jets. Additionally, the number of b-jets is restricted to be exactly one in order to reject $\mathrm{t\bar{t}}$ signatures.

- The scalar sum H_{T}, defined in Eq. (4.14), must satisfy $H_{\mathrm{T}} > 160\,\mathrm{GeV}$ for the 2-jet bin (this cut is not applied in the 3- and 4-jet bin). This requirement cuts away only W+jets and QCD multi-jets events, as can be seen in Fig. 4.13e for the electron channel in the 2-jet bin.

The selected sample resulting from applying all the above cuts up to the b-tag requirement is referred to as the *pretag* sample in the following as opposed to the *tag* sample that includes all the cuts of the *pretag* sample as well as the subsequent requirement of exactly one b-jet in the event.

4.4.3. Scale Factors for Event Reweighting

After having applied all preselection cuts, the MC events are reweighted according to the kind of selected objects they contain; this is done in order to match object-specific selection efficiencies in MC to those in data.

Electrons

In order to correct the electron reconstruction, identification and trigger efficiencies in MC simulation to those in data, scale factors $\epsilon_{\mathrm{data}}/\epsilon_{\mathrm{MC}}$ are applied to all events in the MC samples. The reconstruction and trigger efficiency scale factors are measured with the so-called "tag-and-probe method" [ATL12f] on a $\mathrm{Z} \to e^+e^-$ sample for 9 and 18 bins in η, respectively. The identification efficiency scale factor associated with the "tight" electron selection is derived from combined $\mathrm{Z} \to e^+e^-$ and $\mathrm{W} \to e\nu$ samples in 9 η bins. Still another scale factor, also measured on a $\mathrm{Z} \to e^+e^-$ sample, is utilized to correct the efficiency of the electron isolation cut in the "tight" selection; this scale factor is computed using 18 η and 8 E_{T} bins, and depends on pile-up effects,

the underlying event model as well as the production process (W/Z boson or top quark). The overall scale factor of an event amounts to the product of the individual scale factors of the signal electron.

Muons

Also in the muon case, scale factors for the reconstruction, identification and trigger efficiencies as well as for the efficiency of the muon isolation cut are applied to the MC events. They originate from "tag-and-probe" measurements performed on $Z \to \mu^+\mu^-$ samples. The trigger efficiency is parametrized in η and ϕ of the muon, and is split into the three different run periods B-I, J-K and L-M (cp. Tab. 4.1). Again, the overall scale factor of a MC event amounts to the product of the individual scale factors of the signal muon.

Jets

For jets, two different kinds of scale factors are employed: one for the calorimeter jet reconstruction efficiency and four for the JVF cut efficiency. The jet reconstruction efficiency scale factor was derived by applying a "tag-and-probe" technique on minimum bias[25] and QCD dijet events:[26] Jets are firstly reconstructed from tracks and the highest p_T track-jet is taken to be the "tag" jet (which must have $p_T > 15\,\text{GeV}$) and matched to a calorimeter jet within $\Delta R < 0.4$; a track-jet in the opposite event hemisphere ($\Delta\phi \geq 2.8$) then acts as the "probe" jet. The reconstruction efficiency is defined as the fraction of "probe" jets that could be matched to a calorimeter jet; the difference between the efficiency values in data and MC is applied to MC events by discarding jets at random with the corresponding probability. Regarding the p_T dependent scale factor for the JVF > 0.75 cut efficiency, two efficiency and two inefficiency factors are considered, derived from a comparison of $Z \to e^+e^-$ and $Z \to \mu^+\mu^-$ data and MC events:[27]

- A scale factor $K^{\epsilon,\text{HS}}$ for the efficiency of selecting hard-scatter jets, applied to jets matched to a hard-scatter truth jet and passing the JVF cut,
- A scale factor $K^{\text{i,HS}}$ for the inefficiency of selecting hard-scatter jets (i.e. a hard-scatter jet is misclassified as pile-up jet), applied to jets not matched to a hard-scatter truth jet but passing the JVF cut,
- A scale factor $K^{\epsilon,\text{PU}}$ for the efficiency of rejecting pile-up jets, applied to jets not matched to a hard-scatter truth jet and not passing the JVF cut,

[25] The term "minimum bias" denotes events with no bias from restricted trigger conditions.

[26] N. Ghodbane. *ATLAS TWiki: Top Jet Reconstruction Efficiency*. Jan. 2012. URL: `https://twiki.cern.ch/twiki/bin/viewauth/AtlasProtected/TopJetReconstructionEfficiency`.

[27] M. Owen. *ATLAS TWiki: Top Common Scales 2011*. July 2012. URL: `https://twiki.cern.ch/twiki/bin/viewauth/AtlasProtected/TopCommonScales2011`; K. J. Grahn. *ATLAS TWiki: Jet Recommendations for R17 Analyses*. Oct. 2012. URL: `https://twiki.cern.ch/twiki/bin/viewauth/AtlasProtected/TopJetLiaisonR17Recommendations`.

- A scale factor $K^{\mathrm{i,PU}}$ for the inefficiency of rejecting pile-up jets (i.e. a pile-up jet is misclassified as hard-scatter jet), applied to jets matched to a hard-scatter truth jet but not passing the JVF cut.

The final event weight, applied to MC events, then consists of the product of the scale factors assigned to all respective jets in the event.

B-Tagging of Jets

Also the efficiency of correctly tagging a jet as a b-jet needs to be calibrated in MC to match the situation in data; a further tagging efficiency is formulated for the b-tagging of jets containing charm-quarks as well as a mistagging efficiency, defined via the probability for tagging light flavour jets (from gluons or u-, d-, s-quarks) mistakenly as b-jets. Firstly, the b-tag, c-tag and mistag efficiencies $\epsilon_{\mathrm{b}}^{\mathrm{data}}$, $\epsilon_{\mathrm{c}}^{\mathrm{data}}$ and $\epsilon_{\mathrm{mistag}}^{\mathrm{data}}$ (as well as the corresponding inefficiencies $(1 - \epsilon_{\mathrm{b/c/mistag}}^{\mathrm{data}})$) are estimated by applying the b-tagging algorithm to dedicated data samples; the data samples used for the calibrations are enriched in QCD multi-jets [ATL12h], muons [Bou+12] or $\mathrm{t\bar{t}}$ [ATL12n; Hei12] signatures and in D^* mesons for the c-tag part [ATL12e], and different calibration methods are employed, respectively [ATL11b]. Then, the efficiencies are compared to their counterparts from MC samples[28], $\epsilon_{\mathrm{b}}^{\mathrm{MC}}$, $\epsilon_{\mathrm{c}}^{\mathrm{MC}}$ and $\epsilon_{\mathrm{mistag}}^{\mathrm{MC}}$, yielding b-tag, c-tag and mistag efficiency scale factors

$$\kappa_{\epsilon_{\mathrm{b/c/mistag}}}^{\mathrm{MC}\to\mathrm{data}} = \frac{\epsilon_{\mathrm{b/c/mistag}}^{\mathrm{data}}}{\epsilon_{\mathrm{b/c/mistag}}^{\mathrm{MC}}} \tag{4.18}$$

for the reweighting of MC events, dependent on the jet's p_{T} and η. The inefficiency scale factors are obtained in an analogous way. The scale factors of Eq. (4.18) are found to be independent of the MC sample type. In each MC event, each b-tagged jet is assigned the applicable (b-tag, c-tag or mistag) efficiency scale factor corresponding to its true flavour content and its kinematics, while each untagged jet is assigned the applicable inefficiency scale factor. The MC event is then reweighted by the product of the scale factors of all selected jets.

Pile-Up

A pile-up reweighting of MC events is necessary since MC samples are generated only with an estimated average number of pile-up interactions μ_{MC}. However, the average number of pile-up interactions in real data, μ_{data}, varies not only between ATLAS data-taking runs but even between the smaller intervals of lumi blocks (cp. Sec. 3.2.1). To model the pile-up conditions more accurately, the MC events must be reweighted such that the actual pile-up distribution measured during data-taking is matched. This is achieved by multiplying the MC event weight with an appropriate correction factor. This factor is computed by comparing the μ distributions from data

[28] The true jet flavour in MC is defined by matching the jet's constituents to generator level partons.

and MC: The distribution of the number of pile-up interactions in data corresponds to the distribution of μ_{data}, averaged over all bunch crossings (BC) in a lumi block (LB), i.e. $\langle\mu_{\text{data}}\rangle_{\text{LB,BC}}$. Hence, the data distribution differs between data-taking runs and data-taking periods. For all MC samples, in contrast, a fixed predefined $\langle\mu_{\text{MC}}\rangle$ distribution exists. Now, to mirror the division of the complete data sample into run periods, each event in a MC sample is assigned to one particular run period in data; this is done in the correct proportion, i.e. according to the ratios of luminosities of the data run periods. Thus, each MC event now carries a value of $\langle\mu_{\text{MC}}\rangle$ and a value of the run period. The pile-up weight of a certain MC event with a value $\langle\mu_{\text{MC}}\rangle = m$ and a data period P is then calculated as the product of a "period weight" and a "period-wise μ weight",

$$W_{\text{pile-up}} = W_{\text{period}} \cdot W_{\mu} = \frac{\mathscr{L}_P/\mathscr{L}}{N_P/N} \cdot \frac{\mathscr{L}_m/\mathscr{L}_P}{N_m/N_P}\,, \tag{4.19}$$

where $\mathscr{L}_m$ is that fraction of the data luminosity that has $\langle\mu_{\text{data}}\rangle_{\text{LB,BC}} = m$ and belongs to period P, $\mathscr{L}_P$ is the total data luminosity of period P and $\mathscr{L}$ is the luminosity of the complete data sample. N_m, N_P and N denote the number of events in the MC sample with $\langle\mu_{\text{MC}}\rangle = m$ and belonging to period P, the total number of MC events assigned to period P and the complete number of MC events in the sample, respectively.

4.4.4. Control Distributions

In this section, the effects of the event preselection and reweighting depicted in the last sections are visualized via corresponding control distributions. Two stages of the preselection are considered: the *pretag* and the *tag* sample (defined in Sec. 4.4.2).

Normalization of MC Histograms and Treatment of Statistical Errors

In order to compare the data distribution to the prediction from MC, the MC histograms of all processes need to be normalized to the total integrated luminosity $\mathscr{L}_{\text{data}}$ of the data sample. This is achieved by scaling the number of entries $N_{\text{MC},i}$ of the MC histograms of each process i according to

$$N^{\text{norm}}_{\text{MC},i} = N_{\text{MC},i} \frac{\mathscr{L}_{\text{data}}}{\sigma_{\text{MC},i} \cdot N^{\text{sample}}_{\text{MC},i}} \tag{4.20}$$

where $N^{\text{norm}}_{\text{MC},i}$ denotes the normalized number of entries, $\sigma_{\text{MC},i}$ is the MC cross-section of the respective process and $N^{\text{sample}}_{\text{MC},i}$ is the total number of simulated events of this MC sample. The sum $\sum N^{\text{norm}}_{\text{MC},i}$ of all MC histograms is then compared to the data histogram. The uncertainties of the bin entries are computed as follows: If the Poisson-distributed number of entries is large enough, its uncertainty is taken to be the width of the Poisson distribution, $\Delta N_{\text{MC}} = \sqrt{N_{\text{MC}}}$, yielding a symmetrical error. If the

number of bin entries is rather low, the uncertainties are estimated by the Feldman-Cousins method [FC98] which allows for asymmetrical errors, avoiding unphysical error-intervals that exceed the domain of the variable in question. For ever larger numbers of bin entries, the Feldman-Cousins errors become Poissonian/Gaussian, and in this study, 33 bin entries were chosen as a suitable threshold for the transition. Once computed, the errors are scaled according to Eq. (4.20) to yield $\Delta N^{\text{norm}}_{\text{MC},i}$. The total uncertainty of the stacked MC histograms in each bin then follows from simple error propagation:

$$\Delta N^{\text{total}}_{\text{MC}} = \sqrt{\sum_i (\Delta N^{\text{norm}}_{\text{MC},i})^2}\,. \tag{4.21}$$

Throughout this study, the error $\Delta N^{\text{total}}_{\text{MC}}$ is denoted by the pink hatched areas above the stacked histograms of all MC samples. Rarely, there are zero entries of at least one MC process in a particular bin which results in a large bin error (see e.g. Fig. 4.9a).

Pretag Control Distributions

The *pretag* control distributions of $E_{\text{T}}^{\text{miss}}$ and m_{T}^{W} are given here for the electron channel in the 2-jet bin representative of the other channels of the analysis (for the lepton and jet kinematics as well as the $E_{\text{T}}^{\text{miss}}$ azimuthal angle in the pretag selection in the 2 jet bin, see App. A). The magnitude of the missing transverse energy as well as the transverse mass of the W boson serve as control distributions for the W+jets scale factor estimation detailed in Sec. 4.3.2 and are given in Fig. 4.8. The signal and background MC samples, including W+jets, are normalized to their cross-sections according to Tab. 4.2, as described in the previous paragraph; the QCD multi-jets part is normalized according to the fractions listed in Tab. 4.3. However, the sum of all MC samples has been subsequently scaled with an overall factor ($f^{\text{e,2 jets}}_{\text{norm,pretag}} = 1.17$) to best fit the data yield since no W+jets scale factors were extracted for the *pretag* yields in this study; these scale factors were solely derived for normalizing W+jets in the *tag selection* to data (cp. Sec. 4.3.2). As can be seen from the figures, the pretag region is dominated by W+jets processes. The sum of the signal and background samples fits the shape of the data distribution well.

Tag Control Distributions

The control distributions for the *tag selection* are also only shown for the electron channel in the 2-jet bin here, representative of all other analysis channels. However, the signal muon kinematics from the muon channel in the 2-jet bin are displayed as well. As in the *pretag* case, all MC samples are normalized to the data luminosity, utilizing the cross-sections listed in Tab. 4.2, whereas the data-driven QCD multi-jets estimate is normalized according to Tab. 4.3. In contrast to the *pretag* case, however, the W+jets contributions are now normalized with the proper W+jets scale factors for the yields in the *tag selection*, given in Tab. 4.5, that were determined from the data-driven method.

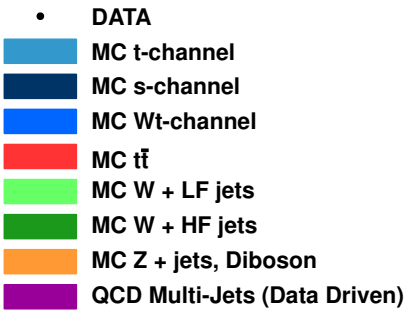

(a) Legend

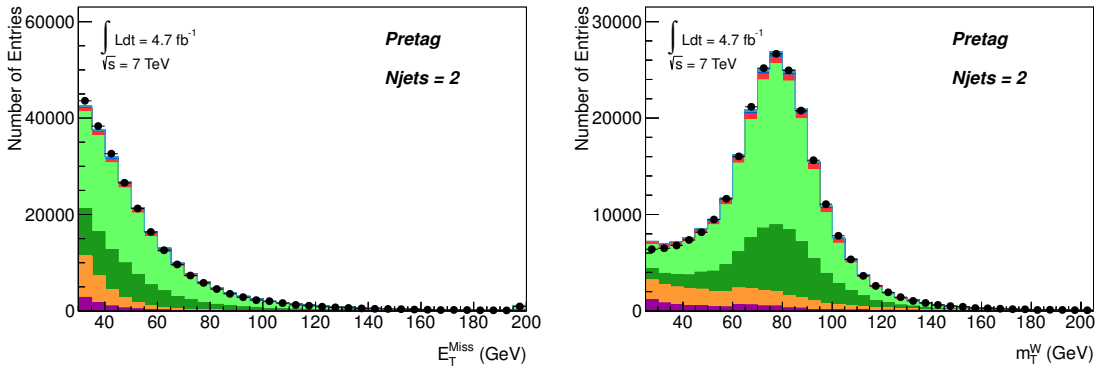

(b) $E_{\mathrm{T}}^{\mathrm{miss}}$ magnitude **(c)** $m_{\mathrm{T}}^{\mathrm{W}}$

Figure 4.8. Magnitude of $E_{\mathrm{T}}^{\mathrm{miss}}$ (b) and transverse W boson mass $m_{\mathrm{T}}^{\mathrm{W}}$ (c) in the *pretag selection* for the electron channel in the 2-jet bin. The signal and background samples are scaled to fit the data distribution.

The signal lepton kinematics in form of p_{T}, η and ϕ are shown in Fig. 4.9 for the electron and in Fig. 4.10 for the muon channel. Requiring a minimum b-tag weight of 0.905363 for b-jet candidates (cp. Sec. 4.4.2), the list of jets is now split into b-jets and non-b-jets; the b-tag weight distribution from the *pretag selection* is shown in Fig. 4.11e where also the b-tag weight cut is indicated. As can be seen, the b-tag requirement mainly reduces W+jets processes with light flavour jets. The kinematics of the selected b-jets (one per event in the 2-jet bin) are displayed as well in Fig. 4.11 as E_{T}, η and ϕ distributions. In Fig. 4.12, the kinematics of the selected non-b-jets (also one per event in the 2 jet bin) are shown. The magnitude of the missing transverse energy and its ϕ angle are depicted in Fig. 4.13 along with the transverse mass of the W boson which serves as control distribution for the W+jets scale factor estimation; additionally, the distribution of the cut variable H_{T} is shown in this figure. Here, the cut that is applied, $H_{\mathrm{T}} > 160\,\mathrm{GeV}$, is marked with an exclusion graph and it is clearly visible, as mentioned in Sec. 4.4.2, that it almost only rejects W+jets and QCD multi-jets events. Also in the *tag* sample, the sum of the signal and background samples reflects the shape of the data distribution well.

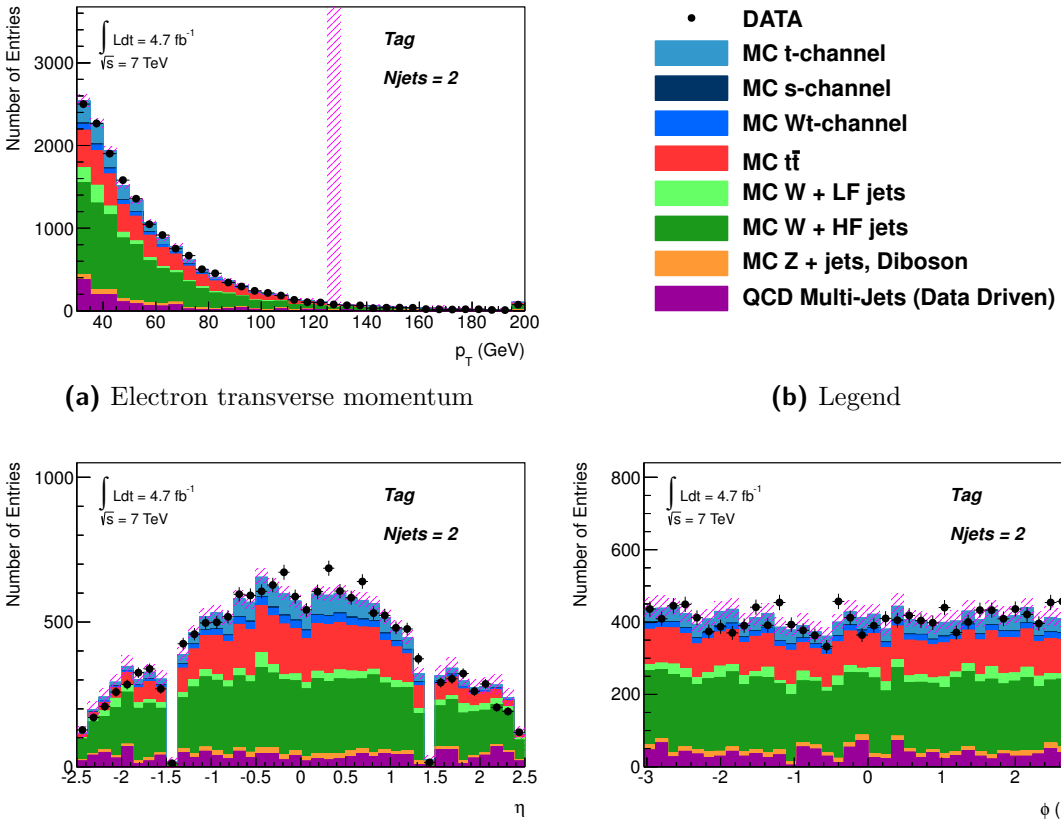

(a) Electron transverse momentum

(b) Legend

(c) Electron pseudorapidity

(d) Electron azimuth

Figure 4.9. Signal lepton kinematics in the *tag selection* for the electron channel in the 2-jet bin. The signal and background samples are normalized to the data luminosity. In (a), the bin of highest p_{T} includes the overflow count. The cut-out region in (c) corresponds to the crack region $1.37 < |\eta_{\mathrm{cluster}}| < 1.52$ in the EMCAL (cp. Sec. 3.2.4).

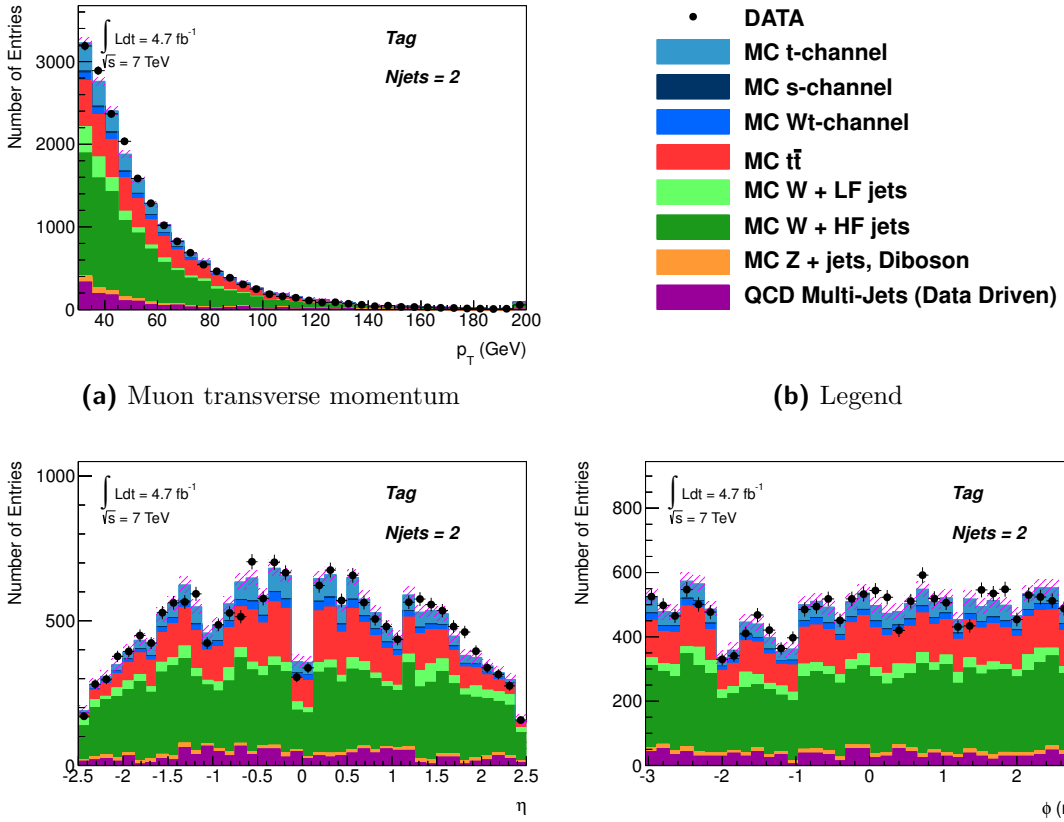

(a) Muon transverse momentum

(b) Legend

(c) Muon pseudorapidity

(d) Muon azimuth

Figure 4.10. Signal lepton kinematics in the *tag selection* for the muon channel in the 2-jet bin. The signal and background samples are normalized to the data luminosity. In (a), the bin of highest p_{T} includes the overflow count. The η-symmetrical dips in (c) correspond to cracks in the geometrical acceptance of the ID and the MS systems. The drop in (d) in the range $-1 < \phi < -2$ originates from the lower support structure of the ATLAS detector.

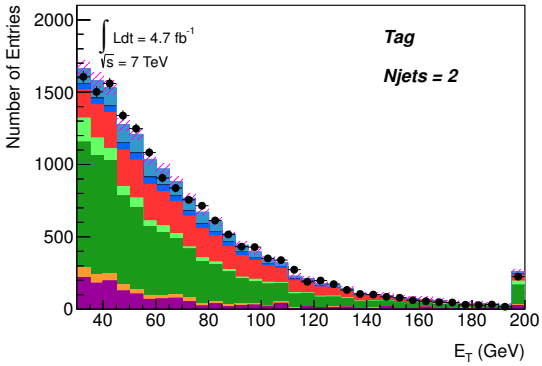

(a) B-jet transverse energy

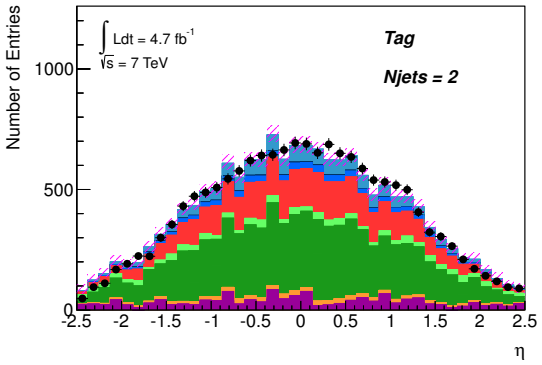

(b) B-jet pseudorapidity

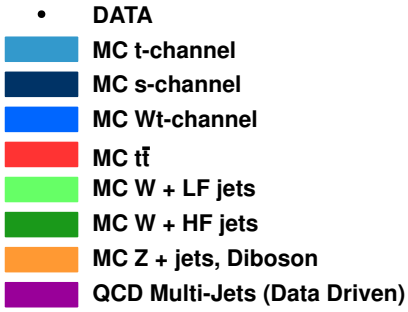

(c) Legend

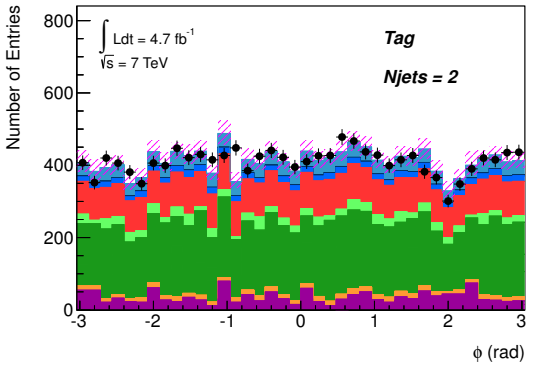

(d) B-jet azimuth

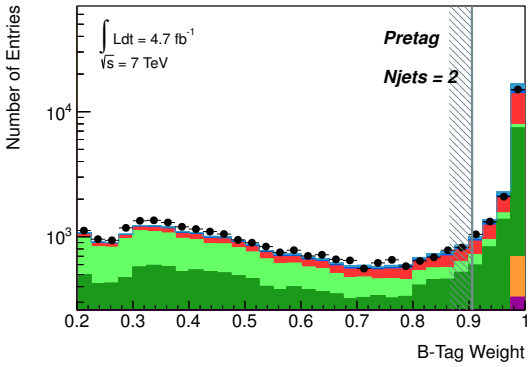

(e) B-tag weight

Figure 4.11. Kinematics of b-jets (a), (b), (d), in the *tag selection* and b-tag weight distribution of all selected jets (e) in the *pretag selection* for the electron channel in the 2-jet bin. The signal and background samples are scaled to fit the data distribution in the *pretag* case and normalized to the data luminosity in the *tag* case. In (a), the bin of highest E_{T} includes the overflow count. The exclusion graph in (e) illustrates the b-tag weight cut.

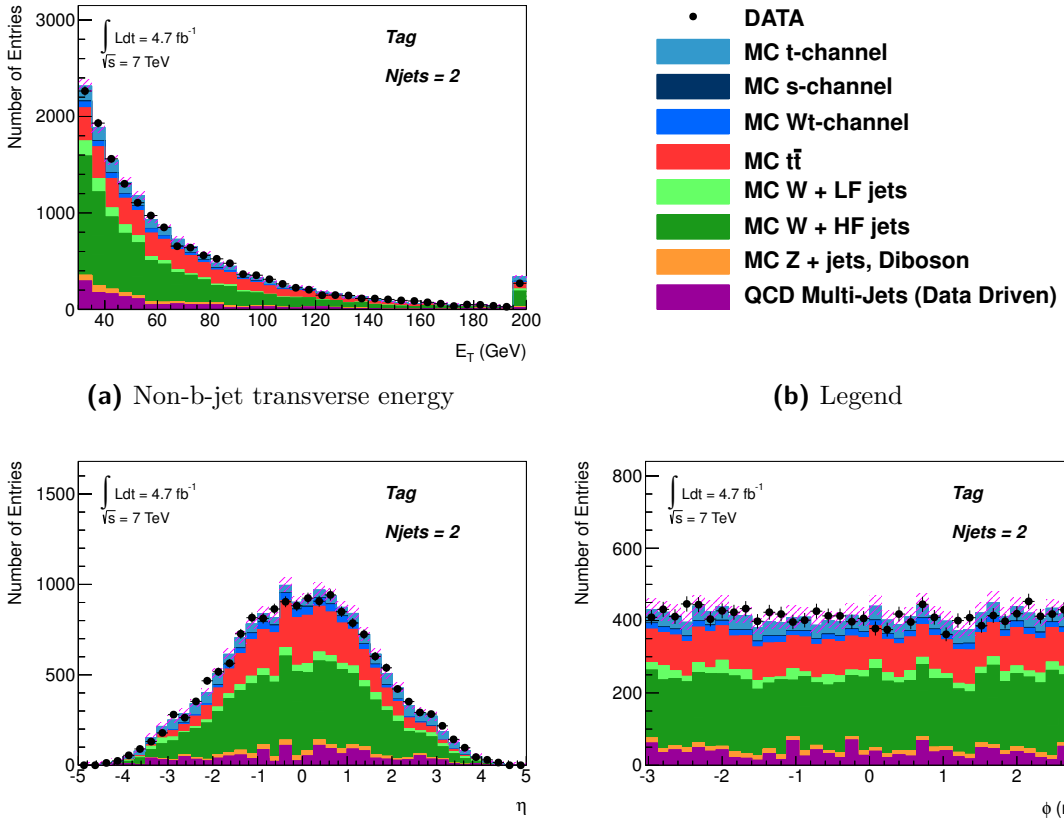

(a) Non-b-jet transverse energy

(b) Legend

(c) Non-b-jet pseudorapidity

(d) Non-b-jet azimuth

Figure 4.12. Kinematics of non-b-jets in the *tag selection* for the electron channel in the 2-jet bin. The signal and background samples are normalized to the data luminosity. In (a), the bin of highest E_{T} includes the overflow count.

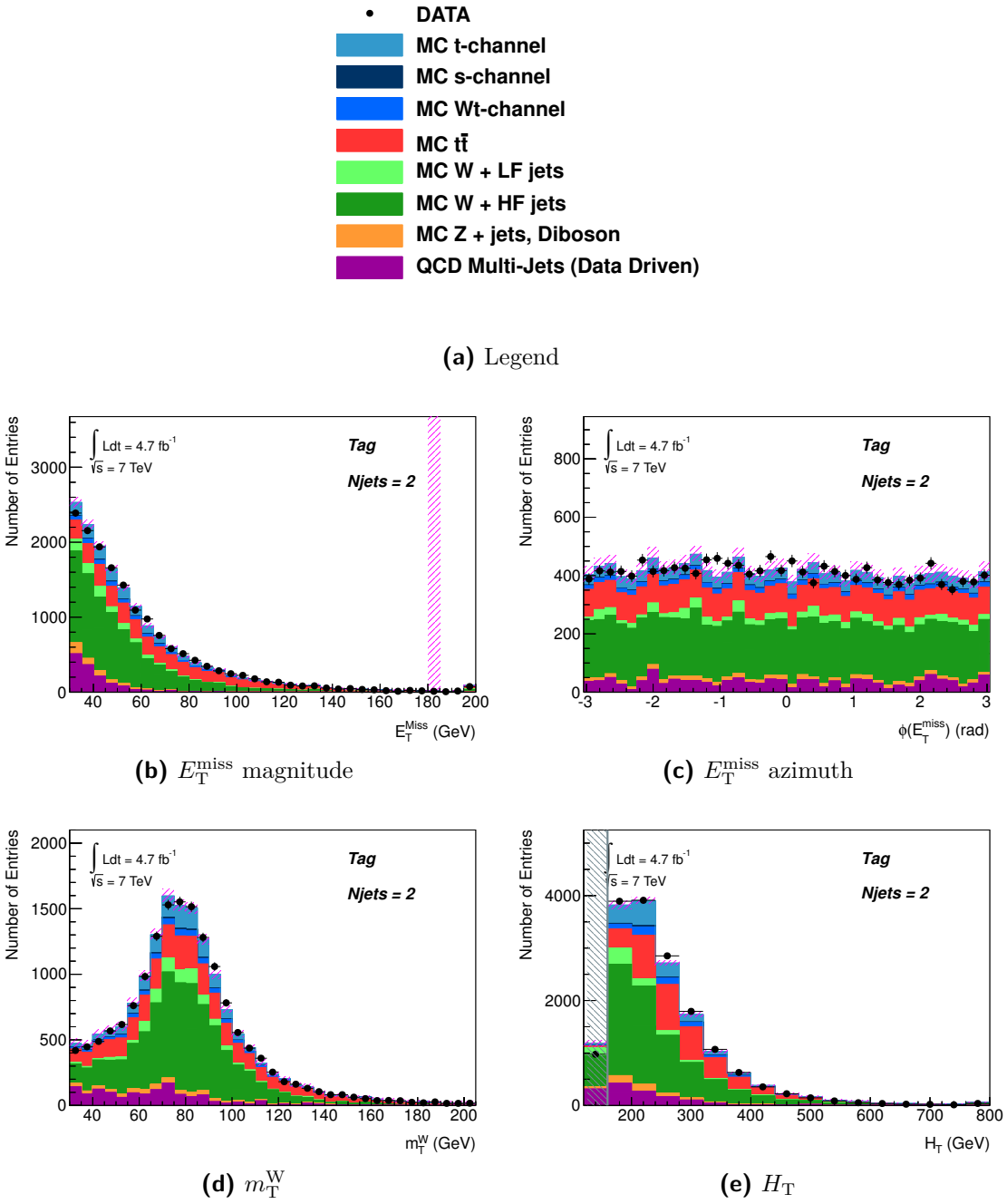

(a) Legend

(b) $E_{\mathrm{T}}^{\mathrm{miss}}$ magnitude

(c) $E_{\mathrm{T}}^{\mathrm{miss}}$ azimuth

(d) $m_{\mathrm{T}}^{\mathrm{W}}$

(e) H_{T}

Figure 4.13. Magnitude and azimuthal angle of $E_{\mathrm{T}}^{\mathrm{miss}}$ (b), (c), and transverse W boson mass (d) and H_{T} (e) in the *tag selection* for the electron channel in the 2-jet bin. The signal and background samples are normalized to the data luminosity. In (b), the bin of highest $E_{\mathrm{T}}^{\mathrm{miss}}$ includes the overflow count. In (e), the analysis cut applied on H_{T} is marked with an exclusion graph.

Du wolltest Algebra,
und nun hast du vollauf.
Jules Verne, Reise um den Mond

5. Kinematic Fitting

This chapter is dedicated to describing the analysis method used in this study, a kinematic fit. In Sec. 5.1, the basics of the method are reviewed: Section 5.1.1 details the generic mathematical description of a least-squares fit with non-linear constraints while in Sec. 5.1.2, the concrete implementation of the method within the KinFitter framework is outlined. Section 5.2 then deals with the application of the method to the reconstruction of single-top events in the t-channel: After discussing the general concept of the analysis in Sec. 5.2.1, the derivation of the covariance matrices used as input to the kinematic fit is depicted in Sec. 5.2.2, and the complete analysis setup is described in Sec. 5.2.3 where also the relevant control distributions for judging the quality of the kinematic fitting analysis are presented.

5.1. The Kinematic Fitter

The kinematic fit performs a hypothesis test of a final state or a decay chain given the measured particle momenta in the final state. To start with, certain invariant masses of the decaying particles and the final state particles are assumed. These hypothesized particle identities then determine the kinetic energies of the outgoing particles. Other fit constraints can complement the invariant mass constraints, e.g. requirements on momentum conservation. Eventually, the hypothesis is accepted or declined according to the maximum likelihood of the fit, or in this case, the resulting minimal χ^2 value.

A kinematic fit is frequently used for the reconstruction of particle decays or decay chains. Not only is it capable of removing physical background originating from similar processes. By testing the fit hypothesis for all possible combinations of outgoing momenta, it is also able to substantially reduce combinatorial background: A subsequent comparison of the resulting χ^2 values allows to correctly assign the single objects. Beside the assignment of particle tracks, the fitter also corrects the momentum of each final state particle individually, which in turn reduces systematic errors. Furthermore, the kinematic fitter can be used to extend the measurement: Unmeasured momentum components of the final state particles can be determined by the fitter, provided that the number of constraints in the fitting procedure exceeds the number of unknown parameters.

The latter property is exploited in the kinematic reconstruction of single-top t-channel events: Here, the neutrino coming from the leptonically decaying W boson does not interact with the detector. The only information on the neutrino is contained in the missing transverse energy, and thus its polar angle is an unmeasured input

parameter in the fit. As will be shown, the fit is able to properly reconstruct this unknown variable.

5.1.1. Least Squares and Non-Linear Constraints

The fit method used here is presented in detail in [Lyo96]. In general, a kinematic fit is based upon n unbiased measurements $\{y_i\}_{i=1,2,\ldots,n}$ and p unmeasured parameters $\{a_j\}_{j=1,2,\ldots,p}$. It also relies on the covariance matrix of the measurements, denoted by $C_\mathbf{y}$ in the following.

According to the given model hypothesis, the fitter determines statistical estimators for the measurements $\mathbf{y}$ as well as solutions for the unmeasured parameters $\mathbf{a}$. The estimators to be found are supposed to better approximate the true values $\bar{\mathbf{y}}$ which are the expectation values of the measurements $\mathbf{y}$. Let $\bar{\mathbf{a}}$ be the true parameter values which are restricted by the m model-specific constraints via

$$f_k(\bar{\mathbf{a}}, \bar{\mathbf{y}}) = 0 \ , \quad k = 1, 2, \ldots, m \, . \tag{5.1}$$

Generally, the measurements deviate from $\bar{\mathbf{y}}$, and their corresponding variances are given by $C_\mathbf{y}$. Therefore, corrections $\mathbf{\Delta y}$ must be applied, ensuring that the sum $\mathbf{y} + \mathbf{\Delta y}$ fulfils the given constraints. At the same time, the deviations from the measurements are required to be small. For the simple case of uncorrelated measurements $C = \mathrm{diag}(\sigma_1^2, \ldots, \sigma_n^2)$ this can be achieved by minimizing the expression

$$\chi^2 = \sum_{i=1}^{n} \frac{(\Delta y_i)^2}{\sigma_i^2} = \mathbf{\Delta y}^T C_\mathbf{y}^{-1} \mathbf{\Delta y} \, . \tag{5.2}$$

However, for the general case the last term must be extended. If the measurements are correlated, i.e. the matrix $C_\mathbf{y}^{-1}$ is not diagonal, a linear transformation of the $\mathbf{y}$ along with the corresponding error propagation serves to diagonalize the matrix $C_\mathbf{y}$. The so transformed χ^2 is identical to that in Eq. (5.2).

Taking fit constraints into account, the minimization is more involved. One approach is to use Lagrangian multipliers λ_k:

$$L = \chi^2(\mathbf{y}) + 2 \sum_{k=1}^{m} \lambda_k f_k(\mathbf{a}, \mathbf{y}) \, . \tag{5.3}$$

Here, the Lagrange function L is the sum of the χ^2 function in Eq. (5.2) and the constraints in Eq. (5.1), multiplied by the factors λ_k.[1] The minimization of the χ^2 now requires the partial derivatives of L with respect to all y_i and λ_k to vanish. Also, since the χ^2 implicitly depends on the unmeasured parameters $\mathbf{a}$, the requirement $\partial L / \partial a_j = 0 \, \forall j$ is needed as well.

In case of linear constraints, this analytical approach solves the problem. In case of non-linear constraints, a solution must be obtained numerically. To this end,

[1] The factor 2 is by convention.

the constraints are linearized and the solutions iterated until either certain convergence criteria are met or the procedure is terminated unsuccessfully after too many iterations.

Let $\mathbf{y}_0$ and $\mathbf{a}_0$ denote the starting values of the iteration. Conveniently, the measurements themselves serve as $\mathbf{y}_0$. The starting values of the unmeasured parameters $\mathbf{a}_0$ have to be chosen in a meaningful way according to the problem at hand.

Let $\mathbf{y}^*$ and $\mathbf{a}^*$ denote the values after the preceding iteration and $\boldsymbol{\Delta}\mathbf{y}^* = \mathbf{y}^* - \mathbf{y}_0$ and $\boldsymbol{\Delta}\mathbf{a}^* = \mathbf{a}^* - \mathbf{a}_0$ the respective corrections. In the first iteration the corrections are $\boldsymbol{\Delta}\mathbf{y}^* = 0$ and $\boldsymbol{\Delta}\mathbf{a}^* = 0$. Furthermore, $\mathbf{y}$ and $\mathbf{a}$ are the values to be determined in the succeeding iteration. The respective corrections are given by $\boldsymbol{\Delta}\mathbf{y} = \mathbf{y} - \mathbf{y}_0$ and $\boldsymbol{\Delta}\mathbf{a} = \mathbf{a} - \mathbf{a}_0$. Thus, the linearized constraints become

$$\begin{aligned} f_k(\mathbf{a},\mathbf{y}) &\approx f_k(\mathbf{a}^*,\mathbf{y}^*) + \sum_{i=1}^{p} \frac{\partial f_k}{\partial a_i}(a_i - a_i^*) + \sum_{i=1}^{n} \frac{\partial f_k}{\partial y_i}(y_i - y_i^*) \\ &= f_k(\mathbf{a}^*,\mathbf{y}^*) + \sum_{i=1}^{p} \frac{\partial f_k}{\partial a_i}(\Delta a_i - \Delta a_i^*) + \sum_{i=1}^{n} \frac{\partial f_k}{\partial y_i}(\Delta y_i - \Delta y_i^*) \\ &= f^* + A(\boldsymbol{\Delta}\mathbf{a} - \boldsymbol{\Delta}\mathbf{a}^*) + B(\boldsymbol{\Delta}\mathbf{y} - \boldsymbol{\Delta}\mathbf{y}^*) \stackrel{!}{=} 0 \quad \forall k\,. \end{aligned} \tag{5.4}$$

Here, the matrices $A \in \mathbb{R}^{m\times p}$, $B \in \mathbb{R}^{m\times n}$ and the vector $\mathbf{f}^* \in \mathbb{R}^m$ are defined as

$$A_{ij} = \frac{\partial f_i}{\partial a_j}(\mathbf{a}^*,\mathbf{y}^*)\,, \quad B_{ij} = \frac{\partial f_i}{\partial y_j}(\mathbf{a}^*,\mathbf{y}^*)\,, \quad f_i^* = f_i(\mathbf{a}^*,\mathbf{y}^*)\,. \tag{5.5}$$

The vector $\mathbf{c} \in \mathbb{R}^m$ is

$$\mathbf{c} := A\boldsymbol{\Delta}\mathbf{a}^* + B\boldsymbol{\Delta}\mathbf{y}^* - f^*\,, \tag{5.6}$$

leading to a Lagrange function

$$L = \boldsymbol{\Delta}\mathbf{y}^T C_{\mathbf{y}}^{-1}\boldsymbol{\Delta}\mathbf{y} + 2\boldsymbol{\lambda}^T(A\boldsymbol{\Delta}\mathbf{a} + B\boldsymbol{\Delta}\mathbf{y} - \mathbf{c}) \tag{5.7}$$

with the vector of multipliers $\boldsymbol{\lambda}$. The requirements $\partial L/\partial y_i = \partial L/\partial \Delta y_i = 0$ as well as $\partial L/\partial a_j = \partial L/\partial \Delta a_j = 0$ and $\partial L/\partial \lambda_k = 0\ \forall\, i,j,k$ lead to a linear system of $n+p+m$ equations from which the corrections $\boldsymbol{\Delta}\mathbf{a}$, $\boldsymbol{\Delta}\mathbf{y}$ and $\boldsymbol{\lambda}$ can be obtained:

$$\begin{pmatrix} C_{\mathbf{y}}^{-1} & 0 & B^T \\ 0 & 0 & A^T \\ B & A & 0 \end{pmatrix} \begin{pmatrix} \boldsymbol{\Delta}\mathbf{y} \\ \boldsymbol{\Delta}\mathbf{a} \\ \boldsymbol{\lambda} \end{pmatrix} = \begin{pmatrix} 0 \\ 0 \\ \mathbf{c} \end{pmatrix}. \tag{5.8}$$

For convenience, the following matrices are defined:

$$C_B = (BC_{\mathbf{y}}B^T)^{-1}\,, \tag{5.9}$$

$$C_A = (A^T C_B A)\,. \tag{5.10}$$

The solution is then given by

$$\boldsymbol{\Delta}\mathbf{y} = C_{\mathbf{y}} B^T C_B (1 - A C_A^{-1} A^T C_B)\mathbf{c}\,, \tag{5.11}$$

$$\boldsymbol{\Delta}\mathbf{a} = C_A^{-1} A^T C_B \mathbf{c}\,, \tag{5.12}$$

$$\boldsymbol{\lambda} = C_B (A C_A^{-1} A^T C_B - 1)\mathbf{c}\,. \tag{5.13}$$

Furthermore, to compute the variances and correlations the following matrices are helpful:

$$C_{11} = \; C_{\mathbf{y}}(1 - B^T C_B B C_{\mathbf{y}} + B^T C_B A C_A^{-1} A^T C_B B C_{\mathbf{y}})\,, \tag{5.14}$$

$$C_{21} = -C_A^{-1} A^T C_B B C_{\mathbf{y}}\,, \tag{5.15}$$

$$C_{22} = \; C_A^{-1}\,. \tag{5.16}$$

The covariance matrix for the vector $(\mathbf{y}, \mathbf{a})$ then results from error propagation:

$$C_{(\mathbf{y},\mathbf{a})} = \begin{pmatrix} C_{11} & C_{21}^T \\ C_{21} & C_{22} \end{pmatrix}. \tag{5.17}$$

In order to ensure that the χ^2 function has reached a local minimum, convergence criteria must be formulated. Firstly, the value of the χ^2 function should stabilize and only vary by a small value ε_{χ^2} between consecutive iterations. At the same time, the constraints $f_k = 0$ must be fulfilled; to this end, the sum of all constraints is required to not exceed a small value ε_f. The complete convergence criteria are thus:

$$|\chi^2(\mathbf{y}) - \chi^2(\mathbf{y}^*)| < \varepsilon_{\chi^2}\,, \tag{5.18a}$$

$$\sum_{k=1}^{m} |f_k(\mathbf{a}, \mathbf{y})| < \varepsilon_f\,. \tag{5.18b}$$

This procedure represents the most general form of a least-squares approach. Its results are interpreted in terms of the χ^2 value computed as $\boldsymbol{\Delta}\mathbf{y}^T C_{\mathbf{y}}^{-1} \boldsymbol{\Delta}\mathbf{y}$. In the case of linear constraints and Gaussian distributed errors this variable follows a χ^2 distribution with $m - p$ degrees of freedom: In the application at hand, each particle's measured momentum component adds one degree of freedom to the fit, but since these n measurements are allowed to vary within their resolutions, they at the same time add fit parameters which reduce the number of degrees of freedom by one, respectively. Then again, the constraints provide additional information and thus give additional degrees of freedom whilst those are reduced by any unmeasured parameters.

This χ^2 distribution, however, is not expected to be unbiased, since real measurements are used for the fit that are subject to various systematic effects. Furthermore, the underlying model could be flawed. In order to judge the consistency of the fit results, the pull distributions of the input variables are considered. The pull is defined

as the normalized correction

$$p_i := \frac{\Delta y_i}{\sigma(\Delta y_i)} \,. \tag{5.19}$$

Here, the standard deviations $\sigma(\Delta y_i)$ of the corrections Δy_i are given by $\sigma(\Delta y_i) = \sqrt{(C_{\mathbf{y}} - C_{\mathbf{yo}})_{ii}}$. In an ideal fit that is perfectly consistent with the underlying model assumptions the pull distributions are expected to follow standardized Gauss distributions with mean at zero and a standard deviation of one.

5.1.2. The KinFitter Package

The fitting procedure described above is implemented in the KinFitter library [SG09] and written in C++ based upon the RooT [Ant+09] analysis framework. Whereas it is a part of the ATLAS software framework ATHENA, it can also run independently.[2] The KinFitter library offers several pre-defined constraints and particle parametrizations. It is thus well equipped to handling a vast number of event and decay topologies. The associated particles and their constraints have to be provided by the user. In Fig. 5.1, the basic scheme of the KinFitter library is depicted. For the computation of the corrections $\mathbf{\Delta y}$ and of the unknown parameters $\mathbf{a}$, the fitter requires the latest values of the constraints $\mathbf{f}(\mathbf{a}^*, \mathbf{y}^*)$ and of the matrices A und B in every iteration step. The partial derivatives of the constraints are obtained most conveniently in Cartesian coordinates $\{P_i\}_{i=1,\ldots,n}$. Since the particles are often parametrized differently, $\{y_i\}_{i=1,\ldots,n}$, the following transformation is in order:

$$\frac{\partial f_k}{\partial y_i} = \sum_{j=1}^{n} \frac{\partial f_k}{\partial P_j} \cdot \frac{\partial P_j}{\partial y_i} \,. \tag{5.20}$$

Since the partial derivatives $\partial f_k / \partial P_j$ are computed solely from the constraints and the $\partial P_j / \partial y_i$ solely from the parametrizations of the particles, the structure of the KinFitter library is split in a compact and flexible way as shown in Fig. 5.1: To start with, objects representing the particles and their constraints are constructed. From those, the partial derivatives and other necessary quantities are calculated. Eventually, all required information is passed on to a central fit object which in turn provides the final results. In detail, the iterative procedure is the following:

Step 1: The current values of the constraints $\mathbf{f}(\mathbf{a}^*, \mathbf{y}^*)$ are given to the fitter object.

Step 2: The derivatives $\partial f_k / \partial P_j$ of the constraints and the derivatives $\partial P_j / \partial y_i$, $\partial P_j / \partial a_i$ of the particles are computed and transferred to the fitter.

Step 3: The derivatives of the matrices A and B are calculated using the proper transformation.

[2] The version of the KinFitter library used in this study contains some improvements that are not yet part of the version included in ATHENA.

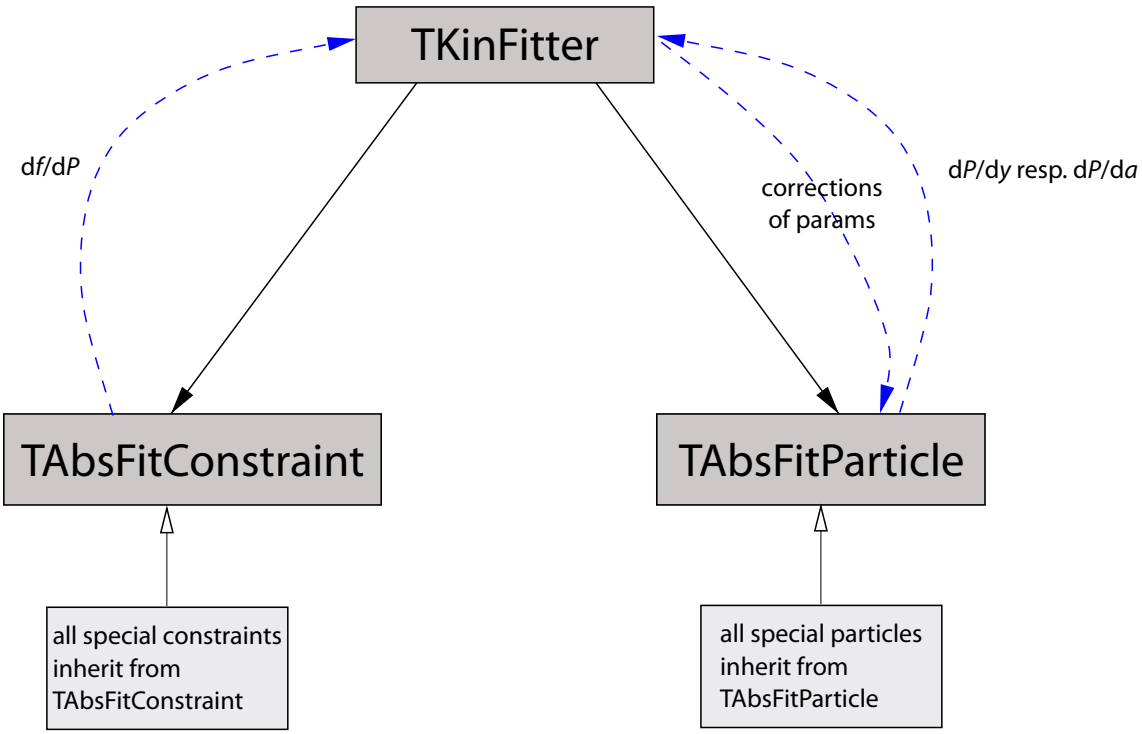

Figure 5.1. Scheme of the KinFitter software based on [SG09]. The constraints (of class TAbsFitConstraint) and particles (of class TAbsFitParticle) are realized as individual objects and connected to the central fit object (of class TKinFitter) that performs the actual fit: It obtains the derivatives of the constraints and the particles, performs all the matrix multiplications and calculates the corrections of the measured and unmeasured particle momenta. The corrections are then passed back to the particle, and the new four-vector is computed.

Step 4: The fitter evaluates the corrections $\mathbf{\Delta y}$ and $\mathbf{\Delta a}$. The only additional ingredient for this computation is the predefined covariance matrix $C_{\mathbf{y}}$ that is already loaded into memory at this stage. Finally, the new corrections are applied to the particles and the constraints.

Step 5: The fitter checks the convergence criteria. If they are not fulfilled the procedure is resumed with step 1.

As for the parametrizations, the particles' coordinates can be given e.g. in $(p_\mathrm{T}, \eta, \varphi)$ or $(p_\mathrm{T}, \vartheta, \varphi)$. Here, the fitter ensures that the value of p_T is always positive.[3]

The fit constraints in this study are all mass constraints. The fitter supports either a fixed mass or a mass distribution with finite width. The mass is implemented by an additional variable that is treated like a measurement during the fitting process. Its starting value is set to the most probable mass. For Gaussian mass distributions

[3] If a correction leads to a negative p_T value then the norm of the respective correction vector is halved until p_T becomes positive.

the mass constraint is given by

$$f_M(\mathbf{a},\mathbf{y}) = \|\sum_i p_i(\mathbf{a},\mathbf{y})\| - \alpha M \stackrel{!}{=} 0\,, \tag{5.21}$$

where the p_i denote the particle momenta while $\|\cdot\|$ indicates the corresponding invariant mass and M is the most probable mass. The variable α is then added quadratically to the χ^2 function, weighted with the relative mass width Γ/M:

$$\chi^2 = \cdots + \frac{(\alpha-1)^2}{(\Gamma/M)^2}\,. \tag{5.22}$$

Hence, the fitter prefers a value of α close to one which is equivalent to the most probable invariant mass M of the particle in question.

The KinFitter framework described has already successfully been applied in the reconstruction of several particle decay topologies such as the decay of the Z boson to charged leptons [Bil10], Λ^0 decays [Kin10], K^0_S [Beu10] and D^* decays [Sch10]. It was also employed to isolate a semi-leptonic $t\bar{t}$ signature [Tho11; Hei12]. The method was developed and tested for application to the single-top t- and Wt-channel in [Rie10] where a toy-MC study was performed to determine the method's efficiency. For any further information on the KinFitter's capabilities, see also [Beu+12].

5.2. Reconstruction of Single-Top Events

5.2.1. General Idea

In order to employ the method of kinematic fitting to reconstructing single-top events in the t-channel, the physical objects entering the fit need to be defined and their covariance matrices need to be provided. The covariance matrices are discussed in detail in Sec. 5.2.2. Furthermore, the fit constraints carrying the information about the hypothesis to be tested must be formulated.

The topology of a single-top t-channel event consists of a top quark and a light flavour quark in the final state (see Fig. 2.11a). Within the current standard model framework, the top quark decays almost exclusively into a W boson and a b-quark. In this analysis, only those channels are considered in which the W boson in turn decays to a charged lepton and a neutrino; a hadronically decaying W would result in an all-hadronic final state that is hard to discriminate against the overwhelming background originating from QCD multi-jet production.

At the detector level, the final state objects are thus a charged lepton and missing transverse energy from the neutrino, both associated with the W decay, that in combination with a b-jet originate from the top quark decay. Additionally, there is a light-flavour jet that is preferably situated in the forward region of the detector. In this study, only electrons and muons are selected as signal leptons.

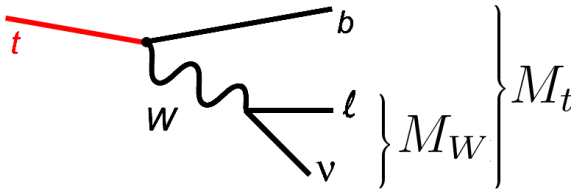

Figure 5.2. Reconstruction of the top quark by a kinematic fit with W boson and top quark mass constraints.

Of these final state objects, only the ones originating from the top quark decay are considered in this approach to a kinematic fit in the single-top t-channel: the charged lepton, the missing transverse energy and the b-jet. In this analysis, the forward jet does not enter the kinematic fit. The procedure therefore consists of fitting a top quark four-momentum with these three objects respecting the W boson and top quark mass constraints as indicated in Fig. 5.2. In the preselection described in Sec. 4.4 it is assumed that the charged lepton with the highest transverse momentum of the selected ones is the actual signal lepton, and a veto is placed on more than one lepton of signal quality in the event. Thus, the remaining combinatorial freedom is in choosing a b-jet from the list of all selected b-jets. Exploiting this freedom of choice in the fitting procedure means adding quite some combinatorics to be tested for the top quark decay. In fact, it turns out that fitting the top quark four-momentum with each b-jet in every event and then selecting the best combination as this event's top quark candidate does not yield considerable improvement over simply using the highest p_{T} b-jet. The latter is thus a viable choice for the treatment of b-jets in this analysis. Moreover, since the $\mathrm{t\bar{t}}$ contribution in events with at least two b-jets is clearly dominating the t-channel contribution, it is an obvious and time-saving simplification to even completely restrict oneself to events with exactly one b-tagged jet (see again Sec. 4.4). Another important reason for this restriction is to avoid an elaborate treatment of the systematic error of the b-tagging scale factors (cp. Sec. 6.1.2) that would be necessary due to the interplay of the scale factors associated with multiple b-jets in an event.

For the resulting combination of the signal lepton and the transverse missing energy with the selected b-jet, the top quark fit determines a total χ^2. If the fit shows convergence, the combination is accepted as a top quark candidate. By requiring the p-value (cp. Eq. (5.37)) associated with this χ^2 to exceed a certain threshold, signal-like events can be enriched in the final selection. For the single-top t-channel, the kinematic fit returns a χ^2 with one degree of freedom (NDoF = 1) due to two mass constraints (W boson and top quark) and one unknown parameter (p_{z} of the neutrino), as explained in Sec. 5.1.1. Since the kinematic fit eventually determines the full four-momenta of the fit objects, the neutrino p_{z} component can be reconstructed by this method.

5.2.2. Covariance Matrices

The covariance matrices carry the information within which range the kinematic fit may vary the four-momentum components. Thus, the covariance matrices of all fit objects, the electron or muon, the jets and the $E_{\mathrm{T}}^{\mathrm{miss}}$, need to be known. For the leptons, the covariance matrices are already provided by the track fit of the ATLAS reconstruction; they need to be transformed to another coordinate system to be compatible with the requirements of the KinFitter framework, though. For jet and $E_{\mathrm{T}}^{\mathrm{miss}}$ covariances, the situation is entirely different from a simple track fit, since jets and the $E_{\mathrm{T}}^{\mathrm{miss}}$ are composite objects first defined in the ATLAS reconstruction step; no covariances for them are supplied by the reconstruction. Therefore, the jet and $E_{\mathrm{T}}^{\mathrm{miss}}$ covariance matrix elements need to be computed on a statistical basis from a comparison of true and reconstructed physics objects in MC samples.

Covariances of Leptons

For the lepton, the track and its covariances from the ATLAS reconstruction are described by the helix parameters (d_0, z_0, θ, ϕ, q/p), where q/p is the ratio of the track's charge and its momentum, and d_0, z_0 were defined in Sec. 3.3.2. The kinematic fitter, however, uses a different parametrization, i.e. (p_{T}, η, ϕ). Therefore a momentum vector $\vec{x}$ of the former coordinate system has to be transformed to $\vec{y}$ in the latter coordinate system with some function $\vec{y} = f(\vec{x})$. A Taylor expansion around the measurement $\vec{\hat{x}}$,

$$y_i = f_i(\vec{\hat{x}}) = T_{ij}(x_j - \hat{x}_j) + \mathcal{O}(T^2)\,, \tag{5.23}$$

yields, by neglecting all higher order terms,

$$\vec{y} = \mathrm{const} + T\vec{x}\,. \tag{5.24}$$

The constant terms are eliminated for the covariances

$$C_{y_{ij}} = \mathrm{E}[(y_i - \hat{y}_i)(y_j - \hat{y}_j)]\,, \tag{5.25}$$

such that

$$C_{\vec{y}} = TC_{\vec{x}}T^T \tag{5.26}$$

follows. The transformation matrix T is defined as $T_{ij} = \partial y_i/\partial x_j$. Its explicit form is

$$T = \begin{pmatrix} -\frac{q}{\pi^2}\sin\theta & \frac{q}{\pi^2}\cos\theta & 0 \\ 0 & -\frac{1}{\sin\theta} & 0 \\ 0 & 0 & 1 \end{pmatrix} \tag{5.27}$$

with $\pi = q/p$. The resulting transformation equations are then given by

$$\eta = -\ln(\tan(\theta/2))\,, \tag{5.28}$$

$$p_{\mathrm{T}} = \frac{q}{\pi}\sin\theta\,, \tag{5.29}$$

$$\phi = \phi\,. \tag{5.30}$$

For each track, all helix parameters and the covariance matrix can be retrieved from its track fit results. One should keep in mind that the helix parameters are given with respect to a certain reference point. For vertex-fitted tracks this is either the primary or secondary vertex, for tracks without a vertex constraint this is usually the point of closest approach to the beam-line.

For one of the background samples used in this analysis, no lepton covariance matrices from a track fit exist: This is the jet-electron sample (cp. Sec. 4.3.1). Since in this fake-lepton estimate, jets replace the genuine leptons, the lepton (co)variances have to be sampled at random according to some template distributions derived from data. To this end, the procedure depicted in [Bil12] is adopted: The single elements of the covariance matrix of track fit coordinates

$$C_x = \begin{pmatrix} \mathrm{Cov}(p_{\mathrm{T}}, p_{\mathrm{T}}) & \mathrm{Cov}(p_{\mathrm{T}}, \eta) & \mathrm{Cov}(p_{\mathrm{T}}, \phi) \\ \mathrm{Cov}(p_{\mathrm{T}}, \eta) & \mathrm{Cov}(\eta, \eta) & \mathrm{Cov}(\eta, \phi) \\ \mathrm{Cov}(p_{\mathrm{T}}, \phi) & \mathrm{Cov}(\eta, \phi) & \mathrm{Cov}(\phi, \phi) \end{pmatrix} \tag{5.31}$$

are histogrammed for electrons and muons on the complete data sample (cp. Sec. 4.1). The resulting distributions are fitted either to a Gaussian

$$f_{\mathrm{Gauss}}(x) = N_0 \exp\left[-0.5\left(\frac{x - x_0}{\sigma}\right)^2\right] \tag{5.32}$$

or to a Landau function

$$f_{\mathrm{Landau}}(x) = N_0 \int_0^\infty \exp\left[-t\ln t - \frac{x - x_0}{\sigma}t\right]\sin(\pi t)\,\mathrm{d}t \tag{5.33}$$

to determine the parameters x_0, σ and N_0. The distributions are then normalized to unity and serve as probability densities from which the required (co)variances are drawn at random for each kinematic fitting procedure. A detailed account of the single distributions and their parameters for electrons and muons as well as a direct comparison to the original data distributions is also given in [Bil12].

Covariances of Jets and Missing Transverse Energy

Since the jets and the $E_{\mathrm{T}}^{\mathrm{miss}}$ are complex objects in the reconstruction, it is impossible to extract their covariance matrices directly from the data. As opposed to the case of electrons and muons, for which the covariance matrices are obtained from the parameters of the track fits in data (see section 5.2.2), for the jets and the $E_{\mathrm{T}}^{\mathrm{miss}}$

case they must be evaluated on a statistical basis from MC samples. The need of simulation input implies that the modelling of the covariance matrices is to some extent arbitrary and not unambiguous. The choices made at this level of the analysis directly translate to the quality of the kinematic fit and of the pull plots of the fitted objects. The chosen procedure to evaluate the terms of the covariance matrices is the comparison between the reconstructed and the truth level information in simulation samples by means of the signed residual. The *diagonal terms* of the matrix, e.g. the reconstruction resolution of the kinematic variables, are obtained by fitting the residual distributions of the variable x in question,

$$(x_{\text{Reco}} - x_{\text{MC-truth}})\,, \tag{5.34}$$

to Gaussian distributions. Then, the squares of their widths are extracted in order to arrive at the averages of the desired variances, cp. Fig. 5.3a. Similarly, to obtain the *off-diagonal terms* (covariances), the products of the residuals of the two variables x and y involved,

$$(x_{\text{Reco}} - x_{\text{MC-truth}})(y_{\text{Reco}} - y_{\text{MC-truth}})\,, \tag{5.35}$$

are histogrammed and the mean values of the resulting histograms are then identified with the desired off-diagonal elements, see Fig. 5.3b. The x and y variables in Equations (5.34) and (5.35) represent any of the reconstructed kinematic quantities of the jet (p_{T},η,ϕ) or the reconstructed missing transverse energy ($E_{\text{T}}^{\text{miss}}$,$\phi$). Now, to obtain a more detailed model of the covariance matrices, the quantities calculated according to Equations (5.34) and (5.35) are binned in p_{T} and η of the truth-level objects. Given the limited MC statistics available for such a detailed study, the binning is chosen such as to ensure a good fit of the Gaussian function throughout the entire acceptance region of the ATLAS detector. Moreover, the statistics available does not suffice to also bin the jet kinematic resolution with respect to the azimuthal angle ϕ; however, a cross-check confirms the rotational invariance around the z-axis and guarantees that each distribution is flat in ϕ. It is therefore not necessary to introduce an additional binning in ϕ to achieve a refined modelling.

To obtain the jet covariances, only jets from MC samples of semileptonic $\text{t}\bar{\text{t}}$ and single-top (all three channels) events are used, since the analysis aims to extract a signal from a top quark event topology. Particular care must be taken when choosing the true object which is compared to the reconstructed item. For the jet case, the most suitable "truth" candidate is the hadron-level jet, identified by the very same jet algorithm that is used for the reconstructed jet (anti-k_{T} algorithm employing topological clustering with $\Delta R = 0.4$, cp. Sec. 3.3.4). For the choice of the "truth" object, the hadron-level jet is preferable to the outgoing parton from the "hard" MC process, since the latter cannot always be matched unambiguously to a truth object (e.g. in NLO). Therefore, the hadron-level jet is identified as the most viable choice for probing the resolution of the reconstruction. The truth-matching is realized by computing the χ^2-type measure d defined as

$$d = (\eta_{\text{dl}} - \eta_{\text{hl}})^2 + (\varphi_{\text{dl}} - \varphi_{\text{hl}})^2 + (p_{\text{t, dl}} - p_{\text{t, hl}})^2 / p_{\text{t, hl}}^2\,. \tag{5.36}$$

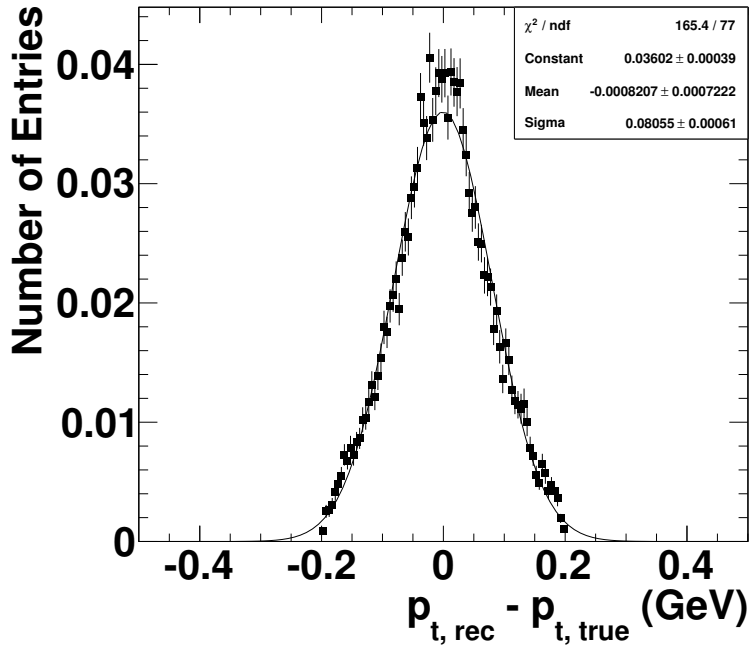

(a) Determination of jet $(\Delta p_\mathrm{T})^2$

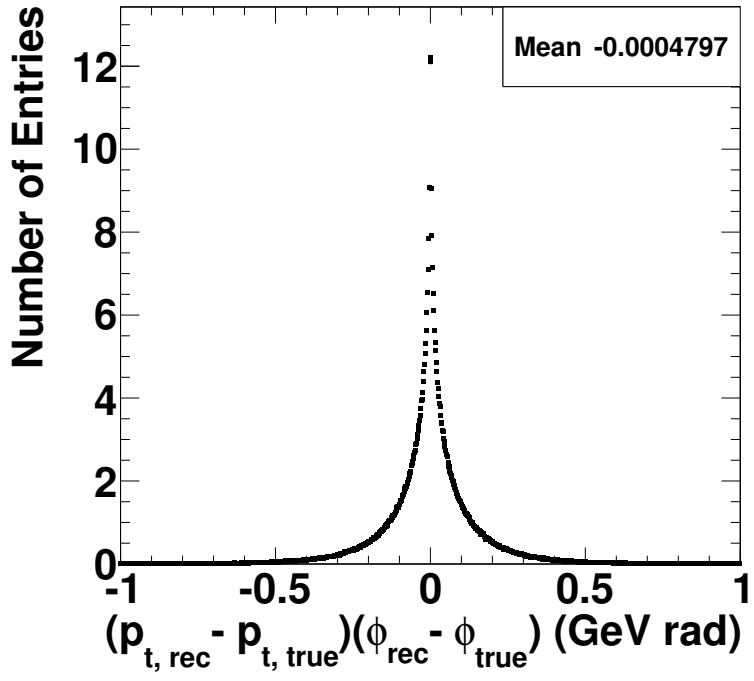

(b) Determination of jet $\Delta p_\mathrm{T} \Delta\phi$

Figure 5.3. Examples for the determination of the covariance matrix elements [Beu+12]. In (a) the determination of a diagonal element is shown. A Gaussian is fitted to the residual distribution of the element in question (here p_T for jets) and the resulting width squared is taken. For the off-diagonal elements (b) the products of the residuals of both variables (here p_T and ϕ) are histogrammed. The mean value of the histogram gives the desired off-diagonal element.

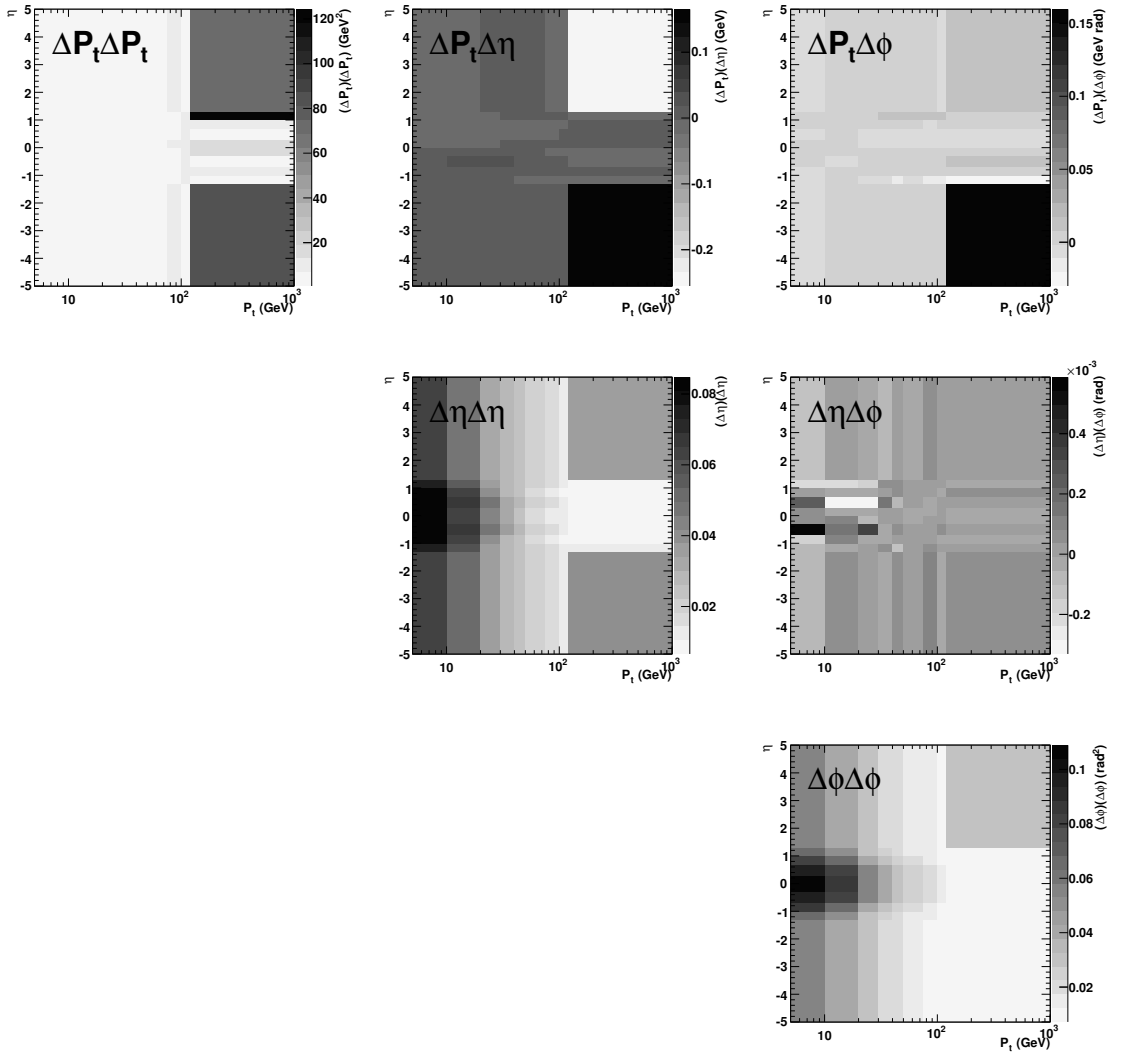

Figure 5.4. Two-dimensional histogramming of the six covariance matrix elements for the three-momentum vectors of the jets in $(p_\mathrm{T}, \eta, \phi)$ coordinates [Beu+12]. The matrix elements are binned in p_T and η of the hadron level jets in a suitable way to accommodate the smaller statistics available in the range of high p_T and large η, respectively.

utilizing the vicinity in the spatial coordinates (i.e. ΔR) and in relative p_T of the hadron-level (hl) jet and the detector-level (dl) jet. In this manner, each reconstructed jet is compared to the full list of hadron-level jets. The combination associated with the lowest d value is matched, and only the covariances of this selected pair are fitted, where a binning in p_T and η of the hadron-level jet is applied. The two-dimensionally binned covariance matrix elements of the jets are shown in Fig. 5.4. Here, the reconstructed jets have already passed analysis selection criteria like the overlap-removal (cp. Sec. 4.4) and satisfy $|\eta| < 4.5$ and $p_\mathrm{T} > 10\,\mathrm{GeV}$.

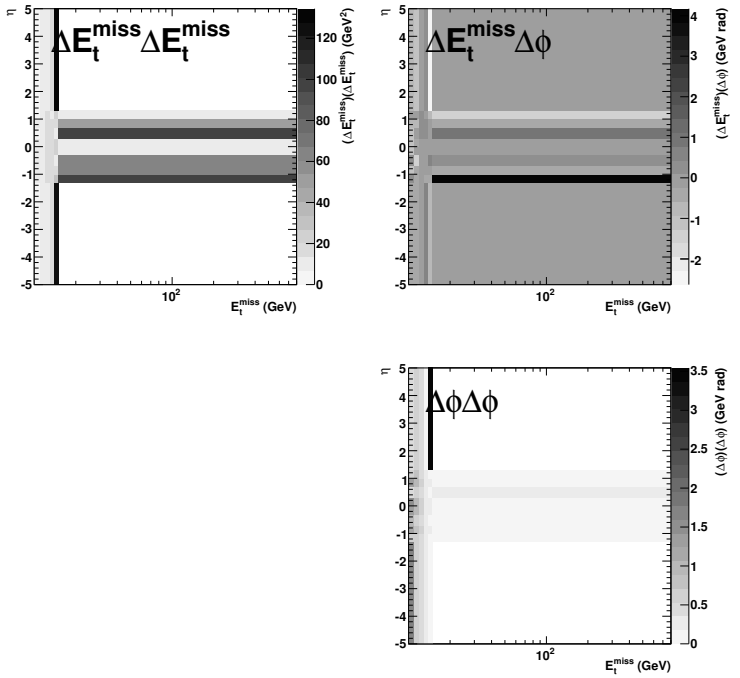

Figure 5.5. Two-dimensional histogramming of the three covariance matrix elements of the $E_{\mathrm{T}}^{\mathrm{miss}}$ two-vector in $(E_{\mathrm{T}}^{\mathrm{miss}}, \phi)$ coordinates [Beu+12]. The matrix elements are binned in p_{T} $(= E_{\mathrm{T}}^{\mathrm{miss}})$ and η of the neutrino in a suitable way to accommodate the smaller statistics available in the range of high p_{T} and large η, respectively.

Deriving the covariance matrix of $E_{\mathrm{T}}^{\mathrm{miss}}$, i.e. the neutrino, requires yet different choices. First of all, the missing transverse energy is fully assigned to the leading neutrino resulting from the W boson decay in the events containing top quarks. This assumption in the modelling already represents an optimization in that it forces the fit to assign low χ^2 values to semileptonic events, thus automatically discarding background sources. Hence, in order to obtain the matrix of the $(E_{\mathrm{T}}^{\mathrm{miss}}, \phi)$ resolution, again only MC samples of semileptonic $\mathrm{t\bar{t}}$ and single-top (all three channels) events are used as input to the analysis extracting the covariances.[4] Their respective contributions are weighted according to their production cross-sections. There is no minimal requirement on the magnitude of the $E_{\mathrm{T}}^{\mathrm{miss}}$. As in the jet case, the matrix terms of the $E_{\mathrm{T}}^{\mathrm{miss}}$ are binned in the kinematical phase space: In order to allow for a more precise fit of the total 4-momentum of the neutrino in the event, a binning of the matrix terms in p_{T} and η of the leading neutrino is employed. The two-dimensionally binned covariance matrix elements of the $E_{\mathrm{T}}^{\mathrm{miss}}$ are displayed in Fig. 5.5.

[4]The original $\mathrm{t\bar{t}}$ MC sample used also contains dileptonic events, but since the preselection of the analysis is already applied on the samples used and includes a veto on a second lepton in the event, the semi-leptonic event signature is ensured.

Particle	Mass (GeV)	Width (GeV)
W	80.399	2.085
t	172.9	1.99

Table 5.1. Masses and decay widths of the W boson and the top quark used as constraints in the kinematic fits [Nak+10].

As mentioned in the beginning of this section, the quality of the truth-matching and of the parametrization choices for the respective objects are reflected in the flatness of the distribution of the χ^2 probability of the kinematic fit and the correct shape of the pull plots obtained to evaluate the results of the fit (see Sec. 5.1.1). It is noteworthy that the derivation of the jet and $E_{\mathrm{T}}^{\mathrm{miss}}$ covariances from MC samples represents the only simulation input to the reconstruction procedure by kinematic fitting, as opposed e.g. to multivariate techniques that need to be trained on the model as well. Further details on the extraction of jet and $E_{\mathrm{T}}^{\mathrm{miss}}$ covariances used in this study can be found in [Pro12] and [Beu+12] where the values were calculated.

5.2.3. Analysis Setup

In this section, the complete setup of the KinFitter analysis is presented in detail and selected control plots are shown. The analysis procedure consists of three steps: the main kinematic fit of a *single top quark* (signal hypothesis) and two kinematic veto fits (background hypotheses) to identify and reject events with an *additional hadronically decaying W boson* and *semi-leptonic $t\bar{t}$ signatures*, respectively.

Signal Single Top Quark Fit

As already outlined in Sec. 5.2.1, the fit of the four-momentum of the single top quark in the event proceeds by combining the information from the signal lepton, the b-jet and the $E_{\mathrm{T}}^{\mathrm{miss}}$. In Figures 5.6, 5.7 and 5.8, the kinematic distributions of the input objects of the fit are displayed exemplary for the electron channel in the 2-jet bin. Here, the kinematics of the objects *entering* the fit are shown, but the histogram entries are only recorded for events that are eventually accepted in the final selection according to the full analysis chain described below (cp. also Fig. 5.9); these distributions are not filled for every event in order to compare before and after fit results especially for the interesting events. A good agreement of the simulated distributions with the data distribution can be seen, also for the other analysis channels (electron channel 3- and 4-jet bin and, likewise, the 2-, 3- and 4-jet bins of the muon channel) where the distributions look similar and are not included here for reasons of brevity.

In the fitting procedure, the W boson and top quark mass constraints shown in Fig. 5.2 are respected. Here, Gaussian mass constraints according to Eq. (5.21) are employed. The exact values of the W and top quark masses and decay widths used

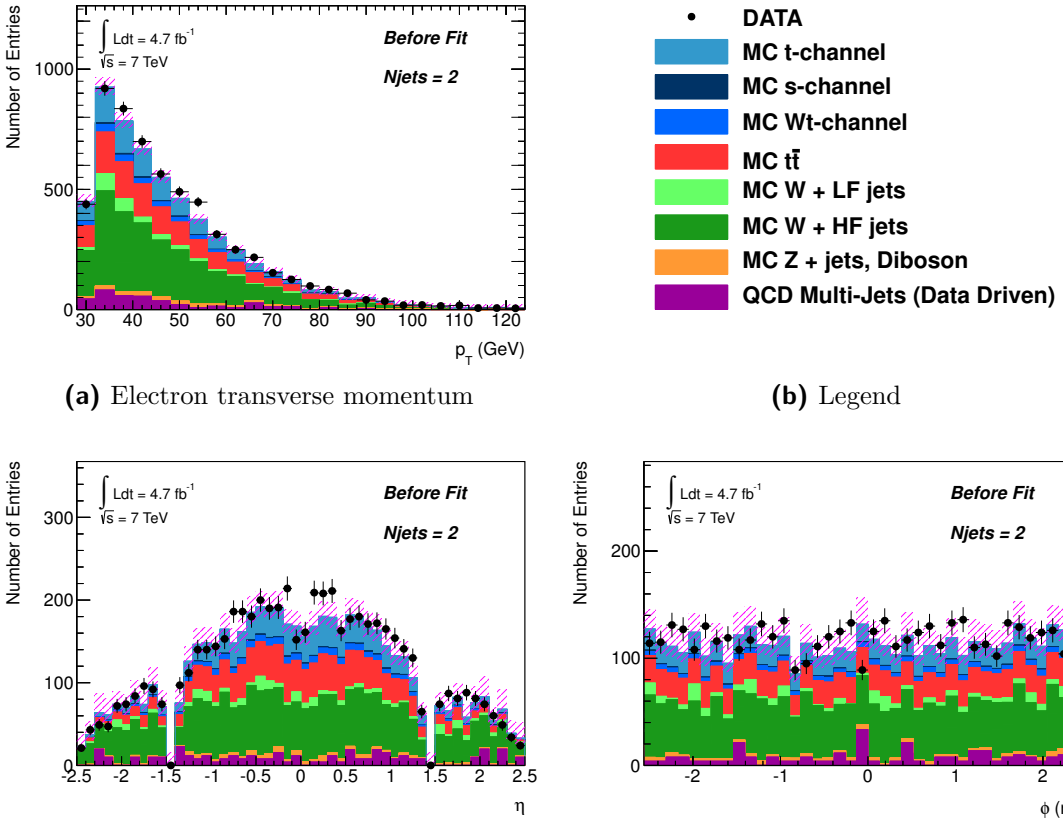

(a) Electron transverse momentum

(b) Legend

(c) Electron pseudorapidity

(d) Electron azimuth

Figure 5.6. The kinematic distributions of p_{T} (a), η (c) and ϕ (d) of the signal electron entering the main kinematic top quark fit in the 2-jet bin in the electron channel. Only events accepted in the final selection are included. All MC distributions are normalized to the data luminosity. The cut-out region in (c) corresponds to the crack region $1.37 < |\eta_{\mathrm{cluster}}| < 1.52$ in the EMCAL (cp. Sec. 3.2.4).

Parameter	Value
$N_{\mathrm{iter}}^{\mathrm{max}}$	100
ε_{χ^2}	$5 \cdot 10^{-5}$
ε_f	$1 \cdot 10^{-4}$

Table 5.2. Detailed settings of the KinFitter used for this analysis. $N_{\mathrm{iter}}^{\mathrm{max}}$ denotes the maximum number of iterations in a fit, ε_{χ^2} is the maximum deviation of the minimum function for successive iterations and ε_f is the maximum value of the constraints (cp. Equations (5.18)). The values are the same ones as used in [Rie10].

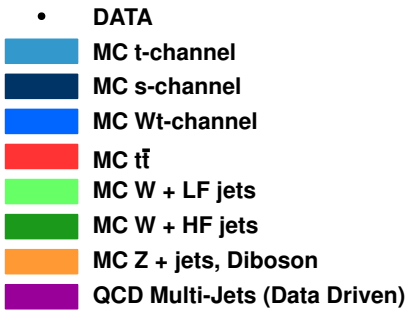

(a) Legend

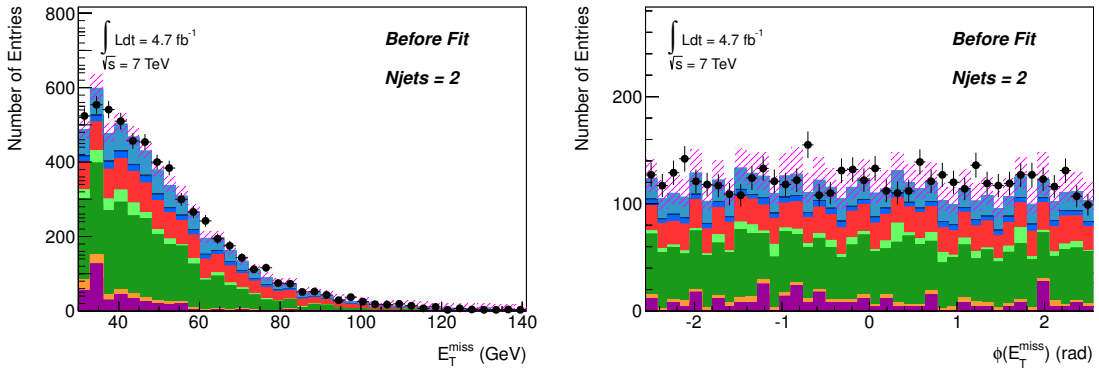

(b) $E_{\mathrm{T}}^{\mathrm{miss}}$ magnitude **(c)** $E_{\mathrm{T}}^{\mathrm{miss}}$ azimuth

Figure 5.7. Magnitude and azimuthal angle of $E_{\mathrm{T}}^{\mathrm{miss}}$ (b), (c) entering the main kinematic top quark fit in the 2-jet bin in the electron channel. Only events accepted in the final selection are included. All MC distributions are normalized to the data luminosity.

for the fit constraints are taken from [Nak+10] and are listed in Tab. 5.1. The fit of the single top quark returns an overall χ^2 value, and the fit is said to have converged if the criteria in Equations (5.18) are fulfilled. In Tab. 5.2, the detailed settings of the KinFitter's convergence criteria are collected. These values have been optimized in [Rie10] to ensure that the true global minimum is found whilst not spending too many iterations in case the event does not match the signal hypothesis. Thus, in order for the event to count as a single top candidate event, the iterative fitting procedure must have converged. The χ^2 probability

$$\mathcal{P}(\chi^2) = \int_{\chi^2}^{\infty} \tilde{\chi}^2 \, \mathrm{d}\tilde{\chi}^2 \,, \tag{5.37}$$

often referred to as the *p-value*, is a direct measure of the significance of the fit result. For the detailed properties of the $\mathcal{P}(\chi^2)$ quantity, see App. B. Events with a *p*-value below a certain threshold are eventually rejected. The whole fitting procedure

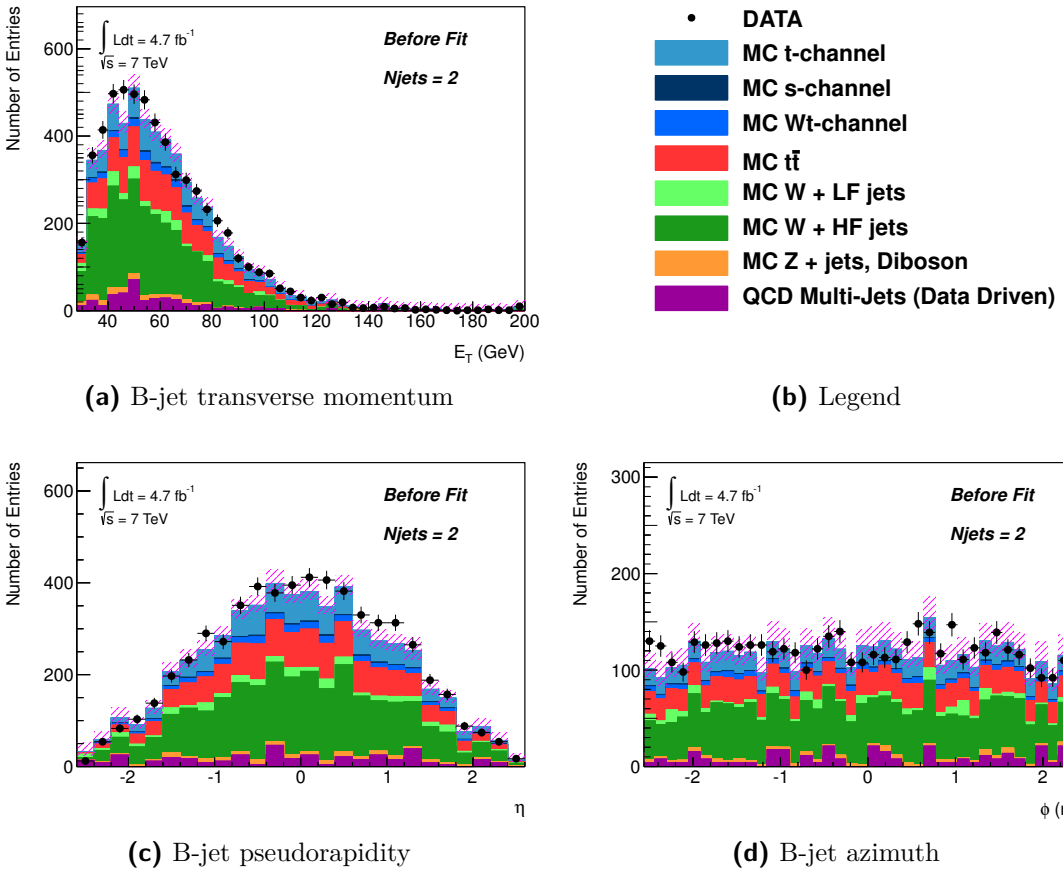

(a) B-jet transverse momentum

(b) Legend

(c) B-jet pseudorapidity

(d) B-jet azimuth

Figure 5.8. Transverse momentum (a), pseudorapidity (c) and azimuthal angle (d) of the b-jet entering the main kinematic top quark fit in the 2-jet bin in the electron channel. Only events accepted in the final selection are included. All MC distributions are normalized to the data luminosity. In (a), the bin of highest E_{T} includes the overflow count.

including the vetos on background events that are detailed in the following two subsections is summarized in Fig. 5.9. As can be seen in the figure, the convergence requirement for the main single top quark fit must be met before the $\mathrm{t\bar{t}}$ veto fit and the hadronic W boson veto fit are executed (in case the veto fits are applicable for the current jet bin; see corresponding sections on the veto fits below) and their respective $\mathcal{P}(\chi^2)$ requirements are queried.[5] Only afterwards, the $\mathcal{P}_{\text{main fit}}(\chi^2)$ requirement for the main single top quark fit is tested. This order is chosen to immediately reject events that hardly resemble the signal hypothesis by requiring the main single-top quark fit to at least converge. Then, the corresponding $\mathcal{P}_{\text{main fit}}(\chi^2)$ cut is postponed until the decisions of the veto fits are taken to allow for an optimization of this cut including the vetos: It turns out that a cut requiring $\mathcal{P}_{\text{main fit}}(\chi^2) > 0.05$ yields an optimal signal enrichment.

[5] This implies that the veto fits have converged.

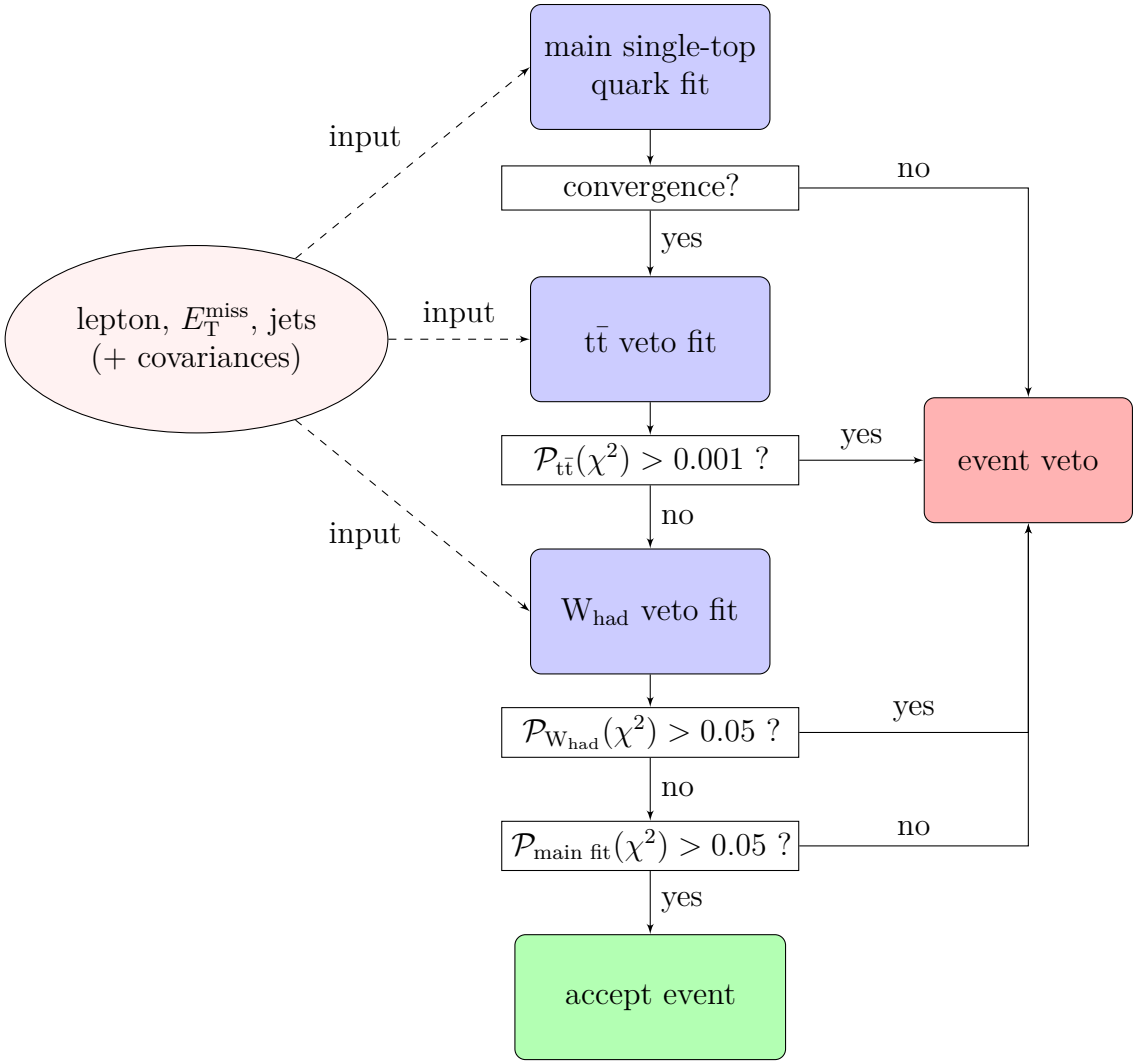

Figure 5.9. Flow-chart of the full kinematic fitting procedure for single-top t-channel events including the veto fits to reject background events. The veto fit of an additional hadronically decaying W boson is only done in the 3- and 4-jet bin, the $\mathrm{t\bar{t}}$ veto fit solely in the 4-jet bin. The $\mathcal{P}_{\mathrm{main\ fit}}(\chi^2)$ cut is postponed in these cases to ensure an optimized signal-to-background ratio including the veto decisions.

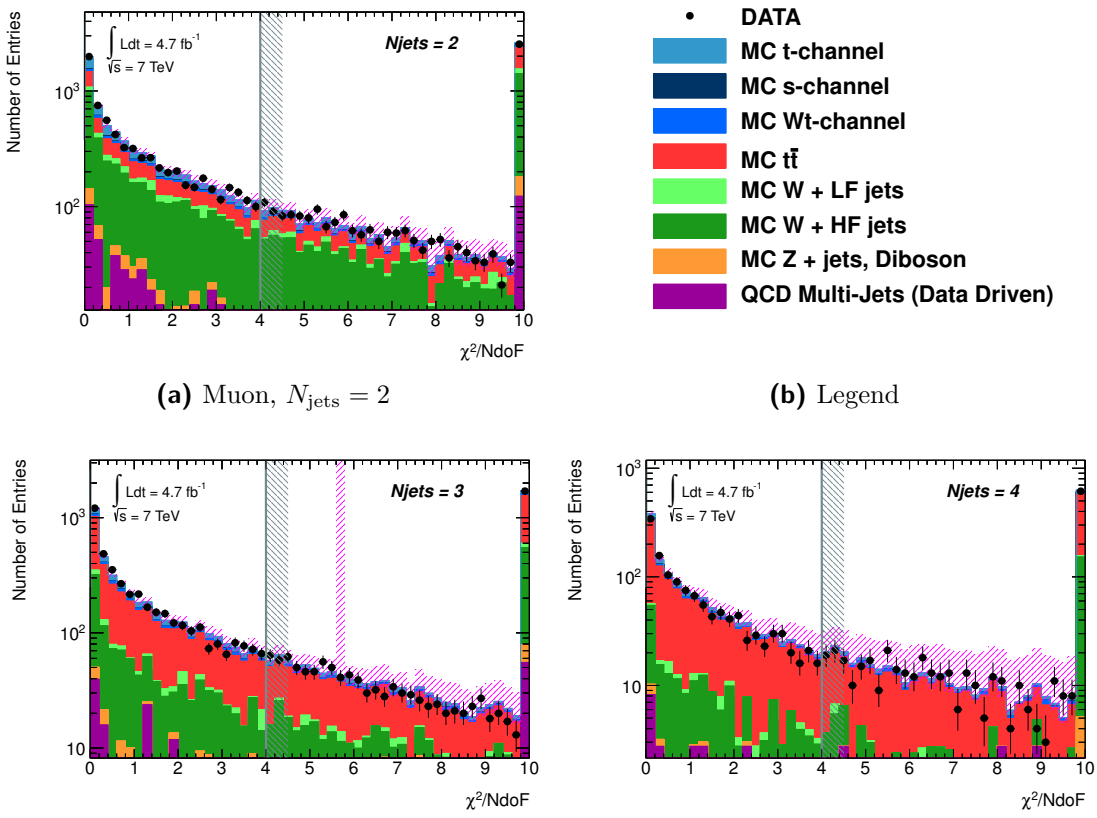

(a) Muon, $N_{\text{jets}} = 2$ **(b)** Legend

(c) Muon, $N_{\text{jets}} = 3$ **(d)** Muon, $N_{\text{jets}} = 4$

Figure 5.10. Semi-logarithmic distributions of the χ^2 resulting from the main kinematic top quark fit for 2, 3 and 4 jets per event in the muon channel, see (a), (c) and (d). The exclusion lines indicate the $\chi^2 < 4$ requirement which corresponds to the cut on the χ^2 probability at $\mathcal{P}_{\text{main fit}}(\chi^2) > 0.05$. The vetos on background events as described in the following two subsections are already applied. All MC distributions are normalized to the data luminosity. The rightmost bin is the overflow bin.

Exemplary, this can be seen for the muon channel in Figures 5.10 to 5.12 (the corresponding figures for the electron channel can be found in App. C): In Fig. 5.10, the χ^2 distributions for all three jet bins are shown with an exclusion line indicating the cut $\chi^2 < 4$ corresponding to the requirement $\mathcal{P}_{\text{main fit}}(\chi^2) > 0.05$. The $\mathcal{P}_{\text{main fit}}(\chi^2)$ distributions themselves are displayed in Fig. 5.11 for the same channels with the cut at 0.05 indicated: The semi-logarithmic distributions on the left hand side are seen to level out for values greater than 0.3; by employing a logarithmic binning and a double-logarithmic axis display, the region of low $\mathcal{P}_{\text{main fit}}(\chi^2)$ is enlarged in the plots on the right hand side, where the cut value of 0.05 can be seen to ensure a good signal-to-background ratio with only a small loss of signal events. As the jet multiplicity increases, the sample composition changes: whereas the background in the 2-jet bin consists mainly of W in association with heavy flavour jets and a smaller

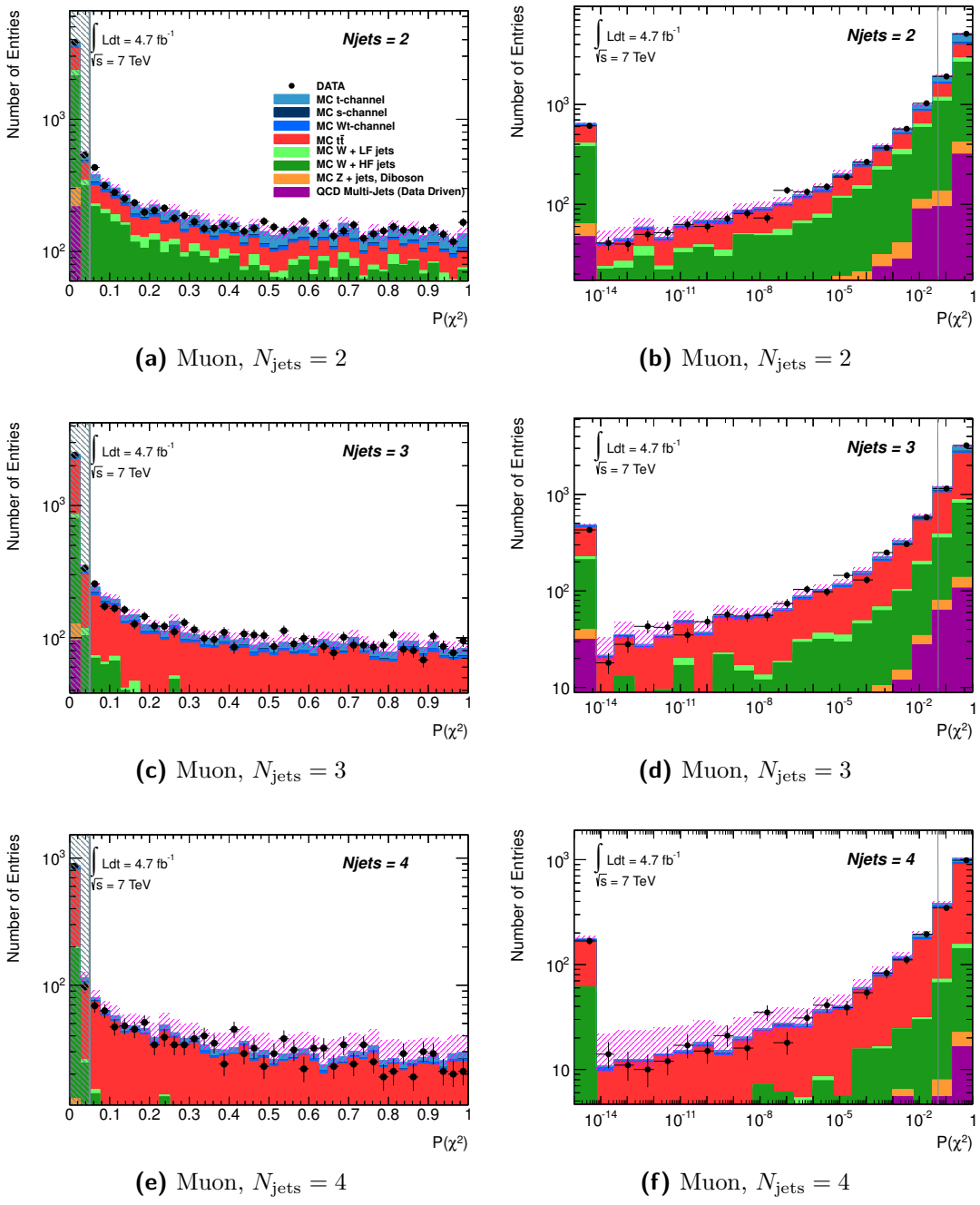

(a) Muon, $N_{\text{jets}} = 2$ **(b)** Muon, $N_{\text{jets}} = 2$

(c) Muon, $N_{\text{jets}} = 3$ **(d)** Muon, $N_{\text{jets}} = 3$

(e) Muon, $N_{\text{jets}} = 4$ **(f)** Muon, $N_{\text{jets}} = 4$

Figure 5.11. Semi-logarithmic $\mathcal{P}_{\text{main fit}}(\chi^2)$ distributions of the main kinematic top quark fit for 2, 3 and 4 jets per event in the muon channel, see (a), (c), (e), and the corresponding double-logarithmic $\mathcal{P}_{\text{main fit}}(\chi^2)$ distributions, see (b), (d), (f). The vetos on background events as described in the following two subsections are already applied. The exclusion lines indicate the cut used for signal enrichment, $\mathcal{P}_{\text{main fit}}(\chi^2) > 0.05$. All MC distributions are normalized to the data luminosity.

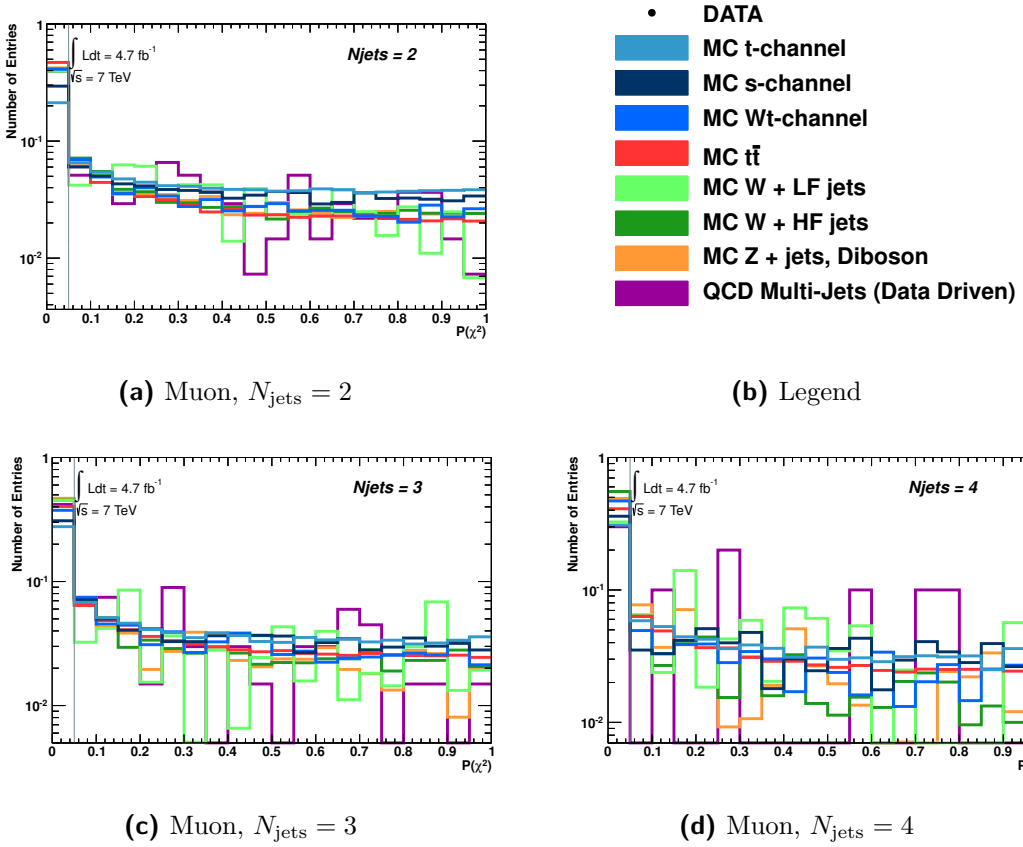

(a) Muon, $N_{\text{jets}} = 2$ **(b)** Legend

(c) Muon, $N_{\text{jets}} = 3$ **(d)** Muon, $N_{\text{jets}} = 4$

Figure 5.12. Semi-logarithmic $\mathcal{P}_{\text{main fit}}(\chi^2)$ distributions of the main kinematic top quark fit for 2, 3 and 4 jets per event in the muon channel, see (a), (c), (d). The vetos on background events as described in the following two subsections are already applied. The grey vertical lines indicate the cut used for signal enrichment, $\mathcal{P}_{\text{main fit}}(\chi^2) > 0.05$. All MC distributions are normalized to unity and overlaid for shape comparison.

amount of $t\bar{t}$, the situation is inverted in the 3-jet bin, and the 4-jet bin, finally, is completely dominated by $t\bar{t}$. In Fig. 5.12, the efficiency of the $\mathcal{P}_{\text{main fit}}(\chi^2)$ cut in separating the signal from the background is illustrated by the overlaid distributions from the MC samples, normalized to unity: Especially in the 2-jet bin, the signal t-channel MC distribution is rather flat in $\mathcal{P}_{\text{main fit}}(\chi^2)$ whereas the background MC distributions show a steeper rise towards low p-values. Like in the previous two figures, looking at the 4-jet bin distribution the lack of statistics becomes obvious. Regarding the efficiency of the selection in the 2-jet bin, where no other event vetos based on background fits are applied, the cut on $\mathcal{P}_{\text{main fit}}(\chi^2)$ reduces the overall background by about 43 % at a signal cost of 21 % in both lepton channels. This corresponds to an increase of the signal-to-background ratio from 14 % to 20 %.

Thus, signal-like events are enriched in the final sample. Furthermore, the fit resolves the twofold ambiguity of the neutrino's p_z component in the W decay that

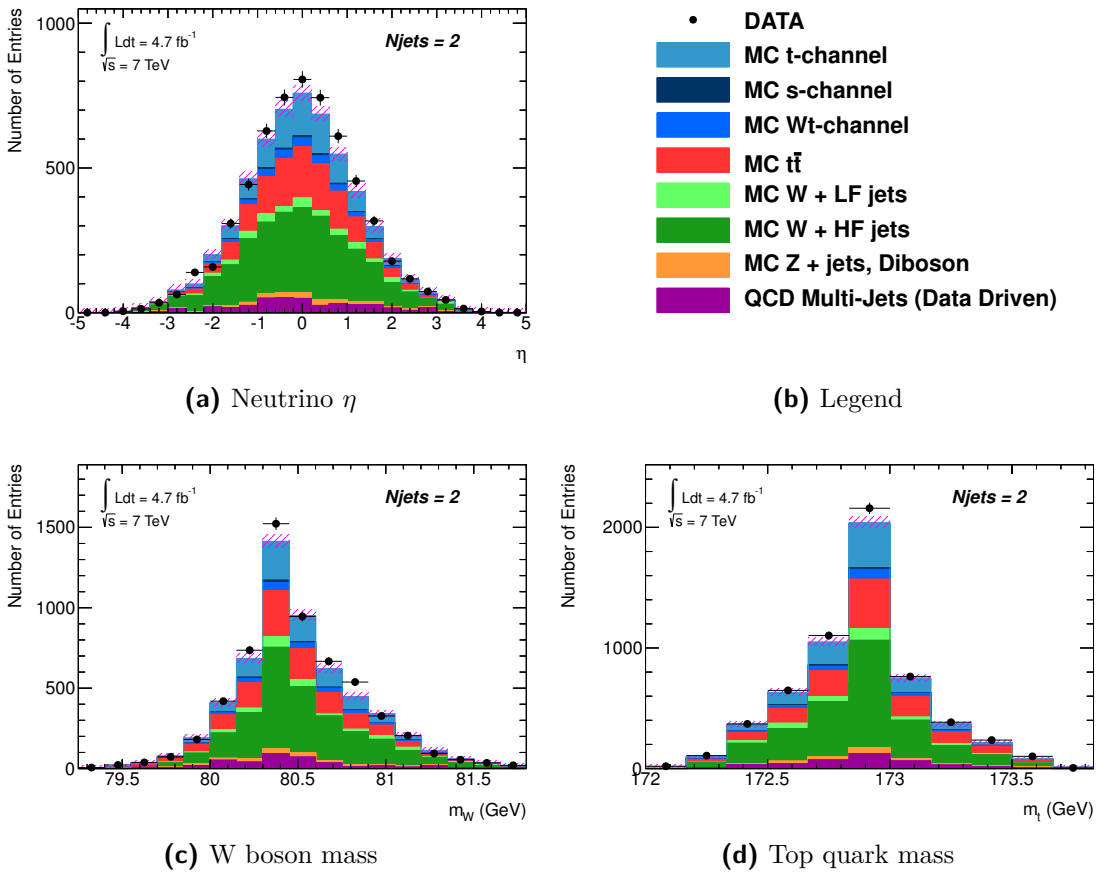

(a) Neutrino η **(b)** Legend

(c) W boson mass **(d)** Top quark mass

Figure 5.13. Pseudorapidity of the neutrino (a), mass of the W boson (c) and mass of the top quark (d), reconstructed by the main kinematic top quark fit with a cut on the p-value of $\mathcal{P}_{\text{main fit}}(\chi^2) > 0.05$ in the 2-jet bin in the electron channel. The MC distributions are all normalized to the data luminosity.

results from constraining the invariant mass of the lepton-neutrino system to m_{W}.[6] It is therefore able to fully reconstruct the four-momentum vectors of the W boson and the top quark, yielding the invariant masses of the W and the top quark. The pseudorapidity distribution of the neutrino reconstructed by the main single-top quark fit is displayed in Fig. 5.13a, and the invariant masses of the W boson and the top quark from the fit are shown in Figures 5.13c and 5.13d, respectively, for the 2 jet bin in the electron channel. Since these distributions look very similar in all other analysis channels, they are omitted here for the sake of brevity.

In the minimization process, the fitter also computes corrections to the momenta of the given final state objects; these corrections are expected to reduce the analysis' dependence on the energy scale uncertainty of the jets and the missing transverse energy (cp. Sec. 6.1). To judge this, e.g. for the b-jet, the residuals of the b-jet E_{T}

[6] P. Sturm. *ATLAS TWiki: Neutrino Pz in Top Decays*. Sept. 2011. URL: `https://twiki.cern.ch/twiki/bin/viewauth/AtlasProtected/NeutrinoPz`.

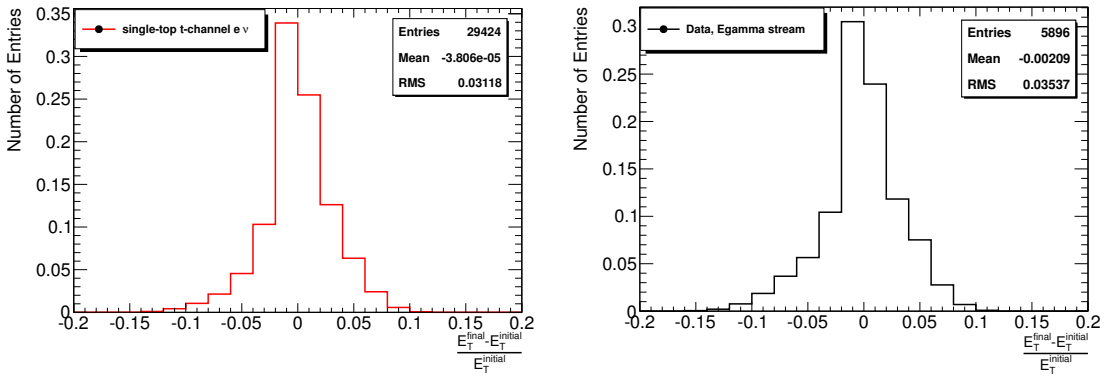

(a) B-jet transverse energy (signal MC) **(b)** B-jet transverse energy (Data)

Figure 5.14. Residual distributions of the transverse energy of the b-jet from the main kinematic top quark fit in the electron channel in the 2-jet bin: The residual from the signal single-top t-channel $e\nu$ MC (a) and from the *Egamma* stream in data (b) are displayed. Only events accepted in the final selection are included.

w.r.t. the matched hadron level (hl) jet before and after the fit

$$\frac{E_{\mathrm{T}}^{\text{before fit}} - E_{\mathrm{T}}^{\mathrm{hl}}}{E_{\mathrm{T}}^{\mathrm{hl}}}, \quad \frac{E_{\mathrm{T}}^{\text{after fit}} - E_{\mathrm{T}}^{\mathrm{hl}}}{E_{\mathrm{T}}^{\mathrm{hl}}} \tag{5.38}$$

would have to be compared; the widths of the residual distribution after the fit should be smaller, and, ideally, the distribution should be unbiased in contrast to the one before the fit. However, such a truth-level study has not been done in this work. In order to demonstrate the fitter's sensitivity to the true top quark kinematics, Fig. 5.14 shows the residuals of the b-jet E_{T}

$$\frac{E_{\mathrm{T}}^{\text{after fit}} - E_{\mathrm{T}}^{\text{before fit}}}{E_{\mathrm{T}}^{\text{before fit}}} \tag{5.39}$$

for the signal MC in the electron channel (single-top t-channel $e\nu$) as well as for the corresponding selection in data from the *Egamma* stream. Only events accepted in the final signal sample, i.e. after the $\mathcal{P}_{\text{main fit}}(\chi^2) > 0.05$ cut, are included. The mean of the distribution is very close to zero for the signal MC and non-vanishing for the data. This is expected because of the composition of the data sample that is dominated by W+jets events after all selection cuts (cp. Fig. 5.6d for example), i.e. the fitter attempts to match to the wrong model in most cases, which results in large residuals.

A sensitive consistency check of the fitting procedure is provided by the pull distributions of the kinematic variables. The pull of a variable is its residual, computed from its value before and after the fit, normalized by the standard deviation of this residual, cp. Eq. (5.19). If this quantity follows a standardized Gaussian distribution,

the assumptions made for the covariance matrix elements entering the kinematic fit are correct, and the model expectations formulated in the mass constraints are met.

In Fig. 5.15, the pull distributions in the 2-jet bin in both lepton channels are shown for the transverse momenta of the electron and the muon and for the b-jet as well as for the magnitude of the missing transverse energy; the histograms are filled for convergent top quark fits only. The fitting here is done on simulated events of the signal channel (single-top t-channel $e\nu$ and $\mu\nu$) where the hypothesis to be tested is correct. A quite good agreement with standardized Gaussian distributions is observed, although there is always a broadening in the tails, giving a σ larger than one, and the values also display a small bias.

As can be seen, the magnitude of the mean's bias is very similar for the three fit objects. It does also not depend on the jet bin. The sign of the bias, however, is always negative for the lepton p_{T} and the $E_{\mathrm{T}}^{\mathrm{miss}}$ whereas it is positive for the b-jet p_{T}, regardless of the lepton flavour and the jet bin. This behaviour could be attributed to a systematic miscalibration of the jets: If the JES (cp. Sec. 3.3.4) is chosen such that the jet energy is systematically underestimated, the fit would compensate for this with positive residuals $\mathbf{\Delta y}$ for the b-jet. In turn, the opposite sign of the $E_{\mathrm{T}}^{\mathrm{miss}}$ bias could be explained by the resulting overestimation of $E_{\mathrm{T}}^{\mathrm{miss}}$ due to an underestimated jet term in events with an unbalanced jet distribution throughout the detector (as is mostly the case for single-top t-channel events). Moreover, the $E_{\mathrm{T}}^{\mathrm{miss}}$ is always prone to be underestimated due to dead material in the detector geometry that is not accounted for. The lepton p_{T}, in contrast, is a well known quantity with a good resolution; a systematic shift associated with the jet energies nevertheless also affects the lepton p_{T} pull and the pull of the magnitude of the $E_{\mathrm{T}}^{\mathrm{miss}}$ in the fitting procedure. The *angular* pull distributions of all three fit objects, however, remain rather unaffected by this shift since the orientation of the fit objects inside the detector is measured to a high degree of precision.

Regarding the widths of all pull distributions, the broadening is seen to increase with the jet multiplicity. This could be due to the growing number of wrong assignments of the b-jet: Already in the 2-jet bin there is the possibility to pick either the spectator b-jet from the gluon splitting (if the b-tagging is correct) or, more rarely, the forward jet (if the jet is mistakenly b-tagged) instead of the b-jet from the top decay. In the higher jet bins, this problem becomes ever more pronounced. If the b-jet is not correctly identified, the top quark mass constraint is only poorly fulfilled and large residuals result. Furthermore, the jet energy resolution degrades with an increasing number of jets because of a higher overall activity in the detector.

Background Veto Fit of an Additional Hadronic W

The method of a kinematic fit is also used to identify and veto possible background events of the single-top t-channel topology. Since QCD multi-jets background events result mostly from fake leptons, they cannot easily be suppressed by exploiting kinematic particularities. Furthermore, W+jets production is not accessible by a kinematic fit with an invariant mass constraint for the W, because the number of

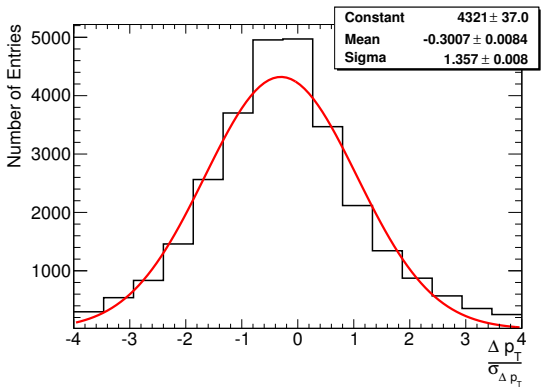

(a) Electron transverse momentum

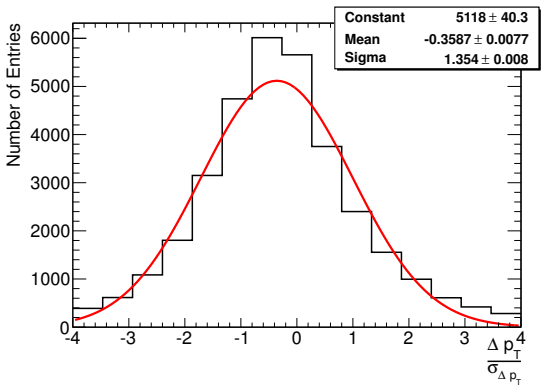

(b) Muon transverse momentum

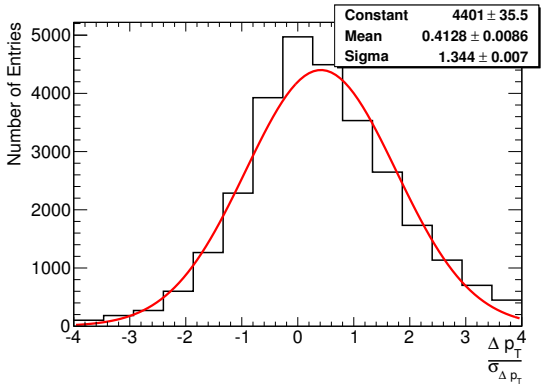

(c) Electron, b-jet transverse momentum

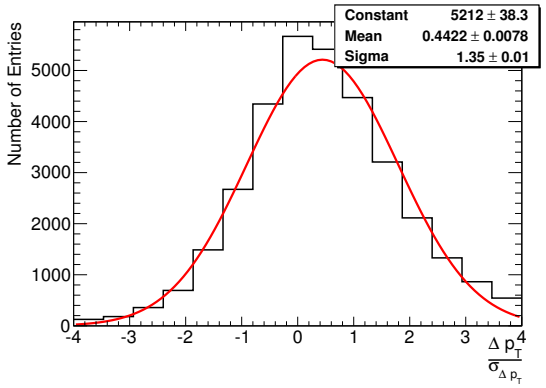

(d) Muon, b-jet transverse momentum

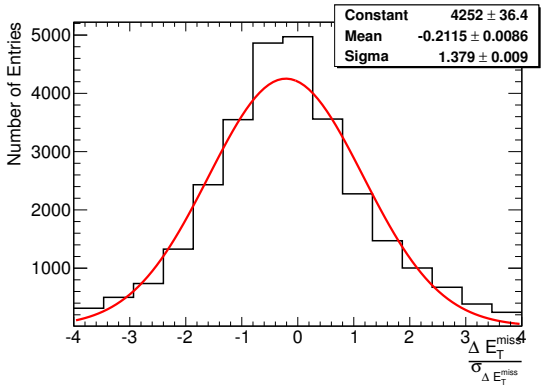

(e) Electron, missing transverse energy

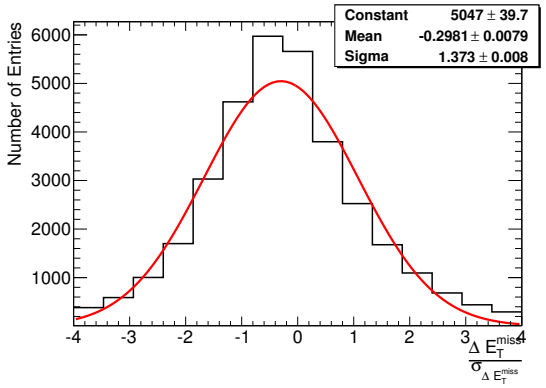

(f) Muon, missing transverse energy

Figure 5.15. Pull distributions from the main kinematic top quark fit for the transverse momenta of the final state objects entering the kinematic fit: For the electron channel, the pulls of the p_T of the electron (a), the b-jet p_T (c) and the magnitude of the E_T^{miss} (e) are shown. For the muon channel, the pulls of the p_T of the muon (b), the b-jet p_T (d) and the magnitude of the E_T^{miss} (f) are displayed. The distributions are taken from simulated signal events in the electron and muon channel (single-top t-channel $e\nu$ and $\mu\nu$, respectively) in the 2 jet bin. Only convergent top quark fits are considered.

degrees of freedom of the fit would be zero[7] and thus, the fit would amount to only solving an equation. Moreover, the ambiguity in the reconstruction of the p_z-component of the neutrino would persist. In contrast, the reconstruction of Z+jets events by a kinematic fit could be achieved [Beu10][8], and a veto could be placed on events successfully fitted to the Z mass hypothesis. However, this is not needed here since the event selection includes a veto on events containing a second lepton of signal quality which already removes most of the Z+jets background events. The rate of single-top production in the s-channel finally is very low and thus does not merit an elaborate method of rejection.

The remaining background is constituted of $\mathrm{t\bar{t}}$ and single-top Wt-channel events that have the common feature of two W bosons in the final state which distinguishes them from the signal topology. Of these, at least one W boson must decay leptonically to pass the event preselection – the case of two leptonically decaying W bosons is mostly removed by the veto on a second signal lepton. Therefore, a fit of an additional hadronically decaying W is employed to identify these background processes; NDoF = 1 in this fit.[9] In contrast to the $\mathrm{t\bar{t}}$ veto fit described in the next section, the hadronic W fit cannot only be executed in the 4-jet but also in the 3-jet bin, allowing it to identify $\mathrm{t\bar{t}}$ events where one of the b-jets is not found in the ATLAS reconstruction.

In the hadronic W boson fit, a Gaussian mass constraint is utilized, and the KinFitter settings correspond again to the ones listed in Tab. 5.2. Each combination of two jets in the event is tested, except the b-jet used in the main top quark fit. Thus, this veto is effective for the ≥ 3 jets case. The jets entering the fit of the hadronic W are restricted to $|\eta| < 2$. This is done since the decay products of a heavy particle like the W boson are expected to be found centrally in the detector, but also, even more importantly, to avoid the forward jet of the signal t-channel topology. A minimum p-value of the best resulting χ^2 of $\mathcal{P}_{\mathrm{W_{had}}}(\chi^2) > 0.05$ is required to veto an event based upon this fit.

In Fig. 5.16, the p-value distribution is shown exemplary for the electron channel in the 3- and 4-jet bins (for the corresponding figure in the muon channel, see App. C), and the requirement of $\mathcal{P}_{\mathrm{W_{had}}}(\chi^2) > 0.05$ is indicated: On the left hand side, the stacked MC histograms are shown, and it can be seen that the background is comprised mostly of $\mathrm{t\bar{t}}$ and Wt-channel events. The $\mathcal{P}_{\mathrm{W_{had}}}(\chi^2) > 0.05$ cut removes a great amount of $\mathrm{t\bar{t}}$ and Wt-channel background while resulting only in a small loss of signal events. This is again illustrated by the overlaid $\mathcal{P}_{\mathrm{W_{had}}}(\chi^2)$ distributions of the MC samples on the right hand side of the figure: It is clearly visible that towards high p-values, the t-channel distribution shows a steep decline whereas the distributions of $\mathrm{t\bar{t}}$ and Wt-channel production level out. In the 3-jet bin, where no $\mathrm{t\bar{t}}$ veto can be

[7] The NDoF of the fit of a W+jets event is zero because only one mass constraint can be formulated, the W mass constraint, that is opposed to one unknown parameter, the neutrino's p_z (see Sec. 5.1.1).

[8] In the Z+jets case, one mass constraint of the Z boson is opposed to no unknown parameter, since there is no neutrino in the event. Hence, NDoF = 1 in this case.

[9] This fit has a χ^2 distribution with 1 degree of freedom since there is one m_{W} constraint and no unmeasured parameter.

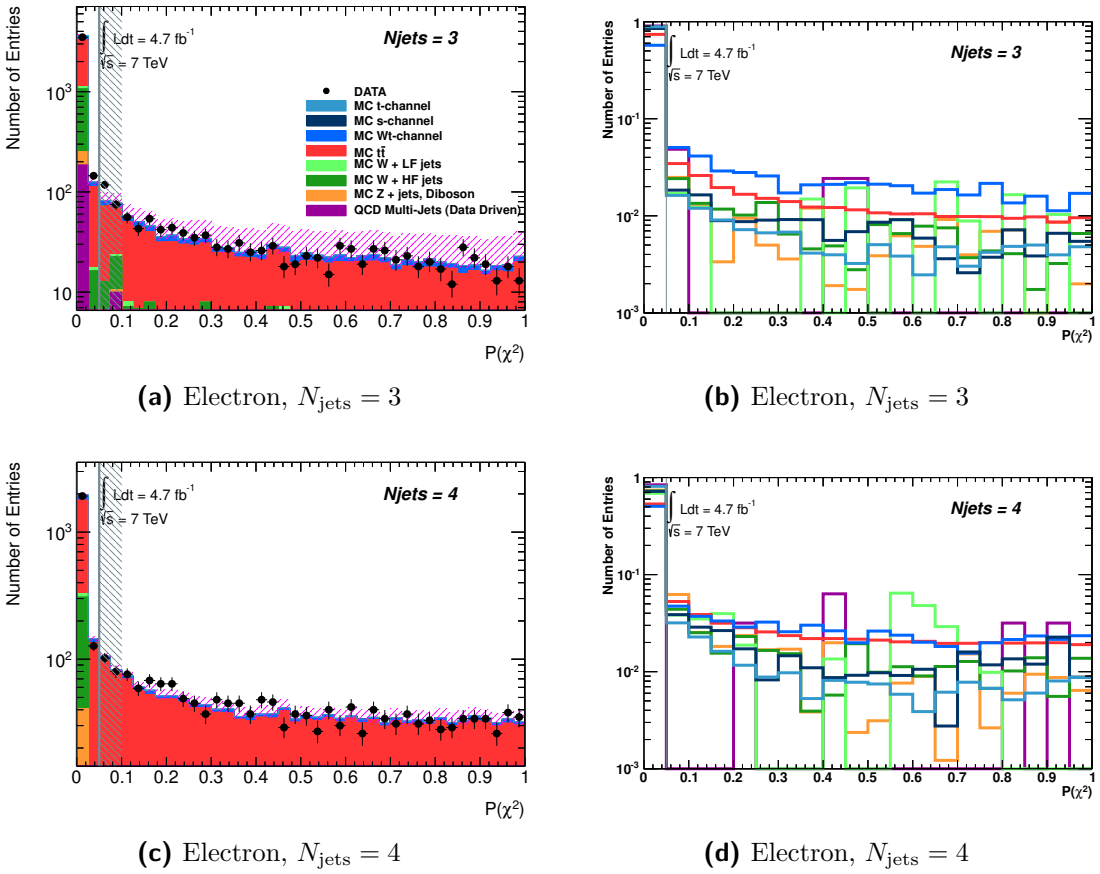

(a) Electron, $N_{\text{jets}} = 3$

(b) Electron, $N_{\text{jets}} = 3$

(c) Electron, $N_{\text{jets}} = 4$

(d) Electron, $N_{\text{jets}} = 4$

Figure 5.16. Semi-logarithmic $\mathcal{P}_{\text{W}_{\text{had}}}(\chi^2)$ distributions of the veto fit of an additional hadronically decaying W boson in the 3- and 4-jet bin, see (a) and (c), in the electron channel. All events with $\mathcal{P}_{\text{W}_{\text{had}}}(\chi^2) > 0.05$ are rejected. Also shown are the corresponding $\mathcal{P}_{\text{W}_{\text{had}}}(\chi^2)$ distributions of the single processes, (b) and (d), where all MC distributions are normalized to unity and overlaid for shape comparison. Here, the grey vertical lines indicate the veto cut used for background rejection, $\mathcal{P}_{\text{W}_{\text{had}}}(\chi^2) > 0.05$.

applied, the cut on $\mathcal{P}_{\text{W}_{\text{had}}}(\chi^2)$ reduces the Wt-channel and $\text{t}\bar{\text{t}}$ contributions by about 31 % and 19 %, respectively, at a signal loss of only 4 % in both lepton channels. This results in an increase of the signal-to-background ratio from 8 % to 9 %. This ratio is increased further to 11 % by the succeeding cut on $\mathcal{P}_{\text{main fit}}(\chi^2)$ which is mainly due to the reduction of $\text{t}\bar{\text{t}}$ by 40 %. However, the associated signal cost of 27 % is rather high.

The pull distributions of this veto fit are, in the spirit of the idea of this event veto, only filled for events that have a convergent top quark fit but are rejected because of a successful hadronic W fit. On the Wt-channel sample, the hypothesis of an additional hadronically decaying W boson is correct, and the corresponding pulls are displayed in Fig. 5.17 for both lepton channels in the 3-jet bin. Nevertheless,

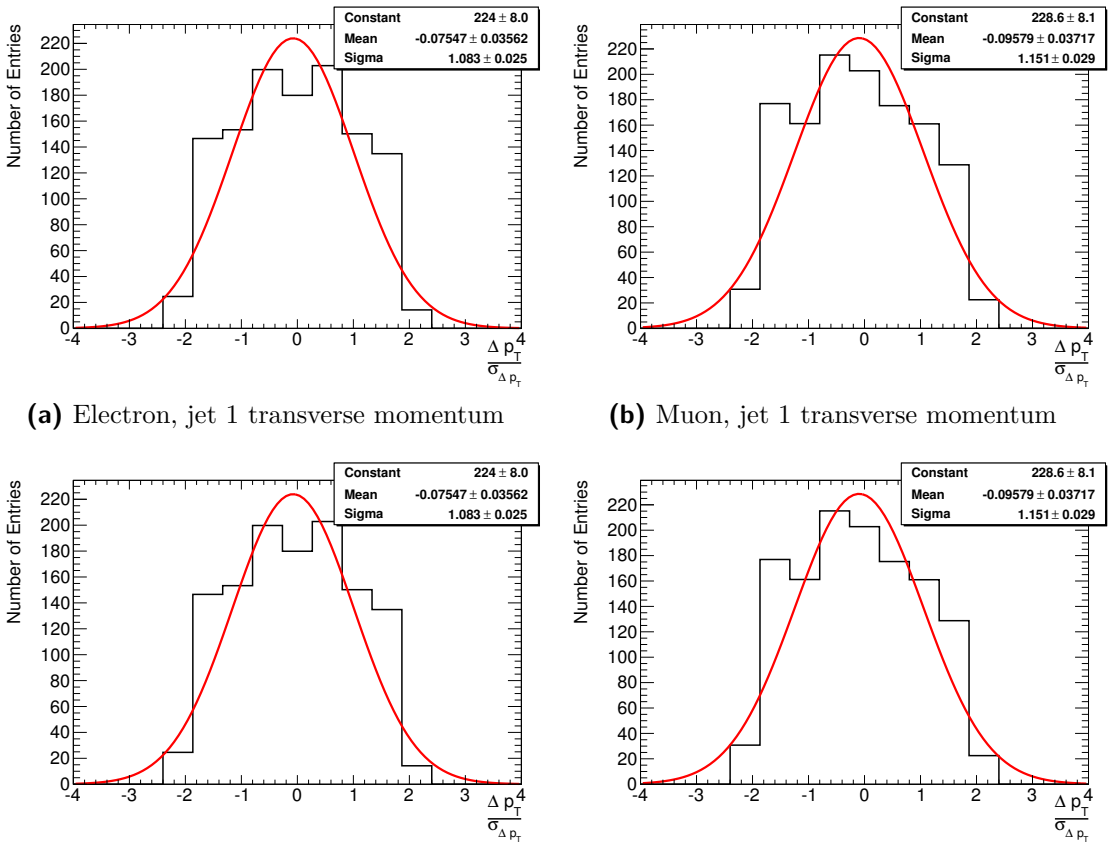

(a) Electron, jet 1 transverse momentum

(b) Muon, jet 1 transverse momentum

(c) Electron, jet 2 transverse momentum

(d) Muon, jet 2 transverse momentum

Figure 5.17. Pull distributions of the two jets entering the kinematic fit of an additional hadronically decaying W boson: For the electron channel, the pulls of the p_{T} of the first jet (a) and the second jet (c) are shown; for the muon channel, as well, the pulls of the p_{T} of the first (b) and second jet (d) are displayed. The distributions are taken from simulated events of the Wt-channel background, analyzed in the electron and muon channel in the 3-jet bin.

they look quite distorted; especially the range of high residuals is hardly populated. Since this issue is not observed for b-jets (cp. the b-jet p_{T} pulls of the main top quark fit 5.15c, 5.15d or the respective pulls of the $\mathrm{t\bar{t}}$ veto fit 5.20b, 5.20c in the following subsection) this is likely due to an inadequate description of low p_{T} jets. In the statistical determination of the jets' covariance matrices, a criterion on the relative p_{T} of the reconstructed and the hadron level jet enters the truth-matching (see Eq. (5.36)). If the relative p_{T} difference exceeds the maximum threshold for most light jets, these are seldom matched at all. The resulting covariance matrices do not properly represent the light jet kinematics and, consequently, the jets' p_{T} is greatly corrected by the fit, giving large values of the denominator $\sigma(\Delta y)$ of the pull.

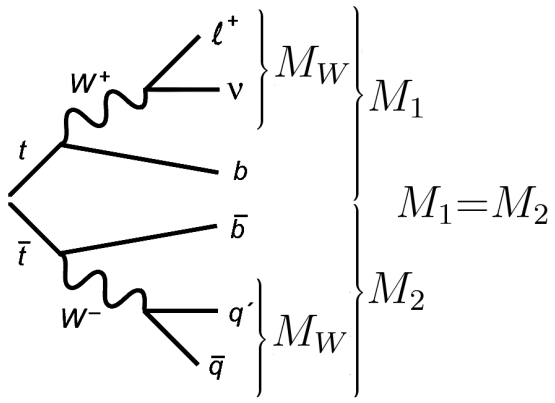

Figure 5.18. Reconstruction of a $t\bar{t}$ event by a kinematic fit with a leptonic and a hadronic W boson mass constraint and a same-mass constraint for the two top quarks.

Background Veto Fit of Semi-Leptonic $t\bar{t}$ Production

Since the $t\bar{t}$ background consists of events with two top quarks in the final state, a dedicated veto fit can be applied as indicated in Fig. 5.18. It includes two W mass constraints, a leptonic and a hadronic one, as well as a same-mass requirement for the two particles decaying into a W and a b-jet. The same-mass constraint for the top quarks means that the top mass itself is a free parameter in the fit – only the masses of the semi-leptonic top quark candidate and its hadronic counterpart must be equal, resulting in an overall NDoF = 2 for this fit.[10] Also here, Gaussian mass constraints are employed. The KinFitter setup for the $t\bar{t}$ veto fit is again given by Tab. 5.2. This veto fit can only be used if at least four jets are present and is thus only effective in the 4-jet bin. The result of this veto fit is queried after the main single top quark fit has converged and before the fit of an additional hadronically decaying W boson is done (cp. Fig. 5.9). The order of the convergence requirement of the main fit and the $t\bar{t}$ veto is to a certain extent arbitrary. It must be kept in mind, though, that the top mass does not explicitly enter the $t\bar{t}$ fit with the same-mass constraint; under the assumption that only top quarks are involved, however, any $t\bar{t}$ event should allow the main single top quark fit to converge. Only after excluding that the event is a $t\bar{t}$ event by the $t\bar{t}$ veto fit, the reconstruction of a single hadronic W boson is attempted in order to reject Wt-channel events or such $t\bar{t}$ events where the reconstruction with the same-mass constraint failed.

The $t\bar{t}$ reconstruction by kinematic fitting is technically done by a separate tool, the one developed in the analysis [Tho11]. This analysis setup is optimized to identify $t\bar{t}$ events and has thus minor differences to the setup of the main single top quark fit from Sec. 4.4.2: Here, all four jets entering the fit (two b-jets and two jets from the hadronic W decay) are required to have $|\eta| < 2.5$, regardless of the flavour (in

[10] The χ^2 distribution has 2 degrees of freedom since two m_{W} constraints and a same-mass constraint are involved and the neutrino's p_{z} is again an unmeasured quantity.

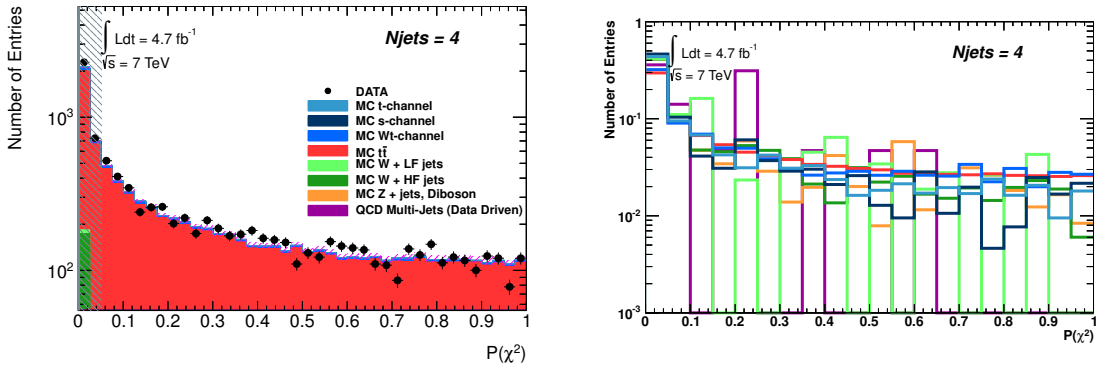

(a) Electron, $N_{\text{jets}} = 4$ **(b)** Electron, $N_{\text{jets}} = 4$

Figure 5.19. Semi-logarithmic $\mathcal{P}_{\text{t}\bar{\text{t}}}(\chi^2)$ distribution of the veto fit of semi-leptonic $\text{t}\bar{\text{t}}$ production, (a), in the 4-jet bin in the electron channel. All events with $\mathcal{P}_{\text{t}\bar{\text{t}}}(\chi^2) > 0.001$ are eventually rejected. Also shown is the corresponding $\mathcal{P}_{\text{t}\bar{\text{t}}}(\chi^2)$ distribution of the single processes, (b), where all MC distributions are normalized to unity and overlaid for shape comparison. Here, the grey vertical line indicates the veto cut used for background rejection, $\mathcal{P}_{\text{t}\bar{\text{t}}}(\chi^2) > 0.001$.

contrast to the selection of generic jets within $|\eta| < 4.5$ and the b-jets selected within $|\eta| < 2.5$ here). Furthermore, at least one b-jet is required, but the number of b-jets is not restricted to one. There is also no cut on m_{T}^{W} applied. Aside from these differences, the object and event selection is the one described in Sec. 4.4.2. In case there is only one b-tagged jet among the four jets, this b-jet must be used as the b-jet in the leptonically or the hadronically decaying top quark branch. Respecting this requirement, all possible assignments of jets to the four required jets are considered. In case several alternatives give a convergent fit, the combination yielding the lowest χ^2 value is chosen as the $\text{t}\bar{\text{t}}$ candidate. For a comprehensive description of the kinematic $\text{t}\bar{\text{t}}$ fit, see also [Tho11; Hei12] where the setup is depicted in more detail.

Here, a minimum value of $\mathcal{P}_{\text{t}\bar{\text{t}}}(\chi^2) > 0.001$ of the fit is required to classify the event as $\text{t}\bar{\text{t}}$ production. In Fig. 5.19, the $\mathcal{P}_{\text{t}\bar{\text{t}}}(\chi^2)$ distribution is shown for the electron channel in the 4-jet bin (for the corresponding figure in the muon channel, see App. C), and the veto cut is indicated. Since the $\text{t}\bar{\text{t}}$ fit is done with a slightly different object and event selection, as stated above, and also prior to the main single top quark fit[11], the $\mathcal{P}_{\text{t}\bar{\text{t}}}(\chi^2)$ and pull distributions shown in this section refer to this analysis setup they are optimized on.[12] The discriminatory power of this cut is illustrated on the right hand side of Fig. 5.19 where the $\mathcal{P}_{\text{t}\bar{\text{t}}}(\chi^2)$ distribution of the overlaid MC samples, normalized to unity, is displayed. As in the case of the hadronic W boson veto fit, the t-channel distribution is seen to increase towards the low end of

[11] The result of the $\text{t}\bar{\text{t}}$ veto fit, however, is only queried after convergence of the single top quark fit.

[12] This implies that the convergence criterion of the single top quark fit is not necessarily fulfilled for the events entering the histograms.

the p-value range whereas the $\mathrm{t\bar{t}}$ distribution is rather flat throughout the whole range of p-values. Quantitatively, the cut on $\mathcal{P}_{\mathrm{t\bar{t}}}(\chi^2)$ reduces the $\mathrm{t\bar{t}}$ and Wt-channel background by 44 % and 36 %, respectively, at a signal cost of 13 %. Since the 4-jet bin is completely dominated by $\mathrm{t\bar{t}}$, this raises the signal-to-background ratio from 5 % to 7 %. The additional cuts on $\mathcal{P}_{\mathrm{W_{had}}}(\chi^2)$ and $\mathcal{P}_{\text{main fit}}(\chi^2)$ increase this ratio further to 8 % and 9 %, respectively, by cutting away another 21 % and 41 % of $\mathrm{t\bar{t}}$. The associated signal loss is 8 % and 31 %. Hence, the hadronic W veto, succeeding the cut on $\mathcal{P}_{\mathrm{t\bar{t}}}(\chi^2)$, is just as effective in the 4-jet bin as the $\mathrm{t\bar{t}}$ veto, and should not be skipped. In view of the performance of the hadronic W fit in the 3-jet bin as well as the decreasing discriminatory power of the cut on $\mathcal{P}_{\text{main fit}}(\chi^2)$ with increasing jet multiplicity, these numbers motivate the use of dedicated veto fits for background topologies.

The pull plots of the p_{T} of all physical objects used in the $\mathrm{t\bar{t}}$ veto fit (four jets, the signal lepton and the $E_{\mathrm{T}}^{\mathrm{miss}}$), taken from the $\mathrm{t\bar{t}}$ MC sample, are shown in Fig. 5.20 for the electron channel in the 4-jet bin; the corresponding pull distributions of the object kinematics for the muon channel look similar and are thus omitted here for the sake of brevity. The pull histograms are filled only for events passing the selection of the $\mathrm{t\bar{t}}$ analysis. The overall good agreement of the pull distributions with standardized Gaussian distributions allows to conclude that the quality of the kinematic $\mathrm{t\bar{t}}$ veto fit is good: For the leptonic top quark branch, the pulls' bias exhibits the same sign tendencies as in the main top quark fit (cp. Fig. 5.15), but the excursions are smaller. In the hadronic top quark branch, the pulls of the two light jets from the hadronic W boson, however, display the same distortions as mentioned in the last subsection and the same comments apply here. Also in the $\mathrm{t\bar{t}}$ veto fit, the pulls are slightly broadened, although the effect is smaller than in the main top quark fit. This could partly be due to the fact that three times as many $\mathrm{t\bar{t}}$ events than single-top events underlie the statistical determination of the covariance matrices (cp. Tab. 4.2) and hence, the kinematics of the $\mathrm{t\bar{t}}$ topology is modelled better, giving well-balanced values of the denominator $\sigma(\Delta y)$ of the pull. Another reason could be that in the $\mathrm{t\bar{t}}$ topology in the 4-jet bin each jet is needed for the complete reconstruction of the top quark pair, and, in contrast to the main fit of a single top quark, the $\mathrm{t\bar{t}}$ analysis tests all possible combinations of jets and picks the best one. Thus, the model expectation is fulfilled more often and reasonable residuals result.

5.2.4. Event Yields

In Tab. 5.3, the final event yields that result from the kinematic fitting analysis after all cuts are quoted for all analysis channels, and the corresponding signal-to-background ratios are listed. As can be seen, the data statistics decreases with increasing jet multiplicity: There is almost a factor of two between the 2- and 3-jet bin yields, and the number of events in the 2-jet bin is five times that in the 4-jet bin. As expected, the signal-to-background ratio is at its best in the 2-jet bin and amounts to 20 %, whereas it is about the same, namely 10 %, for the 3- and 4-jet bins. The first drop of S/B by 10 % is due to the $\mathrm{t\bar{t}}$ yield that is the only one to increase

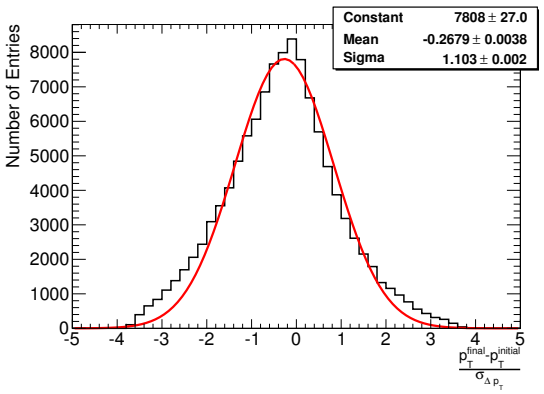

(a) Electron transverse momentum

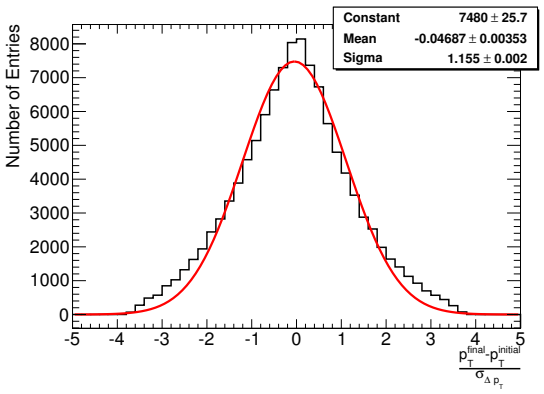

(b) Electron, hadr. b-jet transverse momentum

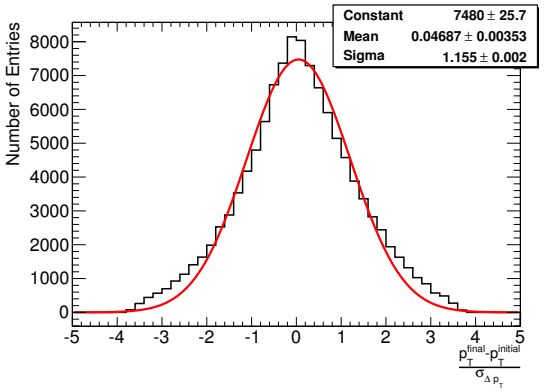

(c) Electron, leptonic b-jet transverse momentum

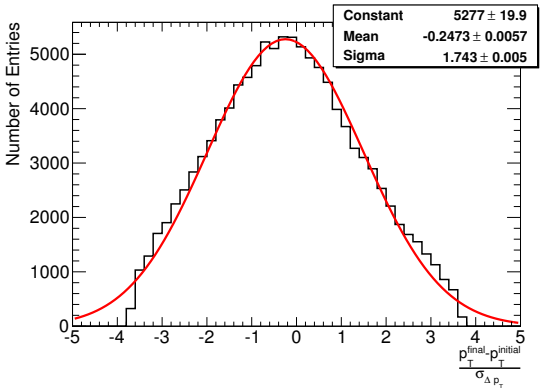

(d) Electron, jet 1 transverse momentum

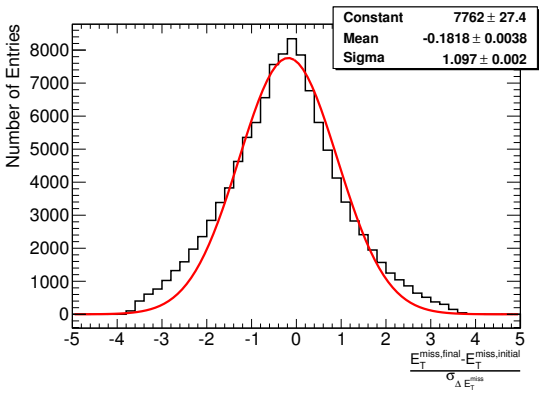

(e) Electron, $E_{\mathrm{T}}^{\mathrm{miss}}$ magnitude

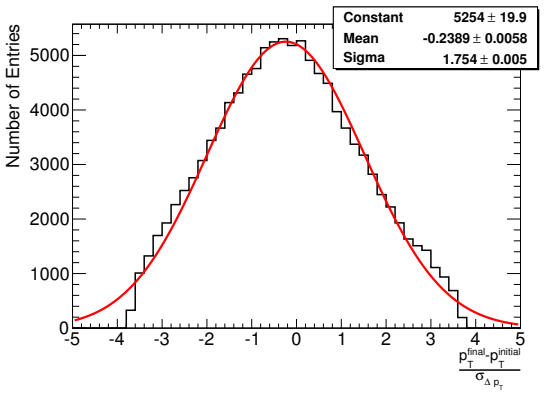

(f) Electron, jet 2 transverse momentum

Figure 5.20. Pull distributions of the transverse momenta of the objects used in the $\mathrm{t\bar{t}}$ veto fit. On the left hand side, the pulls associated with the semi-leptonically decaying top quark are displayed: The pulls of the p_{T} of the electron (a), of the p_{T} of the b-jet (c) and of the magnitude of the $E_{\mathrm{T}}^{\mathrm{miss}}$ (e) are shown. On the right hand side, the pulls associated with the hadronically decaying top quark are shown: the pulls of the p_{T} of the b-jet (b), of the p_{T} of the first jet from the W decay (d) and the second jet from the W decay (f). The distributions are taken from simulated $\mathrm{t\bar{t}}$ events in the electron channel in the 4-jet bin.

	Electron			Muon		
Process	2 Jets	3 Jets	4 Jets	2 Jets	3 Jets	4 Jets
Data	5896.00	3430.00	1113.00	6641.00	4130.00	1263.00
t-Channel	937.41	363.55	100.61	1102.80	419.29	113.32
Total Background	4680.76	3240.06	1029.77	5526.45	3663.01	1216.18
s-channel	53.48	15.33	2.46	65.34	19.50	3.31
Wt-channel	207.10	138.82	35.35	237.97	168.08	39.97
$t\bar{t}$	1190.24	1990.98	828.77	1367.31	2288.75	965.69
W+LF	259.49	56.25	7.47	351.67	96.43	16.97
W+HF	2442.45	742.13	132.93	2976.05	893.50	162.95
Z, Diboson	146.10	67.94	16.80	136.47	42.71	8.07
QCD	381.90	228.60	6.01	391.64	154.06	19.23
S/B	0.20	0.11	0.10	0.20	0.11	0.09

Table 5.3. Final event yields of all processes and signal-to-background ratios for all analysis channels.

from the 2- to the 3-jet bin. From the 3- to the 4-jet bin, the W+HF contribution is reduced by a factor of six, but the $t\bar{t}$ rate drops only by a factor of 2.5 opposed to a signal reduction by a factor of 3.5, resulting in a stable signal-to-background ratio. Despite the fair S/B in the 4-jet bin, the small overall statistics hinders the exploitation of the information from this channel, as detailed in the next chapter.

Der Worte sind genug gewechselt,
lasst mich auch endlich Taten sehn.
Johann Wolfgang von Goethe, Faust I

6. Analysis Results

With the full analysis setup discussed in the previous chapter, the procedure of finally extracting the single-top t-channel cross-section is the topic of this last chapter. It is understood that the final cross-section result includes uncertainties associated with the limited statistics of the data and MC samples utilized; however, the cross-section determination also suffers from systematic uncertainties of the reconstruction methods. The different sources leading to systematic uncertainties that enter the cross-section result are depicted and quantified in Sec. 6.1. The manner of signal extraction itself, considering all of these systematic uncertainties, is then detailed in Sec. 6.2: The template-fitting tool BILL (BInned Log Likelihood) is applied for the extraction of the cross-section, as described in Sec. 6.2.1, as well as for the computation of the total cross-section uncertainty and of the significance of the analysis result, outlined in Sections 6.2.2 and 6.2.3, respectively. The final cross-section results are then presented in Sec. 6.2.4.

6.1. Sources of Systematic Uncertainties

Several sources of systematic errors are taken into account and evaluated following the standard prescriptions released by the top physics working group of ATLAS [Ach+12] and according to the recommendations of the ATLAS combined physics performance teams. They can be subdivided into the two general classes of uncertainties ascribed to the modelling of physics processes, outlined in Sec. 6.1.1, and to the detector modelling, described in Sec. 6.1.2. Each systematic variation entails a symmetrical excursion of the parameter to be investigated (2-sided systematics), resulting in an upward and a downward variation of the nominal analysis results.

6.1.1. Monte Carlo Simulation

Parton Distribution Functions

The parton distribution functions used in the MC event generation process are associated with systematic uncertainties. First of all, since the PDF sets are themselves extracted from fits to experimental data, they possess an intrinsic uncertainty; this so-called "intra-PDF" uncertainty is considered by comparing the analysis results on the "best fit set" (also denoted "central value set") with those on dedicated "error PDF sets" provided for each particular choice of PDF set. The exact prescriptions on how to employ the error PDF sets to evaluate the *intra-PDF* uncertainty can differ from one PDF set to another. In this study, three different PDF sets with their

respective error PDFs were considered for all analyzed MC samples in a fully correlated way, respectively: CT10 [Lai+10], MSTW2008nlo [Mar+09b] and NNPDF20 [Bal+10]. CT10 offers 52 error PDFs, and its *intra-PDF* uncertainty for an observable X is computed via a method called the "symmetric Hessian" as

$$\delta X = \frac{1}{2}\sqrt{\sum_{i=1}^{n}(X_{i,+} - X_{i,-})^2}\,, \tag{6.1}$$

where $X_{i,\pm}$ denote the values of the observable on the error PDF sets gained from varying parameter i of the n uncorrelated parameters of the PDF set up and down by one σ. In contrast, the MSTW2008nlo contains 42 error PDFs, and its *intra-PDF* uncertainty is obtained by employing an "asymmetric" Hessian,

$$\delta X_{\text{up}} = \sqrt{\sum_{i=1}^{n}(X_i - X_0)^2} \quad \text{if } (X_i - X_0) > 0\,, \tag{6.2}$$

$$\delta X_{\text{down}} = \sqrt{\sum_{i=1}^{n}(X_i - X_0)^2} \quad \text{if } (X_i - X_0) < 0\,, \tag{6.3}$$

with X_0 denoting the value of the observable on the central value PDF set. The NNPDF20 PDF set, finally, does not possess a best fit PDF set or error PDFs, but instead consists of an ensemble of PDFs extracted from fits to the input data; here, the best fit set is the mean of the ensemble, and its uncertainty is simply given by the sample standard deviation of the ensemble mean $\bar{X}$, i.e.

$$\delta X = \sqrt{\frac{1}{n-1}\sum_{i=1}^{n}(X_i - \bar{X})^2}\,. \tag{6.4}$$

Furthermore, the choice of PDF set in the first place generates an additional uncertainty: This error, associated with switching PDF sets, is called "inter-PDF" uncertainty. The *inter-PDF* uncertainty is evaluated by comparing the central value sets of the two given PDF sets. The combined PDF error from *intra-* and *inter-PDF* uncertainties is then estimated via the total envelope that results for the given observable in the analysis [Bot+11]: This means that all *intra-PDF* uncertainties of the given PDF sets are evaluated first and then the combined error is defined as half the width of the envelope formed by the overall minimum and maximum deviations for the observable in question.[1]

In general, these two PDF uncertainties can be assessed by iterating the analysis on several sets of all signal and background MC samples that are produced employing different PDF sets and different fits of each PDF set. In practice, however, the much more economic method of PDF reweighting [CHS07; WBG05] is used: Each event in

[1] Thus, the symmetric total PDF error interval is not determined around the nominal central value PDF set of the analysis; once computed, it is applied to this nominal PDF, though.

the sample produced with the central value set of the nominal PDF set, here denoted by PDF_0, is reweighted in order to mirror the impact of a modified PDF set PDF_1 (this can belong to an *intra-* or an *inter-PDF* uncertainty). This event weight reads[2]

$$W_{\mathrm{PDF}} = \frac{\mathrm{PDF}_1(x_1, f_1, Q^2) \cdot \mathrm{PDF}_1(x_2, f_2, Q^2)}{\mathrm{PDF}_0(x_1, f_1, Q^2) \cdot \mathrm{PDF}_0(x_2, f_2, Q^2)}\,, \tag{6.5}$$

where x_1, x_2 are the partonic momentum fractions, f_1, f_2 denote the particle types of the partons involved and Q^2 is the energy scale of the interaction (cp. Eq. (2.31)). The reweighting method has been implemented for this analysis in [Sta13b] and is well documented.[3]

Thus, the two resulting shifted analysis outcomes (combined error associated with the PDFs varied upward and downward) are passed to the signal extraction fit as a systematic variation.

MC Matrix Element Generators

A systematic uncertainty of the analysis is expected to result from the choice of a particular MC matrix element generator. In this study, the effect of varying the matrix element generator of the single-top t-channel and the $\mathrm{t\bar{t}}$ MC samples is assessed in an uncorrelated manner, i.e. only one of these processes is varied up or down at a time.

For the t-channel (all lepton flavours), the uncertainty is estimated by comparing the p_{T} distribution of the spectator b-quark from the gluon splitting in the initial state, obtained from the AcerMC sample listed in Tab. 4.2, with the one originating from a NLO calculation in the four-flavour scheme[4] [Cam+09] using the MCFM tool [CE10; CE00]: A percental difference of 7.1 % is observed [ATL12i]. The corresponding variation sample is thus constructed by shifting the nominal t-channel yields, already normalized to the data luminosity, up and down by this constant fraction, e.g.

$$N_{t\text{-channel}} \cdot (1 \pm 0.071)\,. \tag{6.6}$$

For the $\mathrm{t\bar{t}}$ case, a sample produced with an alternative generator, POWHEG-BOX [Nas04; FNO07] instead of MC@NLO, is considered (the parton shower part is still provided by Herwig/Jimmy). A major difference of MC@NLO and POWHEG-BOX resides in the way of treating the first emission of the parton shower in order to match the matrix element to the shower [Buc+11a]. The systematic variation is then

[2] D. B. Ta. *ATLAS TWiki: Top PDF Uncertainty*. Aug. 2012. URL: `https://twiki.cern.ch/twiki/bin/viewauth/AtlasProtected/TopPdfUncertainty`.

[3] S. Stamm. *PdfReweightingTool Reference Guide*. Dec. 2013. URL: `https://ms2.physik.hu-berlin.de/~stamm/PdfReweightingTool/htmldoc/index.html`.

[4] The NLO calculation is done based upon the $2 \to 3$ process shown in Fig. 2.12a instead of the $2 \to 2$ process of Fig. 2.11a. Whereas the calculation of the latter in the so-called five-flavour scheme implies the use of a b-quark PDF and neglects all effects from the "spectator b-quark", the former four-flavour scheme keeps a finite b-quark mass and is able to model the spectator b-quark's kinematics.

obtained as

$$N_{\mathrm{t\bar{t}}} \pm (N_{\mathrm{t\bar{t}},\ \text{POWHEG-BOX}} - N_{\mathrm{t\bar{t}}})\,. \tag{6.7}$$

The four thus modified analysis results regarding the matrix element generator choice (upward and downward variation for each of the two channels separately) are passed to the BILL fit as systematic variations.

Parton Shower Modelling

Also the choice of the PS generator has an impact on the expected MC event yields. Here, only variations of the $\mathrm{t\bar{t}}$ MC sample are considered since for the t-channel, there is no comparison sample available at the time of this analysis to assess the PS generator systematic variation.[5]

For $\mathrm{t\bar{t}}$-production, the difference between a POWHEG-BOX+Herwig/Jimmy and a POWHEG-BOX+Pythia variant is evaluated and symmetrized around the nominal MC@NLO+Herwig/Jimmy sample:

$$N_{\mathrm{t\bar{t}}} \pm (N_{\mathrm{t\bar{t}},\ \text{POWHEG-BOX+Herwig/Jimmy}} - N_{\mathrm{t\bar{t}},\ \text{POWHEG-BOX+Pythia}})\,. \tag{6.8}$$

Thus, for the PS modelling two modified analysis results are passed to BILL as systematic variations.

Initial and Final State Radiation

The impact of the uncertainty related to the modelling of the initial and final state radiation (ISR/FSR) is estimated in a correlated way for all single-top channels (t-channel, Wt-channel and s-channel) and $\mathrm{t\bar{t}}$ production from a set of AcerMC+Pythia samples for the respective processes. These samples are generated with different tunes of the parameters PARP(67) and PARP(64), directly controlling the ISR/FSR emissions in Pythia. The parameters are varied by a factor of 2 up and down, resulting in more or less underlying event activity. These parameter variations are constrained by a study on collision data [ATL12m]. In this analysis, the associated systematic variation of the yields is implemented as

$$N_{\mathrm{nominal}} \pm \frac{1}{2}(N_{\mathrm{moreIFSR}} - N_{\mathrm{lessIFSR}})\,. \tag{6.9}$$

The two resulting shifted analysis outcomes (upward and downward for each channel, respectively) are then passed to the BILL fit as a systematic variation.

Theoretical Cross-Section Normalization

For most background samples, the production cross section predictions from Tab. 4.2 are used to compute the number of expected events. For the $\mathrm{t\bar{t}}$, Z+jets, diboson and

[5] This is quite a shortcoming since the PS generator systematic of the signal channel could have a large impact on the total systematic error of the analysis.

single-top backgrounds, the errors from the theory computation are used to assign an uncertainty on the rate prediction entering the signal extraction fit. These rate uncertainties are collected in Tab. 6.2.

QCD Background Normalization

The QCD background is normalized to data by the fitting method employed for the jet-electron sample (electron and muon channel), cp. Sec. 4.3.1. In compliance with the instructions of the authors of the QCD estimate, a systematic uncertainty of 50 % is assigned to the QCD yield from this fit [ATL12i]. It originates from a comparison with an alternative QCD estimate by the so-called "Matrix Method"[6] [Abi+10], and also from a consideration of pile-up effects. Whilst the rate uncertainty of the QCD contribution is set to zero in the BILL fit of the nominal analysis results (see Tab. 6.2), a dedicated systematic is defined with the nominal analysis results in which the QCD yields are varied up and down by 50 %. These two additional shifted analysis results are then passed to the BILL fit as a systematic variation.

This method of treating the QCD cross-section uncertainty has been criticized in [Sta13b], pointing out that this way, the QCD contribution itself cannot be adapted in the QCD systematic fit (cp. Sec. 6.2.2 for details on the error computation); thus, no further information on the only roughly known normalization can be gained. Moreover, by neglecting the QCD cross-section uncertainty in the extraction of the signal cross-section on the nominal analysis sample, correlations of the QCD background rate with the rates of all other processes are ignored, and it is furthermore also assumed that the QCD fraction and shape are independent of any other systematic variation (except for the W+jets systematic described in the next paragraph).

W+Jets Background Normalization

As detailed in Sec. 4.3.2, the normalization of the W+jets background is extracted by a data-driven approach using a fitting procedure based upon the notion of charge asymmetry and the event counts in the *pretag* and *tag* selections. The sources of the errors associated with these input yields include

- the uncertainty on the expected number of events of $t\bar{t}$, Wt-channel, the other single-top channels (t- and s-channel are combined here), Z+jets, diboson and QCD multi-jet production,
- the statistical errors on the determinations of the heavy flavour fraction scale factors K_{c}, K_{cc} and K_{bb}, as well as on the overall normalization scale factor W_{norm}, obtained from pseudo-experiments on the data yields,

[6] This method employs efficiencies of a *tight* lepton selection w.r.t. to a *loose* one as well as the overall number of events in the *tight* and *loose* samples to determine the fractions of real and fake lepton events in the *tight* selection in collision data, where the number of fake lepton events is virtually identical to the QCD background; a detailed description of the method can be found e.g. in [Pro12].

Error Source	Variation up/down [%]
Event Yields	
$t\bar{t}$	+9.9/-8.94
Wt-channel	+7.4/-7.4
t- and s-channel	+100/-100
Z+jets	+60/-60
Diboson	+5/-5
QCD multi-jets	+50/-50
Scale Factor Statistics	
K_{c}	$+\sigma_{\mathrm{c}}/-\sigma_{\mathrm{c}}$
K_{cc}	$+\sigma_{\mathrm{cc}}/-\sigma_{\mathrm{cc}}$
K_{bb}	$+\sigma_{\mathrm{bb}}/-\sigma_{\mathrm{bb}}$
W_{norm}	$+\sigma_{\mathrm{norm}}/-\sigma_{\mathrm{norm}}$
Charge Misidentification	+1/-1

Table 6.1. Sources of systematic uncertainties in the extraction of the W+jets overall normalization factor and their percental variations considered. σ_{xx} denotes the standard deviation of the normalized Gauss distribution resulting from the respective pseudo-experiment.

- the uncertainty associated with a charge misidentification of the lepton involved since the charge asymmetry of the lepton in the final state is exploited.

The exact values of the above uncertainties are listed in Tab. 6.1 and are, aside from the statistical errors on the scale factors, independent of the lepton channel. To conclude on the impact of a systematic, the source of the systematic error is subjected to an upward/downward variation and the scale factor W_{norm} is extracted anew from the shifted yields. In the end, the overall error on the W+jets normalization is computed by quadratically summing up the relative deviations with respect to the nominal case, resulting from all systematic error sources j listed in Tab. 6.1,

$$\delta W_{\mathrm{norm}} = \frac{W^{j}_{\mathrm{norm}} - W_{\mathrm{norm}}}{W_{\mathrm{norm}}} \,. \tag{6.10}$$

This is done separately for the positive ($\delta W_{\mathrm{norm}} > 0$) and negative ($\delta W_{\mathrm{norm}} < 0$) contributions, and the square root is taken, respectively. The error computation is done jet bin- and lepton channel-wise, but since the results do not vary much, the largest error is chosen as a conservative estimate, amounting to $\pm(4.5)/(8.2)/(12.5)\%$ for the (2)/(2+3)/(2+3+4) jet bin combinations, respectively. This symmetrical total error of the W+jets normalization is then propagated to the event rate uncertainties used in the final signal extraction fit which are shown in Tab. 6.2.

W+Jets Flavour Fraction Scale Factors

As outlined in Sec. 4.3.2, the W+jets overall normalization scale factor is determined simultaneously with the flavour fraction scale factors. The intrinsic uncertainties related to the estimation of the W+jets flavour fraction scale factors are therefore estimated in an analogous manner to the error of the overall normalization scale factor in the previous paragraph. Aside from the W+jets overall normalization, there is a remaining shape-uncertainty originating from the unknown

- relative amounts of W+LF and W+HF events,
- relative yields of W+c and the combined W+cc/W+bb contribution.[7]

As described above, the underlying yields of the scale factor estimation are shifted according to the systematics listed in Tab. 6.1 and the scale factors are extracted anew. However, in contrast to the above treatment, the resulting scale factors K_{LF}, K_{c}, K_{cc} and K_{bb} are applied to the nominal yields, thus providing four additional systematically shifted analysis results that are passed to the BILL fit: two for the upward/downward variation of the ratio of W+LF and W+HF events, $R_{\mathrm{LF/HF}}$, and two for varying the ratio of W+c to the sum of W+cc and W+bb events, $R_{\mathrm{c/ccbb}}$. Hence, these systematic contributions are assessed for each jet bin and lepton channel of the analysis.

6.1.2. Detector Modelling

Lepton Energy Scale and Resolution

The effect of the lepton energy scale on the acceptance is taken into account by applying a variation of one standard deviation on the lepton $E_{\mathrm{T}}/p_{\mathrm{T}}$ in the MC simulation samples. For electrons, the dominant uncertainties originate from the dependence of the electron cluster energy scale s_{cluster} on the detector material and the presampler energy scale (see Sec. 4.4.1), amounting to a total error of about $\pm 1.5\,\%$ [Ach+12]. For the muons, the analogous uncertainty is estimated by the difference of applying the p_{T} scale and not applying it, and then using this shift to define a symmetrical error around the values using the nominal scale.[8] To this end, the analysis yields of the upward and downward variation samples are computed according to

$$N_{\mathrm{nominal}} \pm (N_{\mathrm{scaled}} - N_{\mathrm{nominal}})\,. \tag{6.11}$$

Lepton energy and momentum resolution effects are also included in the treatment of systematic errors by shifting up and down the central smearing values on the MC samples. As outlined in Sec. 4.4.1, the energy/momentum smearing is applied differently in the electron and in the muon case: In contrast to the electron

[7] The relative fractions of W+cc and W+bb events have already been fixed for the scale factor estimate, cp. Sec. 4.3.2.

[8] M. Owen. *ATLAS TWiki: Top Common Scales 2011*. July 2012. URL: `https://twiki.cern.ch/twiki/bin/viewauth/AtlasProtected/TopCommonScales2011`.

energy measurement, the muon momentum measurement combines the uncorrelated information from both the ID and the MS systems; the systematic effects of both resolutions are therefore considered separately.

The analysis is rerun on the samples modified by the upward and downward scale (only one scaled version in the muon case) and resolution variations, respectively, and the ten results are then passed to the signal extraction fit. Thus, the related systematic uncertainties are propagated through the full analysis chain in order to assess their impact on the selection acceptance.

Lepton Selection Efficiency Scale Factors

As described in Sec. 4.4.3, scale factors for event reweighting are applied to correct the lepton reconstruction, identification and trigger efficiencies in MC simulation samples to those in data. The scale factors are derived from Z and W decays in data, and their corresponding uncertainties are evaluated by varying the lepton and signal selections as well as the normalizations of the backgrounds subtracted from data. In order to propagate the resulting uncertainties to the final analysis result, an upward/downward variation of one standard deviation (typically of the order of 3 % for electrons and 1.5 % for muons [Ach+12]) is applied to the total scale factor associated with the lepton in the selected MC events. The two analysis results thus modified are passed to the BILL fit for the corresponding lepton channel considered (the electron scale factor systematic is only applied in the electron channel and the muon scale factor systematic only in the muon channel).

Pile-Up Effects

The pile-up modelling is done by reweighting the events in all MC samples to match the $\langle\mu\rangle$ distribution (average interactions per bunch crossing) seen in data, as described in Sec. 4.4.3. There is no single dedicated pile-up systematic performed that rigorously propagates the error on this pile-up event reweighting to the final analysis results. However, pile-up uncertainties are already included in the total systematic uncertainty assumed for the scales of calorimeter objects (electrons, jets) as well as in the flavour tagging and JVF scale factor systematic variations. An exception is the $E_{\mathrm{T}}^{\mathrm{miss}}$ for which a dedicated pile-up systematic is evaluated: A scale uncertainty of the Jet, SoftJet and CellOut terms of the $E_{\mathrm{T}}^{\mathrm{miss}}$ (cp. Sec. 3.3.6) of 6.6 % was determined from comparing the $\langle\sum E_{\mathrm{T}}\rangle$ distribution dependent on the number of primary vertices in $\mathrm{Z} \to \mu\mu$ events in data to the one in MC using three different η ranges (central, end-cap, forward region) [Ach+12];[9] the ratio of $\langle\sum E_{\mathrm{T}}\rangle$ in data and MC was then fitted to the expectation of a flat line, respectively, and the mean deviations of the values in data to this fit, $\Delta(\sum E_{\mathrm{T}})_{\eta}$, were combined to

[9] V. Kaushik. *ATLAS TWiki: Top Etmiss Liaison Moriond 2012*. Feb. 2012. URL: https://twiki.cern.ch/twiki/bin/viewauth/AtlasProtected/TopETmissLiaisonMoriond12.

yield the final systematic uncertainty of the $E_{\mathrm{T}}^{\mathrm{miss}}$ due to pile-up effects:

$$\Delta E_{\mathrm{T}}^{\text{pile-up}} = \sqrt{2}\left(\sum_{\eta \text{ regions}} \Delta^2 (\sum E_{\mathrm{T}})_{\eta} \right)^{1/2} . \tag{6.12}$$

This systematic is thus realized by scaling the Jet, SoftJet and CellOut terms of the $E_{\mathrm{T}}^{\mathrm{miss}}$ upward and downward by 6.6 %, respectively, rerunning the analysis and passing the resulting two modified analysis outcomes to the BILL fit as a systematic variation.

Jet Energy Scale

The determination of the EM+JES calibration depicted in Sec. 3.3.4 is affected by many sources of systematic uncertainties [Ado+12]:

- The three different *in situ* calibration techniques employed suffer from systematic uncertainties related to the fact that the assumed p_{T} balance between the jet and the respective reference object is only approximately fulfilled as well as from systematic uncertainties of this reference object itself. Including also statistical uncertainties, there are all in all 54 uncertainty sources associated with the *in-situ* calibration step that can be classified as originating from effects of either the detector or the physics modelling, or from a combination of detector and physics modelling effects, or from statistics and the analysis methods utilized. However, by virtue of a covariance matrix diagonalization method accounting for correlations of the different sources with sufficient accuracy and with the restriction to the range $p_{\mathrm{T}}^{\mathrm{jet}} < 600\,\mathrm{GeV}$, the number of uncertainty sources can be reduced to 6 [Ach+12]. The overall JES uncertainty of the *in-situ* calibration is obtained from a combination of the uncertainties of the three techniques and amounts to about 2.5 % for $p_{\mathrm{T}}^{\mathrm{jet}} = 25\,\mathrm{GeV}$, decreasing to below 1 % for $55\,\mathrm{GeV} \leq p_{\mathrm{T}}^{\mathrm{jet}} \leq 500\,\mathrm{GeV}$. There is an increased uncertainty for forward jets ($|\eta| > 1.2$) that for very forward low p_{T} jets ($p_{\mathrm{T}} \approx 25\,\mathrm{GeV}$, $|\eta| \approx 4$) can be as large as 6 %.
- An additional source of error in the JES computation arises from light jet flavour response uncertainties: Since dedicated event signatures with p_{T} balances of a jet and a reference object are used to derive the *in-situ* calibration, they are likely biased towards jets induced by high-p_{T} quarks whilst analysis samples also abundantly contain gluonic jets. Therefore, the impact of fragmentation differences of quark and gluon initiated jets on the jet response is quantified by assigning a systematic error that is analysis-dependent. Also an a priori uncertainty on the flavour composition of light jets is considered that is MC sample-dependent.
- Jets originating from b-quarks are treated separately with a dedicated p_{T}-dependent b-JES uncertainty quantifying the error associated with the calorimeter response to b-jets. It is applied to b-tagged jets instead of the light jet

flavour composition uncertainty depicted in the last item. This uncertainty is estimated from MC and validated on data by a comparison of track jets and calorimeter b-jets and is found to be less than 2.5 %.

- Since the JES calibration is determined on isolated jets from MC, the effect of close-by jet topologies on the calorimeter jet response needs to be considered as another systematic uncertainty. To this end, the p_{T} ratios of calorimeter jets matched to track jets are studied dependent on the distance of the main jet to a close-by jet in the calorimeter: A threshold of $\Delta R < 1.0$ is defined for non-isolated jets, and the ratio of calorimeter/track jet p_{T} ratios of non-isolated and isolated jets compared between data and MC simulation. The corresponding JES uncertainty is about 2 % to 3 % for $p_{\mathrm{T}}^{\mathrm{jet}} < 100\,\mathrm{GeV}$.

- Another non-negligible contribution to the total JES uncertainty originates from the error on the pile-up offset correction applied in the very first step of the jet calibration (see Fig. 3.13): The effect of a mismodelling of the pile-up offset in the MC is analyzed by studying $p_{\mathrm{T}}^{\mathrm{jet}}$ w.r.t. a stable reference (e.g. a track jet associated with the primary vertex) as a function of N_{PV} and μ in a data sample. The ratio of the offsets in data and MC gives the corresponding JES uncertainty, amounting to at most 3 % for $p_{\mathrm{T}}^{\mathrm{jet}} > 40\,\mathrm{GeV}$ and the highest pile-up conditions in the year 2011.

The last four items above refer to uncertainties dependent on the analysis selection at hand. An example distribution for the composition of the total JES uncertainty resulting from all listed contributions as a function of $p_{\mathrm{T}}^{\mathrm{jet}}$ is shown in Fig. 6.1a for forward light jets and in Fig. 6.1b for central b-jets from a semi-leptonic $\mathrm{t\bar{t}}$ selection. The analysis is rerun on the two samples modified by an upward and a downward variation of the total JES uncertainty, and the resulting distributions are passed to the BILL fit as a systematic variation. Obviously, the systematic effect of the JES increases when considering higher jet bins of the analysis.

Jet Energy Resolution

Although there is no need for a jet energy resolution (JER) smearing in MC, as mentioned in Sec. 4.4.1, a possible systematic effect is probed by applying a one-sided smearing of the JER according to the 1-σ error of the *in-situ* techniques employed to establish this agreement of MC and data. The two *in-situ* techniques used are the dijet balance method and the bisector method [Rom+11]: In the dijet balance method, events with two back-to-back jets in the same y (defined in Eq. (3.1)) region, assumed to be balanced in p_{T}, are required and a Gaussian fit to the asymmetry of their transverse momenta

$$A(p_{\mathrm{T},1}, p_{\mathrm{T},2}) = \frac{p_{\mathrm{T},1} - p_{\mathrm{T},2}}{p_{\mathrm{T},1} + p_{\mathrm{T},2}} \tag{6.13}$$

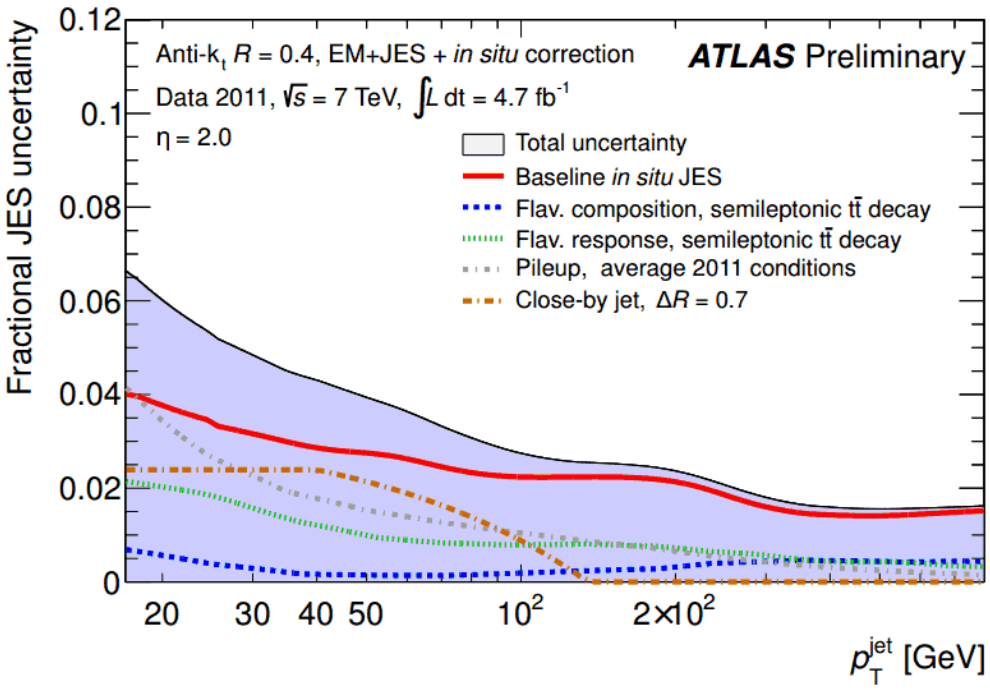

(a)

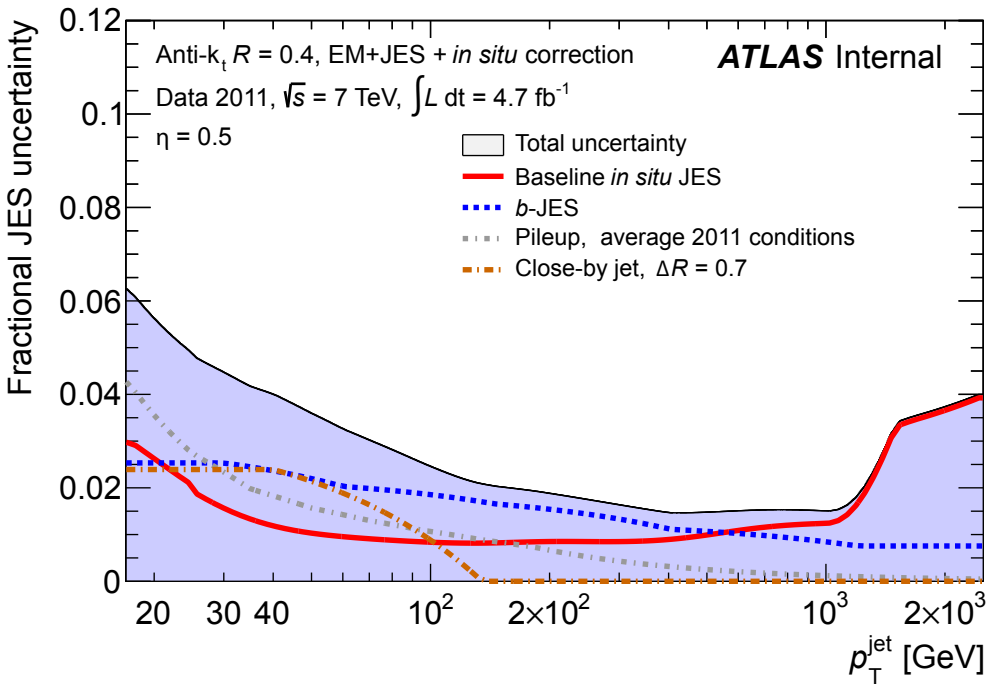

(b)

Figure 6.1. Jet energy scale systematic uncertainties for anti-k_T ($R = 0.4$) EM+JES light jets with $\eta = 2$ (a) and b-jets with $\eta = 0.5$ (b) from a semi-leptonic $t\bar{t}$ selection, dependent on p_T^{jet}. The different contributions of the overall uncertainty are shown as well as the total resulting JES uncertainty [Ado+12].

is exploited to conclude on the JER, i.e. $\frac{\sigma_{p_\mathrm{T}}}{p_\mathrm{T}}$ of the jet. Alternatively, the bisector method is based upon the definition of a transverse momentum imbalance vector $p_\mathrm{T}^\mathrm{imb}$ which is defined as the vector sum of the two leading jets in the dijet event, again required to be in the same y region. Two sectors are then formed by placing one axis of the coordinate system at half the opening angle between the two jets and considering the projections of $p_\mathrm{T}^\mathrm{imb}$ onto the thus newly defined axes ($p_\mathrm{T}^\mathrm{imb} = 0$ for a perfectly balanced dijet event). These projections are expected to display the same non-zero variance at the particle level due to isotropic ISR w.r.t. that coordinate system. Deviations from this behaviour are again a measure of $\frac{\sigma_{p_\mathrm{T}}}{p_\mathrm{T}}$. The total JER uncertainty is then obtained from a combination of the uncertainties associated with both methods: These originate from varying $\Delta\phi$ cuts for the back-to-back criterion and soft radiation modelling in the dijet balance case, and from the precision with which the assumptions of equal variances of both $p_\mathrm{T}^\mathrm{imb}$ coordinate projections are fulfilled when varying the cut on the maximum p_T of a third soft jet in the event in the bisector case. The overall JER uncertainty is thus quoted to be within 10 % for $30\,\mathrm{GeV} < p_\mathrm{T}^\mathrm{jet} < 500\,\mathrm{GeV}$ and in the range $|y| < 2.8$. Since this uncertainty is applied as a one-sided (p_T and y dependent) smearing, it is again symmetrized on the analysis yields of the nominal and the shifted samples according to

$$N_\mathrm{nominal} \pm (N_\mathrm{smeared} - N_\mathrm{nominal})\,. \tag{6.14}$$

The two resulting upward and downward fluctuated analysis outcomes are then passed to the signal extraction fit as a systematic variation. Like in the JES case, the rate uncertainty caused by this variation also increases according to the number of jets used in the analysis.

Jet Reconstruction Efficiency

The tag-and-probe method employed on minimum bias and QCD dijet events to determine the calorimeter jet reconstruction efficiency, described in Sec. 4.4.3, is affected by systematic uncertainties related to [ATL10]

- the choice of the ΔR cut for matching a track jet to a calorimeter jet,
- the chosen minimal p_T of this "tag" jet,
- the $\Delta\phi$ requirement defining the opposite hemispheres of the two jets.

By comparing the derived efficiencies in data and MC, an overall uncertainty on the jet reconstruction efficiency of 2 % is assigned. This is again a one-sided systematic, evaluated by rerunning the analysis on a sample in which the probability to discard jets at random is modified correspondingly; subsequently, the effect is symmetrized again w.r.t. the yields of the nominal sample according to

$$N_\mathrm{nominal} \pm (N_\mathrm{modified} - N_\mathrm{nominal})\,. \tag{6.15}$$

The two resulting upward and downward fluctuated analysis outcomes are then passed to the BILL fit as a systematic variation. Again, the impact associated with this systematic uncertainty is the more pronounced the more jets are considered in the analysis.

B-Tag, C-Tag and Mistag Scale Factors

The event reweighting done with scale factors correcting the MC b-tag, c-tag and mistag efficiencies to the values observed in data (cp. Sec. 4.4.3) also involves systematic uncertainties. The uncertainties associated with all scale factors are derived by comparing different calibration methods within their full systematic error evaluation. In general, the uncertainty depends on the b-tagging algorithm, the chosen working point and the jet p_{T} bin and jet η range considered. The relative uncertainties measured for the MV1 tagger at a working point corresponding to 60 % for intermediate ranges in $p_{\mathrm{T}}^{\mathrm{jet}}$, relevant in this study, amount to about 5 % to 15 % for b-tag scale factors obtained from $\mathrm{t\bar{t}}$-based analyses [ATL12n], to about 20 % to 26 % for c-tag scale factors extracted from D^* events [ATL12e], and to about 20 % to 50 % for the mistag scale factors gained from QCD multi-jet selections [ATL12h]. Since the three kinds of scale factors are derived by independent measurements of the associated selection efficiencies, the b-tag, c-tag and mistag contributions are treated as uncorrelated; the corresponding inefficiency scale factors are by definition anti-correlated, respectively. The b-tag, c-tag and mistag scale factors are therefore varied independently of each other by applying a one σ variation to the scale factor at hand. Thus, the six modified analysis outcomes for independently varying the b-tag, c-tag and mistag scale factors upward and downward are passed to the signal extraction fit as systematic variations. As the overall scale factor applied to an event is composed of the product of all single-jet scale factors, this uncertainty also increases with increasing jet multiplicity.

Jet Vertex Fraction Scale Factor

There are also systematic uncertainties associated with the JVF scale factors discussed in Sec. 4.4.3. One is the uncertainty related to the selection criteria used in the definition of hard-scatter jets: This is evaluated by varying the minimal value of $\Delta\phi$ between the leading jet and the Z boson candidate as well as the cut on the p_{T} of the Z boson in the reconstruction. The other error source resides in the quality of the fit that is done in order to parametrize the JVF scale factors as a function of the jet p_{T}: To assess this effect, the fit uncertainty is enlarged by a factor of $\sqrt{\chi^2/n_d}$ with χ^2 denoting the fit residual and n_d the NDoF of the fit. In this analysis, the combined JVF scale factor uncertainties are taken into account by applying modified

event weights according to[10]

$$W_{\text{up/down}} = W_{\text{nominal}} \left(1 \pm \sqrt{ \left(\frac{\Delta K^{\epsilon,\text{HS/i,HS}}_{\text{up/down}}}{K^{\epsilon,\text{HS}}_{\text{nominal}} K^{\text{i,HS}}_{\text{nominal}}} \right)^2 + \left(\frac{\Delta K^{\epsilon,\text{PU/i,PU}}_{\text{up/down}}}{K^{\epsilon,\text{PU}}_{\text{nominal}} K^{\text{i,PU}}_{\text{nominal}}} \right)^2 } \right) \quad (6.16)$$

where $K^{\text{i,HS}}_{\text{nominal}}$ etc. are the nominal JVF scale factors of hard-scatter (HS) and pile-up (PU) jets and the differences are given by

$$\Delta K^{\epsilon,\text{HS/i,HS}}_{\text{up/down}} = K^{\epsilon,\text{HS}}_{\text{up/down}} K^{\text{i,HS}}_{\text{up/down}} - K^{\epsilon,\text{HS}}_{\text{nominal}} K^{\text{i,HS}}_{\text{nominal}} , \quad (6.17)$$

$$\Delta K^{\epsilon,\text{PU/i,PU}}_{\text{up/down}} = K^{\epsilon,\text{PU}}_{\text{up/down}} K^{\text{i,PU}}_{\text{up/down}} - K^{\epsilon,\text{PU}}_{\text{nominal}} K^{\text{i,PU}}_{\text{nominal}} . \quad (6.18)$$

The two analysis results thus varied upward and downward are passed to the BILL fit as a systematic fluctuation. As for all systematic uncertainties related to the jets, the overall effect increases according to the number of selected jets in the analysis.

Computation of Missing Transverse Energy

The systematic errors of the $E_{\text{T}}^{\text{miss}}$ computation originate from the scale and resolution uncertainties of the objects entering the different constituent terms of the $E_{\text{T}}^{\text{miss}}$, as well as from additional calorimeter energy from pile-up events. The latter pile-up part of the $E_{\text{T}}^{\text{miss}}$ systematic was already discussed above (see paragraph on pile-up effects). The former uncertainty due to the objects in the $E_{\text{T}}^{\text{miss}}$ composition is already treated internally in the respective scale and resolution systematics (see paragraphs on leptons and jets above) by propagating the respective shifts to the $E_{\text{T}}^{\text{miss}}$ and recomputing it accordingly. There are, however, two more systematic effects associated exclusively to the $E_{\text{T}}^{\text{miss}}$ computation: the uncertainties related to calorimeter topoclusters not belonging to any reconstructed object (CellOut term) and to soft jets from underlying event activity (SoftJet term). Since both effects are generated by a common source (UE), the total uncertainty resulting from both terms is fully correlated and treated as one systematic variation in this study. The CellOut term uncertainty was extracted from a QCD multi-jet Pythia MC sample by employing alternative PS models, different minimum bias tunes and variations in the amount of dead material in the detector simulation step [Ach+12]; the scale uncertainty on the CellOut term was found to be about 13 % for a wide range in $\sum E_{\text{T}}^{\text{CellOut}}$. Similarly, the fractional uncertainty of the SoftJet term was determined to be about 10 %, evaluated as a function of $\sum E_{\text{T}}^{\text{SoftJet}}$. These two systematic contributions are combined by applying the upward/downward fluctuations to both terms and recomputing the $E_{\text{T}}^{\text{miss}}$, thus giving the upward/downward $E_{\text{T}}^{\text{miss}}$-only systematic variation. As for all other object systematics, the analysis is rerun on the thus

[10] K. J. Grahn. *ATLAS TWiki: Jet Recommendations for R17 Analyses*. Oct. 2012. URL: `https://twiki.cern.ch/twiki/bin/viewauth/AtlasProtected/TopJetLiaisonR17Recommendations`.

shifted samples, yielding two modified analysis results that are passed to the signal extraction fit as a systematic variation.

Luminosity

The error associated with the luminosity measurement depicted in Sec. 3.2.1 is composed of several parts: Firstly, the method of the "van der Meer scan" is affected by uncertainties originating from the measurement of the bunch population product $n_{\mathrm{p1}}n_{\mathrm{p2}}$ (cp. Eq. (3.6)) and other calibration uncertainties [ATL12g]; this is the main contribution of systematic error. Secondly, the particular beam conditions in the year 2011 necessitated the assessment of afterglow effects[11] and the stability of the BCM output used in the calibration[12], resulting in further systematic uncertainties. Eventually, the extrapolation of the luminosity scale calibration from the dedicated sample used for luminosity determination to the whole 2011 data taking run produces additional error sources that can be divided into a μ dependence[13] and a long-term consistency contribution. In combination, these effects amount to a systematic uncertainty on the total integrated luminosity of the 2011 data set of $\delta\mathscr{L}/\mathscr{L} = \pm 1.8\,\%$ [ATL12g].[14] This systematic error is passed directly to the signal extraction fit as the uncertainty on the data yield.

6.2. Signal Extraction

The way of extracting the single-top t-channel contribution in this study is to exploit the shape differences of the signal and background channels by executing a template fit on the distribution of a suitable discriminating variable. This is done using the BILL tool [Wag11; Sar12b].[15] In BILL, the t-channel cross section and its uncertainty are determined by a template-based maximum likelihood fit[16], described in the following two paragraphs. Furthermore, a third paragraph depicts the computation of the significance of the analysis result, that is also done within the BILL framework. For a detailed study of the application of the BILL tool for the signal extraction

[11] This is a term describing the small level of activity in the LUCID and BCM detectors for bunch-crossings without hard scattering that directly follow a proton-proton collision bunch-crossing. The effect dies away asymptotically for subsequent bunch-crossings and is most likely due to photons from nuclear de-excitation induced by the hadronic cascades of the preceding pp-collision.

[12] The BCM response must be corrected for short-term changes during runs that occur due to an increasing gain with rising irradiation levels ("pumping").

[13] The calibration results from the different detectors and algorithms employed are supposed to be linearly dependent on the interaction rate μ; any deviation from this behaviour is interpreted as a systematic excursion and is evaluated by comparing the available methods.

[14] A. Lister. *ATLAS TWiki: Top Systematic Uncertainties*. Aug. 2012. URL: `https://twiki.cern.ch/twiki/bin/viewauth/AtlasProtected/TopSystematicUncertainties2011`.

[15] G. Sartisohn. *ATLAS TWiki: The BILL Tool*. July 2012. URL: `https://twiki.cern.ch/twiki/bin/viewauth/AtlasProtected/BillTool`.

[16] The same method was also used in [ATL11e].

Background Process	$\delta\sigma$ [%]
s-channel single-top	6.0
Wt-channel single-top	10.0
$t\bar{t}$ (semi-/dileptonic)	11.0
W+ light flavour jets	4.5/8.2/12.5
W+ heavy flavour jets	4.5/8.2/12.5
Z + jets and Diboson	60.0
QCD multi-jets	0.0

Table 6.2. Estimated relative errors on the background sample cross-sections used by the BILL tool to extract the t-channel single-top signal from the kinematic fitting analysis [Kid12; But+10; Ach+10].[17,18] The W+jets uncertainties depend on the highest jet bin involved in the fit.

of this analysis, including a comparison to another statistics approach as well as criticism of some of its techniques, refer to [Sta13b].

The cross-sections of the single background processes passed to the BILL tool are listed in Tab. 4.2 and the corresponding estimated errors on the cross-sections are given in Tab. 6.2. Here, the theoretical cross-section uncertainties are utilized for the single-top background processes [Kid12] as well as for $t\bar{t}$ [17], whose cross-section with corresponding errors is computed by the HATHOR tool [Ali+11], and for Z+jets and diboson production [But+10; Ach+10].[18] In contrast, the QCD contribution from the data-driven jet-electron model is fixed, as explained in Sec. 6.1.1, and the errors on the rates of the W+jets processes are taken from the data-driven estimate, as outlined in Sec. 6.1.1. Since the W+jets rate estimates are done separately for each lepton flavour and jet bin, the error is adjusted depending on the highest jet bin involved in the BILL fit: As a conservative estimate for the combination of jet bins, the largest error, i.e. the one belonging to the highest jet multiplicity, is applied. Thus, the values in the table correspond to the maxima w.r.t. the lepton flavour in the 2-/3-/4-jet bin, respectively.

6.2.1. Extraction of the Signal Cross-Section

The output distributions of the signal and background processes from the nominal analysis are passed to the BILL tool for the extraction of the signal cross-section. The tool fits these nominal templates to the observed data distribution by a binned

[17] L. Mijovic. *ATLAS TWiki: Top group's MC11(a,b,c) Samples For 2011 Data Analyses*. Dec. 2012. URL: https://twiki.cern.ch/twiki/bin/viewauth/AtlasProtected/TopMC11.

[18] A. Lister. *ATLAS TWiki: Top Systematic Uncertainties*. Aug. 2012. URL: https://twiki.cern.ch/twiki/bin/viewauth/AtlasProtected/TopSystematicUncertainties2011.

negative log-likelihood fit based upon the following maximum likelihood function:

$$L(\beta_1, ..., \beta_{N_{\text{proc}}}) = \prod_{k=1}^{N_{\text{bins}}} \frac{e^{-\mu_k} \cdot \mu_k^{N_k^{\text{obs}}}}{N_k^{\text{obs}}!} \cdot \prod_{j=2}^{N_{\text{proc}}} G(\beta_j; 1.0, \delta\sigma_j) \,. \tag{6.19}$$

Here, N_{proc} denotes the number of processes considered – these are eight: the seven background contributions of Tab. 6.2 ($j = 2, ..., 8$) and the single-top t-channel signal ($j = 1$). The number of observed events N_k^{obs} in each bin k of the N_{bins} bins enters the likelihood function in the form of a Poisson term whose expectation value μ_k is given by

$$\mu_k = \sum_{j=1}^{N_{\text{proc}}} \mu_{jk} \,. \tag{6.20}$$

Here, μ_{jk} is the mean number of events of the respective process j in the bin k,

$$\mu_{jk} = \nu_j \cdot \beta_j \cdot \alpha_{jk} \,, \tag{6.21}$$

which is the product of the total number of expected events of this process in all bins, denoted by ν_j, and the relative observed cross-section

$$\beta_j \equiv \frac{\sigma_{j,\text{obs}}}{\sigma_{j,\text{SM}}} \,, \tag{6.22}$$

i.e. the observed cross-section σ_{obs} normalized to the cross-section predicted by the Standard Model σ_{SM}. The third factor is the relative fraction of events of this process in the particular bin k, termed α_{jk}. The latter carry the information on the shape of the corresponding template and fulfil the normalization condition

$$\sum_{k=1}^{N_{\text{bins}}} \alpha_{jk} = 1 \,. \tag{6.23}$$

The actual parameters of the fit are the scaling parameters β_j of the different processes, see Eq. (6.22). Since there is already a priori knowledge of the background rates, the parameters $\beta_2, ..., \beta_{N_{\text{proc}}}$ can be constrained in the fit according to standardized Gaussian distributions. In the likelihood of Eq. (6.19), they are thus defined as

$$G(\beta_j; 1.0, \delta\sigma_j) = \frac{1}{\sqrt{2\pi(\delta\sigma_j)^2}} \exp\left(-\frac{1}{2}\left(\frac{\beta_j - 1}{\delta\sigma_j}\right)^2\right) \,, \tag{6.24}$$

with the relative cross-section uncertainties $\delta\sigma_j$ listed in Tab. 6.2. Since the data-driven QCD contribution is supposed to be fixed here ($\beta_{\text{QCD}} = 1$), a Gaussian constraint for it is included with a very small error (it is $\delta\sigma_{\text{QCD}} = 1 \cdot 10^{-7}$). The signal contribution β_1, however, is a free parameter in the fit. In order to ensure

numerical stability, the negative log-likelihood function, corresponding to Eq. (6.19),

$$-\ln L(\beta_1, ..., \beta_{N_{\text{proc}}}) \;=\; \sum_{k=1}^{N_{\text{bins}}} -(\mu_k + N^{\text{obs}} \cdot \ln \mu_k) \;+\; \sum_{j=2}^{N_{\text{proc}}} -\frac{1}{2}\left(\frac{\beta_j - 1}{\delta\sigma_j}\right)^2 , \quad (6.25)$$

is then minimized using the program Minuit [JR75]. Equation (6.19) corresponds to the maximum likelihood employed to fit a single channel of the analysis, e.g. the electron two jet bin result. It is also possible to do a combined fit of N_{chan} channels utilizing a product of several likelihood functions

$$L_{\text{comb}}(\beta_1, ..., \beta_{N_{\text{proc}}}) \;=\; L_1(\beta_1, ..., \beta_{N_{\text{proc}}}) \cdot ... \cdot L_{N_{\text{chan}}}(\beta_1, ..., \beta_{N_{\text{proc}}}) \,. \quad (6.26)$$

This is done for four single channels in this study: The 2- and 3-jet bin results of the electron and muon channel are combined (see Sec. 6.2.4)

6.2.2. Estimation of the Total Cross-Section Uncertainty

In order to obtain the total error of the cross-section result, also the systematically shifted analysis results are passed to the BILL tool and are used to probe the impact of all systematic uncertainties described in Sec. 6.1. Furthermore, the data and MC statistical errors need to be computed and the error associated with the cross-section uncertainties must be evaluated. This is done in a frequentist manner by employing pseudo-experiments that scan the "parameter space" of the associated variations.

Data Statistical Uncertainty

The data statistical error, due to a limited set of data recorded, is assessed by drawing the total number of events belonging to each of the eight physics processes in the considered channel, ν_j, randomly anew. This is done on the nominal templates by drawing from a Poisson distribution whose expectation value is given by the original number ν_j, giving $N_j^{\text{data stat}}$. The template shapes are not altered. Adding up the resulting templates of all processes, a pseudo-data outcome is thus created which the nominal templates are fitted to again according to the procedure outlined in Sec. 6.2.1. All in all, 10,000 such pseudo-experiments are run to evaluate the data statistical uncertainty.

MC Statistical Uncertainty

The MC statistical error, arising from limited MC sample sizes, leads to uncertainties in the template shapes. Therefore, the bin contents of all nominal templates are drawn at random from a Gauss distribution with mean corresponding to the original bin content N_{jk}^{obs} and a σ given by the statistical bin error $\sqrt{\sum_i w_i^2}$, computed from the sum of squares of weights w_i of all bin entries. Then, the total number of events $N_j^{\text{MC stat}}$ to fill the new shape is randomly determined by drawing it from a Poisson

distribution of expectation value given by the original event yield ν_j. Again, the resulting templates of all processes are added and used to replace the data in a fit with the nominal templates. As for the data statistical error, this is done in each of 10,000 dedicated pseudo-experiments.

Cross-Section Uncertainty

To probe the systematic cross-section uncertainty of the measurement, the cross-section values of all background processes are varied. To this end, a random number x is drawn from a log-normal distribution[19] with a mean of one and a standard deviation equal to the corresponding cross-section uncertainty $\delta\hat{\sigma}_j$ from Tab. 6.2:

$$\ln \mathcal{N}(x; \mu_j, \sigma_j) = \frac{1}{x\sqrt{2\pi\sigma_j^2}} \exp\left(-\frac{1}{2}\left(\frac{\ln x - \mu_j}{\sigma_j}\right)^2\right) \tag{6.27}$$

with

$$\mu_j = -\frac{1}{2}\sigma_j^2\,, \tag{6.28}$$

$$\sigma_j^2 = \ln[(\delta\hat{\sigma}_j)^2 + 1]\,. \tag{6.29}$$

In Equations (6.27), (6.28) and (6.29), μ_j and σ_j are the two parameters of the log-normal distribution belonging to process j; σ_j is not to be mistaken for the predicted cross-section of the process j. Thus, the expectation value of the nominal total number of events of a background process j in the given channel m, denoted by ν_{mj}, is changed to $\tilde{\nu}_{mj} = x \cdot \nu_{mj}$. Now, the number of events is drawn at random according to a Poissonian with expectation value $\tilde{\nu}_{mj}$ to yield N_{mj}^{xsec}. The template shapes remain unaltered. The sum of the shifted templates serves again as pseudo-data in the fit of the nominal templates, and the procedure is iterated 10,000 times.

Systematic Uncertainties

The impact of all other systematic uncertainties has to be assessed by including their effect on the *total rates* of the processes on one hand, and on the *shapes of the templates* of the processes on the other hand.

The *rate uncertainties* are taken into account as follows: The expected number of events ν_{mj} is varied according to

$$\nu_{mj}^{\text{syst}} = \nu_{mj} \cdot \left(1 + \sum_i^{N_{\text{syst}}} \delta_i \cdot [\Theta(\delta_i) \cdot \epsilon_{imj+} + \Theta(-\delta_i) \cdot \epsilon_{imj-}]\right)\,. \tag{6.30}$$

Here, ν_{mj}^{syst} is the expectation value of the shifted total yield of the process j in the

[19] A log-normal distribution is preferred here over a Gauss distribution to avoid unphysical negative values by construction.

channel m, including the effect of all N_{syst} systematic uncertainties on the acceptance of the process: This is accomplished by drawing a random number δ_i from a standardized Gaussian distribution (with mean at zero and standard deviation of one). This nuisance parameter δ_i then defines the strength and sign of the systematic excursion i in the current pseudo-experiment, and is applied consistently to all processes. $\Theta(\delta_i)$ denotes the Heavyside-theta-function and serves to distinguish between the relative acceptance uncertainties ϵ_{imj} resulting from a $+1\sigma$ variation of the corresponding source i (ϵ_{imj+}) and a -1σ variation thereof (ϵ_{imj-}). In the special case of the uncertainty associated with the luminosity measurement, ν_{mj} is also varied at random according to Eq. (6.30), but the efficiencies are given by $\epsilon_{imj\pm} = \pm(\delta\mathscr{L}/\mathscr{L})$, and no subsequent shape variation (as described in the paragraph below) is done. Finally, since ν_{mj}^{syst} represents the expectation value of the shifted total yield, it is again taken as the mean of a Poisson distribution from which the total number of observed events in the current pseudo-experiment, N_{mj}^{syst}, is randomly determined.

Now, to also assess the *shape uncertainties* resulting from the systematic variations, the relative fractions α_{mjk} of the process j in bin k in the analysis channel m are systematically shifted as

$$\alpha_{mjk}^{\text{syst}} = \alpha_{mjk} + \sum_{i=1}^{N_{\text{syst}}} |\delta_i| \cdot \left[(\alpha_{mjki}^{+} - \alpha_{mjk}) \cdot \Theta(\delta_i) + (\alpha_{mjki}^{-} - \alpha_{mjk}) \cdot \Theta(-\delta_i) \right] , \quad (6.31)$$

where $\alpha_{mjki}^{\pm}$ denote the fractions belonging to a $\pm1\sigma$ variation, respectively, of the underlying template w.r.t. the systematic uncertainty i. The random numbers δ_i are identical to those in Eq. (6.30) and ensure a consistent treatment of each systematic error source. Eventually, given the new shape information $\alpha_{mjk}^{\text{syst}}$ (normalized to unity), the outcome of the current pseudo-experiment is then obtained by drawing N_{mj}^{syst} random numbers according to the shape $\alpha_{mjk}^{\text{syst}}$ for each process j and then adding up the resulting templates of all processes for the respective channel m.

This pseudo-data outcome is in turn again treated like the real data in the extraction of the cross-section on the nominal analysis sample, depicted in Sec. 6.2.1, i.e. the nominal analysis templates are fitted to the pseudo-data 10,000 times using the likelihood of Eq. (6.19).

Every time the likelihood fit is redone in a pseudo-experiment, it gives new values of the β_j parameters defined in Eq. (6.22). The standard deviation $\sigma_i(\beta_{t\text{-channel}})$ of the $\beta_{t\text{-channel}}$ distribution from 10,000 pseudo-experiments is an estimator of the error of the respective systematic i on the t-channel cross-section measured. In this study, the procedure for the evaluation of all error sources by pseudo-experiments outlined in this section is executed 10,000 times for each single systematic (data statistical error, MC statistical error, cross-section uncertainty and each single systematic error source) to judge the single impacts of the error sources. This is accomplished by just considering the respective term of the sum in Equations (6.30) and (6.31). In addition, a combined pseudo-experimental setup is run 10,000 times in order to determine the impact of the correlations among the error sources. This is done

step-wise:

1. The number of events N_j^{gen} to be generated for each process is determined, incorporating the cross-section uncertainty as well as all acceptance effects of the other systematic uncertainties.

2. The modified template shapes α_{jk}^{gen} need to be derived, including the effects of the MC statistics uncertainty as well as the shape variations of all systematic error sources considered.

3. At last, N_j^{gen} random numbers are drawn from the shape templates α_{jk}^{gen}, giving a resulting distribution $\mathcal{A}_{jk}^{\text{gen}}$ for each process.

The outcome of the correlated approach is then the distribution

$$\mathcal{A}_k^{\text{gen}} = \sum_{j=1}^{N_{\text{proc}}} \mathcal{A}_{jk}^{\text{gen}} \tag{6.32}$$

for each pseudo-experiment. The standard deviation of $\beta_{t\text{-channel}}$ from this procedure, taking into account all correlations of systematic error sources, is used as the error on the final cross-section result. The data statistics error is not included here since it is not a systematic uncertainty; it is therefore always quoted separately. The results from both, the single and the correlated runs, are shown in Sec. 6.2.4.

6.2.3. Computation of the Significance

In order to arrive at a significance of the cross-section result obtained as described above, a hypothesis test can be performed with BILL [Sar12b; Cow+11]. To this end, two ensembles of pseudo-experiments are generated from the nominal templates of the involved processes: an ensemble implementing the background-only hypothesis H_0,

$$\mathcal{A}_k^{\text{gen},0} = \sum_{j=2}^{N_{\text{proc}}} \mathcal{A}_{jk}^{\text{gen}} \,, \tag{6.33}$$

in which the signal t-channel process is absent ($\beta_{\text{t-chan}} = 0$), and an ensemble representing the signal-plus-background hypothesis H_1,

$$\mathcal{A}_k^{\text{gen},1} = \sum_{j=1}^{N_{\text{proc}}} \mathcal{A}_{jk}^{\text{gen}} \,, \tag{6.34}$$

considering the t-channel with its predicted cross-section σ_{SM} ($\beta_{\text{t-chan}} = 1$). The hypothesis test is now to decide which hypothesis is preferred by the measurement in data. According to the Neyman-Pearson lemma [NP33], the most efficient hypothesis test consists of forming the likelihood ratio. Therefore, the test statistic Q is defined

as

$$Q = -2 \ln \frac{L(\beta_{\text{t-chan}} = 1, \{\beta'_{j,\text{bkg}}\})}{L(\beta_{\text{t-chan}} = 0, \{\beta''_{j,\text{bkg}}\})}\,, \tag{6.35}$$

where $\{\beta_{j,\text{bkg}}\}$ denotes the set of β-values of all background processes. For each pseudo-experiment in the ensemble $\mathcal{A}_k^{\text{gen},0}$, the nominal templates are now fitted to the pseudo-data twice: once taking the t-channel contribution into account ($\beta_{\text{t-chan}} = 1$) and once disregarding it ($\beta_{\text{t-chan}} = 0$), yielding the two corresponding likelihood values that are combined to give the Q-value from Eq. (6.35) for this pseudo-experiment. The resulting Q-value distribution q_0 of the whole ensemble $\mathcal{A}_k^{\text{gen},0}$ is then normalized to unity, denoted by $\hat{q}_0$, and represents the probability density distribution belonging to the H_0 hypothesis. The $\mathcal{A}_k^{\text{gen},1}$ ensemble is treated in an analogous way, such that a Q-value distribution q_1 is gained and normalized to obtain the probability density distribution $\hat{q}_1$ belonging to the H_1 hypothesis. Furthermore, the observed Q-value Q_{obs} is calculated by fitting the nominal templates to the real collision data with and without including the t-channel template.

Now, the value Q_{obs} must be compared to the $\hat{q}_0$ and $\hat{q}_1$ distributions in order to decide which of the two hypotheses, H_0 or H_1, is preferred by the observed data. To this end, the overlap of the $\hat{q}_0$ and $\hat{q}_1$ distributions is considered, see Fig. 6.2: A small overlap corresponds to a good discriminatory power of the analysis w.r.t. the two hypotheses. Therefore, a quantity called the p-value is defined as

$$p(Q) = \int_{-\infty}^{Q} \hat{q}_0(Q')\,\mathrm{d}Q'\,, \tag{6.36}$$

which involves an expected value p_{exp} given by choosing the upper boundary Q to be the median of the $\hat{q}_1$ distribution. Thus, p_{exp} signifies the threshold below which any p-value will lie with a probability of 50 % given that hypothesis H_1 is true. This p_{exp} can be compared to the observed p-value p_{obs}, resulting from choosing the upper boundary to be Q_{obs}. If one now assumes the null-hypothesis H_0 to be valid, the threshold p_{obs} represents the probability of obtaining a Q-value as compatible or even less compatible with H_0 than the one measured from data. In other words: p_{obs} is a measure of the error associated with rejecting the background-only hypothesis H_0 based upon the observed data. Consequently, a high significance of the t-channel analysis result is expected for small values of p_{obs}. By convention, this p-value significance is expressed in Gaussian standard deviations σ: A standardized Gaussian distribution ($\mu = 0$, $\sigma = 1$) is integrated on one side until the integral amounts to the value p_{obs} at a point x_p. The resulting distance of x_p to the mean μ is then quoted in units of σ. A thus converted p-value of $1.35 \cdot 10^{-3}$ corresponds to 3σ, and below this p-value, an analysis is said to show evidence of a signal. If the p-significance is even less than $2.87 \cdot 10^{-7}$, corresponding to 5σ, an observation of the signal is claimed. Thus, the signal-plus-background hypothesis H_1 is accepted by observing a certain number of candidate signal events in the analysis that have a probability of only 3σ or 5σ to be pure background fluctuations.

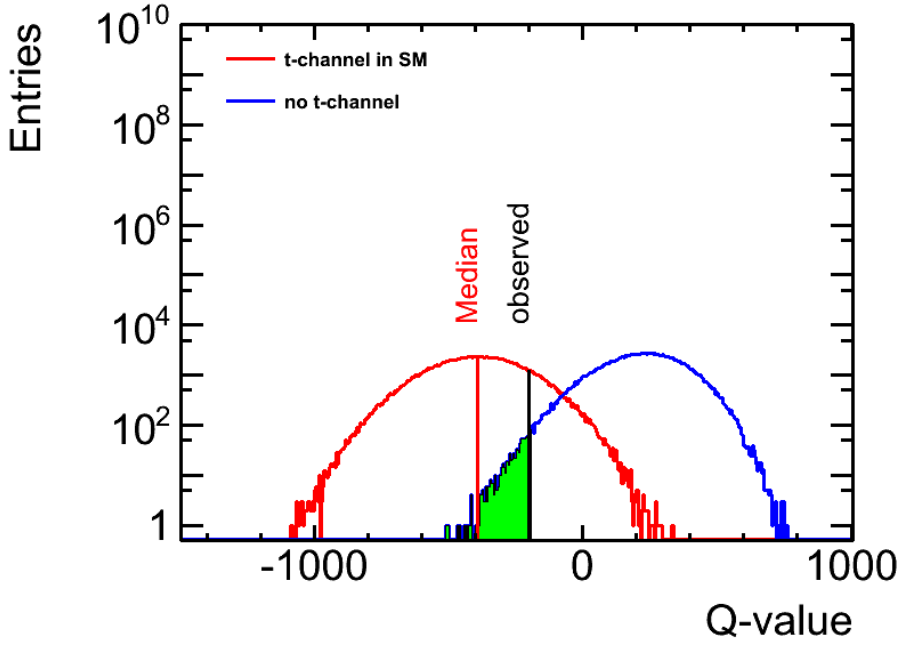

Figure 6.2. Example of the overlapping distributions $\hat{q}_0$ and $\hat{q}_1$, associated with the no-signal (no t-channel) and signal (t-channel in SM) hypotheses, respectively. The median of the $\hat{q}_1$ distribution and the observed Q-value are shown as well. The area shaded green indicates the integral that is p_{obs}.

6.2.4. Results of the Signal Extraction

Discriminating Variable

The template fit method of the BILL tool is used on a variety of distributions resulting from the KinFitter analysis in order to find the variable with the highest discriminatory power. It turns out that the best variable is derived from a two-dimensional distribution of the vectorial p_{T} sum of the top quark reconstructed in the kinematic fit and the leading non-b-jet in the event,

$$\left|\vec{p}_{\text{T,top}} + \vec{p}_{\text{T,lead non-b-jet}}\right| , \tag{6.37}$$

versus the η of this leading non-b-jet.[20] The variable (6.37) is a measure of the p_{T} balance of the top quark and the leading non-b-jet in the event. In a single-top t-channel event at tree-level, the leading non-b-jet is the jet originating from the light quark in the final state of the scattering process (see Fig. 2.11a); thus the value of this variable should be small in signal events, signifying that the p_{T} balance is met. Furthermore, as mentioned in Sec. 5.2.1, in single-top t-channel events, the light quark jet is preferably found in the forward region of the detector

[20] Due to the requirement of exactly one b-tagged jet in the event (cp. Sec. 4.4.2), the leading non-b-jet is always the second leading jet in the event except when its p_{T} is even larger than the b-jet p_{T} in which case it is the leading jet.

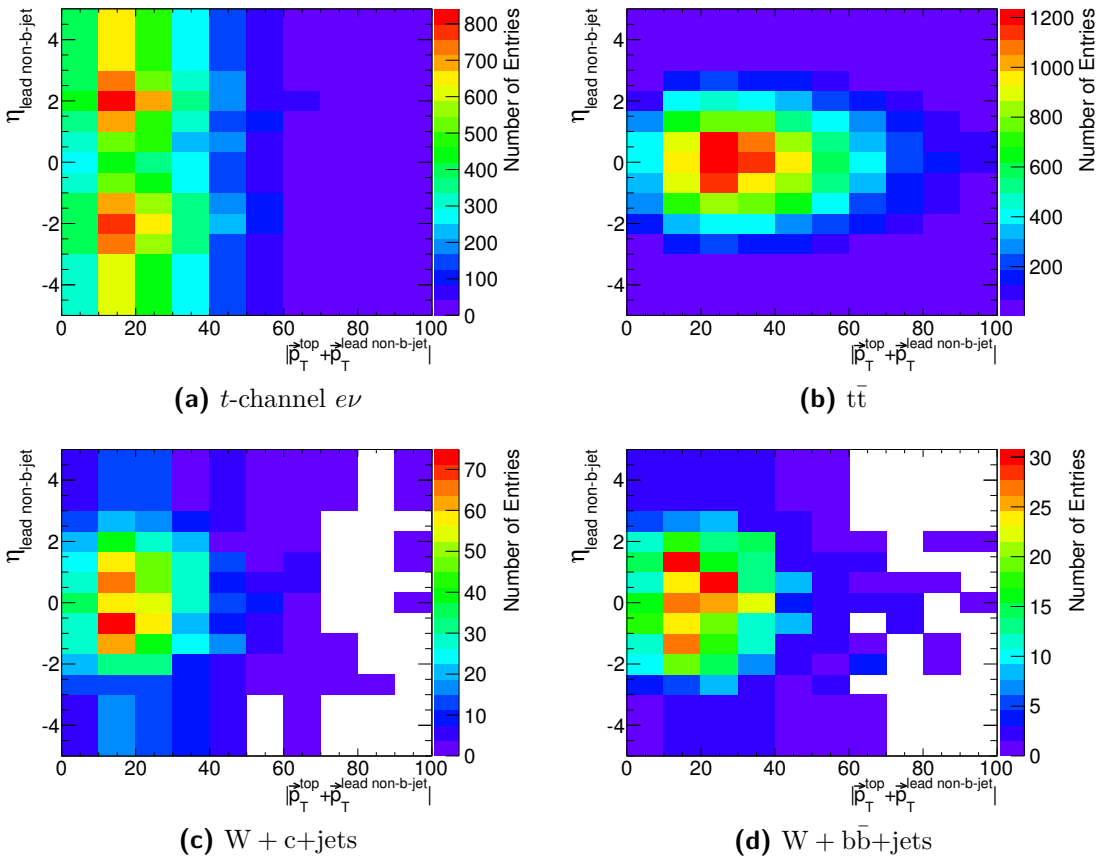

(a) t-channel $e\nu$ **(b)** $\mathrm{t\bar{t}}$

(c) $\mathrm{W}+\mathrm{c}$+jets **(d)** $\mathrm{W}+\mathrm{b\bar{b}}$+jets

Figure 6.3. Two-dimensional distribution of the p_{T} balance of the top quark reconstructed by the kinematic fit and the leading non-b-jet in the event versus η of the leading non-b-jet. The histogram is shown in the electron channel in the 2-jet bin for the t-channel (a) as well as for the main background processes in this jet bin, i.e. $\mathrm{t\bar{t}}$ (b), $\mathrm{W}+\mathrm{c}$+jets (c) and $\mathrm{W}+\mathrm{b\bar{b}}$+jets (d) production.

which is perhaps the only truly unique feature of this process. Since the leading non-b-jet in the signal events is mostly this forward jet, considering the p_{T} balance as a function of $\eta_{\text{lead non-b-jet}}$ offers a good discriminatory power, as can be seen in Fig. 6.3, showing the corresponding two-dimensional distribution for the t-channel as well as the dominant background contributions ($\mathrm{t\bar{t}}$ and W+jets processes): It is visible that the p_{T} balance is rather fulfilled for the t-channel than for $\mathrm{t\bar{t}}$, but it does not offer a good separation w.r.t. W+jets production. However, $\mathrm{t\bar{t}}$ as well as W+jets processes display clearly smaller values of $|\eta_{\text{lead non-b-jet}}|$ than the t-channel signal. Therefore, the greatest discriminatory power is expected from exploiting the combined information of these two variables.

With increasing jet multiplicity, the barycentre of the distribution shifts to higher values of $|\vec{p}_{\mathrm{T,top}} + \vec{p}_{\mathrm{T,lead\ non\text{-}b\text{-}jet}}|$ and the discriminatory power decreases. Looking at the corresponding distributions in the 3-jet bin in Fig. 6.4, the p_{T} balance is seen to degrade as the overall energy in the event gets distributed amongst three jets.

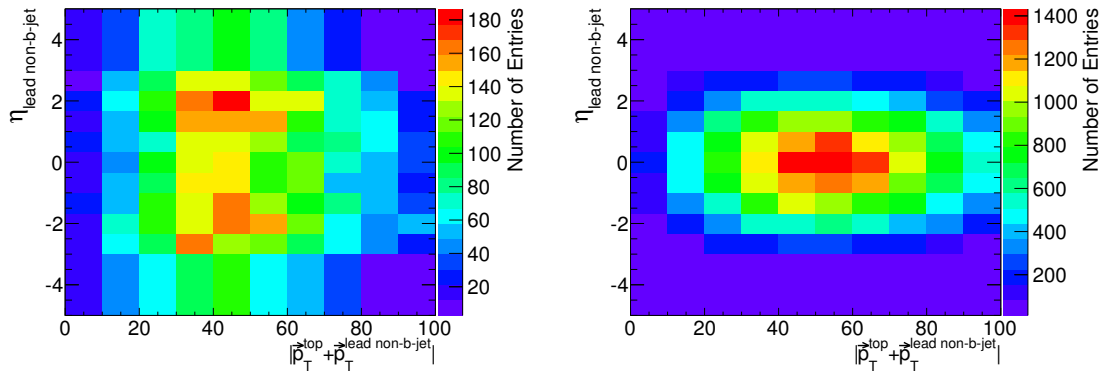

(a) t-channel $e\nu$ **(b)** $t\bar{t}$

Figure 6.4. Two-dimensional distribution of the p_T balance of the top quark reconstructed by the kinematic fit and the leading non-b-jet in the event versus η of the leading non-b-jet. The histogram is shown in the electron channel in the 3-jet bin for the t-channel (a) as well as for the main background process in this jet bin, $t\bar{t}$ (b).

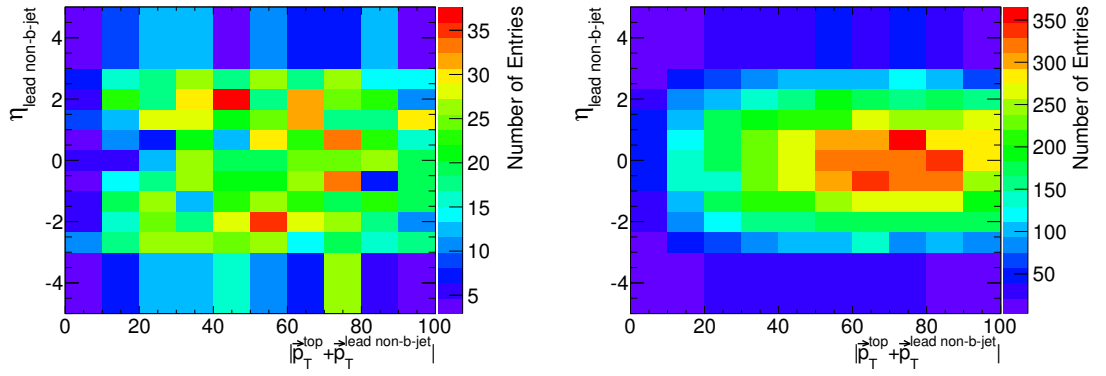

(a) t-channel $e\nu$ **(b)** $t\bar{t}$

Figure 6.5. Two-dimensional distribution of the p_T balance of the top quark reconstructed by the kinematic fit and the leading non-b-jet in the event versus η of the leading non-b-jet. The histogram is shown in the electron channel in the 4-jet bin for the t-channel (a) as well as for the main background process in this jet bin, $t\bar{t}$ (b).

The third jet in the t-channel originates from ISR/FSR, and in the FSR case, the p_T balance is not met; if the b-jet from the gluon splitting in the initial state is not recognized as a b-jet, this jet can also contribute here and would not compromise the p_T balance. However, judging by the persistence of the gap in $\eta_{\text{lead non-b-jet}}$, the forward jet is still assigned correctly as the leading non-b-jet in most cases. In the $t\bar{t}$ process, which is the dominant background now, one more of the jets in the final state is reconstructed and a coincidental fulfilment of the p_T balance is more unlikely.

In the 4-jet bin, see Fig. 6.5, the degradation of the p_T balance is even more pronounced, as is expected. Moreover, in the t-channel distribution, the gap in

$\eta_{\text{lead non-b-jet}}$ is blurred since now the full impact of the combinatorics of the jets sets in. Thus, the signal distribution in this jet bin is very similar to the one of the dominant background, $t\bar{t}$ production, which now has its complete set of four jets. Furthermore, the statistics is very low, as already pointed out in Sec. 5.2.4 of the previous chapter. Because of this lack of discriminatory power along with insufficient statistics, the 4-jet bin is not included in the combined fit to extract the signal cross-section.

Now, in order to pass a one-dimensional distribution to the BILL tool for template fitting, the two-dimensional distribution is sliced in $\eta_{\text{lead non-b-jet}}$. This is shown for the muon channel in the 2- and 3-jet bins in Figures 6.6 and 6.7, respectively. The range of the p_{T} sum for each of the 11 slices is [0,100] GeV. The η slices are not chosen equidistantly in order to guarantee sufficient statistics also for large $|\eta|$, and thus cover the following ranges:

$$[-5, -3, -2\tfrac{1}{3}, -1\tfrac{2}{3}, -1, -\tfrac{1}{3}, +\tfrac{1}{3}, +1, +1\tfrac{2}{3}, +2\tfrac{1}{3}, +3, +5]\,. \tag{6.38}$$

As can be seen from the figures, the sum of the MC histograms agrees well with the data distribution within the statistical errors except for the two outermost bins in $\eta_{\text{lead non-b-jet}}$ in the 2 jet case: Here, the MC stack undershoots the data distribution a little. A similar problem with the η of the forward jet has already been observed in [ATL12j] where the impact of this mismodelling is studied by introducing a dedicated systematic variation: Alternative MC distributions are produced by reweighting with the histogram obtained from taking the bin-wise ratio $N_{\eta_{\text{observed}}}/N_{\eta_{\text{MC}}}$ in the *pretag* selection. In the study at hand, this is not done, though, since no mismodelling is visible in the $\eta_{\text{non-b-jet}}$ control histogram in the *tag* selection (see Fig. 4.12c). It must be kept in mind, however, that the outermost $\eta_{\text{lead non-b-jet}}$ bins in the signal extraction histogram correspond to the quite large range $3 < |\eta_{\text{lead non-b-jet}}| < 5$, and discrepancies between data and MC are thus more prominent than in the control distribution. The disagreement of data and MC for high $|\eta_{\text{lead non-b-jet}}|$ is discussed further in the following paragraphs.

Cross-Section Scale Factors

The β values of all processes, as defined in Eq. (6.22), resulting from the cross-section extraction on this distribution are listed in Tab. 6.3 for all channels in the 2- and 3-jet bin combination and in Tab. 6.4 for all channels in the lepton combination of the 2-jet bin results. As mentioned in the introduction to Sec. 6.2, the β values in the single channels are different for the two variants since the W+jets rate uncertainty is adapted according to the highest jet bin involved in the combined fit. The comparison of the signal extraction histogram before and after the fit is shown in Fig. 6.8 for the muon channel in the 2-jet bin: In the distributions after the fit, the processes are scaled by the β values resulting from the combined fit of the electron and muon channels in the 2-jet bin, cp. the third column in Tab. 6.4. As is visible in Figures 6.8a and 6.8b, the large value of $\beta_{t\text{-channel}}$ in the nominal fit results from an attempt to

	Electron		Muon		Electron+Muon
	2 Jets	3 Jets	2 Jets	3 Jets	2+3 Jets
$\beta_{t\text{-channel}}$	1.86 ± 0.10	1.66 ± 0.10	1.42 ± 0.21	0.86 ± 0.20	1.72 ± 0.07
$\beta_{\text{Wt-channel}}$	1.00 ± 0.10	1.00 ± 0.10	1.00 ± 0.10	1.01 ± 0.10	1.04 ± 0.10
$\beta_{\text{s-channel}}$	1.00 ± 0.06	1.00 ± 0.06	1.00 ± 0.06	1.00 ± 0.06	1.00 ± 0.06
$\beta_{\text{t}\bar{\text{t}}}$	1.08 ± 0.06	1.10 ± 0.06	0.91 ± 0.05	1.07 ± 0.05	0.99 ± 0.02
$\beta_{\text{W+LF}}$	0.94 ± 0.08	0.97 ± 0.08	0.97 ± 0.08	0.98 ± 0.08	0.91 ± 0.08
$\beta_{\text{W+HF}}$	0.81 ± 0.05	0.75 ± 0.04	0.88 ± 0.08	0.97 ± 0.07	0.78 ± 0.03
$\beta_{\text{Z,Diboson}}$	0.38 ± 0.52	0.59 ± 0.56	0.82 ± 0.56	1.15 ± 0.58	0.74 ± 0.46
β_{QCD}	1.00 ± 0.00	1.00 ± 0.00	1.00 ± 0.00	1.00 ± 0.00	1.00 ± 0.00

Table 6.3. Results for the cross-section scale factors β of all processes from fitting the nominal templates to the data distribution. The associated statistical fit error is also quoted. The fit results are obtained from the p_{T} balance vs. $\eta_{\text{lead non-b-jet}}$ distribution and are shown for the single lepton channels in the 2- and 3-jet bin as well as for the overall combination.

	Electron	Muon	Electron+Muon
	2 Jets		
$\beta_{t\text{-channel}}$	1.76 ± 0.09	1.54 ± 0.09	1.72 ± 0.07
$\beta_{\text{Wt-channel}}$	0.98 ± 0.10	0.98 ± 0.10	0.98 ± 0.10
$\beta_{\text{s-channel}}$	1.00 ± 0.06	1.00 ± 0.06	1.00 ± 0.06
$\beta_{\text{t}\bar{\text{t}}}$	1.05 ± 0.06	1.06 ± 0.06	1.10 ± 0.05
$\beta_{\text{W+LF}}$	0.98 ± 0.04	0.98 ± 0.04	0.97 ± 0.04
$\beta_{\text{W+HF}}$	0.90 ± 0.04	0.85 ± 0.03	0.82 ± 0.03
$\beta_{\text{Z,Diboson}}$	0.04 ± 0.51	0.16 ± 0.54	−0.00 ± 0.48
β_{QCD}	1.00 ± 0.00	1.00 ± 0.00	1.00 ± 0.00

Table 6.4. Results for the cross-section scale factors β of all processes from fitting the nominal templates to the data distribution. The associated statistical fit error is also quoted. The fit results are obtained from the p_{T} balance vs. $\eta_{\text{lead non-b-jet}}$ distribution and are shown for the single lepton channels in the 2-jet bin as well as for their combination.

match the simulation to the data in the two outer $\eta_{\text{lead non-b-jet}}$ bins. In Fig. 6.8c, the distribution resulting from scaling the JES up systematics samples by these β values is shown: This modified simulation can be seen to fit the shape of the data better than the previous two, especially w.r.t. the high $|\eta_{\text{lead non-b-jet}}|$ region. This suggests that the issue of the data-MC disagreement mentioned earlier is likely due to the high JES uncertainty for light forward jets (see Fig. 6.1a), i.e. that the JES is systematically underestimated in the current simulation setup of ATLAS – a conclusion already drawn from the examination of the pull plots in Fig. 5.15. Also the detailed analysis of systematic error sources in [Sta13b], which is a study based on the analysis chain of this work, supports this observation.

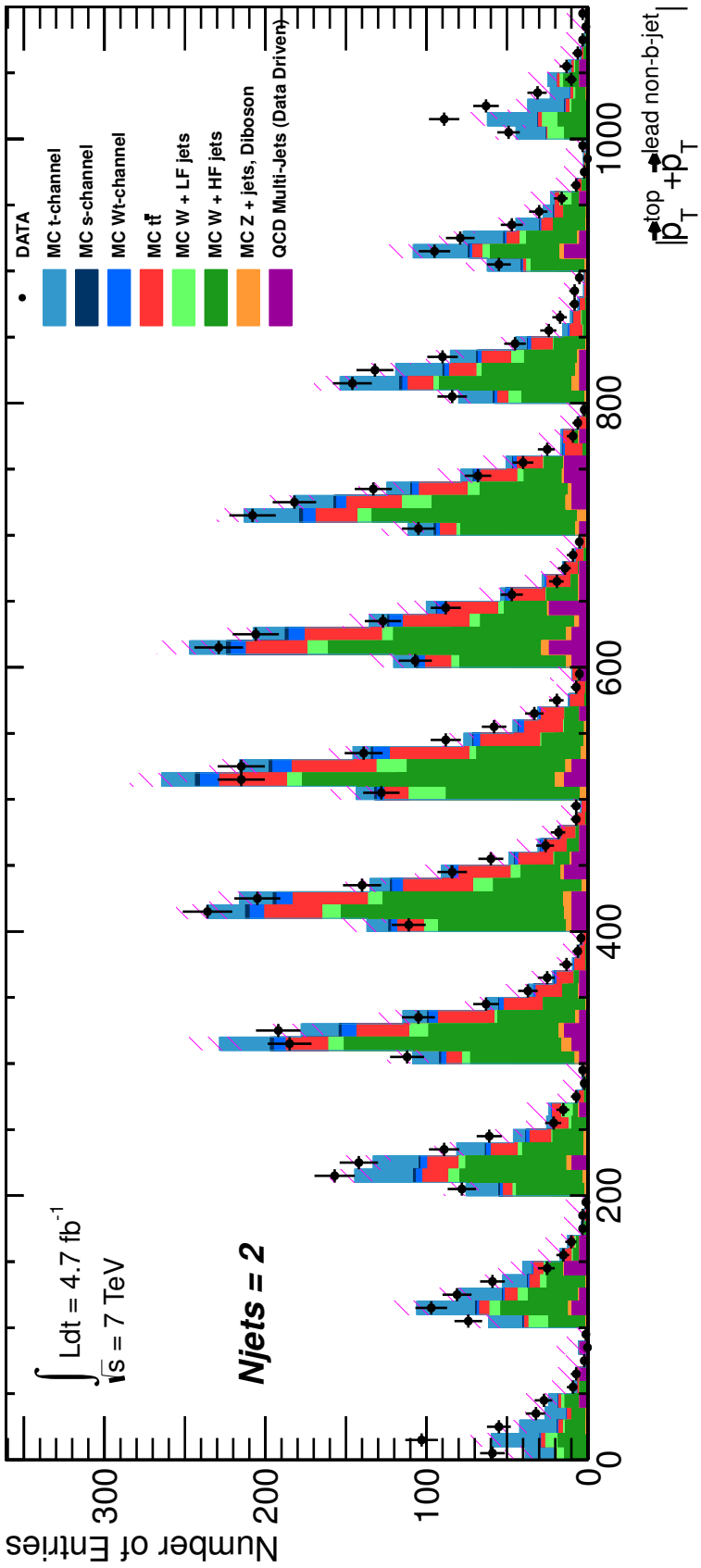

Figure 6.6. Distribution of the p_{T} balance of the top quark reconstructed by the kinematic fit and the leading non-b-jet in the event. The p_{T} balance is split in 11 slices of the η of the leading non-b-jet. The range of the p_{T} sum for each slice is [0,100] GeV, such that the abscissa x in slice i ($i = 1, 2..., 11$) corresponds to a value of the p_{T} balance of $(x - 100 \cdot (i-1))$ GeV. This variable is used for the signal extraction by the BILL template fit in the muon channel in the 2-jet bin. The MC distributions are normalized to the data luminosity.

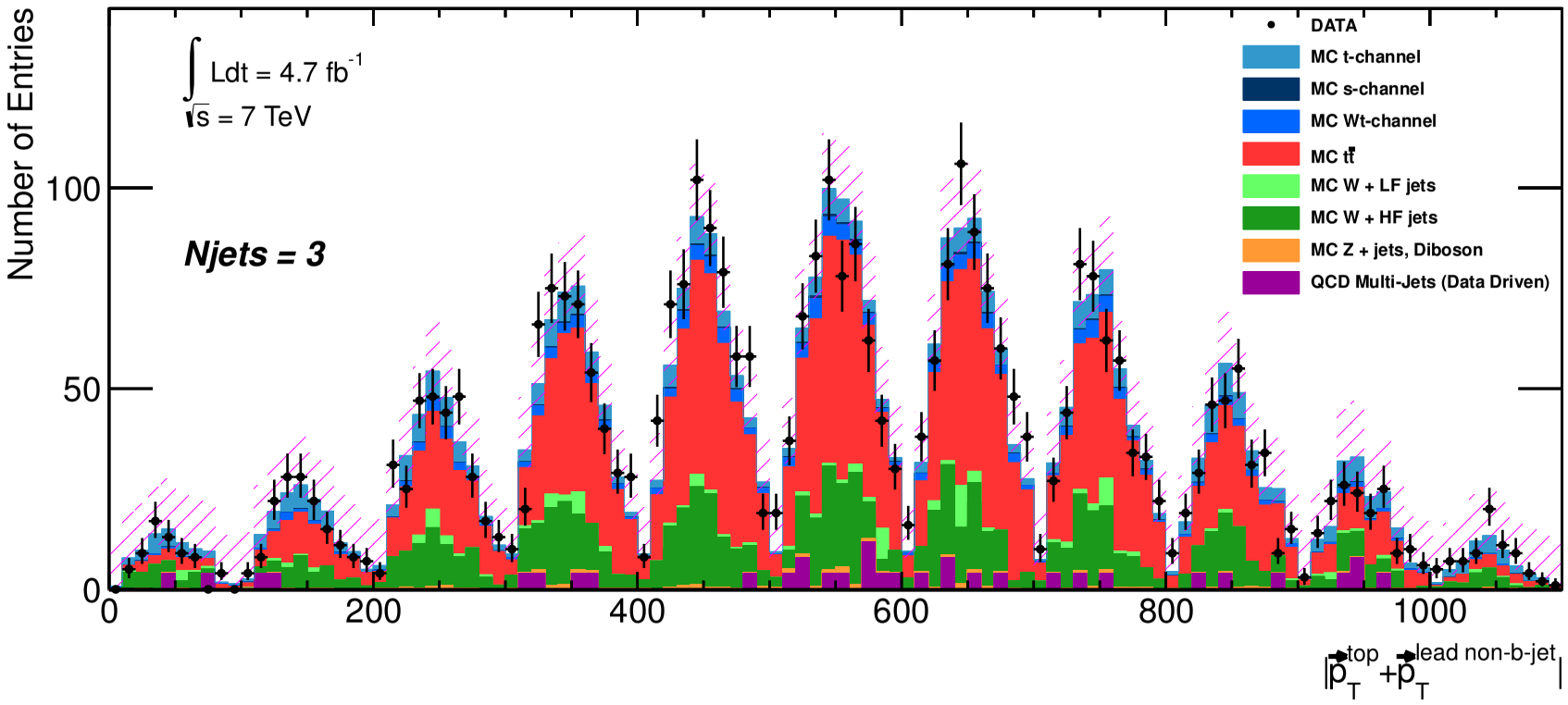

Figure 6.7. Distribution of the p_{T} balance of the top quark reconstructed by the kinematic fit and the leading non-b-jet in the event. The p_{T} balance is split in 11 slices of the η of the leading non-b-jet. The range of the p_{T} sum for each slice is [0,100] GeV, such that the abscissa x in slice i ($i = 1, 2..., 11$) corresponds to a value of the p_{T} balance of $(x - 100 \cdot (i-1))$ GeV. This variable is used for the signal extraction by the BILL template fit in the muon channel in the 3 jet bin. The MC distributions are normalized to the data luminosity.

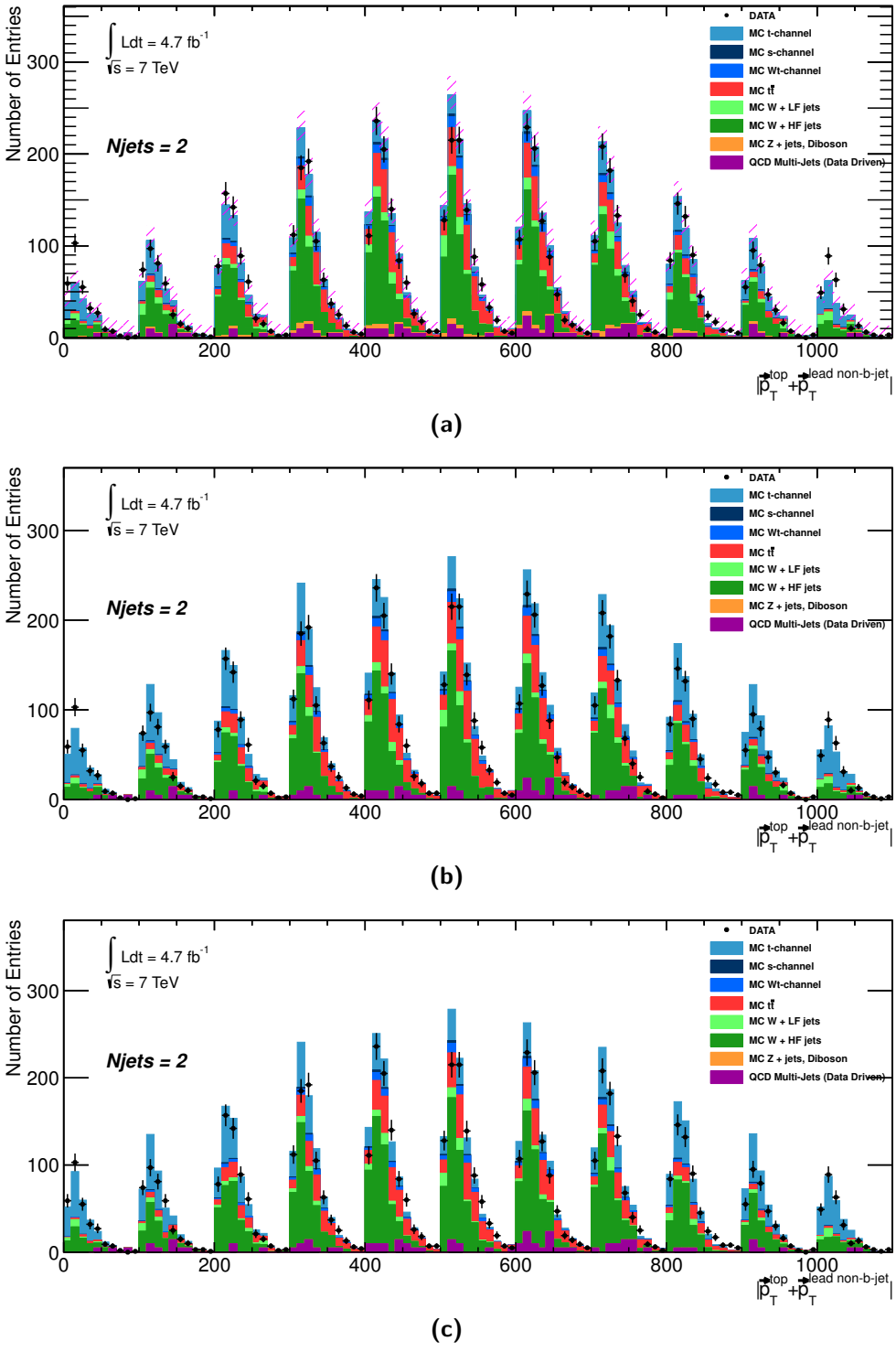

Figure 6.8. Comparison of the signal extraction histogram of the muon channel in the 2-jet bin before (a) and after the nominal BILL signal extraction fit (b) as well as after the fit of the systematically altered JES up samples (c). In (b) and (c), all MC processes are scaled by their β values resulting from the nominal fit of the lepton combination in the 2-jet bin.

The correlation matrices associated with the nominal β fits are shown in Fig. 6.9a for the combination of the 2- and 3-jet bins of both lepton channels and in Fig. 6.9b for the lepton combination in the 2-jet bin. In these figures, it is understood that each process is fully correlated to itself (main diagonals). Also, due to the fixed β_{QCD}, there is no correlation between the rate of QCD multi-jets production and the other processes.

In the 2- and 3-jet bin combination, the $\beta_{t\text{-channel}}$ can be seen to be anti-correlated to the rates of W+jets processes in association with heavy flavour jets as well as, to a lesser degree, to Wt-channel and s-channel single-top production. It is furthermore correlated to $\beta_{\mathrm{t\bar{t}}}$. There is almost no correlation to W in association with light flavour jets, Z+jets or diboson production. The strong anti-correlation with W+HF is likely due to the fact that it is the only process that is also present in the high $|\eta_{\text{lead non-b-jet}}|$ region of the signal extraction histogram (cp. Fig. 6.6 and 6.7), and thus, only raising the W+HF contribution can compensate for a decrease of the t-channel production rate in this crucial range, and vice versa. With $\mathrm{t\bar{t}}$, the opposite is true: Since the $\mathrm{t\bar{t}}$ topology prefers low values of $|\eta_{\text{lead non-b-jet}}|$, this background process fills the central $|\eta_{\text{lead non-b-jet}}|$ gap of the t-channel such that an increase of the t-channel content of the sample must be accompanied by an increase of $\mathrm{t\bar{t}}$.

In the lepton combination of the 2-jet bin there is less statistics than in the 2- and 3-jet bin combination, and there is much less $\mathrm{t\bar{t}}$ contamination. The anti-correlation of $\beta_{t\text{-channel}}$ to the rate of W+HF jets is again strong, although the Wt-channel rate is stronger anti-correlated; here, even $\mathrm{t\bar{t}}$ is anti-correlated to the signal process. This means that in the 2-jet bin the signal contribution is quite high and can only be mimicked by increasing the rates of all other background processes: In particular, the error on the W+jets cross-section is lower in the restriction to the 2-jet bin, and thus, the Wt-channel rate must be increased if the t-channel contribution drops in order to properly model the low values of the p_{T} balance distribution in the fit (cp. Fig. 6.6); this effect is not as pronounced in the 3-jet bin where $\mathrm{t\bar{t}}$ processes are also found at low $|\vec{p}_{\mathrm{T,top}} + \vec{p}_{\mathrm{T,lead\ non\text{-}b\text{-}jet}}|$, not only in the tails. In the 2-jet bin, however, the $\mathrm{t\bar{t}}$ rate also needs to increase at the same time to make up for a decrease of the signal cross-section. The smaller anti-correlations to s-channel, Z+jets and diboson as well as W+LF jets production mirror the situation in the 2- and 3-jet bin combination.

Systematic Errors

The impact of the systematic uncertainties from the 27 sources discussed in Sec. 6.1 is also analyzed and the results are listed in Tab. 6.5 for the (2+3)-jet bin combination of both lepton channels (the detailed results for the individual analysis channels are collected in App. D). In this table, each systematic-specific relative error $\pm\delta\beta^{i}_{t\text{-channel}}$, which is at the same time the relative error on the signal cross-section $\pm\delta\sigma^{i}_{t\text{-channel}}$, is derived from 10,000 dedicated pseudo-experiments for that particular systematic error source i. The quoted bias in the third column of the table is the offset of the

(a) 2+3 Jets, e+μ

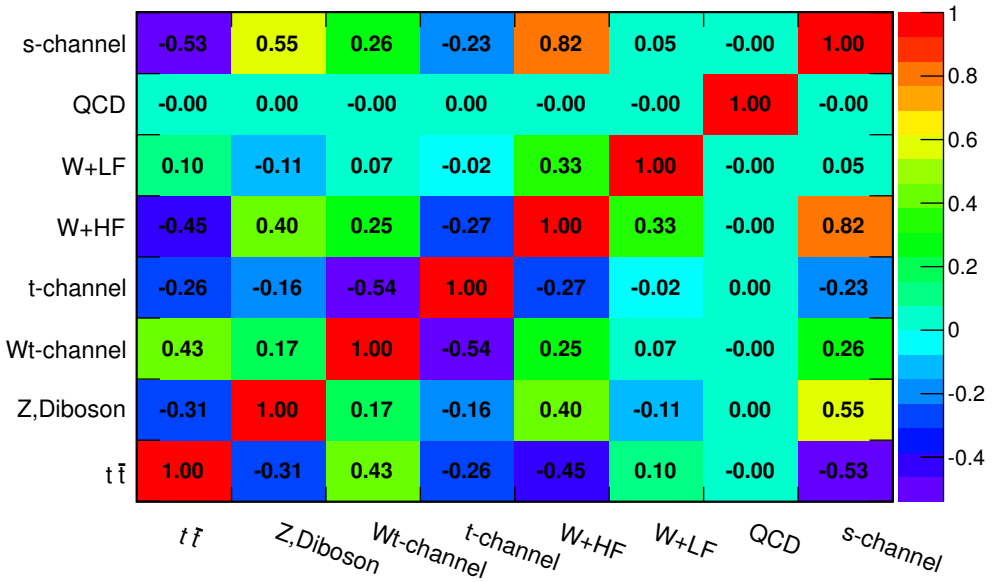

(b) 2 Jets, e+μ

Figure 6.9. Correlation matrices of the β values of all processes from the BILL signal extraction fit on the combination of the 2 and 3-jet bin of both lepton channels, (a) , and on the combination of both lepton channels in the 2-jet bin, (b).

mean $\bar{\beta}^i_{t\text{-channel}}$ from one in the $\beta^i_{t\text{-channel}}$ distribution,

$$\text{Bias}(\beta^i_{t\text{-channel}}) = \bar{\beta}^i_{t\text{-channel}} - 1\,. \tag{6.39}$$

This bias is already included in the respective error of the same sign in the sense that the table entries correspond to

$$\begin{aligned} \delta\beta^{i,+}_{t\text{-channel}} &= \sqrt{\sigma_i(\beta_{t\text{-channel}})^2 - \sigma_{\text{data stat}}(\beta_{t\text{-channel}})^2 + \text{Bias}(\beta^i_{t\text{-channel}})^2}\,, \\ \delta\beta^{i,-}_{t\text{-channel}} &= \sqrt{\sigma_i(\beta_{t\text{-channel}})^2 - \sigma_{\text{data stat}}(\beta_{t\text{-channel}})^2}\,, \end{aligned} \tag{6.40}$$

for a positive bias ($\text{Bias}(\beta^i_{t\text{-channel}}) \geq 0$), and to

$$\begin{aligned} \delta\beta^{i,+}_{t\text{-channel}} &= \sqrt{\sigma_i(\beta_{t\text{-channel}})^2 - \sigma_{\text{data stat}}(\beta_{t\text{-channel}})^2}\,, \\ \delta\beta^{i,-}_{t\text{-channel}} &= \sqrt{\sigma_i(\beta_{t\text{-channel}})^2 - \sigma_{\text{data stat}}(\beta_{t\text{-channel}})^2 + \text{Bias}(\beta^i_{t\text{-channel}})^2}\,, \end{aligned} \tag{6.41}$$

for a negative bias ($\text{Bias}(\beta^i_{t\text{-channel}}) < 0$). Here, $\sigma_{\text{data stat}}(\beta_{t\text{-channel}})$ is subtracted, since the pseudo-experiments done for each systematic i also entail the computation of the data statistical error by construction.

In contrast to these single systematic-specific errors, the "Total (syst)" error originates from applying all systematic variations listed at once (except data statistics) and running 10,000 correlated pseudo-experiments, as explained in Sec. 6.2.2. This error thus corresponds to the total systematic error including correlations among error sources. The "Total (syst+stat)" error, finally, amounts to the "Total (syst)" error and the data statistics error, added in quadrature. Again, the quoted bias is already included in the error of the respective sign.

The systematic tables of the separate jet bins listed in App. D are only summarized shortly here to facilitate the interpretation of the combined result. The results are mainly independent of the lepton flavour.

In the 2-jet bin, the simulation uncertainties are just as large as the reconstruction uncertainties. Especially the modelling of ISR/FSR has a huge impact. This can be attributed to the high t-channel contribution in the 2-jet bin sample: The associated systematic variation involves modified p_{T} thresholds and η distributions of the jets from ISR/FSR, which can alter the number of jets in the event. This apparently affects the t-channel more than $\text{t}\bar{\text{t}}$, since the ISR/FSR uncertainty in the $\text{t}\bar{\text{t}}$ dominated 3-jet bin is negligible (cp. e.g. Tab. D.5), and the ISR/FSR variation is only assessed for the processes involving top quarks. Here, the difference of ME and PS generators used for the variation samples as compared to the ones employed to model the nominal $\text{t}\bar{\text{t}}$ production could play a role; also, there is hardly any FSR in the $\text{t}\bar{\text{t}}$ topology due to the top quark final state, whereas in the t-channel, the light forward jet can radiate gluons. Furthermore, the PDFs, the $\text{W} + \text{c}/(\text{W} + \text{c}\bar{\text{c}} + \text{W} + \text{b}\bar{\text{b}})$ ratio and the t-channel matrix element generator are important. The large PDF error originates on one hand from the sizeable $\text{t}\bar{\text{t}}$ fraction in the 2-jet bin, but on the other hand also from W+jets: $\text{t}\bar{\text{t}}$ production proceeds mainly via the gluon fusion

process (cp. Fig. 2.7) and one production mechanism of W+jets also has a gluon in the initial state (cp. Fig. 4.5b). The gluon PDF, however, is very sensitive to α_S and thus suffers from large theoretical uncertainties of α_S. The W+HF flavour composition is influential since W+b$\bar{\text{b}}$+jets events in principle contain exactly the same objects as signal events, and their relative rate in W+HF is therefore crucial. The large uncertainty from the t-channel matrix element generator, finally, is due to the high fraction of t-channel events in this jet bin. Of the reconstruction related systematics, the JES, as expected, shows the highest contribution, comparable to that of ISR/FSR, since the JES is not very well known (cp. Sec. 6.1.2) and applies to each jet in the event. The b-tagging efficiency is a sizeable error source, too, due to the importance of the b-tagging in this analysis. Also, already in the 2-jet bin, the MC and data statistics errors are of the same magnitude as the leading systematics.

With increasing jet multiplicity, the relative weights of the simulation systematics are shifted. In the 3-jet bin, the t$\bar{\text{t}}$ related systematics overtake the t-channel and W+jets related errors due to the t$\bar{\text{t}}$ dominated sample composition in the 3-jet bin: The PDF uncertainty completely dominates the simulation systematics, followed by the t$\bar{\text{t}}$ matrix element generator; the t$\bar{\text{t}}$ PS generator also plays a role now. The errors from the t-channel matrix element generator and the W+HF flavour composition are still about the same as in the 2-jet bin. However, since there are much less t-channel events in the 3 jet bin, the ISR/FSR systematic is now negligible. On the reconstruction side, the JES uncertainty grows with increasing number of jets in the event and is, as in the 2-jet bin, at the same level as the largest simulation systematics. The second highest reconstruction systematic again results from the b-tagging that degrades with increasing jet multiplicities as the ID tracking is compromised. Here, the JER becomes sizeable as well due to a higher level of activity in the calorimetry complicating the contouring in the jet finding. The MC and data statistical errors are again at a level comparable to the highest systematic contributions.

Having considered the situation in the 2- and 3-jet bins separately, the breakdown of the systematic error sources of the combined channels in Tab. 6.5 can be understood. Since there are about twice as many events in the 2-jet bin than in the 3-jet bin (see Tab. 5.3), the ISR/FSR contribution on the simulation side is still high and only little smaller than the PDFs that are important in both jet bins. The errors from the t-channel matrix element generator and the W+HF flavour composition are independent of the jet bin and thus unchanged in the combination. For the reconstruction part, the JES is a little higher than for the 2-jet bin alone, and the same applies to the b-tagging. Naturally, the data statistics is improved w.r.t. the single channels. For the MC statistical error, this is not necessarily true, since the MC statistics decreases with increasing jet multiplicity and the results are scaled up to the data luminosity, giving large errors; this effect is not counteracted much by an increased acceptance from combining the yields of several analysis channels.

Now, if the result from the 2- and 3-jet bin combination is compared to the one from only combining the two lepton channels in the 2-jet bin, see Tab. 6.6, it becomes apparent that nothing can be gained by including the 3-jet bin. This is due to smaller t$\bar{\text{t}}$ related errors (PDFs and t$\bar{\text{t}}$ matrix element generator), smaller jet

related errors (JES, JER and b-tagging) and a smaller MC statistical error in the 2-jet bin. The larger relative weight of the t-channel related ISR/FSR error resulting from a restriction to the 2-jet bin does not obliterate these advantages. Therefore, the final cross-section result is quoted only for the 2-jet bin combination of both lepton channels.

Finally, a remark on the asymmetry of the overall cross-section error is in order: As can be seen in Tables 6.5 and 6.6 as well as in App. D, the overall bias on the measurement almost exclusively results from the bias of the MC statistics uncertainty. This can be attributed to the small statistics of the Z+jets/diboson contribution whose rate is basically downscaled to zero in the 2-jet bin signal extraction fit. With very little entries of this process to start with in combination with the huge cross-section uncertainty assigned to it (cp. Tab. 6.2), the new yields randomly determined in each pseudo-experiment (according to Sec. 6.2.2) often turn out to be negative. They are therefore forced to zero to avoid unphysical event counts, and this, in turn, corresponds to an effective overestimation of the Z+jets/diboson yield. If Z+jets/diboson production is omitted altogether, the bias disappears. It is not obvious why this process produces a positive bias on $\beta_{t\text{-channel}}$, though, since this is likely caused by a complex interconnection of the shapes of all processes involved.

Single-Top t-Channel Cross-Section and V_{tb}

The final result of the single-top t-channel cross-section is now computed as

$$(\sigma^{e\nu}_{t\text{-channel}} + \sigma^{\mu\nu}_{t\text{-channel}} + \sigma^{\tau\nu}_{t\text{-channel}}) \cdot \beta_{t\text{-channel}} \tag{6.42}$$

where $\sigma^{\ell\nu}_{t\text{-channel}}$, $\ell \in \{e, \mu, \tau\}$, are the cross-section values of the signal MC samples, taken from Tab. 4.2, already including the k-factors, and $\beta_{t\text{-channel}}$ is the signal cross-section scale factor from Tab. 6.4 for the 2-jet bin combination of both lepton channels. Considering the Total(syst+stat) error from Tab. 6.6 as the overall error on the cross-section measurement, the observed t-channel cross-section amounts to

$$\sigma_{t\text{-channel,leptonic}} = \left(36.0^{+9.5}_{-9.0}\right)\text{ pb} = \left(36.0^{+2.2}_{-2.2}(\text{stat.})^{+9.2}_{-8.7}(\text{syst.})\right)\text{ pb} \tag{6.43}$$

for the leptonic decay modes. Considering the exact leptonic branching ratio of the W boson used in the MC samples,

$$\sum_{\ell=e,\mu,\tau} BR_{\text{MC}}(\text{W} \to \ell\nu) = 0.324\,, \tag{6.44}$$

the total t-channel cross-section under the assumption of Eq. (2.15) thus becomes

$$\sigma_{t\text{-channel}} = \left(111.0^{+29.2}_{-27.7}\right)\text{ pb} = \left(111.0^{+6.7}_{-6.7}(\text{stat.})^{+28.5}_{-26.9}(\text{syst.})\right)\text{ pb}\,. \tag{6.45}$$

With Eq. (2.15), the reconstruction efficiency of the analysis is solely determined by the t-channel production via b-quarks.

(2+3)-Jet Bin, Electron and Muon Channel Combination

Systematic	$\delta\sigma_{t\text{-channel}}$ Up[%]	Down[%]	Bias[%]
Data Statistics	6.11	−6.11	0.00
Luminosity	1.78	−1.78	0.01
MC Statistics	11.59	−5.73	10.08
Background Cross-Sections	1.37	−1.37	0.10
PDFs	13.06	−13.06	−0.11
Matrix Element Generator (t-channel)	7.26	−7.26	0.05
Matrix Element Generator ($t\bar{t}$)	4.91	−4.91	0.07
Parton Shower Generator ($t\bar{t}$)	0.19	−0.18	0.06
ISR/FSR	10.99	−10.99	0.09
QCD Normalization	0.48	−0.48	−0.05
Ratio W+LF/W+HF	2.08	−2.06	0.26
Ratio W+c/(W+c$\bar{c}$ + W+b$\bar{b}$)	8.33	−8.24	1.22
Electron Energy Scale	0.39	−0.39	0.08
Electron Energy Resolution	0.87	−0.87	−0.11
Muon p_{T} Scale	0.42	−0.40	0.13
Muon p_{T} Resolution (ID)	0.70	−0.70	−0.08
Muon p_{T} Resolution (MS)	0.38	−0.38	−0.07
Lepton Reconstruction Efficiency	1.63	−1.63	0.06
Jet Energy Scale	16.39	−16.39	0.45
Jet Energy Resolution	3.72	−3.32	1.69
Jet Reconstruction Efficiency	0.29	−0.29	−0.02
B-Tagging Efficiency	8.16	−8.16	0.12
C-Tagging Efficiency	0.66	−0.65	0.12
Mistagging Efficiency	1.07	−1.07	0.06
JVF	0.28	−0.28	0.05
$E_{\mathrm{T}}^{\mathrm{miss}}$ Pile-Up	0.85	−0.63	0.57
$E_{\mathrm{T}}^{\mathrm{miss}}$ CellOut+SoftJet	0.41	−0.34	0.23
Total (syst)	31.86	−28.38	14.48
Total (syst+stat)	32.44	−29.03	14.48

Table 6.5. All systematic uncertainties resulting from the pseudo-experiments executed to estimate the total error of the single-top t-channel cross-section measurement.

2-Jet Bin, Electron and Muon Channel Combination

Systematic	$\delta\sigma_{t\text{-channel}}$ Up[%]	Down[%]	Bias[%]
Data Statistics	6.04	−6.04	0.00
Luminosity	1.74	−1.74	0.06
MC Statistics	8.20	−5.47	6.12
Background Cross-Sections	2.13	−2.13	0.06
PDFs	8.85	−8.85	−0.08
Matrix Element Generator (t-channel)	6.96	−6.96	−0.13
Matrix Element Generator ($\mathrm{t\bar{t}}$)	1.66	−1.66	0.05
Parton Shower Generator ($\mathrm{t\bar{t}}$)	0.71	−0.71	0.02
ISR/FSR	12.32	−12.32	−0.23
QCD Normalization	2.53	−2.53	−0.10
Ratio W+LF/W+HF	2.10	−2.07	0.34
Ratio W+c/(W+$\mathrm{c\bar{c}}$ + W+$\mathrm{b\bar{b}}$)	7.22	−7.15	0.99
Electron Energy Scale	0.09	−0.09	−0.04
Electron Energy Resolution	0.27	−0.36	−0.24
Muon p_{T} Scale	0.45	−0.45	−0.00
Muon p_{T} Resolution (ID)	0.48	−0.48	0.06
Muon p_{T} Resolution (MS)	0.34	−0.37	−0.13
Lepton Reconstruction Efficiency	0.75	−0.75	0.04
Jet Energy Scale	13.74	−13.74	−0.03
Jet Energy Resolution	1.33	−1.17	0.63
Jet Reconstruction Efficiency	0.26	−0.23	0.11
B-Tagging Efficiency	6.26	−6.26	0.20
C-Tagging Efficiency	0.64	−0.61	0.16
Mistagging Efficiency	0.86	−0.86	0.04
JVF	0.51	−0.51	0.05
$E_{\mathrm{T}}^{\mathrm{miss}}$ Pile-Up	1.35	−1.26	0.49
$E_{\mathrm{T}}^{\mathrm{miss}}$ CellOut+SoftJet	1.58	−1.58	−0.02
Total (syst)	25.64	−24.23	8.40
Total (syst+stat)	26.34	−24.97	8.40

Table 6.6. All systematic uncertainties resulting from the pseudo-experiments executed to estimate the total error of the single-top t-channel cross-section measurement.

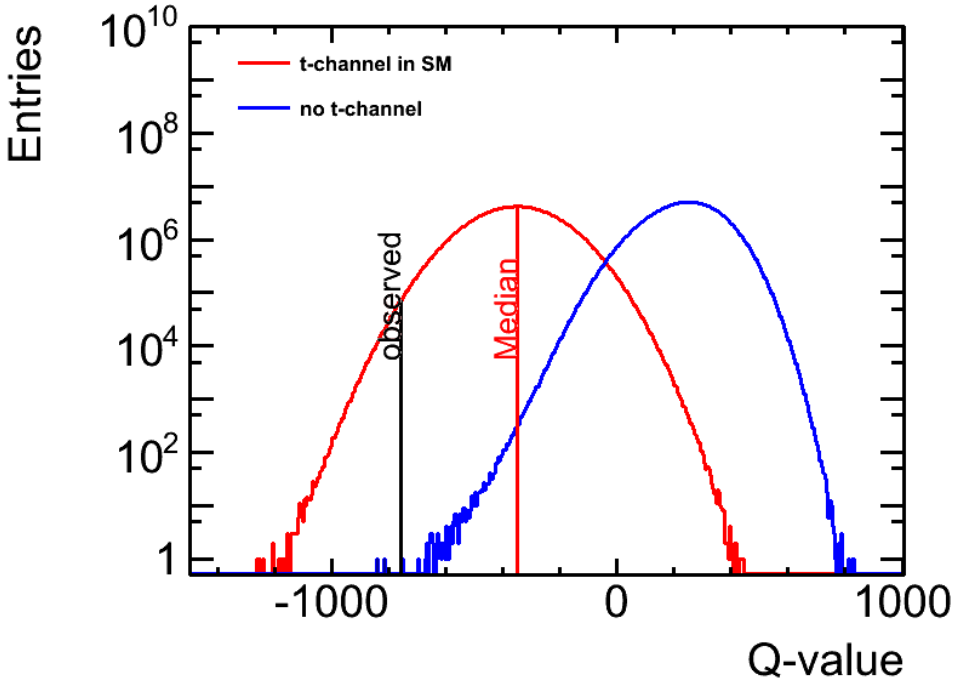

Figure 6.10. Overlapping distributions $\hat{q}_0$ and $\hat{q}_1$, associated with the no-signal (no t-channel) and signal (t-channel in SM) hypotheses, respectively. The median of the $\hat{q}_1$ distribution and the observed Q-value are shown as well. There are only two pseudo-experiments left of Q_{obs}.

In order to compute the significance of the measurement according to Sec. 6.2.3, $\mathcal{O}(10^8)$ pseudo-experiments are generated, resulting in the Q-value distributions of the signal and the null hypothesis shown in Fig. 6.10. There are only two pseudo-experiments left of the observed Q-value, resulting in $p_{\text{obs}} = 6.7 \cdot 10^{-9}$ and a significance of

$$N_{\sigma}^{t\text{-channel}} = 5.7\,. \tag{6.46}$$

Thus, the measurement in this work with a significance of 5.7 σ (expected significance is 4.3 σ) signifies an observation of the single-top t-channel process, confirming the observations by other recent studies at the Tevatron and at the LHC.

From the measured cross-section value, the CKM matrix element $|V_{\text{tb}}|$ can now be determined (cp. Sec. 2.2). The measured $\sigma_{t\text{-channel}}$ corresponds to the product of the total single-top t-channel cross-section and the branching ratio

$$R(\text{t} \to \text{b} + \text{W}) = \frac{|V_{\text{tb}}|^2}{|V_{\text{td}}|^2 + |V_{\text{ts}}|^2 + |V_{\text{tb}}|^2}\,. \tag{6.47}$$

With the assumption of Eq. (2.15), this simplifies to $R(\text{t} \to \text{b} + \text{W}) \approx 1$, allowing for the computation of $|V_{\text{tb}}|$ according to Eq. (2.14): Here, $|V_{\text{tb}}^{\text{SM}}|$ is set to the value $|V_{\text{tb}}^{\text{MC}}| = 0.99152$ used in the MC samples (cp. Sec. 4.3.6), and the predicted cross-

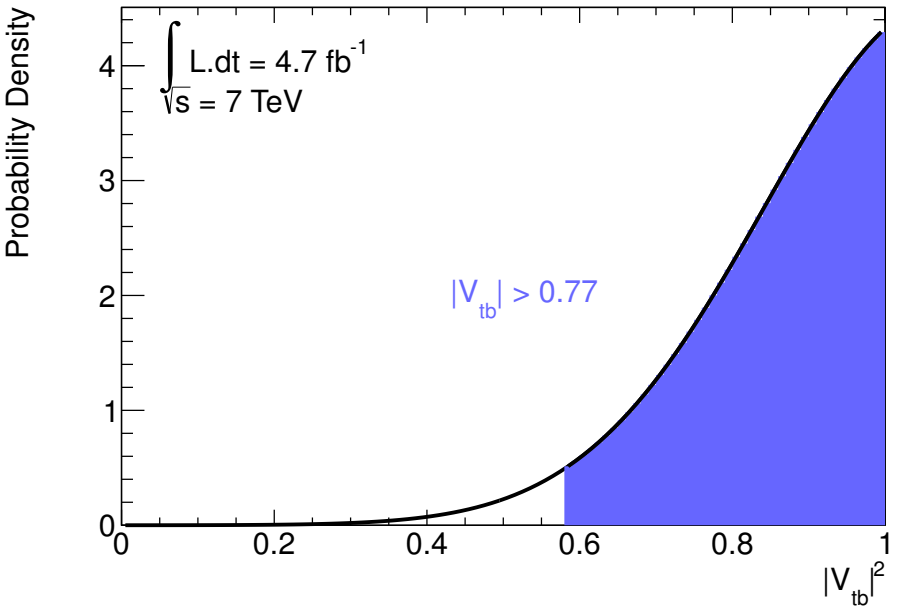

Figure 6.11. Observed probability density of the CKM matrix element $|V_{\mathrm{tb}}|^2$ and observed lower limit at 95 % C.L. for the standard model scenario $0 < |V_{\mathrm{tb}}| < 1$.

section $\sigma^{\mathrm{SM}}_{t\text{-channel}} = 64.57\,\mathrm{pb}$ at $m_{\mathrm{t}} = 172.5\,\mathrm{GeV}$ (cp. Tab. 2.4) is utilized. Also, the W-t-b interaction is taken to be of a (V − A), CP-conserving nature. As mentioned in Sec. 2.2, no further assumptions, i.e. on the number of quark generations or the unitarity of the CKM matrix, are required. If anomalous couplings at the W-t-b vertex are allowed, an additional anomalous form factor f_1^{L} must be considered (see Eq. (2.21)): In this case, the coupling strength $f_1^{\mathrm{L}} = 1$ is not guaranteed anymore, but can even take on values greater than unity, thus rescaling the single-top cross-section [KLY92]. Hence, only the strength of the (V − A) coupling can be calculated to be

$$|V_{\mathrm{tb}} f_1^{\mathrm{L}}| = 1.30^{+0.13}_{-0.16}\,. \tag{6.48}$$

Here, the errors are computed via standard error propagation to second order in the Taylor series expansion, and the error of the prediction is small compared to the one of the measurement. On the basis of the precision of $|V_{\mathrm{tb}} f_1^{\mathrm{L}}|$ reached in this work, no particular scenario beyond the standard model can be favoured over another.

If the standard model scenario $0 \leq |V_{\mathrm{tb}}| \leq 1$ and $f_1^{\mathrm{L}} = 1$ is assumed, a limit on $|V_{\mathrm{tb}}|$ can be obtained by fitting a Gaussian to the interval [0,1] of the $\beta_{t\text{-channel}}$ distribution resulting from the 10,000 pseudo-experiments done for all correlated systematics; the fit curve is then normalized to unity, yielding a probability density for $|V_{\mathrm{tb}}|^2$, as depicted in Fig. 6.11. The lower limit on the value of the CKM matrix element is thus set at 95 % confidence level (C.L.) to be

$$0.77 < |V_{\mathrm{tb}}| \leq 1\,. \tag{6.49}$$

6.3. Comparison with other Studies

The cross-section and $|V_{\mathrm{tb}}|$ results presented above can be compared to those of other studies. Since the t-channel cross-section depends on the centre-of-mass energy $\sqrt{s}$ and the type of the colliding hadrons, a meaningful comparison is possible only with other measurements at $\sqrt{s} = 7\,\mathrm{TeV}$ on proton-proton collisions. The value of $|V_{\mathrm{tb}}|$, in contrast, is independent of these features. In Fig. 6.12, the theoretical $\sqrt{s}$ dependence is shown for leading (LO) as well as next-to-leading (NLO) order along with measurement results from the Tevatron on $\sqrt{s} = 1.96\,\mathrm{TeV}$ $\mathrm{p\bar{p}}$ collisions (small box) as well as from the LHC experiments at $\sqrt{s} = 7\,\mathrm{TeV}$ and $\sqrt{s} = 8\,\mathrm{TeV}$; the cross-section measured in the study at hand is also included and marked in red. The error on the theory prediction is generally composed of a term originating from the choice of the scales $\mu_{\mathrm{R}}, \mu_{\mathrm{F}}$ as well as of the underlying PDF set[21], and also an influence of the assumed m_{t} can be considered. In this plot, however, the theory error band only signifies the scale uncertainty from varying $\mu_{\mathrm{R}} = \mu_{\mathrm{F}} = \mu$ by a factor of 1/2 and 2 w.r.t. m_{t}. The predicted cross-section dependence is computed using the CT10 NNLO PDF set [Lai+10] and $m_{\mathrm{t}} = 173.5\,\mathrm{GeV}$.

As can be seen in the figure, there are two published results for $\sqrt{s} = 7\,\mathrm{TeV}$, one from ATLAS [ATL12j] and one from CMS [CMS12a]. These are based on a smaller dataset than the study at hand. Furthermore, there is another unpublished measurement by ATLAS [ATL12i] based on the same integrated luminosity as this work. The four cross-section measurements are collected for direct comparison in Fig. 6.13. The theory predictions at NLO and approximate next-to-next-to-leading order (aNNLO) are quoted as well; the difference between them is minor and cannot be resolved in the figure. Similarly, the comparison of five results for $|V_{\mathrm{tb}}|$ is shown for the Tevatron and LHC experiments in Fig. 6.14; in the latest ATLAS internal study, no $|V_{\mathrm{tb}}|$ value is quoted. The theoretical $|V_{\mathrm{tb}}|$ value shown is the one used in the simulation samples. The overview of measured $|V_{\mathrm{tb}}|$ values and corresponding 95 % C.L. lower limits is given in Tab. 2.1.

The figures show that the result of this work does not increase the precision of the cross-section and $|V_{\mathrm{tb}}|$ measurements w.r.t. previous studies: The overall error is larger. In the following, the pair-wise comparison of the result presented here with the previous measurements will be drawn.

In the CMS measurement [CMS12a], the two lepton flavours are treated differently, such that it is based on $1.17\,\mathrm{fb}^{-1}$ in the electron and on $1.56\,\mathrm{fb}^{-1}$ in the muon channel. The quoted cross-section is a combination of three analyses. One analysis is cut-based and evaluates a maximum-likelihood fit to the $|\eta_{\text{light jet}}|$ distribution in the 2-jet bin with the requirement of exactly one b-tagged jet; this analysis is therefore the most similar approach to this study. The other two analyses employ multivariate methods: One "Neural Network" (NN) and one "Boosted Decision Tree" (BDT) approach are pursued. The cut-based analysis and the multivariate analyses complement each

[21] This usually includes the uncertainties from the PDF fits as well as the α_{s} dependence due to the PDFs used.

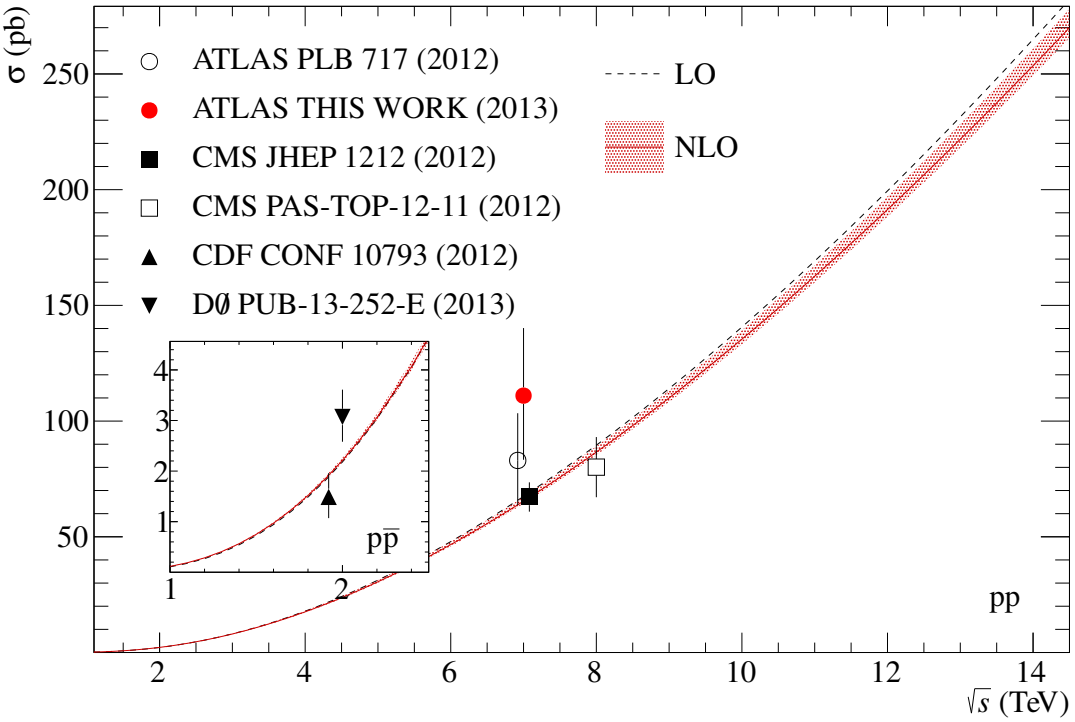

Figure 6.12. Single-top t-channel cross-section depending on the centre-of-mass energy (plot taken from [Kan+13]). The theoretical curve is shown as well as the measurements done by the LHC experiments ATLAS [ATL12j] and CMS [CMS12a; CMS13a] and the Tevatron experiments CDF [CDF13] and D0 [D0 13] (see box that zooms in on low $\sqrt{s}$ region). The red marker denotes the result of this study. The uncertainty bands of the theory predictions are drawn as shaded areas and indicate the full scale uncertainty (μ_{R} and μ_{F}) for the given order of the calculation in perturbative QCD, done by HATHOR[Ali+11]; there are no PDF uncertainties included. The underlying PDF set is CT10 NNLO.

other in that the former is robust and hardly model dependent whereas the latter are capable of a more precise signal discrimination at the cost of a higher dependence on the simulation, and they allow for cross-checks of one another. All three analyses perform the cross-section extraction on the signal enriched categories (i.e. the 2- and 3-jet bin with one b-tagged jet), whilst, in contrast to this work, the background dominated categories (e.g. the 2-jet bin with zero b-tagged jets, which is mainly composed of W+jets), are used for a simultaneous fit of the background rates. In the cut-based analysis, such a side-band region is defined as being outside of the top quark mass window $130\,\mathrm{GeV} < m_{\mathrm{t}} < 220\,\mathrm{GeV}$ and is used to extract the W+jets contribution. The CMS work furthermore utilizes different MC generators while the object definitions and the event preselection largely resemble the one of the study at hand.

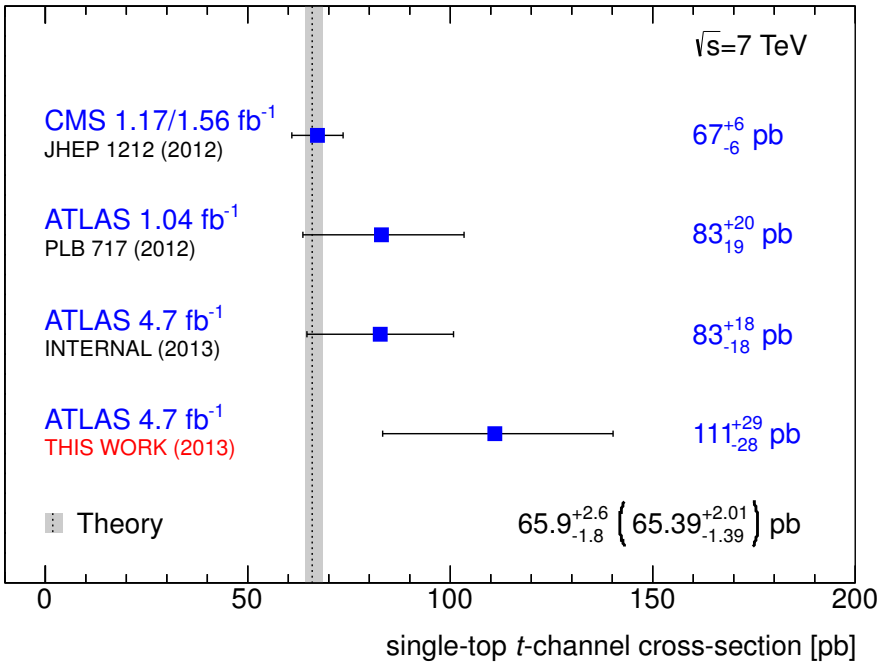

Figure 6.13. Single-top t-channel cross-section measurements at $\sqrt{s} = 7\,\text{TeV}$ by ATLAS and CMS. The theoretical prediction at approximate NNLO [Kid12] (and at NLO [Kan+13] in brackets) is also shown as a dashed line along with the scale and PDF uncertainties that are depicted by a grey band.

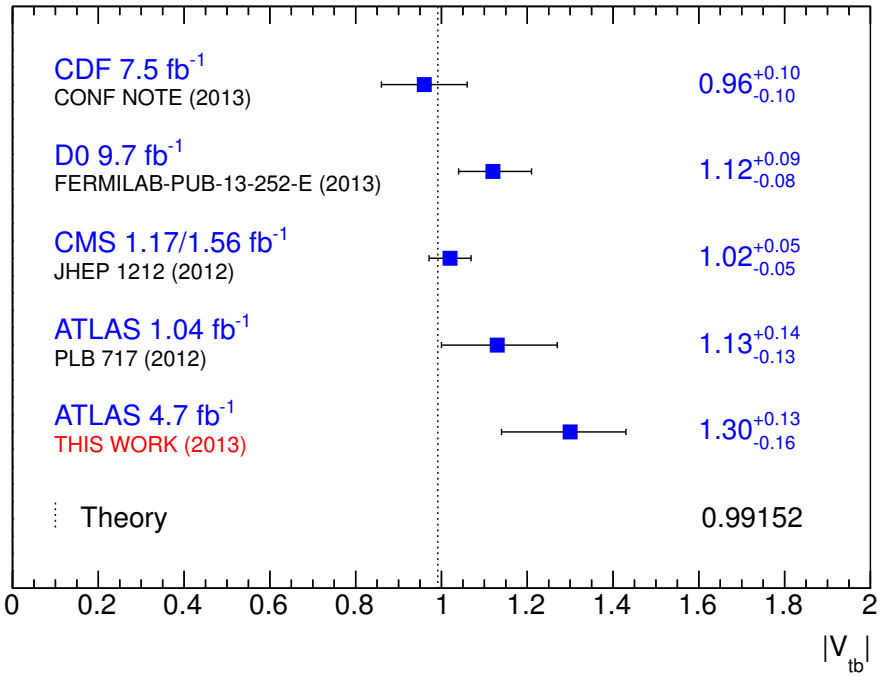

Figure 6.14. Measurements of the CKM matrix element $|V_{\text{tb}}|$ by CDF and D0 at $\sqrt{s} = 1.96\,\text{TeV}$ and by ATLAS and CMS at $\sqrt{s} = 7\,\text{TeV}$. The standard model expectation is also shown as a dashed line.

It is noteworthy, though, that the jet reconstruction in the CMS detector is done with a large cone radius of $\Delta R = 0.5$ of the anti-k_T algorithm and proceeds differently, namely via the so-called "particle-flow" (PF) algorithm [CMS10]: this reconstructs particles combining the information of all sub-detectors and also exploits the fact that in the CMS detector, as opposed to ATLAS, the calorimetry is submerged in the magnetic field of the huge solenoid magnet. The PF method improves the JER by a factor of three and the resolution of the $E_\mathrm{T}^\mathrm{miss}$ by a factor of two compared to the calorimeter-based jet reconstruction, and yields JES and $E_\mathrm{T}^\mathrm{miss}$ uncertainties at the percent level [CMS10]. As for the systematic error sources considered, on the experimental side, the lepton p_T scale and resolution uncertainties as well as the JVF are not included – perhaps the former are minor and thus not quoted; the latter may not apply for the CMS reconstruction due to the use of the PF algorithm. On the theoretical side, the $\mathrm{t\bar{t}}$ ME and PS generators are not considered, and the ISR/FSR systematic variation is done for $\mathrm{t\bar{t}}$, W+jets and Z+jets, but not for single-top. However, there are μ_F and μ_R scale uncertainties for the single-top, $\mathrm{t\bar{t}}$ and W+jets processes included that this study does not contain.

Firstly, comparing the present study to the cut-based approach of CMS with a precision of 14 %, the major differences reside in the JES uncertainty, the ISR/FSR error, the variation of the PDFs and the t-channel ME generator, in descending order of importance. This seems to be due to a better performance of the CMS jet reconstruction, to the omission of ISR/FSR variations of single-top processes in the CMS study, a more limited treatment of PDF errors therein (only one *intra-* and one *inter*-PDF error are included) and a lesser dependence on the signal model. For the multivariate methods, reaching a precision of about 10 %, respectively, this dependence is stronger, but all other systematics are smaller than for the cut-based analysis, and the JES and JER errors are only about one percent. All in all, comparing the combined CMS result with a precision of 9 % to this work, it can be concluded that the combination of cut-based and multivariate approaches is able to majorly improve on a result coming from an analysis of a cut-based type alone, because the multivariate methods are more powerful. That said, the cut-based analysis can also complement the multivariate techniques since there seems to be a lesser correlation of the cut-based approach with the multivariate approaches than between the multivariate methods. The $|V_\mathrm{tb}|$ measurement from this combination is in agreement with the SM and yields a 95 % C.L. lower limit of 0.92, which is a more accurate result than the one from this study, which is also merely compatible with the SM expectation.

The ATLAS measurement [ATL12j] on a smaller dataset of $1.04\,\mathrm{fb}^{-1}$ employs also a NN and is cross-checked by a cut-based analysis. The 2- and 3-jet bin and both lepton flavours are combined, and exactly one b-tagged jet is required. The MC generators used are the same as in this study and the object definitions are virtually identical. Concerning the event preselection, the lepton and jet $p_\mathrm{T} > 25\,\mathrm{GeV}$ and $E_\mathrm{T}^\mathrm{miss} > 25\,\mathrm{GeV}$ thresholds are all raised to 30 GeV in the work at hand, and the triangular cut $m_\mathrm{T}^\mathrm{W} > (60\,\mathrm{GeV} - E_\mathrm{T}^\mathrm{miss})$ done there is tightened to a $m_\mathrm{T}^\mathrm{W} > 30\,\mathrm{GeV}$ cut here; a cut on $H_\mathrm{T} > 210\,\mathrm{GeV}$ is only applied by the cut-based analysis, which

additionally requires the top mass window $150\,\text{GeV} < m_\text{t} < 190\,\text{GeV}$ as well as the very restrictive cut of $|\eta_{\text{light jet}}| > 2$ [22]. In the 2-jet bin, the cut-based analysis also demands $|\Delta\eta(\text{b-jet, light jet})| > 1$, whereas in the 3-jet bin the combined mass of the three jets must exceed 450 GeV. Furthermore, the combined b-tagging algorithm used is very similar to the one in this study, but the performance is already improved here. In both analyses, the W+jets contributions are determined in a data-driven manner by dedicated methods: In the NN case, the W+jets background is fitted simultaneously in the signal extraction step (like in the multivariate analyses of CMS) whereas the cut-based analysis employs a method akin to the one used in this work, only that the normalization factors are extracted from the 1- and 2-jet bin *pretag* and *tag* information (cp. Sec. 4.3.2).

The final signal extraction from the NN discriminant distribution and from the event yield histograms of the cut-based analysis is done in an analogous manner to this work with the BILL tool, as is the treatment of systematic errors. Regarding the systematic uncertainties of the two analyses, the t-channel PS generator is considered that is not included in this work due to reasons of availability; also, a shape uncertainty arising from a μ_R and μ_F variation of the W+jets ME generator is taken into account that is not regarded here. The JVF systematic is a source newly added at the time of this study, whereas the previous analyses assign an uncertainty for a mismodelling of forward jets that is not applied here since it is not deemed necessary (cp. Sec. 6.2.4).

All in all, being based on the same reconstruction and simulation setup, the results of these two approaches are comparable to a high degree with this work. The NN analysis achieves a precision of 24 % and dominates the combination of both results where the cut-based approach only reaches about 29 %; this is due to a larger model dependence of the latter, especially the ISR/FSR and the PS part. The comparison of systematic errors w.r.t. the study at hand shows that, on the reconstruction side, the impact of JES and b-tagging is reversed: The b-tagging here is obviously improved, but a doubling of the JES can be observed. Like this analysis, the two approaches are dominated by theoretical uncertainties, the ISR/FSR error being the highest. The relatively high PS contribution cannot meaningfully be compared to the low one in this work because the signal PS generator is not assessed here. The PDF uncertainty is lower in the previous studies, the ISR/FSR dependence higher, and the additional forward jet systematic yields an intermediate contribution. The quoted significance of the NN analysis is 7.2 σ (6.0 expected). In summary, the result presented here ranges well between the NN and the cut-based approach. The $|V_\text{tb}|$ measurement from this ATLAS combination just about borders on the SM value and corresponds to a 95 % C.L. lower limit of 0.75. This limit is a little lower than the one from the study at hand since the absolute value of the cross-section obtained here is already large.

The second ATLAS measurement of the t-channel cross-section is based on $4.7\,\text{fb}^{-1}$, like this study. Its aim is the measurement of the ratio of top and anti-top quark

[22] In the 3-jet bin, the light jet is defined as the leading non-b-jet.

production by the NN method already employed in the first ATLAS study. As in this previous study, the 2 and 3-jet bin and both lepton flavours are combined, and the lepton and jets are required to satisfy $p_{\mathrm{T}} > 25\,\mathrm{GeV}$; for jets within $2.75 < |\eta| < 3.75$, this threshold is even raised to 50 GeV. The cuts on $E_{\mathrm{T}}^{\mathrm{miss}}$ and on $m_{\mathrm{T}}^{\mathrm{W}}$, in contrast, are the same as in this work. As done in the previous NN study, the W+jets contributions are fitted simultaneously in the signal extraction step, which, like the computation of systematic errors, is again performed with the BILL tool.

Regarding the systematics, the ISR/FSR uncertainty is assessed for the t-channel and $\mathrm{t\bar{t}}$ whereas in this work, the Wt- and s-channel are included as well. Unlike in the study at hand, the $\mathrm{t\bar{t}}$ ME generator is not considered. Furthermore, the errors associated with the choice of the PS generator are omitted altogether. The PDF error is only derived for two alternative PDF sets, whereas three are included in this work; most notably, though, these two are only evaluated on the single-top and $\mathrm{t\bar{t}}$ processes, not on all MC samples, as is done here. However, like for the predecessor analysis, a W+jets shape uncertainty from a μ_{R} and μ_{F} variation of the Alpgen generator is again taken into account that is not included in the study at hand. Also, an analysis-specific systematic concerned with the difference in b-tagging efficiencies between b and $\mathrm{\bar{b}}$ quarks adds to the overall error.

The analysis reaches a precision of 22 % and is completely dominated by the JES uncertainty: The JES error is the same as that of the 2- and 3-jet bin combination in this work, quoted in Tab. 6.5. Similarly, all other reconstruction related systematics agree with the ones shown here for the 2- and 3-jet bin combination. The differences reside in the much smaller PDF and ISR/FSR errors compared to this work and the omittance of the $\mathrm{t\bar{t}}$ ME generator uncertainty. Also, the overall error associated with the W+jets rates is smaller in the NN case. Being the analysis that is probably best suited for comparison to the study presented here, since it is based on the same integrated luminosity of ATLAS data and the same object definitions, and employs an almost identical event selection, it appears that the NN method is either far less model dependent than the kinematic fitting approach or many sources of theoretical uncertainties do not enter the computation of the NN systematic error. Furthermore, in contrast to the study at hand where the reconstruction by kinematic fitting is done anew in each event of the nominal as well as of the systematically altered samples, the training of the NN in this approach is not repeated for the systematics samples.

It is a noteworthy difference between the study at hand and all other quoted t-channel cross-section values that here, only the 2-jet bin is included in the final result whereas the other measurements all consider the 2- and 3-jet bin combination. All in all, the comparison to the NN result on $4.7\,\mathrm{fb}^{-1}$ is the most instructive one, especially w.r.t. the most relevant reconstruction related systematic uncertainty, the JES error. Also, it seems that the increase by a factor of two in the JES uncertainty from the $1.04\,\mathrm{fb}^{-1}$ to the $4.7\,\mathrm{fb}^{-1}$ ATLAS results is due to a refined method of approximation of this error, including more detector effects. The NN and kinematic fitting methods therefore consistently observe this increase for the $4.7\,\mathrm{fb}^{-1}$ data set. From the above comparisons, it is also to be presumed that the three ATLAS results yield a comparatively high cross-section due to the systematic underestimation of

the jet energies in the MC, especially w.r.t. the forward jets: Since the forward jet kinematics is crucial in separating the signal from the background, regardless of the analysis method, this causes the t-channel scale factor $\beta_{t\text{-channel}}$ to assume high values to match the data (cp. also Sec. 6.2.4). It cannot be excluded that the fixation of the QCD (and for the previous two studies even of the W+jets) background rate in the BILL signal extraction fit throughout all three ATLAS analyses also plays a role here.

Last but not least, the latest $|V_{\mathrm{tb}}|$ values obtained by the Tevatron experiments, are both more precise than the one resulting from this analysis; of the two, only the CDF one is in agreement with the SM whereas the D0 value, similar to that of the study at hand, is merely compatible with unity.

The above results now allow to arrive at the following conclusions concerning the kinematic fitting approach as presented in this study:

- An important motivation for employing the kinematic fit in the reconstruction is the expected reduction of the JES uncertainty. However, the JES error is found to be of similar size as in the NN result on the same data set. This is because the kinematic fit corrects the fit objects' momenta, above all the b-jet momentum, but the fit does not include the forward jet at all. This is disadvantageous since the JES error on *light forward* jets is the large one, not the *b-jet* JES uncertainty (cp. Fig. 6.1). Indeed it seems difficult to include the forward jet kinematics in the fitting procedure in a straightforward manner – probably a momentum conservation constraint based on the p_{T} balance (6.37) could be envisaged, which, however, might only prove helpful in the 2-jet bin.

- Since the forward jet is the unique feature of the t-channel but is not included in the kinematic fit, its kinematics need to be exploited differently in order to gain discriminatory power. The signal extraction histogram is chosen accordingly in this study and sliced in $|\eta_{\text{lead non-b-jet}}|$. Here, in turn, the bins of large $|\eta_{\text{lead non-b-jet}}|$ show a data-MC discrepancy producing an artificially large $\beta_{t\text{-channel}}$ which is likely due to the systematic underestimation of jet p_{T} in the ATLAS simulation setup – a problem not resolvable at the analysis level.

- Given that this problem of the ATLAS jet reconstruction is resolved, it is preferable to at least partially cut out the central region of $|\eta_{\text{lead non-b-jet}}|$. This results in a much smaller W+jets background, which is irreducible by kinematic veto fits; this cut has already been realized in [Sta13b], which is a study on the 2-jet bin, based on the analysis developed here: The resulting JES error is indeed smaller, but the JER error is enlarged instead. In combination with a p_{T} balance constraint, as suggested above, the major background remaining in the 2-jet bin, $\mathrm{t\bar{t}}$ production, could probably be diminished further. Additionally, the hadronic W boson and $\mathrm{t\bar{t}}$ veto fits could be employed to reduce the $\mathrm{t\bar{t}}$ contribution further in the 3- and 4-jet bins. In this manner, the virtues of the kinematic fitter can be exploited more efficiently.

- The ability of the kinematic fit to identify the b-jet coming from the top decay, thus reducing combinatorial background in events with more than one b-jet, is not utilized in this study due to the restriction to one b-tagged jet. If more than one b-jet is permitted to be present in the event, though, i.e. the b-jet from the gluon splitting in the t-channel is reconstructed, the sample becomes completely $\mathrm{t\bar{t}}$ dominated. Also, the computation time increases according to the b-jet multiplicity (there are also other reasons for neglecting the category with two b-jets in this study, as outlined in Sec. 5.2.1). In this sense, the method of kinematic fitting is not as beneficial for the reconstruction of the t-channel topology itself as of Wt-channel and $\mathrm{t\bar{t}}$ processes: the latter suffer from ambiguities in the assignments of (b-)jets that can be resolved by suitably chosen fit constraints, a fact recognized by the veto fits in this analysis.

- In order to constrain the major background contributions from W+jets and $\mathrm{t\bar{t}}$ production, it is useful, as seen in other measurements described above, to also consider background dominated regions like the 2-jet bin with zero b-tags or a part of the signal region (2-jet bin with one b-tag): Then, a simultaneous fit of the signal rate with the background rates can be done. Such an approach has also been successfully applied within the framework of this analysis in [Sta13b] for the W+jets background, where the $E_{\mathrm{T}}^{\mathrm{miss}}$ distribution of events vetoed by the kinematic fit is included as a control region in the BILL fit. This analysis yielded an overall systematic error that is reduced by several percent compared to this work.

- A clear advantage of the kinematic fit is the possibility to unambiguously reconstruct the p_{z} of the neutrino, thus giving access to the full four-momentum of the top quark. This information can also be passed on to a more powerful multivariate analysis scheme, thus enhancing the multivariate methodology with a virtue of the kinematic fitting approach.

In summary, the reconstruction of the single-top t-channel topology by kinematic fitting has proven to be a viable alternative to cut-based and multivariate analysis techniques. The comparison to other studies, however, is difficult since the considered sources of systematic errors as well as the treatment of background rates in the signal extraction largely differ, and other setups also look back on a longer period of development than the one in this study.

Wenn du schnell gehen willst, geh allein.
Wenn du weit gehen willst, geh mit anderen.
Afrikanische Weisheit

7. Summary

In this work, the measurement of the single-top t-channel cross-section and the CKM matrix element $|V_{\mathrm{tb}}|$ on $4.7\,\mathrm{fb}^{-1}$ of $\sqrt{s} = 7\,\mathrm{TeV}$ proton-proton LHC collision data, recorded with the ATLAS detector in the year 2011, was presented. The study was motivated by probing the nature of the weak interaction at the W-t-b vertex: The size of $|V_{\mathrm{tb}}|$ is sensitive to physics effects beyond the standard model, such as the presence of additional anomalous couplings or flavour-changing neutral currents. Measuring $|V_{\mathrm{tb}}|$ to a high level of accuracy thus allows to distinguish different models of electroweak symmetry breaking.

The t-channel topology, consisting of a light quark, a top quark decaying into a W boson and a b quark, as well as a spectator b quark, was reconstructed by a χ^2-based kinematic fit with non-linear constraints. Selected semi-leptonic events contained 2, 3 or 4 highly energetic jets, one of them identified as a b-jet, one highly energetic electron or muon as well as missing transverse energy from the neutrino of the top quark decay. The signal was enriched by applying a W boson and a top quark mass constraint in the fit as well as two kinematic veto fits on an additional hadronically decaying W boson and a $\mathrm{t\bar{t}}$ signature. Cutting on the resulting χ^2 probabilities of the kinematic fits yielded a good separation of the signal process from its main backgrounds W+jets and $\mathrm{t\bar{t}}$ production.

For the extraction of the t-channel production cross-section by a template-based maximum likelihood fit, the kinematics of the typical forward light jet were exploited: This was accomplished by slicing a two-dimensional distribution of the forward jet pseudo-rapidity versus the p_{T} balance of the forward jet and the reconstructed top quark. In this distribution, the signal process preferably occupied the region of large forward jet pseudo-rapidity and low values of the p_{T} balance. For W+jets events, the p_{T} balance was also fulfilled in general, whilst the jets resided rather centrally in the detector. In the $\mathrm{t\bar{t}}$ topology, finally, the jets were found at small pseudorapidities and the p_{T} balance was not met.

Due to the unsatisfactory separation power obtained in the $\mathrm{t\bar{t}}$ dominated 4-jet bin, as well as a lack of statistics, this jet bin was excluded. The outermost bins of the forward jet pseudo-rapidity of the signal extraction histogram displayed a gap between the simulation and the data, resulting in a comparatively large cross-section value. This was attributed to a systematic underestimation of jet energies in the ATLAS simulation setup, an effect also surfacing in the pull distributions of the kinematic fit. When compared to previous ATLAS studies with similarly sizeable t-channel cross-sections, this problem seems to have persisted.

The jet energy scale was also found to be a major source of systematic uncertainty, along with the modelling of initial and final state radiation of the signal process as well

as of the PDFs used in all simulation samples. In this context, it must be emphasized that the t-channel parton shower generator could not be evaluated in this work, which might have added another large uncertainty. In view of the total systematic error of the 2- and 3-jet bin combination as opposed to the 2-jet bin alone, the 3-jet bin was eventually disregarded. Thus, the analysis results were only quoted for the 2-jet bin combination of both lepton channels. The single-top t-channel cross-section was observed with a significance of 5.7 σ to be $\sigma_{t\text{-channel}} = (111.0^{+29.2}_{-27.7})\,\text{pb}$, corresponding to a generalized strength of the (V − A)-like, CP-conserving coupling at the W-t-b vertex of $|V_{\text{tb}} f_1^{\text{L}}| = 1.30^{+0.13}_{-0.16}$. This result is compatible with the standard model prediction, but its precision does not allow for a distinction of different scenarios beyond the standard model. With the standard model assumptions $0 \leq |V_{\text{tb}}| \leq 1$ and $f_1^{\text{L}} = 1$, a 95 % confidence level lower limit was set at $0.77 < |V_{\text{tb}}| \leq 1$.

All in all, the precision of this analysis did not surpass that of previous measurements: The overall statistical and systematic error exceeded that of other t-channel cross-section results at the LHC and of the associated values of $|V_{\text{tb}}|$ from Tevatron and LHC experiments. The comparison with the CMS measurement clearly showed that this experiment has developed a superior object reconstruction with the particle flow algorithm, resulting in a very small jet energy scale uncertainty. The modelling systematics were found to be large for ATLAS as well as for CMS, although the studies considered in part different error sources, and no analysis used a complete set. There was also no indication that multivariate approaches are less model dependent in general. Furthermore, in the direct comparison with a multivariate ATLAS analysis on the same data set, the measurement of this work exhibited the same jet energy scale uncertainty.

In conclusion, the approach by kinematic fitting was shown to be a viable alternative to cut-based and multivariate methods in reconstructing this particular channel. A main virtue of the kinematic fit is the ability to unambiguously reconstruct the top quark four-momentum – a quantity that can as well be passed on as an input parameter to a more potent, multivariate reconstruction scheme. The fit is also capable of correcting the energy scale of the b-jet from the top decay; in this context, it is unfortunate, though, that the fit does not have a handle on the important, inaccurately modelled forward jet kinematics. Since the kinematic fit's ability to resolve ambiguities in the assignment of jets is not as helpful for the t-channel topology itself as for $\text{t}\bar{\text{t}}$ and Wt-channel production, this feature is instead exploited in dedicated veto fits of these background modes. A possible improvement of the kinematic fitting approach is the definition of background-enriched regions, allowing for a simultaneous determination of W+jets and $\text{t}\bar{\text{t}}$ production rates in the signal extraction fit; this was already done for W+jets in [Sta13b] and diminished the associated modelling uncertainty. Furthermore, a cut on a minimum value of the forward jet pseudo-rapidity, as also included in [Sta13b], could be combined with a momentum conservation constraint based on the p_{T} balance of the forward jet and the top quark. Only thus, the W+jets background could be further reduced since it is inaccessible by kinematic veto fits. Finally, the covariance matrices of the jets have meanwhile been recomputed in a way ensuring full coverage of the kinematic

range, especially for low p_{T} jets.

In order to derive limits on all four anomalous couplings at the W-t-b vertex, the results of this work could be combined with measurements of the single-top s-channel cross-section[1] as well as of W helicity fractions from the top quark decay and, ideally, also of top quark spin observables.

Now that enough data statistics is available, measurements of a differential, p_{T} and η dependent single-top t-channel cross-section have already been done at the LHC; such an analysis could also be done with the framework presented here. Once the LHC switches to its $\sqrt{s} = 14\,\mathrm{TeV}$ mode, the top quarks are expected to acquire larger boosts, resulting in an increased bundling of their decay products: If the b-jet and the lepton cannot be identified very accurately, this would majorly complicate the application of the kinematic fit. The CMS analysis, in contrast, could then again greatly benefit from employing the particle flow scheme.

At this time, there is a multitude of studies thriving on the large LHC data set and investigating every corner of the standard model framework in search for hints of its proposed extensions. Top quark physics is a major field of research in this enterprise, and many analyses aim at a better understanding of the properties of the heaviest elementary particle known to date. This variety of studies permits the comparison of measurement results for the same process, obtained with different analysis methods. The work at hand is part of such a comparison, providing indispensable cross-checks for the experimenter as well as invaluable insights on possible improvements of the reconstruction setup. So far, the precision reached in experiments allowed to confirm the completeness of the standard model, but was not sufficient to discern physics beyond it. In the end, only a persistent collaborational effort will allow to fill the gap of our present understanding of nature's most basic dynamics, and particularly in the electroweak sector, there is still plenty of room for surprises.

[1] This is feasible once the information is available for the s-channel at $\sqrt{s} = 7\,\mathrm{TeV}$.

A. Additional Control Distributions of the Event Preselection

In this appendix, additional *pretag* control distributions of the analysis in the electron and muon channel 2-jet bin are collected, complementing the ones shown in Sec. 4.4.4: The lepton kinematics are shown for both lepton flavours whereas the jet kinematics and the azimuth of the $E_{\mathrm{T}}^{\mathrm{miss}}$ are given only for the electron case. As explained in Sec. 4.4.4, here again, the sum of all MC samples has been subsequently scaled with an overall factor ($f_{\mathrm{norm,pretag}}^{\mathrm{e,2\ jets}} = 1.17$, $f_{\mathrm{norm,pretag}}^{\mu,\mathrm{2\ jets}} = 1.12$) to allow for a shape comparison of the MC samples with the data.

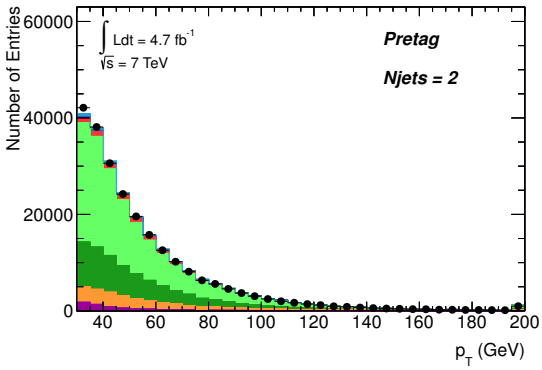

(a) Electron transverse momentum

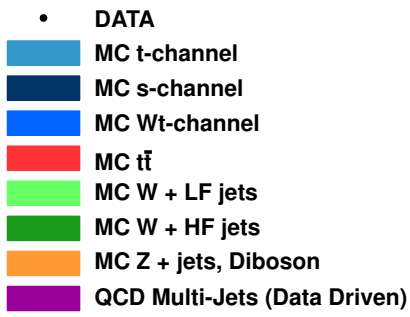

(b) Legend

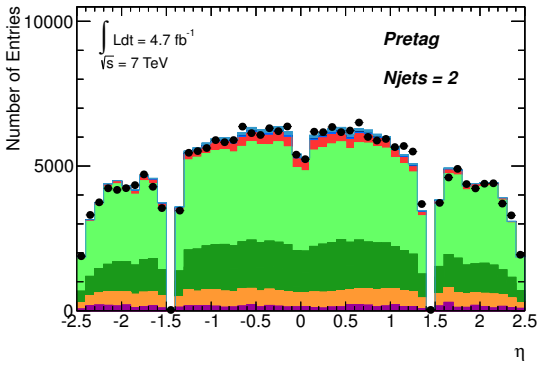

(c) Electron pseudorapidity

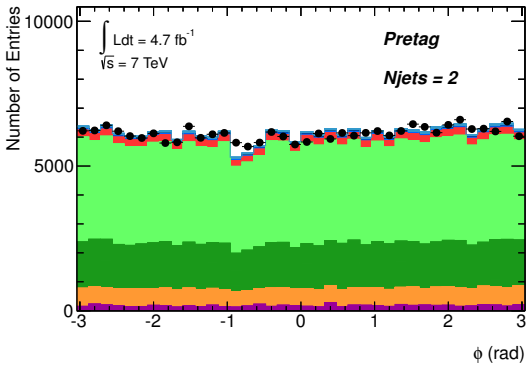

(d) Electron azimuth

Figure A.1. Signal lepton kinematics in the *pretag selection* for the electron channel in the 2-jet bin. The signal and background samples are scaled to fit the data distribution. In (a), the bin of highest p_{T} includes the overflow count. The cut-out region in (c) corresponds to the crack region $1.37 < |\eta_{\mathrm{cluster}}| < 1.52$ in the EMCAL (cp. Sec. 3.2.4).

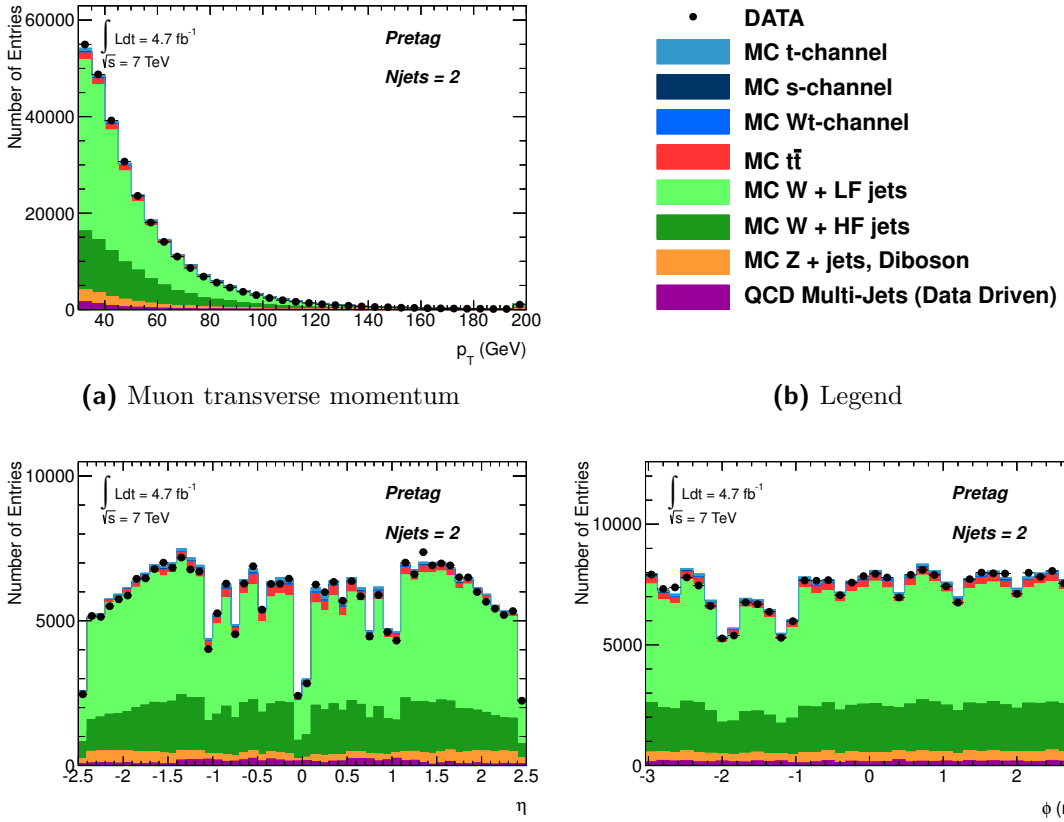

(a) Muon transverse momentum

(b) Legend

(c) Muon pseudorapidity

(d) Muon azimuth

Figure A.2. Signal lepton kinematics in the *pretag selection* for the muon channel in the 2-jet bin. The signal and background samples are scaled to fit the data distribution. In (a), the bin of highest p_{T} includes the overflow count. The η-symmetrical dips in (c) correspond to cracks in the geometrical acceptance of the ID and the MS systems. The drop in (d) in the range $-1 < \phi < -2$ originates from the lower support structure of the ATLAS detector.

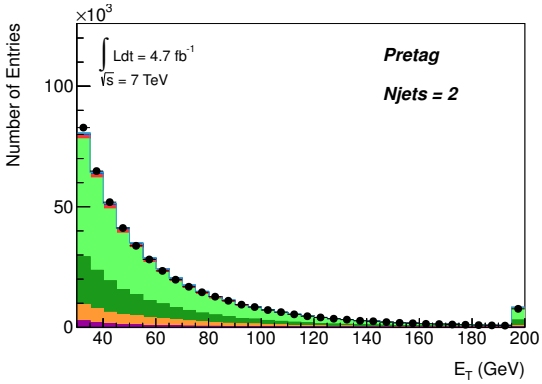

(a) Jet transverse energy

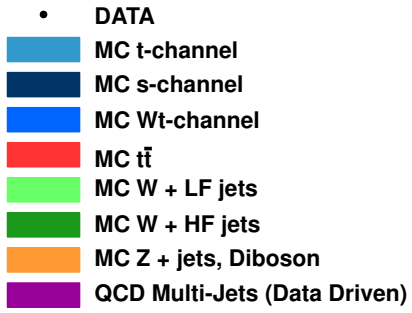

(b) Legend

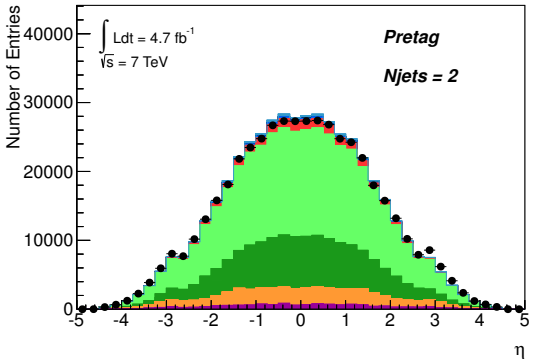

(c) Jet pseudorapidity

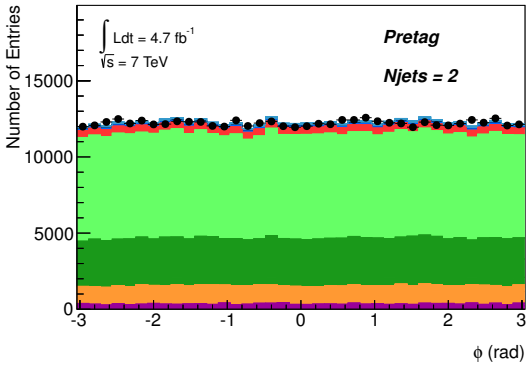

(d) Jet azimuth

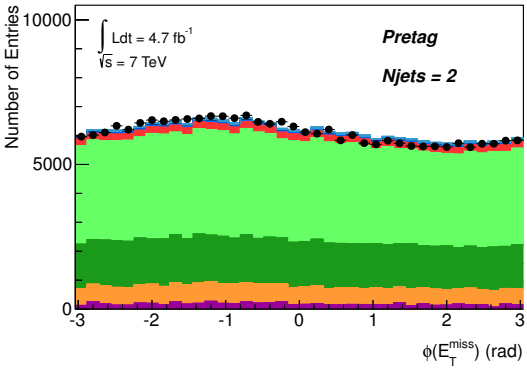

(e) $E_{\mathrm{T}}^{\mathrm{miss}}$ azimuth

Figure A.3. Kinematics of generic jets (a), (c), (d), and azimuth of $E_{\mathrm{T}}^{\mathrm{miss}}$, (e) in the *pretag selection* for the electron channel in the 2-jet bin. The signal and background samples are scaled to fit the data distribution. In (a), the bin of highest E_{T} includes the overflow count. The step in (c) at $|\eta| = 2.5$ is due to the geometry of the HEC calorimetry (see Sec. 3.2.5). The sinusoidal shape in (e), displaying an increased yield for the lower hemisphere of the detector, can be attributed to the additional material of the ATLAS support structure, resulting in an acceptance loss.

B. *p*-Value Distribution of a Kinematic Fit

As described in Chap. 5, the kinematic fit returns a χ^2 value for each event according to how well the physics objects in the event considered by the procedure match the hypothesis to be tested. When fitting a semi-leptonic single top t-channel or a $\mathrm{t\bar{t}}$ topology, the fit has one degree of freedom and the resulting χ^2 probability density function (p.d.f.) has the theoretical form ($x := \chi^2$)

$$f_1(x) = \frac{e^{-\frac{x}{2}}}{\sqrt{2\pi x}}\,. \tag{B.1}$$

The p-value of $f_1(x)$ is then defined as

$$\mathcal{P}(x) = \int_x^\infty f_1(\tilde{x})\mathrm{d}\tilde{x}\,, \tag{B.2}$$

and with the properties of the p.d.f. $f_1(x)$, normalized to unity

$$\int_x^\infty f_1(\tilde{x})\mathrm{d}\tilde{x} = 1 - \int_0^x f_1(\tilde{x})\mathrm{d}\tilde{x}\,, \tag{B.3}$$

it follows that

$$\frac{\mathrm{d}\mathcal{P}}{\mathrm{d}x} = -f_1(x)\,. \tag{B.4}$$

The distribution $f_{1,\mathrm{meas}}(x)$ and the distribution of $\mathcal{P}_{\mathrm{meas}}$, $F(\mathcal{P}_{\mathrm{meas}})$, recorded in the analysis, satisfy

$$N_{\mathrm{evt}} = \int_0^1 F(\mathcal{P}_{\mathrm{meas}})\mathrm{d}\mathcal{P}_{\mathrm{meas}} = \int_0^\infty f_{1,\mathrm{meas}}(x)\mathrm{d}x = \int_0^\infty N_{\mathrm{evt}} f^{\mathrm{norm}}_{1,\mathrm{meas}}(x)\mathrm{d}x \tag{B.5}$$

where N_{evt} is the (weighted) number of events in the corresponding histogram and $f^{\mathrm{norm}}_{1,\mathrm{meas}}(x)$ is normalized to unity. Thus, with Eq. (B.4),

$$\int_0^\infty f_{1,\mathrm{meas}}(x)\mathrm{d}x = \int_1^0 N_{\mathrm{evt}} f^{\mathrm{norm}}_{1,\mathrm{meas}}(x)\left(-\frac{1}{f_1(x)}\mathrm{d}\mathcal{P}\right) = \int_0^1 N_{\mathrm{evt}}\frac{f^{\mathrm{norm}}_{1,\mathrm{meas}}(x)}{f_1(x)}\mathrm{d}\mathcal{P}\,. \tag{B.6}$$

Now, assuming the measured p.d.f. $f^{\mathrm{norm}}_{1,\mathrm{meas}}$ mirrors the theoretical f_1, it follows from equations (B.5) and (B.6) for the measured distribution F of the quantity $\mathcal{P}(\chi^2)$:

$$F(\mathcal{P}_{\mathrm{meas}}(\chi^2)) = N_{\mathrm{evt}} = \mathrm{const.} \tag{B.7}$$

Algorithmically, the χ^2 value of an individual fit result of the KinFitter is used to compute the $\mathcal{P}(\chi^2)$ by integrating the theoretical p.d.f. f_1 according to Eq. (B.2). The resulting distribution $F(\mathcal{P}_{\text{meas}}(\chi^2))$ displays the expected plateau across most of the range $[0, 1]$ but also shows a spike close to zero (cp. Fig. 5.11). Since the tail of high χ^2 values of $f_{1,\text{meas}}$ reflects large fit residuals, it is associated with fits producing W and top quark masses residing at the edges of the theoretical mass distributions. In this region, an agreement with the theoretical distributions is not expected: The mass constraints are here formulated via Gaussian distributions which decrease much faster in the tails than the underlying Breit-Wigner curves of the particle resonances. Therefore, the measured p.d.f. $f_{1,\text{meas}}^{\text{norm}}$ overestimates the theoretical f_1 in this range; the spike of $\mathcal{P}(\chi^2)$ values close to zero reflects this mismodelling. The region in question is at about $\mathcal{P}(\chi^2) \lesssim 0.1$ corresponding to $\chi^2 \gtrsim 10$ and thus represents fits of top-candidates of rather poor quality that are removed in the final selection.

C. Additional Control Distributions of the Kinematic Fit

Here, some control distributions of the kinematic fitting procedure in other analysis channels are collected complementing those shown in Chap. 5: the χ^2 and $\mathcal{P}_{\text{main fit}}(\chi^2)$ distributions as well as the overlaid $\mathcal{P}_{\text{main fit}}(\chi^2)$ distributions for all three jet bins in the electron channel, the stacked and overlaid $\mathcal{P}_{\text{W}_\text{had}}(\chi^2)$ distributions for the 3- and 4-jet bin in the muon channel and the stacked and overlaid $\mathcal{P}_{\text{t}\bar{\text{t}}}(\chi^2)$ distributions for the 4-jet bin in the muon channel.

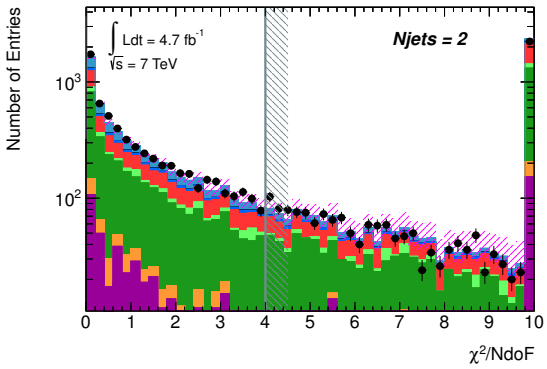

(a) Electron, $N_{\text{jets}} = 2$

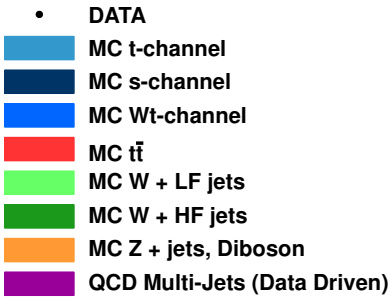

(b) Legend

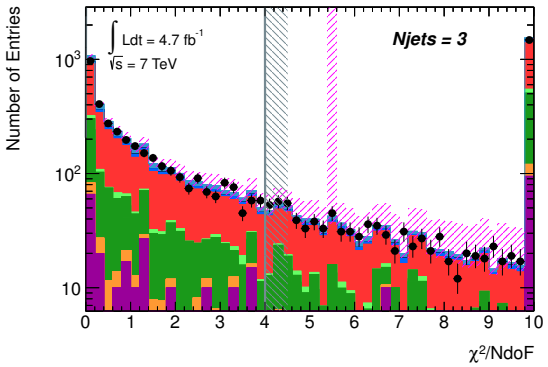

(c) Electron, $N_{\text{jets}} = 3$

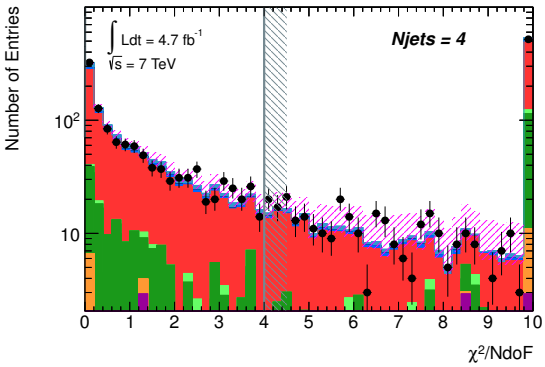

(d) Electron, $N_{\text{jets}} = 4$

Figure C.1. Semi-logarithmic distributions of the χ^2 resulting from the main kinematic top quark fit for 2, 3 and 4 jets per event in the electron channel, see (a), (c) and (d). The exclusion lines indicate the $\chi^2 < 4$ requirement which corresponds to the cut on the χ^2 probability at $\mathcal{P}_{\text{main fit}}(\chi^2) > 0.05$. The vetos on background events as described in Sec. 5.2.3 are already applied. All MC distributions are normalized to the data luminosity. The rightmost bin is the overflow bin.

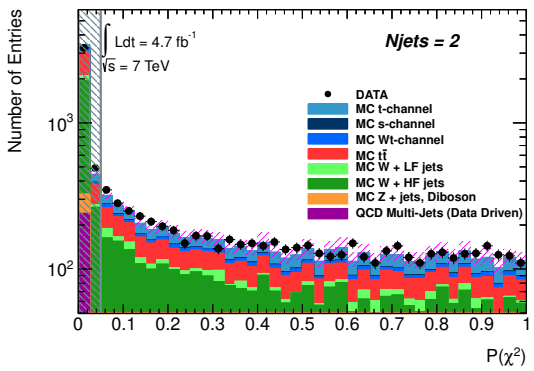

(a) Electron, $N_{\text{jets}} = 2$

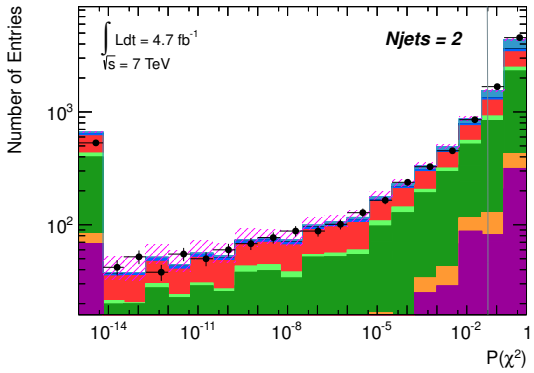

(b) Electron, $N_{\text{jets}} = 2$

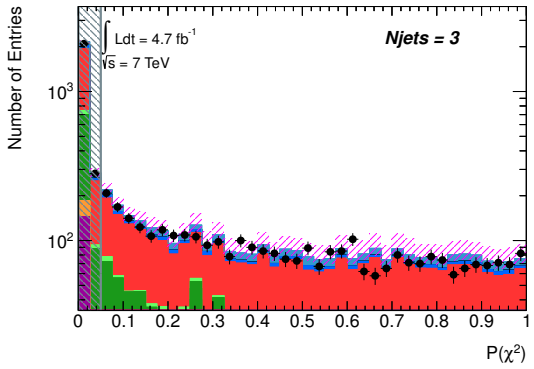

(c) Electron, $N_{\text{jets}} = 3$

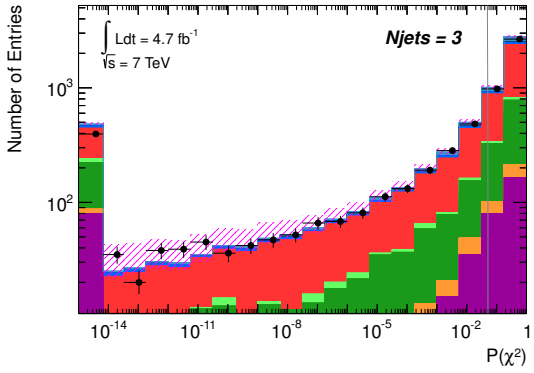

(d) Electron, $N_{\text{jets}} = 3$

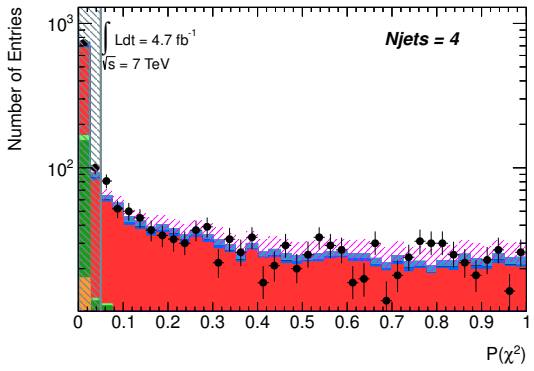

(e) Electron, $N_{\text{jets}} = 4$

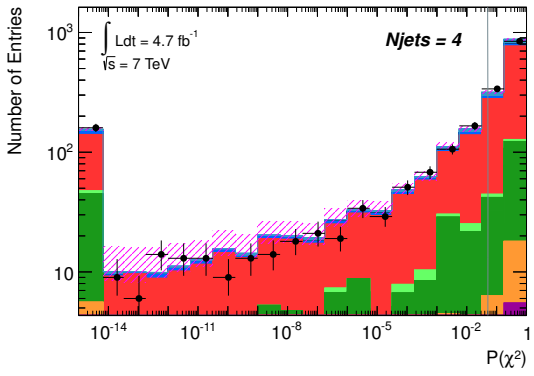

(f) Electron, $N_{\text{jets}} = 4$

Figure C.2. Semi-logarithmic $\mathcal{P}_{\text{main fit}}(\chi^2)$ distributions of the main kinematic top quark fit for 2, 3 and 4 jets per event in the electron channel, see (a), (c), (e), and the corresponding double-logarithmic $\mathcal{P}_{\text{main fit}}(\chi^2)$ distributions, see (b), (d), (f).The vetos on background events as described in Sec. 5.2.3 are already applied. The grey vertical lines indicate the cut used for signal enrichment, $\mathcal{P}_{\text{main fit}}(\chi^2) > 0.05$. All MC distributions are normalized to the data luminosity.

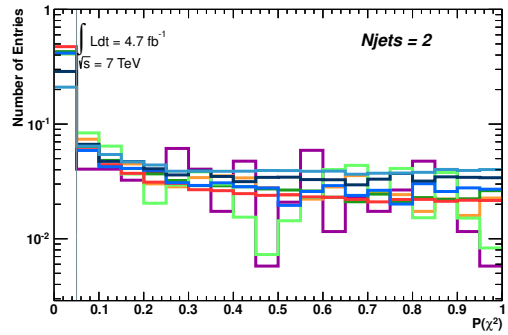

(a) Electron, $N_{\text{jets}} = 2$

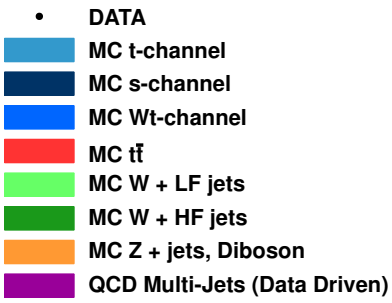

(b) Legend

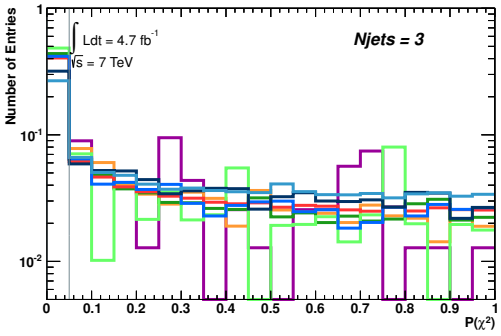

(c) Electron, $N_{\text{jets}} = 3$

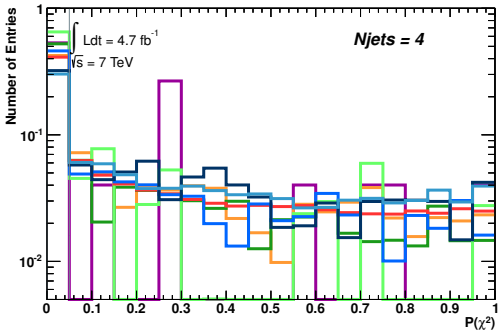

(d) Electron, $N_{\text{jets}} = 4$

Figure C.3. Semi-logarithmic $\mathcal{P}_{\text{main fit}}(\chi^2)$ distributions of the main kinematic top quark fit for 2, 3 and 4 jets per event in the electron channel, see (a), (c), (d). The vetos on background events as described in Sec. 5.2.3 are already applied. The grey vertical lines indicate the cut used for signal enrichment, $\mathcal{P}_{\text{main fit}}(\chi^2) > 0.05$. All MC distributions are normalized to unity and overlaid for shape comparison.

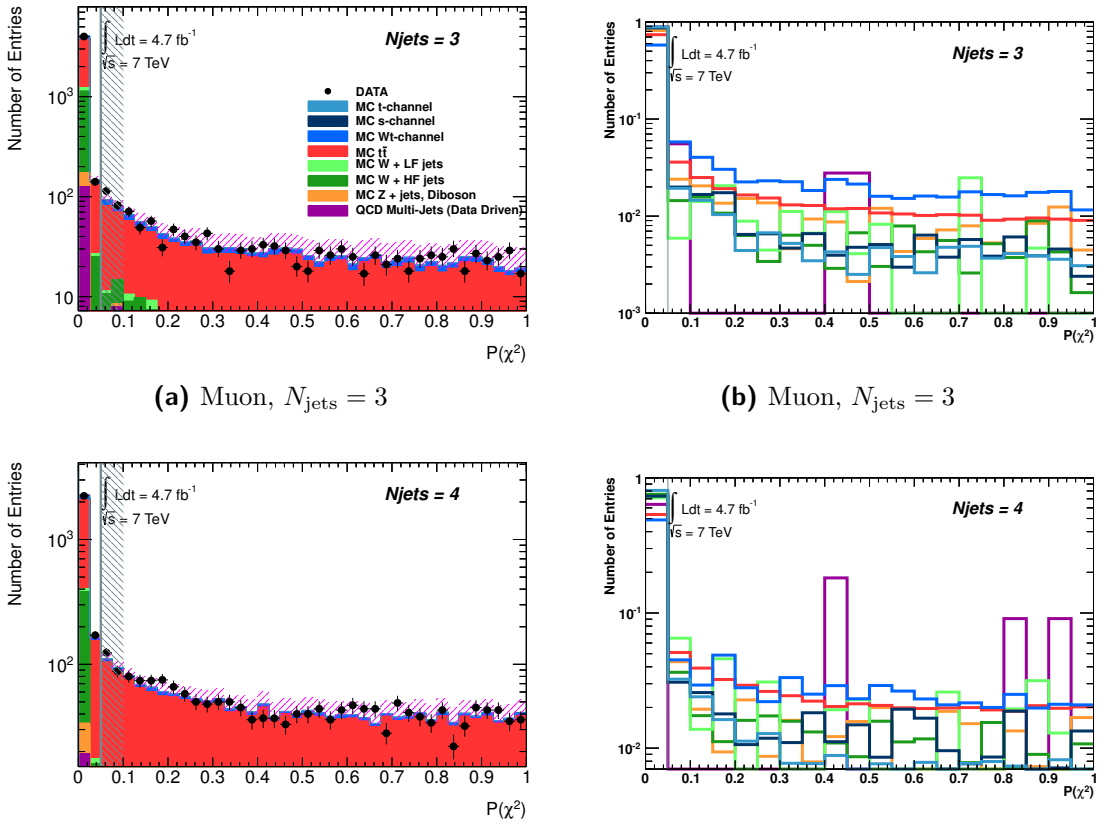

(a) Muon, $N_{\text{jets}} = 3$

(b) Muon, $N_{\text{jets}} = 3$

(c) Muon, $N_{\text{jets}} = 4$

(d) Muon, $N_{\text{jets}} = 4$

Figure C.4. Semi-logarithmic $\mathcal{P}_{\mathrm{W_{had}}}(\chi^2)$ distributions of the veto fit of an additional hadronically decaying W boson in the 3- and 4-jet bin, see (a) and (c), in the muon channel. All events with $\mathcal{P}_{\mathrm{W_{had}}}(\chi^2) > 0.05$ are rejected. Also shown are the corresponding $\mathcal{P}_{\mathrm{W_{had}}}(\chi^2)$ distributions of the single processes, (b) and (d), where all MC distributions are normalized to unity and overlaid for shape comparison. Here, the grey vertical lines indicate the veto cut used for background rejection, $\mathcal{P}_{\mathrm{W_{had}}}(\chi^2) > 0.05$.

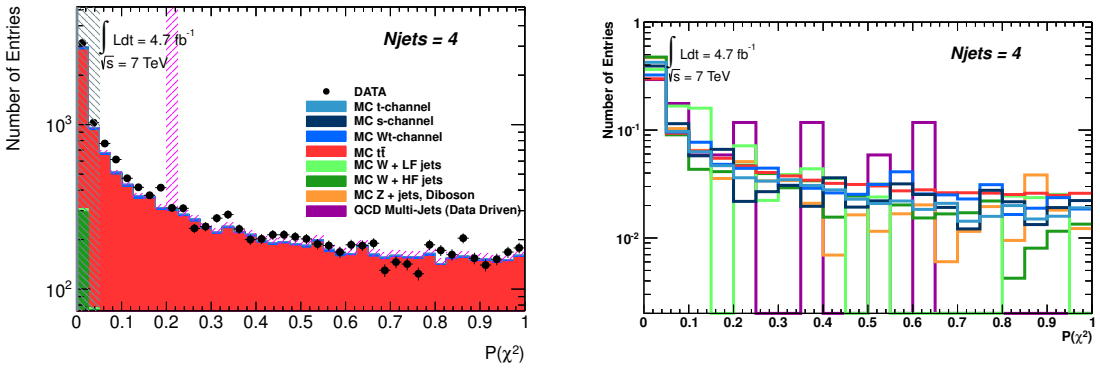

(a) Muon, $N_{\text{jets}} = 4$ **(b)** Muon, $N_{\text{jets}} = 4$

Figure C.5. Semi-logarithmic $\mathcal{P}_{\text{t}\bar{\text{t}}}(\chi^2)$ distribution of the veto fit of semi-leptonic $\text{t}\bar{\text{t}}$ production, (a), in the 4-jet bin in the muon channel. All events with $\mathcal{P}_{\text{t}\bar{\text{t}}}(\chi^2) > 0.001$ are eventually rejected. Also shown is the corresponding $\mathcal{P}_{\text{t}\bar{\text{t}}}(\chi^2)$ distribution of the single processes, (b), where all MC distributions are normalized to unity and overlaid for shape comparison. Here, the grey vertical line indicates the veto cut used for background rejection, $\mathcal{P}_{\text{t}\bar{\text{t}}}(\chi^2) > 0.001$.

D. Detailed Results of All Analysis Channels

In this appendix, the detailed analysis results in terms of the systematic table from Sec. 6.2.4 are presented also separately for the single analysis channels, i.e. for the electron and muon channel 2- and 3-jet bin results. In the table header, the respective channel is printed in bold for better readability.

2-Jet Bin, Electron Channel (From 2 Jets Combination)

Systematic	$\delta\sigma_{t\text{-channel}}$ Up[%]	Down[%]	Bias[%]
Data Statistics	8.18	−8.18	0.00
Luminosity	2.08	−2.08	−0.06
MC Statistics	8.90	−7.74	4.39
Background Cross-Sections	3.64	−3.64	−0.03
PDFs	8.02	−8.02	0.23
Matrix Element Generator (t-channel)	6.49	−6.49	−0.19
Matrix Element Generator ($t\bar{t}$)	1.25	−1.25	−0.03
Parton Shower Generator ($t\bar{t}$)	0.77	−0.77	0.10
ISR/FSR	12.06	−12.06	0.05
QCD Normalization	3.66	−3.67	−0.30
Ratio W+LF/W+HF	1.41	−1.41	0.10
Ratio W+c/(W+c$\bar{c}$ + W+b$\bar{b}$)	6.43	−6.39	0.69
Electron Energy Scale	0.35	−0.43	−0.23
Electron Energy Resolution	0.74	−0.88	−0.49
Muon p_{T} Scale	0.32	−0.34	−0.10
Muon p_{T} Resolution (ID)	0.89	−0.89	−0.01
Muon p_{T} Resolution (MS)	0.13	−0.14	−0.06
Lepton Reconstruction Efficiency	0.76	−0.76	−0.02
Jet Energy Scale	12.78	−12.77	0.51
Jet Energy Resolution	2.45	−2.41	0.43
Jet Reconstruction Efficiency	1.69	−1.69	0.02
B-Tagging Efficiency	4.86	−4.86	0.20
C-Tagging Efficiency	0.85	−0.85	0.10
Mistagging Efficiency	0.85	−0.85	0.05
JVF	0.63	−0.65	−0.15
$E_{\mathrm{T}}^{\mathrm{miss}}$ Pile-Up	2.52	−2.12	1.37
$E_{\mathrm{T}}^{\mathrm{miss}}$ CellOut+SoftJet	3.88	−3.85	0.47
Total (syst)	25.14	−23.96	7.58
Total (syst+stat)	26.43	−25.32	7.58

Table D.1. All systematic uncertainties resulting from the pseudo-experiments executed to estimate the total error of the single-top t-channel cross-section measurement.

2-Jet Bin, Electron Channel (From 2+3 Jets Combination)

Systematic	$\delta\sigma_{t\text{-channel}}$ Up[%]	Down[%]	Bias[%]
Data Statistics	9.06	−9.06	0.00
Luminosity	1.52	−1.52	0.03
MC Statistics	11.57	−8.84	7.46
Background Cross-Sections	3.25	−3.25	0.11
PDFs	9.03	−9.01	0.48
Matrix Element Generator (t-channel)	6.77	−6.77	−0.05
Matrix Element Generator ($t\bar{t}$)	0.50	−0.50	0.05
Parton Shower Generator ($t\bar{t}$)	1.02	−1.02	−0.10
ISR/FSR	12.54	−12.54	0.06
QCD Normalization	1.45	−1.45	−0.12
Ratio W+LF/W+HF	0.84	−0.82	0.21
Ratio W+c/(W+c$\bar{c}$ + W+b$\bar{b}$)	7.01	−6.95	0.90
Electron Energy Scale	0.86	−0.87	−0.15
Electron Energy Resolution	1.20	−1.33	−0.57
Muon p_{T} Scale	1.34	−1.34	−0.07
Muon p_{T} Resolution (ID)	1.17	−1.17	−0.01
Muon p_{T} Resolution (MS)	1.38	−1.38	−0.06
Lepton Reconstruction Efficiency	0.17	−0.19	−0.09
Jet Energy Scale	11.96	−11.96	0.00
Jet Energy Resolution	2.33	−2.22	0.72
Jet Reconstruction Efficiency	0.59	−0.59	0.04
B-Tagging Efficiency	6.24	−6.24	0.06
C-Tagging Efficiency	1.48	−1.48	0.11
Mistagging Efficiency	1.33	−1.33	−0.07
JVF	0.57	−0.57	−0.03
$E_{\mathrm{T}}^{\mathrm{miss}}$ Pile-Up	2.41	−1.55	1.85
$E_{\mathrm{T}}^{\mathrm{miss}}$ CellOut+SoftJet	2.29	−2.08	0.97
Total (syst)	27.88	−25.52	11.22
Total (syst+stat)	29.31	−27.08	11.22

Table D.2. All systematic uncertainties resulting from the pseudo-experiments executed to estimate the total error of the single-top t-channel cross-section measurement.

2-Jet Bin, Muon Channel (From 2 Jets Combination)

Systematic	$\delta\sigma_{t\text{-channel}}$ Up[%]	Down[%]	Bias[%]
Data Statistics	7.82	−7.82	0.00
Luminosity	1.35	−1.35	−0.06
MC Statistics	7.58	−6.31	4.20
Background Cross-Sections	3.21	−3.21	−0.04
PDFs	7.70	−7.70	−0.30
Matrix Element Generator (t-channel)	6.48	−6.48	0.09
Matrix Element Generator ($t\bar{t}$)	1.31	−1.31	0.00
Parton Shower Generator ($t\bar{t}$)	0.72	−0.72	0.00
ISR/FSR	11.56	−11.56	−0.23
QCD Normalization	3.57	−3.57	−0.25
Ratio W+LF/W+HF	2.00	−1.99	0.21
Ratio W+c/(W+c$\bar{c}$ + W+b$\bar{b}$)	7.21	−7.12	1.11
Electron Energy Scale	0.84	−0.84	−0.03
Electron Energy Resolution	1.22	−1.22	0.02
Muon p_{T} Scale	0.47	−0.48	−0.12
Muon p_{T} Resolution (ID)	1.02	−1.02	0.07
Muon p_{T} Resolution (MS)	1.46	−1.47	−0.23
Lepton Reconstruction Efficiency	1.28	−1.28	−0.00
Jet Energy Scale	14.30	−14.30	0.11
Jet Energy Resolution	1.86	−1.80	0.49
Jet Reconstruction Efficiency	1.42	−1.42	−0.05
B-Tagging Efficiency	5.59	−5.59	0.12
C-Tagging Efficiency	1.76	−1.76	0.01
Mistagging Efficiency	0.96	−0.96	0.04
JVF	0.89	−0.89	−0.03
$E_{\mathrm{T}}^{\mathrm{miss}}$ Pile-Up	1.63	−1.77	−0.67
$E_{\mathrm{T}}^{\mathrm{miss}}$ CellOut+SoftJet	0.74	−1.02	−0.70
Total (syst)	24.94	−24.41	5.10
Total (syst+stat)	26.14	−25.63	5.10

Table D.3. All systematic uncertainties resulting from the pseudo-experiments executed to estimate the total error of the single-top t-channel cross-section measurement.

2-Jet Bin, Muon Channel (From 2+3 Jets Combination)

Systematic	$\delta\sigma_{t\text{-channel}}$ Up[%]	Down[%]	Bias[%]
Data Statistics	8.64	−8.64	0.00
Luminosity	1.28	−1.28	−0.02
MC Statistics	10.31	−7.46	7.12
Background Cross-Sections	2.82	−2.82	0.11
PDFs	9.26	−9.26	−0.28
Matrix Element Generator (t-channel)	6.87	−6.87	0.07
Matrix Element Generator ($t\bar{t}$)	1.86	−1.86	−0.06
Parton Shower Generator ($t\bar{t}$)	1.32	−1.32	0.04
ISR/FSR	12.34	−12.34	−0.08
QCD Normalization	1.14	−1.16	−0.21
Ratio W+LF/W+HF	2.50	−2.48	0.34
Ratio W+c/(W+c$\bar{c}$ + W+b$\bar{b}$)	7.84	−7.77	1.01
Electron Energy Scale	1.14	−1.14	−0.06
Electron Energy Resolution	1.08	−1.08	0.04
Muon p_{T} Scale	0.60	−0.60	0.01
Muon p_{T} Resolution (ID)	1.35	−1.35	−0.05
Muon p_{T} Resolution (MS)	1.31	−1.35	−0.30
Lepton Reconstruction Efficiency	1.22	−1.22	−0.08
Jet Energy Scale	14.95	−14.95	0.45
Jet Energy Resolution	3.93	−3.87	0.68
Jet Reconstruction Efficiency	0.59	−0.59	0.00
B-Tagging Efficiency	7.22	−7.22	0.25
C-Tagging Efficiency	1.25	−1.25	0.02
Mistagging Efficiency	1.52	−1.52	−0.02
JVF	1.17	−1.17	0.05
$E_{\mathrm{T}}^{\mathrm{miss}}$ Pile-Up	1.12	−1.36	−0.78
$E_{\mathrm{T}}^{\mathrm{miss}}$ CellOut+SoftJet	0.47	−0.86	−0.72
Total (syst)	27.90	−26.79	7.80
Total (syst+stat)	29.21	−28.15	7.80

Table D.4. All systematic uncertainties resulting from the pseudo-experiments executed to estimate the total error of the single-top t-channel cross-section measurement.

3-Jet Bin, Electron Channel

Systematic	$\delta\sigma_{t\text{-channel}}$ Up[%]	Down[%]	Bias[%]
Data Statistics	19.49	−19.49	0.00
Luminosity	3.00	−3.00	−0.12
MC Statistics	29.97	−18.98	23.20
Background Cross-Sections	6.82	−6.82	0.10
PDFs	28.85	−28.85	0.01
Matrix Element Generator (t-channel)	7.38	−7.39	−0.42
Matrix Element Generator ($t\bar{t}$)	16.18	−16.18	−0.26
Parton Shower Generator ($t\bar{t}$)	4.95	−4.95	−0.07
ISR/FSR	0.48	−0.48	−0.01
QCD Normalization	1.73	−1.73	−0.08
Ratio W+LF/W+HF	2.20	−2.18	0.29
Ratio W+c/(W+c$\bar{c}$ + W+b$\bar{b}$)	6.54	−6.46	1.00
Electron Energy Scale	1.54	−1.54	−0.07
Electron Energy Resolution	2.34	−2.28	0.54
Muon p_{T} Scale	2.28	−2.28	−0.11
Muon p_{T} Resolution (ID)	0.84	−0.89	−0.28
Muon p_{T} Resolution (MS)	1.81	−1.83	−0.23
Lepton Reconstruction Efficiency	2.82	−2.82	−0.19
Jet Energy Scale	22.47	−22.47	0.29
Jet Energy Resolution	6.00	−5.13	3.13
Jet Reconstruction Efficiency	1.80	−1.80	0.01
B-Tagging Efficiency	10.89	−10.89	0.05
C-Tagging Efficiency	1.45	−1.45	−0.10
Mistagging Efficiency	0.46	−0.46	−0.06
JVF	1.99	−1.99	−0.05
$E_{\mathrm{T}}^{\mathrm{miss}}$ Pile-Up	2.45	−2.30	0.84
$E_{\mathrm{T}}^{\mathrm{miss}}$ CellOut+SoftJet	2.32	−2.57	−1.10
Total (syst)	56.63	−49.10	28.22
Total (syst+stat)	59.89	−52.83	28.22

Table D.5. All systematic uncertainties resulting from the pseudo-experiments executed to estimate the total error of the single-top t-channel cross-section measurement.

3-Jet Bin, Muon Channel

Systematic	$\delta\sigma_{t\text{-channel}}$ Up[%]	Down[%]	Bias[%]
Data Statistics	18.97	−18.97	−0.00
Luminosity	1.82	−1.82	−0.07
MC Statistics	21.20	−14.92	15.07
Background Cross-Sections	6.57	−6.57	0.21
PDFs	27.41	−27.41	0.18
Matrix Element Generator (t-channel)	6.33	−6.33	0.08
Matrix Element Generator ($t\bar{t}$)	17.32	−17.32	0.15
Parton Shower Generator ($t\bar{t}$)	6.57	−6.57	−0.11
ISR/FSR	1.83	−1.83	0.06
QCD Normalization	2.86	−2.86	0.15
Ratio W+LF/W+HF	1.99	−1.99	−0.07
Ratio W+c/(W+c$\bar{c}$ + W+b$\bar{b}$)	11.28	−11.16	1.59
Electron Energy Scale	2.67	−2.67	0.04
Electron Energy Resolution	1.11	−1.11	−0.07
Muon p_{T} Scale	2.37	−2.37	0.09
Muon p_{T} Resolution (ID)	1.13	−1.62	−1.16
Muon p_{T} Resolution (MS)	2.06	−2.04	0.27
Lepton Reconstruction Efficiency	1.95	−1.95	−0.14
Jet Energy Scale	19.97	−20.03	−1.49
Jet Energy Resolution	5.94	−2.63	5.32
Jet Reconstruction Efficiency	1.64	−1.64	−0.09
B-Tagging Efficiency	10.93	−10.93	0.45
C-Tagging Efficiency	0.63	−0.63	0.03
Mistagging Efficiency	1.53	−1.53	0.01
JVF	2.61	−2.61	−0.04
$E_{\mathrm{T}}^{\mathrm{miss}}$ Pile-Up	1.09	−1.97	−1.63
$E_{\mathrm{T}}^{\mathrm{miss}}$ CellOut+SoftJet	3.82	−3.82	−0.03
Total (syst)	50.77	−46.81	19.66
Total (syst+stat)	54.20	−50.50	19.66

Table D.6. All systematic uncertainties resulting from the pseudo-experiments executed to estimate the total error of the single-top t-channel cross-section measurement.

Bibliography

[AB10] J. Aguilar-Saavedra and J. Bernabeu. "W polarisation beyond helicity fractions in top quark decays". *Nucl. Phys.* B840 (2010), pp. 349–378. arXiv: `1005.5382 [hep-ph]` (cit. on p. 26).

[Abi+10] B. Abi et al. *Mis-identified lepton backgrounds to top quark pair production: Supporting note 5*. Internal Note ATLAS-COM-PHYS-2010-849. Supporting note for top observation paper. CERN, Oct. 2010 (cit. on pp. 82, 147).

[Ach+10] B. Acharya et al. *Estimation of the W+Jets Background for Top Quark Re-Discovery in the Single Lepton+Jets Channel*. Internal Note ATLAS-COM-PHYS-2010-834. CERN, Oct. 2010 (cit. on p. 158).

[Ach+12] B. Acharya et al. *Object selection and calibration, background estimations and MC samples for the Autumn 2012 Top Quark analyses with 2011 data*. Internal Note ATLAS-COM-PHYS-2012-1197. CERN, Aug. 2012 (cit. on pp. 60, 69, 70, 79, 82, 83, 85, 93, 94, 143, 149–151, 156).

[Ado+12] S. Adomeit et al. *Jet energy scale and its systematic uncertainty in proton-proton collisions at $\sqrt{s}$ = 7 TeV with ATLAS 2011 data*. Internal Note ATLAS-COM-CONF-2012-171. CERN, Aug. 2012 (cit. on pp. 63, 64, 151, 153).

[Ago+03] S. Agostinelli et al. "GEANT4: A Simulation toolkit". *Nucl.Instrum.Meth.* A506 (2003), pp. 250–303 (cit. on p. 78).

[Ali+11] M. Aliev et al. "HATHOR: HAdronic Top and Heavy quarks crOss section calculatoR". *Comput. Phys. Commun.* 182 (2011), pp. 1034–1046. arXiv: `1007.1327 [hep-ph]` (cit. on pp. 30, 32, 34, 158, 183).

[Alv+10] B. Alvarez et al. *B-tagging for top physics analyses with early ATLAS data at $\sqrt{s}$ = 7 TeV*. Internal Note ATLAS-PHYS-INT-2010-133. CERN, Dec. 2010 (cit. on p. 60).

[Alw+07] J. Alwall et al. "Is $V_{\mathrm{tb}} = 1$?" *Eur.Phys.J.* C49 (2007), pp. 791–801. arXiv: `hep-ph/0607115 [hep-ph]` (cit. on p. 37).

[And+83] B. Andersson et al. "Parton Fragmentation and String Dynamics". *Phys. Rept.* 97 (1983), pp. 31–145 (cit. on p. 74).

[And97] B. Andersson. "The Lund model". *Camb. Monogr. Part. Phys. Nucl. Phys. Cosmol.* 7 (1997), pp. 1–471 (cit. on p. 74).

[Ant+09] I. Antcheva et al. "ROOT – A C++ framework for petabyte data storage, statistical analysis and visualization". *Computer Physics Communications* 180.12 (2009), pp. 2499–2512 (cit. on p. 113).

[AP77] G. Altarelli and G. Parisi. "Asymptotic Freedom in Parton Language". *Nucl. Phys.* B126 (1977), p. 298 (cit. on p. 73).

[ATL03] ATLAS Collaboration. *ATLAS high-level trigger, data acquisition and controls: Technical design report*. Tech. rep. CERN, 2003 (cit. on p. 57).

[ATL05] ATLAS Collaboration. *ATLAS computing: Technical design report*. Tech. rep. 2005 (cit. on p. 70).

[ATL08] ATLAS Collaboration. "The ATLAS Experiment at the CERN Large Hadron Collider". *JINST* 3 (2008), S08003 (cit. on pp. 41, 43, 44, 49, 52, 54, 55).

[ATL10] ATLAS Collaboration. *Jet energy resolution and selection efficiency relative to track jets from in-situ techniques with the ATLAS Detector Using Proton-Proton Collisions at a Center of Mass Energy $\sqrt{s}$ = 7 TeV*. Conference Note ATLAS-CONF-2010-054. CERN, July 2010 (cit. on p. 154).

[ATL11a] ATLAS Collaboration. "Charged-particle multiplicities in pp interactions measured with the ATLAS detector at the LHC". *New J. Phys.* 13 (2011), p. 053033. arXiv: `1012.5104 [hep-ex]` (cit. on p. 59).

[ATL11b] ATLAS Collaboration. *Commissioning of the ATLAS high-performance b-tagging algorithms in the 7 TeV collision data*. Conference Note ATLAS-CONF-2011-102. CERN, July 2011 (cit. on pp. 60, 97, 100).

[ATL11c] ATLAS Collaboration. "Luminosity Determination in pp Collisions at $\sqrt{s} = 7$ TeV Using the ATLAS Detector at the LHC". *Eur. Phys. J.* C71 (2011), p. 1630. arXiv: `1101.2185 [hep-ex]` (cit. on p. 46).

[ATL11d] ATLAS Collaboration. *Measurement of the t-channel Single Top-Quark Production Cross Section in 0.70 fb^{-1} of pp Collisions at $\sqrt{s}$ = 7 TeV with the ATLAS detector*. Conference Note ATLAS-CONF-2011-101. CERN, July 2011 (cit. on pp. 35, 36).

[ATL11e] ATLAS Collaboration. "Measurement of the top quark-pair production cross section with ATLAS in pp collisions at $\sqrt{s} = 7$ TeV". *Eur. Phys. J.* C71 (2011), p. 1577. arXiv: `1012.1792 [hep-ex]` (cit. on pp. 30, 31, 157).

[ATL11f] ATLAS Collaboration. *New ATLAS event generator tunes to 2010 data*. Public Note ATLAS-PHYS-PUB-2011-008. CERN, Apr. 2011 (cit. on p. 77).

[ATL11g] ATLAS Collaboration. *Observation of t-Channel Single Top-Quark Production in pp Collisions at $\sqrt{s}$ = 7 TeV with the ATLAS detector*. Conference Note ATLAS-CONF-2011-088. CERN, June 2011 (cit. on pp. 35, 36).

[ATL11h] ATLAS Collaboration. *Searches for Single Top-Quark Production with the ATLAS Detector in pp Collisions at $\sqrt{s}$ = 7 TeV*. Conference Note ATLAS-CONF-2011-027. CERN, Mar. 2011 (cit. on pp. 35, 36).

[ATL12e] ATLAS Collaboration. *B-jet tagging calibration on c-jets containing D^{*+} mesons*. Conference Note ATLAS-CONF-2012-039. CERN, Mar. 2012 (cit. on pp. 100, 155).

[ATL12f] ATLAS Collaboration. "Electron performance measurements with the ATLAS detector using the 2010 LHC proton-proton collision data". *The European Physical Journal C - Particles and Fields* 72 (3 2012), pp. 1–46. arXiv: `1110.3174 [hep-ex]` (cit. on pp. 62, 63, 98).

[ATL12g] ATLAS Collaboration. *Improved Luminosity Determination in pp Collisions at $\sqrt{s}$ = 7 TeV using the ATLAS Detector at the LHC*. Conference Note ATLAS-CONF-2012-080. CERN, July 2012 (cit. on p. 157).

[ATL12h] ATLAS Collaboration. *Measurement of the Mistag Rate with 5 fb^{-1} of Data Collected by the ATLAS Detector*. Conference Note ATLAS-CONF-2012-040. CERN, Mar. 2012 (cit. on pp. 100, 155).

[ATL12i] ATLAS Collaboration. *Measurement of the t-channel single top-quark and top-antiquark production cross-sections and their ratio in pp collisions at $\sqrt{s}$ = 7 TeV*. Conference Note ATLAS-COM-CONF-2012-028. CERN, Feb. 2012 (cit. on pp. 37, 145, 147, 182).

[ATL12j] ATLAS Collaboration. "Measurement of the t-channel single top-quark production cross section in pp collisions at $\sqrt{s} = 7$ TeV with the ATLAS detector". *Physics Letters B* 717 (2012). arXiv: `1205.3130 [hep-ex]` (cit. on pp. 21, 22, 36, 168, 182, 183, 185).

[ATL12k] ATLAS Collaboration. "Measurement of the top quark mass with the template method in the top antitop to lepton + jets channel using ATLAS data". *Eur. Phys. J.* C72 (2012). arXiv: `1203.5755 [hep-ex]` (cit. on p. 18).

[ATL12l] ATLAS Collaboration. "Measurement of the W boson polarization in top quark decays with the ATLAS detector". *JHEP* 1206 (May 2012). arXiv: `1205.2484 [hep-ex]` (cit. on p. 23).

[ATL12m] ATLAS Collaboration. "Measurement of $t\bar{t}$ production with a veto on additional central jet activity in pp collisions at $\sqrt{s} = 7$ TeV using the ATLAS detector". *Eur.Phys.J.* C72 (2012), p. 2043. arXiv: `1203.5015 [hep-ex]` (cit. on p. 146).

[ATL12n] ATLAS Collaboration. *Measuring the b-tag efficiency in a top-pair sample with 4.7 fb^{-1} of data from the ATLAS detector*. Conference Note ATLAS-CONF-2012-097. CERN, July 2012 (cit. on pp. 100, 155).

[ATL12o] ATLAS Collaboration. "Observation of a new particle in the search for the Standard Model Higgs boson with the ATLAS detector at the LHC". *Phys.Lett.* B716 (2012), pp. 1–29. arXiv: `1207.7214 [hep-ex]` (cit. on p. 16).

[ATL12p] ATLAS Collaboration. *Performance of Missing Transverse Momentum Reconstruction in ATLAS with 2011 Proton-Proton Collisions at $\sqrt{s}$ = 7 TeV*. Conference Note ATLAS-COM-CONF-2012-105. CERN, June 2012 (cit. on p. 66).

[ATL12q] ATLAS Collaboration. "Performance of Missing Transverse Momentum Reconstruction in Proton-Proton Collisions at 7 TeV with ATLAS". *Eur. Phys. J.* C72 (2012), p. 1844. arXiv: `1108.5602 [hep-ex]` (cit. on p. 66).

[ATL12r] ATLAS Collaboration. *Statistical combination of top quark pair production cross-section measurements using dilepton, single-lepton, and all-hadronic final states at $\sqrt{s}$ = 7 TeV with the ATLAS detector*. Conference Note ATLAS-CONF-2012-024. CERN, Mar. 2012 (cit. on p. 30).

[ATL13a] ATLAS Collaboration. "Combined coupling measurements of the Higgs-like boson with the ATLAS detector using up to 25 fb^{-1} of proton-proton collision data" (2013) (cit. on p. 16).

[ATL13b] ATLAS Collaboration. "Study of the spin of the Higgs-like boson in the two photon decay channel using 20.7 fb-1 of pp collisions collected at $\sqrt{s}$ = 8 TeV with the ATLAS detector" (2013) (cit. on p. 16).

[ATL13e] ATLAS Collaboration. *Search for CP violation in single top quark events in pp collisions at $\sqrt{s}$ = 7 TeV with the ATLAS detector*. Conference Note ATLAS-CONF-2013-032. CERN, Mar. 2013 (cit. on p. 27).

[ATL96a] ATLAS Collaboration. *ATLAS liquid argon calorimeter: Technical design report*. Tech. rep. CERN, 1996 (cit. on pp. 51–53).

[ATL96b] ATLAS Collaboration. *ATLAS tile calorimeter: Technical design report*. Tech. rep. CERN, 1996 (cit. on p. 52).

[ATL96c] ATLAS Collaboration. *ATLAS calorimeter performance Technical Design Report*. Tech. rep. CERN, 1996 (cit. on pp. 51, 52).

[ATL97a] ATLAS Collaboration. *ATLAS inner detector: Technical design report. Vol. 1*. Tech. rep. CERN, 1997 (cit. on p. 48).

[ATL97b] ATLAS Collaboration. *ATLAS inner detector: Technical design report. Vol. 2*. Tech. rep. CERN, 1997 (cit. on p. 48).

[ATL97c] ATLAS Collaboration. *ATLAS magnet system: Technical design report*. Tech. rep. CERN, 1997 (cit. on p. 47).

[ATL97d] ATLAS Collaboration. *ATLAS barrel toroid: Technical design report*. Tech. rep. CERN, 1997 (cit. on p. 47).

[ATL97e] ATLAS Collaboration. *ATLAS endcap toroids: Technical design report*. Tech. rep. CERN, 1997 (cit. on p. 47).

[ATL97f] ATLAS Collaboration. *ATLAS central solenoid: Technical design report*. Tech. rep. CERN, 1997 (cit. on p. 47).

[ATL97g] ATLAS Collaboration. *ATLAS muon spectrometer: Technical Design Report*. Tech. rep. CERN, 1997 (cit. on p. 54).

[ATL98] ATLAS Collaboration. *ATLAS first level trigger: Technical design report*. Tech. rep. CERN, 1998 (cit. on pp. 56, 57).

[ATL99] ATLAS Collaboration. *ATLAS: Detector and physics performance technical design report. Volume 1*. Tech. rep. CERN, 1999 (cit. on pp. 43, 48, 51, 52, 54, 56, 57, 78).

[AV79] D. Amati and G. Veneziano. "Preconfinement as a Property of Perturbative QCD". *Phys. Lett.* B83 (1979), p. 87 (cit. on p. 74).

[Bal+10] R. D. Ball et al. "A first unbiased global NLO determination of parton distributions and their uncertainties". *Nucl.Phys.* B838 (2010), pp. 136–206. arXiv: `1002.4407 [hep-ph]` (cit. on p. 144).

[BB94] M. Beneke and V. M. Braun. "Heavy quark effective theory beyond perturbation theory: Renormalons, the pole mass and the residual mass term". *Nucl. Phys.* B426 (1994), pp. 301–343. arXiv: `hep-ph/9402364 [hep-ph]` (cit. on p. 19).

[Ber+12] J. Beringer et al. "Review of Particle Physics". *Phys. Rev. D* 86 (1 July 2012), p. 010001 (cit. on pp. 18, 43, 70).

[Beu+12] S. Beumler et al. *Kinematic Fitting of ATLAS Data Using the KinFitter Package*. Internal Note ATLAS-COM-PHYS-2012-1554. CERN, Oct. 2012 (cit. on pp. 115, 120–123).

[Beu10] S. Beumler. "Untersuchungen zur Bestimmung der Fehlidentifikationsraten von Leptonen im ATLAS-Experiment". M.Sc. thesis. Humboldt-Universität zu Berlin, 2010 (cit. on pp. 115, 135).

[BFS96] J. Butterworth, J. R. Forshaw, and M. Seymour. "Multiparton interactions in photoproduction at HERA". *Z. Phys.* C72 (1996), pp. 637–646. arXiv: `hep-ph/9601371 [hep-ph]` (cit. on p. 77).

[Bil10] S. Bilski. "Z-Rekonstruktion aus Elektronen und Myonen bei ATLAS". B.Sc. thesis. Humboldt-Universität Berlin, 2010 (cit. on p. 115).

[Bil12] S. Bilski. "Studien zur elektroschwachen Produktion von Top-Quarks in Proton-Proton-Stößen bei ATLAS". M.Sc. thesis. Humboldt-Universität zu Berlin, 2012 (cit. on p. 118).

[Bin11] C. Bini. *Study of the performance of the ATLAS Muon Spectrometer*. Internal Note ATLAS-COM-MUON-2011-035. CERN, Nov. 2011 (cit. on p. 54).

[Bir+05] I. Bird et al. *LHC computing Grid. Technical design report*. Tech. rep. CERN, 2005 (cit. on p. 58).

[Bly12] S. Blyweert. *Top Quark Mass Measurements at the LHC*. Talk presented at the Moriond QCD and High Energy Interactions Conference, La Thuile, France. 2012 (cit. on p. 18).

[Bol11] D. Boline. "Measurement of the W Boson Mass and Width at the D0 Experiment". *DPF-2011 Conference*. FERMILAB-CONF-11-526-E. 2011. arXiv: `1110.1093 [hep-ex]` (cit. on p. 22).

[Bot+11] M. Botje et al. "The PDF4LHC Working Group Interim Recommendations" (2011). arXiv: `1101.0538 [hep-ph]` (cit. on p. 144).

[Bou+10] J. Boudreau et al. *A search for CP violation in t-channel single top quark decays in pp collisions at $\sqrt{s}$ = 7 TeV using the ATLAS detector*. Internal Note ATLAS-COM-PHYS-2012-001. CERN, Dec. 2010 (cit. on p. 26).

[Bou+12] J. Boudreau et al. *Measurement of the b-tag Efficiency in a Sample of Jets Containing Muons with 5 fb^{-1} of Data from the ATLAS Detector*. Internal Note ATLAS-COM-CONF-2012-021. CERN, Feb. 2012 (cit. on pp. 60, 100).

[Bru+04] O. S. Brüning et al. *LHC Design Report*. CERN, 2004 (cit. on pp. 41, 43).

[Buc+11a] A. Buckley et al. "General-purpose event generators for LHC physics". *Phys. Rept.* 504 (2011), pp. 145–233. arXiv: `1101.2599 [hep-ph]` (cit. on pp. 71, 76, 77, 145).

[Buc+11b] A. Buckley et al. *ATLAS tunes of PYTHIA 6 and Pythia 8 for MC11*. Internal Note ATLAS-COM-PHYS-2011-744. CERN, June 2011 (cit. on p. 76).

[But+10] J. Butterworth et al. *Single Boson and Diboson Production Cross Sections in pp Collisions at $\sqrt{s}$ =7 TeV*. Internal Note ATLAS-COM-PHYS-2010-695. CERN, Aug. 2010 (cit. on p. 158).

[Cac+04] M. Cacciari et al. "The t anti-t cross-section at 1.8 TeV and 1.96 TeV: A Study of the systematics due to parton densities and scale dependence". *JHEP* 0404 (2004), p. 068. arXiv: `hep-ph/0303085 [hep-ph]` (cit. on p. 30).

[Cam+09] J. M. Campbell et al. "Next-to-Leading-Order Predictions for t-Channel Single-Top Production at Hadron Colliders". *Phys.Rev.Lett.* 102 (2009), p. 182003. arXiv: `0903.0005 [hep-ph]` (cit. on p. 145).

[Cao+03] J.-j. Cao et al. "Supersymmetric effects in top quark decay into polarized W boson". *Phys. Rev.* D68 (2003), p. 054019. arXiv: `hep-ph/0306278 [hep-ph]` (cit. on p. 25).

[CDF04] CDF and D0 and Tevatron Electroweak Working Group. *Combination of CDF and D0 results on the top-quark mass*. Public Note. 2004. arXiv: `hep-ex/0404010 [hep-ex]` (cit. on p. 18).

[CDF08] CDF Collaboration. "Measurement of the Single Top Quark Production Cross Section at CDF". *Phys. Rev. Lett.* 101 (2008), p. 252001. arXiv: `0809.2581 [hep-ex]` (cit. on pp. 35, 36).

[CDF09] CDF and D0 and Tevatron Electroweak Working Group. *Combination of CDF and D0 Measurements of the Single Top Production Cross Section*. Public Note. 2009. arXiv: `0908.2171 [hep-ex]` (cit. on pp. 22, 35, 36).

[CDF10] CDF Collaboration. "Observation of Single Top Quark Production and Measurement of $|V_{\mathrm{tb}}|$ with CDF". *Phys. Rev.* D82 (2010), p. 112005. arXiv: `1004.1181 [hep-ex]` (cit. on pp. 21, 22).

[CDF12] CDF Collaboration, D0 Collaboration. "Combination of CDF and D0 measurements of the W boson helicity in top quark decays". *Phys. Rev. D* 85 (2012). arXiv: `1202.5272 [hep-ex]` (cit. on p. 23).

[CDF13] CDF Collaboration. *Measurement of Single Top Quark Production in 7.5 fb^{-1} of CDF Data Using Neural Networks*. Tech. rep. CDF/PUB/TOP/PUBLIC/10793. Tevatron, 2013 (cit. on pp. 22, 183).

[CDF95] CDF Collaboration. "Observation of Top Quark Production in $\bar{\mathrm{p}}\mathrm{p}$ Collisions with the Collider Detector at Fermilab". *Phys. Rev. Lett.* 74 (14 Apr. 1995), pp. 2626–2631 (cit. on pp. 18, 29).

[CE00] J. M. Campbell and R. K. Ellis. "Radiative corrections to Z b anti-b production". *Phys.Rev.* D62 (2000), p. 114012. arXiv: `hep-ph/0006304 [hep-ph]` (cit. on p. 145).

[CE10] J. M. Campbell and R. Ellis. "MCFM for the Tevatron and the LHC". *Nucl.Phys.Proc.Suppl.* 205-206 (2010), pp. 10–15. arXiv: `1007.3492 [hep-ph]` (cit. on p. 145).

[CGM98] J. M. Campbell, E. N. Glover, and C. Maxwell. "Determination of Λ_{QCD} from the measured energy dependence of <1 - thrust>". *Phys. Rev. Lett.* 81 (1998), pp. 1568–1571. arXiv: `hep-ph/9803254 [hep-ph]` (cit. on p. 73).

[CHS07] J. M. Campbell, J. Huston, and W. Stirling. "Hard Interactions of Quarks and Gluons: A Primer for LHC Physics". *Rept.Prog.Phys.* 70 (2007), p. 89. arXiv: `hep-ph/0611148 [hep-ph]` (cit. on p. 144).

[CLY05] C.-R. Chen, F. Larios, and C.-P. Yuan. "General analysis of single top production and W helicity in top decay". *Phys. Lett.* B631 (2005), pp. 126–132. arXiv: `hep-ph/0503040 [hep-ph]` (cit. on pp. 24, 25).

[CMS08] CMS Collaboration. "The CMS experiment at the CERN LHC". *JINST* 3 (2008), S08004 (cit. on p. 41).

[CMS10] CMS Collaboration. "Performance of the particle flow algorithm in CMS". *PoS* ICHEP2010 (2010), p. 002 (cit. on p. 185).

[CMS11a] CMS Collaboration. "Measurement of the t-channel single top quark production cross section in pp collisions at $\sqrt{s} = 7$ TeV". *Phys. Rev. Lett.* 107 (2011), p. 091802. arXiv: `1106.3052 [hep-ex]` (cit. on pp. 35, 36).

[CMS11b] CMS Collaboration. "Measurement of the $\mathrm{t\bar{t}}$ production cross section and the top quark mass in the dilepton channel in pp collisions at $\sqrt{s} = 7$ TeV". *J. High Energy Phys.* (May 2011). arXiv: `1105.5661 [hep-ex]` (cit. on p. 18).

[CMS12a] CMS Collaboration. "Measurement of the single-top-quark t-channel cross section in pp collisions at $\sqrt{s} = 7$ TeV". *JHEP* 1212 (2012), p. 035. arXiv: `1209.4533 [hep-ex]` (cit. on pp. 21, 22, 35, 36, 182, 183).

[CMS12b] CMS Collaboration. "Observation of a new boson at a mass of 125 GeV with the CMS experiment at the LHC". *Phys.Lett.* B716 (2012), pp. 30–61. arXiv: `1207.7235 [hep-ex]` (cit. on p. 16).

[CMS13a] CMS Collaboration. *Measurement of the single-top t-channel charge ratio at 8 TeV*. Tech. rep. CMS-PAS-TOP-12-038. CERN, 2013 (cit. on p. 183).

[CMS13b] CMS Collaboration. *Measurement of top quark polarization in t-channel single-top production*. Tech. rep. CMS-PAS-TOP-13-001. CERN, 2013 (cit. on p. 26).

[Cor+01] G. Corcella et al. "HERWIG 6: An Event generator for hadron emission reactions with interfering gluons (including supersymmetric processes)". *JHEP* 0101 (2001), p. 010. arXiv: `hep-ph/0011363 [hep-ph]` (cit. on pp. 71, 77).

[Cos+05] D. Costanzo et al. *Validation of the GEANT4-Based Full Simulation Program for the ATLAS Detector: An Overview of Performance and Robustness*. Public Note CERN-ATLAS-SOFT-PUB-2005-002. CERN, Mar. 2005 (cit. on p. 78).

[Cow+11] G. Cowan et al. "Asymptotic formulae for likelihood-based tests of new physics". *Eur.Phys.J.* C71 (2011), p. 1554. arXiv: `1007.1727 [physics.data-an]` (cit. on p. 163).

[CS12] G. Chiodini and S. Spagnolo. *ATLAS RPC time-of-flight performance*. Internal Note ATLAS-COM-MUON-2012-001. CERN, Jan. 2012 (cit. on p. 54).

[CSS08] M. Cacciari, G. P. Salam, and G. Soyez. "The Anti-k(t) jet clustering algorithm". *JHEP* 0804 (2008), p. 063. arXiv: `0802.1189 [hep-ph]` (cit. on p. 63).

[CSS86] J. C. Collins, D. E. Soper, and G. F. Sterman. "Heavy Particle Production in High-Energy Hadron Collisions". *Nucl. Phys.* B263 (1986), p. 37 (cit. on p. 28).

[D0 07] D0 Collaboration. "Search for production of single top quarks via tcg and tug flavor- changing neutral current couplings". *Phys.Rev.Lett.* 99 (2007), p. 191802. arXiv: `hep-ex/0702005 [hep-ex]` (cit. on p. 38).

[D0 09] D0 Collaboration. "Observation of Single Top-Quark Production". *Phys. Rev. Lett.* 103 (9 Aug. 2009), p. 092001 (cit. on pp. 35, 36).

[D0 11] D0 Collaboration. "Measurements of single top quark production cross sections and $|V_{tb}|$ in $p\bar{p}$ collisions at $\sqrt{s} = 1.96$ TeV". *Phys. Rev.* D84 (2011), p. 112001. arXiv: `1108.3091 [hep-ex]` (cit. on pp. 21, 22).

[D0 12a] D0 Collaboration. "An Improved determination of the width of the top quark". *Phys. Rev.* D85 (2012), p. 091104. arXiv: `1201.4156 [hep-ex]` (cit. on p. 20).

[D0 12b] D0 Collaboration. "Combination of searches for anomalous top quark couplings with 5.4 fb^{-1} of $p\bar{p}$ collisions". *Phys. Lett.* B713 (2012). arXiv: `1204.2332 [hep-ex]` (cit. on p. 27).

[D0 13] D0 Collaboration. "Evidence for s-channel single top quark production in $p\bar{p}$ collisions at $\sqrt{s} = 1.96\,\text{TeV}$" (2013). arXiv: `1307.0731 [hep-ex]` (cit. on pp. 22, 37, 39, 183).

[D0 95] D0 Collaboration. "Observation of the Top Quark". *Phys. Rev. Lett.* 74 (14 Apr. 1995), pp. 2632–2637 (cit. on pp. 18, 29).

[Dob+04] M. Dobbs et al. "Les Houches guidebook to Monte Carlo generators for hadron collider physics". *3rd Les Houches Workshop: Physics at TeV Colliders*. 2004, pp. 411–459. arXiv: `hep-ph/0403045 [hep-ph]` (cit. on p. 70).

[Dok77] Y. L. Dokshitzer. "Calculation of the Structure Functions for Deep Inelastic Scattering and $e+$ $e-$ Annihilation by Perturbation Theory in Quantum Chromodynamics." *Sov. Phys. JETP* 46 (1977), pp. 641–653 (cit. on p. 73).

[Dol09] I. Dolenc. "The ATLAS Beam Condition and Beam Loss Monitors". *Como 2009, Astroparticle, particle and space physics, detectors and medical physics applications* (2009), pp. 443–448 (cit. on p. 45).

[Eid+04] S. Eidelman et al. “Review of Particle Physics. The Particle Data Group”. *Phys. Lett.* B592 (2004), p. 1 (cit. on pp. 20, 21).

[FC98] G. J. Feldman and R. D. Cousins. “A Unified Approach to the Classical Statistical Analysis of Small Signals”. *Phys.Rev.* D57 (1998), pp. 3873–3889. arXiv: `physics/9711021 [physics.data-an]` (cit. on p. 102).

[Fis+01] M. Fischer et al. “Longitudinal, transverse-plus and transverse-minus W bosons in unpolarized top quark decays at $O(\alpha_s)$”. *Phys. Rev. D* 63 (3 Jan. 2001), p. 031501 (cit. on p. 23).

[Fla+09] H. Flacher et al. “Revisiting the Global Electroweak Fit of the Standard Model and Beyond with Gfitter”. *Eur. Phys. J.* C60 (2009), pp. 543–583. arXiv: `0811.0009 [hep-ph]` (cit. on pp. 16, 19).

[FNO07] S. Frixione, P. Nason, and C. Oleari. “Matching NLO QCD computations with Parton Shower simulations: the POWHEG method”. *JHEP* 0711 (2007), p. 070. arXiv: `0709.2092 [hep-ph]` (cit. on pp. 77, 145).

[FW02] S. Frixione and B. R. Webber. “Matching NLO QCD computations and parton shower simulations”. *JHEP* 0206 (2002), p. 029. arXiv: `hep-ph/0204244 [hep-ph]` (cit. on pp. 71, 76).

[FW80] G. C. Fox and S. Wolfram. “A Model for Parton Showers in QCD”. *Nucl. Phys.* B168 (1980), p. 285 (cit. on p. 74).

[FW83] R. D. Field and S. Wolfram. “A QCD Model for $e+$ $e-$ Annihilation”. *Nucl. Phys.* B213 (1983), p. 65 (cit. on p. 74).

[Gao+13] J. Gao et al. “The CT10 NNLO Global Analysis of QCD” (2013). arXiv: `1302.6246 [hep-ph]` (cit. on p. 34).

[GL72] V. Gribov and L. Lipatov. “Deep inelastic e p scattering in perturbation theory”. *Sov. J. Nucl. Phys.* 15 (1972), pp. 438–450 (cit. on p. 73).

[Gol61] J. Goldstone. “Field Theories with Superconductor Solutions”. *Nuovo Cim.* 19 (1961), pp. 154–164 (cit. on p. 16).

[GP88] G. Gustafson and U. Pettersson. “Dipole Formulation of QCD Cascades”. *Nucl. Phys.* B306 (1988), p. 746 (cit. on p. 73).

[Gro10] J. Groth-Jensen. “Luminosity determination and simulation of the LUCID detector at the ATLAS experiment”. PhD thesis. Lund Univ., 2010 (cit. on p. 45).

[GSW62] J. Goldstone, A. Salam, and S. Weinberg. “Broken Symmetries”. *Phys. Rev.* 127 (1962), pp. 965–970 (cit. on p. 16).

[H1 97] H1 Collaboration. “The H1 detector at HERA”. *Nucl. Instrum. Meth.* A386 (1997), pp. 310–347 (cit. on p. 28).

[Hed11] V. Hedberg. “Precision measurement of the luminosity in the ATLAS experiment”. *PoS* EPS-HEP2011 (2011), p. 4 (cit. on p. 45).

[Hei12] L. Heinrich. "From Top To Bottom: Calibration of b-tagging Algorithms via a Kinematic Fit of Top Quark Pair Decays". M.Sc. thesis. Humboldt-Universität zu Berlin, 2012 (cit. on pp. 97, 100, 115, 139).

[Hir10] F. Hirsch. "Tracking and Vertexing with the ATLAS Detector at the LHC". *5th International Workshop on Semiconductor Pixel Detectors for Particles and Imaging*. ATLAS-INDET-PROC-2010-033. Oct. 2010 (cit. on p. 59).

[JK89] M. Jezabek and J. H. Kuhn. "QCD Corrections to Semileptonic Decays of Heavy Quarks". *Nucl. Phys.* B314 (1989), p. 1 (cit. on p. 20).

[JR75] F. James and M. Roos. "Minuit: A System for Function Minimization and Analysis of the Parameter Errors and Correlations". *Comput.Phys.Commun.* 10 (1975), pp. 343–367 (cit. on p. 160).

[JS92] G. Jikia and S. Slabospitsky. "Single top production at hadron UNK collider". *Sov. J. Nucl. Phys.* 55 (1992), pp. 1387–1392 (cit. on p. 21).

[Kan+13] P. Kant et al. "HATHOR for Single-Top Production". *Paper in Preparation* (2013), p. 33 (cit. on pp. 34, 35, 183, 184).

[KI12] J. Kretzschmar and L. Iconomidou-Fayard. *Electron performances measurements using the 2011 LHC proton-proton collisions*. Internal Note ATLAS-COM-PHYS-2012-1024. CERN, July 2012 (cit. on p. 62).

[Kid06] N. Kidonakis. "Single top production at the Tevatron: Threshold resummation and finite-order soft gluon corrections". *Phys. Rev.* D74 (2006), p. 114012. arXiv: `hep-ph/0609287 [hep-ph]` (cit. on pp. 28, 37).

[Kid10a] N. Kidonakis. "NNLL resummation for s-channel single top quark production". *Phys.Rev.* D81 (2010), p. 054028. arXiv: `1001.5034 [hep-ph]` (cit. on pp. 34, 35).

[Kid10b] N. Kidonakis. "Two-loop soft anomalous dimensions for single top quark associated production with a W- or H-". *Phys.Rev.* D82 (2010), p. 054018. arXiv: `1005.4451 [hep-ph]` (cit. on pp. 34, 35).

[Kid11] N. Kidonakis. "Next-to-next-to-leading-order collinear and soft gluon corrections for t-channel single top quark production". *Phys.Rev.* D83 (2011), p. 091503. arXiv: `1103.2792 [hep-ph]` (cit. on pp. 34, 35).

[Kid12] N. Kidonakis. "Differential and total cross sections for top pair and single top production". *20th International Workshop on Deep-Inelastic Scattering and Related Subjects (DIS 2012)*. 2012. arXiv: `1205.3453 [hep-ph]` (cit. on pp. 34, 35, 158, 184).

[Kin10] T. Kintscher. "Rekonstruktion von Lambda-Zerfällen zur Untersuchung von Elektronfehlidentifikationen durch Protonen bei ATLAS ". B.Sc. thesis. Humboldt-Universität zu Berlin, 2010 (cit. on p. 115).

[KLY92] G. L. Kane, G. Ladinsky, and C. Yuan. "Using the Top Quark for Testing Standard Model Polarization and CP Predictions". *Phys.Rev.* D45 (1992), pp. 124–141 (cit. on p. 181).

[KM73] M. Kobayashi and T. Maskawa. "CP Violation in the Renormalizable Theory of Weak Interaction". *Prog. Theor. Phys.* 49 (1973), pp. 652–657 (cit. on p. 16).

[KR04] B. P. Kersevan and E. Richter-Was. "The Monte Carlo event generator AcerMC version 2.0 with interfaces to PYTHIA 6.2 and HERWIG 6.5" (2004). arXiv: `hep-ph/0405247 [hep-ph]` (cit. on pp. 71, 76).

[Kuh96] J. H. Kuhn. "Theory of top quark production and decay." *Stanford 1995, The top quark and the electroweak interaction*. 1996. arXiv: `hep-ph/9707321 [hep-ph]` (cit. on p. 20).

[Lac12] V. Lacuesta. *Performance of ATLAS tracking detector*. Internal Note ATLAS-COM-INDET-2012-067. CERN, Sept. 2012 (cit. on p. 48).

[Lai+10] H.-L. Lai et al. "New parton distributions for collider physics". *Phys. Rev.* D82 (2010), p. 074024. arXiv: `1007.2241 [hep-ph]` (cit. on pp. 77, 144, 182).

[Lam+08] W. Lampl et al. *Calorimeter Clustering Algorithms: Description and Performance*. Tech. rep. ATL-LARG-PUB-2008-002. ATL-COM-LARG-2008-003. CERN, Apr. 2008 (cit. on p. 62).

[LHC08] LHCb Collaboration. "The LHCb Detector at the LHC". *JINST* 3 (2008), S08005 (cit. on p. 41).

[LMU09] U. Langenfeld, S. Moch, and P. Uwer. "Measuring the running top-quark mass". *Phys. Rev.* D80 (2009), p. 054009. arXiv: `0906.5273 [hep-ph]` (cit. on pp. 30, 31).

[LMU10] U. Langenfeld, S.-O. Moch, and P. Uwer. "Measuring the running Top quark mass". *45th Rencontres de Moriond: QCD and High Energy Interactions*. 2010. arXiv: `1006.0097 [hep-ph]` (cit. on p. 19).

[Lou96] C. Lourenco. "Heavy ion collisions at the LHC: The Alice experiment" (1996), pp. 491–496. arXiv: `hep-ph/9612221 [hep-ph]` (cit. on p. 41).

[LS12] A. Lleres and X. Sun. *Measurement of the Single Top-Quark Polarization with 4.7 fb^{-1}*. Internal Note ATLAS-COM-PHYS-2012-496. CERN, May 2012 (cit. on p. 26).

[Lyo96] L. Lyons. *Statistics for Nuclear and Particle Physics*. 1st ed. Cambridge University Press, 1996 (cit. on p. 110).

[Man+03] M. L. Mangano et al. "ALPGEN, a generator for hard multiparton processes in hadronic collisions". *JHEP* 0307 (2003), p. 001. arXiv: `hep-ph/0206293 [hep-ph]` (cit. on pp. 71, 77).

[Mar+09a] A. Martin et al. "Parton distributions for the LHC". *Eur.Phys.J.* C63 (2009), pp. 189–285. arXiv: 0901.0002 [hep-ph] (cit. on p. 34).

[Mar+09b] A. Martin et al. "Uncertainties on α_s in global PDF analyses and implications for predicted hadronic cross sections". *Eur.Phys.J.* C64 (2009), pp. 653–680. arXiv: 0905.3531 [hep-ph] (cit. on p. 144).

[Mik12] G. Mikenberg. *Improved Performance of the ATLAS MUON Spectrometer*. Internal Note ATLAS-COM-MUON-2011-041. CERN, Dec. 2012 (cit. on p. 54).

[Nad+08] P. M. Nadolsky et al. "Implications of CTEQ global analysis for collider observables". *Phys. Rev.* D78 (2008), p. 013004. arXiv: 0802.0007 [hep-ph] (cit. on pp. 29, 30).

[Nak+10] K. Nakamura et al. "Review of Particle Physics. The Particle Data Group". *J. Phys* G37 (2010), p. 075021 (cit. on pp. 123, 125).

[Nas04] P. Nason. "A New method for combining NLO QCD with shower Monte Carlo algorithms". *JHEP* 0411 (2004), p. 040. arXiv: hep-ph/0409146 [hep-ph] (cit. on p. 145).

[NP33] J. Neyman and E. Pearson. "On the Problem of the Most Efficient Tests of Statistical Hypotheses". *Philosophical Transactions of the Royal Society of London. Series A, Containing Papers of a Mathematical or Physical Character* 231 (1933), pp. 289–337 (cit. on p. 163).

[Per+75] M. L. Perl et al. "Evidence for Anomalous Lepton Production in $e^+ - e^-$ Annihilation". *Phys. Rev. Lett.* 35 (22 Dec. 1975), pp. 1489–1492 (cit. on p. 17).

[Ple09] M.-A. Pleier. "Review of Properties of the Top Quark from Measurements at the Tevatron". *Int. J. Mod. Phys.* A24 (2009), pp. 2899–3037. arXiv: 0810.5226 [hep-ex] (cit. on pp. 79, 81).

[Pro12] U. Prosperi-Porta. "Studien zur Abschätzung des QCD-Untergrundes elektroschwacher Top-Produktion bei ATLAS". M.Sc. thesis. Humboldt-Universität zu Berlin, 2012 (cit. on pp. 123, 147).

[PS95] M. Peskin and D. Schroeder. *An Introduction to Quantum Field Theory*. 1st ed. Perseus Books, 1995 (cit. on p. 24).

[Rie10] P. Rieck. "Entwicklung eines kinematischen Fits zur Untersuchung elektroschwacher Top-Quark-Produktion bei ATLAS". M.Sc. thesis. Humboldt-Universität zu Berlin, 2010 (cit. on pp. 115, 124, 125).

[Rom+11] G. Romeo et al. *Jet Energy Resolution from In-situ Techniques with the ATLAS Detector Using Proton-Proton Collisions at a Center of Mass Energy $\sqrt{s}$ = 7 TeV*. Internal Note ATLAS-COM-PHYS-2011-240. CERN, Mar. 2011 (cit. on p. 152).

[Sar12b] G. Sartisohn. "Higgs Boson Search in the H→WW$^{(*)}$ → $\ell\nu\ell\nu$ Channel using Neural Networks with the ATLAS Detector at 7 TeV". PhD thesis. Berg. Univ. Wuppertal, Mar. 2012 (cit. on pp. 157, 163).

[Sch10] A.-S. Schade. "Rekonstruktion von Kaonspuren bei ATLAS für Analysen zur Elektronfehlidentifikation". B.Sc. thesis. Humboldt-Universität zu Berlin, 2010 (cit. on p. 115).

[SG09] J. Sundermann and T. Goepfert. *KinFitter – A Kinematic Fit with Constraints*. Internal Note ATLAS-COM-SOFT-2009-014. CERN, Sept. 2009 (cit. on pp. 113, 114).

[Sjo12] T. Sjöstrand. *Why MB/UE physics prefer LO PDFs*. Private Communication. June 2012 (cit. on p. 71).

[SL94] T. Stelzer and W. Long. "Automatic generation of tree level helicity amplitudes". *Comput. Phys. Commun.* 81 (1994), pp. 357–371. arXiv: `hep-ph/9401258 [hep-ph]` (cit. on p. 76).

[SMS06] T. Sjöstrand, S. Mrenna, and P. Z. Skands. "PYTHIA 6.4 Physics and Manual". *JHEP* 0605 (2006), p. 026. arXiv: `hep-ph/0603175 [hep-ph]` (cit. on pp. 76, 77).

[Sol12] C. Solans. *Status of the Atlas Calorimeters: their performance after two years of LHC operation and plans for future upgrades.* Internal Note ATLAS-COM-CAL-2012-006. CERN, June 2012 (cit. on pp. 51, 52).

[ST08] A. Sherstnev and R. Thorne. "Different PDF approximations useful for LO Monte Carlo generators". *16th International Workshop on Deep Inelastic Scattering and Related Subjects (DIS 2008)*. 2008, p. 149. arXiv: `0807.2132 [hep-ph]` (cit. on p. 76).

[Sta13b] S. Stamm. "Studien zur Signalextraktion elektroschwacher Top-Quark-Produktion bei ATLAS". M.Sc. thesis. Humboldt-Universität zu Berlin, 2013 (cit. on pp. 58, 145, 147, 158, 169, 188, 189, 192).

[SW07] P. Z. Skands and D. Wicke. "Non-perturbative QCD effects and the top mass at the Tevatron". *Eur. Phys. J.* C52 (2007), pp. 133–140. arXiv: `hep-ph/0703081 [hep-ph]` (cit. on p. 19).

[Tev11] Tevatron Electroweak Working Group, for the CDF and D0 Collaborations. *Combination of CDF and D0 results on the mass of the top quark using up to 5.8 fb^{-1} of data*. Public Note FERMILAB-TM-2504-E, CDF-NOTE-10549, D0-NOTE-6222. 2011. arXiv: `1107.5255 [hep-ex]` (cit. on p. 18).

[Tho11] F. Thomas. "Study of the Properties of Additional Jets in Top Pair Events with the ATLAS Detector". M.Sc. thesis. Technische Universität Dresden, 2011 (cit. on pp. 115, 138, 139).

[TY00] T. M. Tait and C.-P. Yuan. "Single top quark production as a window to physics beyond the standard model". *Phys.Rev.* D63 (2000), p. 014018. arXiv: `hep-ph/0007298 [hep-ph]` (cit. on pp. 26, 32–34, 37, 38).

[Van+07] N. Van Eldik et al. "The ATLAS muon spectrometer: calibration and pattern recognition". PhD thesis. Univ. Amsterdam, Feb. 2007 (cit. on p. 64).

[Vre13] M. Vreeswijk. *Charge Dependence of the Heavy Flavour Fractions of W+Jets*. Private Communication. Jan. 2013 (cit. on p. 87).

[Wag11] W. Wagner. *BILL Tutorial*. Private Communication. Sept. 2011 (cit. on p. 157).

[Was12] C. Wasicki. *Track and vertex reconstruction of the ATLAS Inner Detector in the high multiplicity LHC environment*. Internal Note ATLAS-PHYS-PROC-2012-111. CERN, June 2012 (cit. on p. 59).

[Wat12] G. Watt. "MSTW PDFs and impact of PDFs on cross sections at Tevatron and LHC". *Nucl. Phys. Proc. Suppl.* 222-224 (2012), pp. 61–80. arXiv: `1201.1295 [hep-ph]` (cit. on pp. 29, 30).

[WBG05] M. Whalley, D. Bourilkov, and R. Group. "The Les Houches accord PDFs (LHAPDF) and LHAGLUE" (2005). arXiv: `hep-ph/0508110 [hep-ph]` (cit. on p. 144).

[WZQ05] X.-l. Wang, Q.-l. Zhang, and Q.-p. Qiao. "Studying top quark decay into the polarized W^- boson in the TC2 model". *Phys. Rev.* D71 (2005), p. 014035. arXiv: `hep-ph/0501145 [hep-ph]` (cit. on p. 25).

[ZEU92] ZEUS Collaboration. *The ZEUS experiment at HERA*. Conference Note. 1992, pp. 137–145 (cit. on p. 28).

List of Figures

List of Tables

Acknowledgements

During the time of this study I was supported by so many wonderful people whose contributions should not go unnoticed here:

Above all, I thank Thomas Lohse for giving me the opportunity to enter this exciting field of research and complete the thesis at hand. I also wish to thank him for many helpful discussions – not only on the topic of this work. I am deeply grateful to Oliver Kind for patiently supervising my efforts, constantly offering assistance with all kinds of topical, computational and organizational issues as well as the overall encouragement and just being such a great colleague.

Many thanks also go to Heiko Lacker, Klaus Mönig and Ulrich Husemann for impulses on the analysis side. I am very thankful to Martin zur Nedden for organizing my trigger shifts and for many interesting conversations. I furthermore like to thank Michelangelo Giorgi very much for the continuous fruitful collaboration on the analysis, for the help with getting the show on the road at CERN and for being so fun and keeping my spirits up in hard times. I am much obliged to Patrick Rieck, Felix Thomas, Steven Bilski, Umberto Prosperi-Porta and Sören Stamm as well as to Rocco Mandrysch and Dennis Wendland for their valuable contributions to the analysis framework and support beyond that. I want to thank Holger Schulz for his comments on the MC generation process and Thomas Kintscher for information on the signal cross-section prediction.

Furthermore, I am grateful for the companionship of Andrii Nikiforov and Sergio Grancagnolo who shared the office with me at Humboldt University and at CERN, respectively, and also helped me on several occasions. Last, but not least, I thank Veronika Fetting for her organisational and Olf Epler for his computational support at Humboldt University.

I am proud to be able to thank all of the above as well as the rest of the Humboldt group for their friendship and letting me have a marvellous time!

Many thanks go to the ATLAS collaboration and to CERN for providing the basis for the analysis. This study received funding from the Bundesministerium für Bildung und Forschung.

Thanks to Oliver Kind and to Sebastian Schubert for proofreading and formatting of this thesis.

My final thanks go to my husband Sebastian Schubert and my whole family for their tireless support and endurance and for their love, and to Senta Schubert for letting me finish this work.